The Coevolution of AGN and Their Host Galaxies in Late Stage Mergers

by

Aaron Stemo

B.S., University of Wisconsin, 2015

M.S., University of Colorado, 2018

A thesis submitted to the

Faculty of the Graduate School of the

University of Colorado in partial fulfillment

of the requirements for the degree of

Doctor of Philosophy

Department of Astrophysical and Planetary Sciences

2021

Committee Members:

Julia Comerford, Chair

Dr. Mitchell Begelman

Dr. Jeremy Darling

Dr. Ann-Marie Madigan

Dr. Daniel Stern

Stemo, Aaron (Ph.D., Astrophysical and Planetary Sciences)

The Coevolution of AGN and Their Host Galaxies in Late Stage Mergers

Thesis directed by Dr. Julia Comerford

As galaxies grow and evolve, the supermassive black holes (SMBHs) thought to exist at the center of most galaxies coevolve with them. During periods of growth, these SMBHs can become observable as active galactic nuclei (AGN). My work is focused on studying and understanding the environmental factors that precipitate AGN – galaxy coevolution, and the precise manner in which this coevolution takes place. The first work I present focuses on understanding how a general population of AGN coevolve with their host galaxies; specifically, how AGN luminosity, as a proxy for SMBH growth, relates to host galaxy parameters, such as star formation, in a general AGN population. I then shift my focus to how AGN coevolve with their host galaxies during galaxy merger events. The second work presented is centered around identifying a large sample of AGN host galaxies currently in late-stage mergers — a task that has presented considerable difficulties in the past — and then using this sample to study how AGN coevolve with their host galaxies as a function of their merger environment. The last work I present builds on the previous work by further classifying these AGN host merger systems as either offset AGN or dual AGN systems. This allows me to add nuance to previous findings and further probe key aspects of AGN activation and galaxy coevolution during late stage mergers. Finally, I discuss exciting avenues of future research that can build upon my past work, and expand our knowledge of SMBH – galaxy coevolution. This thesis reflects the entirety of my graduate work, focused on studying the coevolution of AGN and their host galaxies through the rigorous identification and analysis of AGN and the mergers of their host galaxies.

Acknowledgements

First of all, I'd like to thank my advisor, Julie Comerford, for being a great mentor who has always done an amazing job of providing support, instruction, and advice, all while being compassionate and kind; your constant excellence uplifts our department, CU Boulder, and the lives of your students and colleagues. In addition, I'd like to thank all of my colleagues and collaborators; you have taught me and supported me throughout this journey and I look forward to being able to continue working with you far into the future.

I'd also like to thank my family for being a source of constant support; while I may not always be in the same state (or even country), I know that you are there if I need you, and I hope you know the same. The same is true of all of my friends. Moving around a lot has given me the chance to meet a number of great people; and while it's sad to constantly have to say goodbye, know that I think of you often and fondly, and am always looking forward to the next time we chat or see each other again.

Last, I'd like to acknowledge all the dogs that have ever been a part of my life and provided me with happiness, comfort, joy, and companionship. You kept me going; I love and miss you all. Thank you Paisley, Lyla, Lambeau, Hershey, Foxy, and all the others I knew for a few minutes or a few years.

Contents

Chapter

1 Introduction **1**

1.1 Galaxy Structure and Evolution 1

1.2 Active Galactic Nuclei and Selection Techniques 6

1.3 AGN – Galaxy Coevolution 12

1.4 Overview of This Dissertation 19

2 A Catalog of AGN Host Galaxies Observed with HST/ACS: Correlations between Star Formation and AGN Activity **22**

2.1 Introduction 23

2.2 Parent Galaxy Sample 26

2.3 Active Galaxy Selection 26

2.3.1 Infrared AGN Selection 27

2.3.2 X-Ray AGN Selection 29

2.3.3 AGN Selection Comparison 30

2.4 Obtaining Galaxy SEDs 31

2.4.1 Photometric Data 32

2.4.2 SED Fitting 33

2.4.3 Monte Carlo Error Estimation 34

2.5 Galaxy Properties 34

2.5.1 Redshift (z) . . . 37
2.5.2 AGN Bolometric Luminosity ($L_{\rm AGN}$) . . . 39
2.5.3 Stellar Mass (M_*) . . . 41
2.5.4 Star Formation Rate (SFR) . . . 42
2.5.5 Nuclear Column Density ($N_{\rm H}$) . . . 44
2.5.6 Comparison to Other Work . . . 45
2.6 Results . . . 46
2.6.1 Galaxies Hosting AGNs Have Lower SFRs . . . 49
2.6.2 SFR and SMBH Growth are Correlated . . . 52
2.7 Conclusions . . . 56

3 A Catalog of 204 Offset and Dual AGNs: Increased AGN Activation in Major Mergers and Separations under 4 kpc 58

3.1 Introduction . . . 59
3.2 Initial Galaxy Sample . . . 62
3.3 Galaxy Modeling & Merger Identification . . . 63
3.3.1 Galaxy Tiling . . . 64
3.3.2 Source Identification and Fitting . . . 67
3.3.3 False Positive Reduction . . . 71
3.4 Bias Analysis & Correction . . . 73
3.4.1 Simulating Galaxy Mergers . . . 74
3.4.2 Modeling the Simulated Mergers . . . 76
3.4.3 Correcting for Selection Biases . . . 76
3.5 Merging Galaxy Properties & Comparison to ACS-AGN Sample . . . 79
3.5.1 Obtaining Merger Parameters . . . 79
3.5.2 Comparison to the General AGN Sample . . . 81
3.5.3 AGN and Host Galaxy Properties Are Not Correlated with Merger Parameters 85

3.6 Results . . . 88
3.6.1 AGN Activation Peaks at the Smallest Bulge Separations . . . 88
3.6.2 AGN are Preferentially Found in Major Mergers . . . 90
3.7 Conclusions . . . 92

4 Observational Evidence for a Transition from Offset to Dual AGN Predominance in Late Stage Mergers **95**
4.1 Introduction . . . 96
4.2 Methods . . . 97
4.2.1 ACS-AGN Merger Catalog . . . 97
4.2.2 Identification of Dual AGN Using BAYMAX . . . 99
4.2.3 Dual and Offset AGN Sample . . . 102
4.3 Results . . . 105
4.3.1 Dual AGN Prefer the Most Major Mergers . . . 105
4.3.2 As a Population, Offset AGN Transition to Dual AGN at Small Separations . 107
4.4 Conclusions . . . 110

5 How to Expand Our Understanding of the Coevolution of AGN and Their Host Galaxies **112**
5.1 Using New On-Axis *Chandra* Observations to Find Dual AGN in Late-Stage Mergers 113
5.1.1 Introduction . . . 113
5.1.2 How To Build Upon Previous Work . . . 114
5.1.3 Science Questions That Could Be Addressed . . . 117
5.2 Understanding AGN and Star Formation Triggering During Mergers Using Machine Learning . . . 120
5.2.1 Introduction . . . 120
5.2.2 Using Machine Learning Techniques to Identify Mergers in HSC and VRO Data . . . 122
5.2.3 Addressing Open Science Questions . . . 130

6 Conclusions **132**

Bibliography **135**

Tables

Table

2.1 Systematic offsets in source matching 28

2.2 Data Fields in the ACS-AGN Catalog 47

3.1 Data Fields in the ACS-AGN Merger Catalog 68

4.1 Verified Dual X-Ray AGN in the ACS-AGN Merger Catalog 101

Figures

Figure

1.1 A modern interpretation of the Hubble sequence 2

1.2 Color-mass diagram showing the blue cloud and red sequence 4

1.3 Evolution of galaxy morphology 5

1.4 Schematic drawings of the near-accretion regions of AGN 7

1.5 BPT diagrams of Sloan galaxies 10

1.6 Mid-Infrared color-color diagrams for AGN selection 11

1.7 Correlations between SMBH and Host Bulge Properties 13

1.8 Correlations between BHAR and SFR 15

1.9 Schematic outline of a galaxy merger 17

2.1 Venn diagram of identified AGN host galaxies by selection method 31

2.2 Histograms of redshifts for our active galaxy sample 35

2.3 Histogram of the $L_{\rm AGN}$ values for our active galaxy sample 36

2.4 Histogram of the M_*, SFR, and sSFR values for our active galaxy sample 38

2.5 $L_{\rm AGN,SED}$ and SFR as a function $N_{\rm H}$ in our active galaxy sample 43

2.6 Active Galaxy Sample SFR values in comparison to the main sequence 48

2.7 SFR as a function of AGN luminosity (BHAR) for our active galaxy sample 53

2.8 Powerlaw slope of the SFR – AGN luminosity relation as a function of redshift . . . 55

3.1 Flowchart summarizing the steps used to identify and model offset and dual AGNs . 62

3.2 Examples of offset and dual AGNs included in the ACS-AGN Merger Catalog 66

3.3 Bias map of our merger identification pipeline 75

3.4 Histogram of the redshifts and galaxy stellar masses of our merger subsample 77

3.5 Histograms of the AGN and host galaxy property values of our merger subsample . . 80

3.6 Relations between AGN and host galaxy properties and merger parameters 82

3.7 Relations between specific SFR and specific AGN luminosity and merger parameters 86

3.8 Histogram of the AGN fraction as a function of SMBH separation 89

3.9 Histogram of the AGN fraction as a function of merger mass ratio 91

4.1 Differences in galaxy parameters between offset and dual AGN and matched systems 103

4.2 Histograms of offset and dual AGN fraction as a function of merger mass ratio . . . 106

4.3 Histograms of offset and dual AGN fraction as a function of SMBH separation . . . 108

5.1 The benefits of finding additional dual and offset AGN with new *Chandra* observations 117

5.2 Example of mock image creation for machine learning training 125

Chapter 1

Introduction

Preface

Here I present a brief introduction that discusses galaxy structure and evolution, active galactic nuclei (AGN) and their selection methods, and how AGN evolve with their host galaxies. Finally, I end the chapter with a short discussion that connects the work of this thesis with these topics. While I will strive to be both complete and concise, I recognize that this is an inherently contradictory goal; therefore, if the reader would like further material on the subject, I would encourage them to read the many excellent reviews on the subjects, such as Alexander and Hickox (2012), Kormendy and Ho (2013), Conselice (2014), Heckman and Best (2014), and Padovani et al. (2017).

1.1 Galaxy Structure and Evolution

The origins of modern extragalactic astronomy is commonly credited to Edwin Hubble and his pair of seminal discoveries in the 1920's. He discovered that not only was the Andromeda nebula a galaxy unto itself, but also that the universe was expanding (Hubble, 1925, 1929). His establishment of the "Hubble sequence" of galaxy morphology is still the basis of modern galaxy classification. While the original classification model has been refined, its influence can still be seen in modern forms, such as the one depicted in Figure 1.1 from Kormendy and Bender (2012).

The Hubble sequence is based on visual morphological properties of galaxies, and has been frequently updated to encompass as many galaxy types as possible. On the left of the Hubble sequence resides the elliptical galaxies; these are typically spheroidal, with less concentrated light

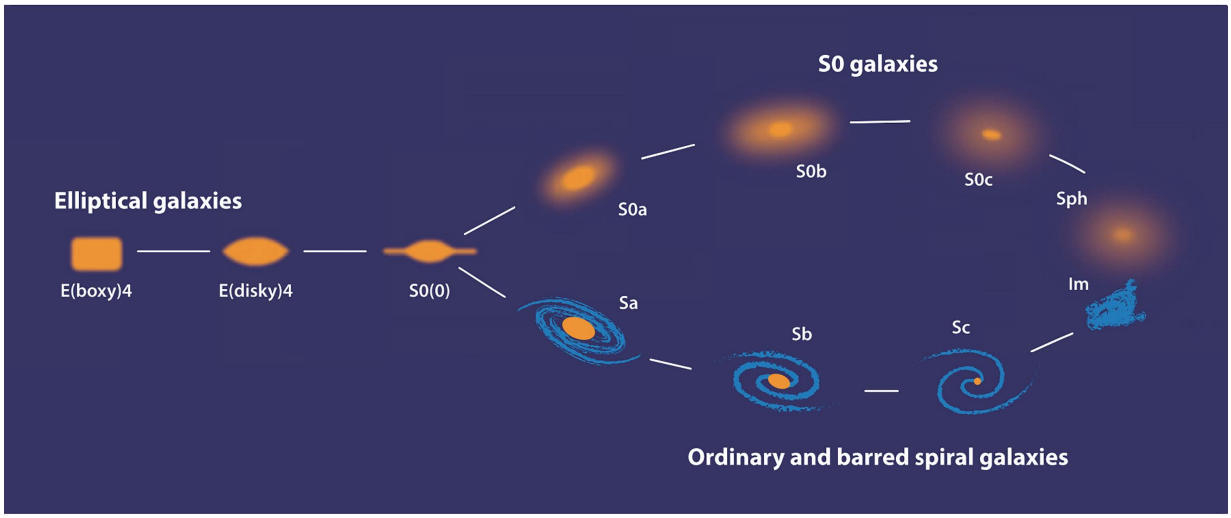

Figure 1.1: A modern interpretation of the Hubble sequence from Kormendy and Bender (2012). The left side of the diagram shows the elliptical sequence, while the right side of the diagram shows parallel branches of spiral galaxies and lenticular galaxies

profiles, and are often reddish in color when seen visually. Classically, on the right of the Hubble sequence lay the spiral galaxies; these have stellar disks with spiral arms, have more concentrated light profiles as well as central bulges or bars, and are often blueish in color when seen visually. On the far right end of the Hubble sequence are the irregular galaxies; these are typically smaller than other galaxies, have no regular shape, and are often very blue in color. Last are the lenticular galaxies, which tend to display characteristics of both spiral and elliptical galaxies. Because of this, they were placed in between the two in the original Hubble sequence. However, as can be seen in the modern interpretation of Figure 1.1, they may have a more complex evolutionary sequence than originally thought. While these classification were first made purely on visual characteristics, they still do a good job of separating galaxies into types that display inherently different underlying properties.

First, let us more closely examine and quantify the morphology of a galaxy. When we discuss a galaxy's morphology, we are inherently talking about what the light emanating from the stars and other radiating bodies in the galaxy looks like. This is a galaxy's light profile, and we quantify

it by measuring how the light intensity of a galaxy changes as a function of its radius. The first detailed study and modeling of the apparent light profiles of galaxies was done by de Vaucouleurs (1948), but a more general form of the light profiles of galaxies was later found by Sérsic (1963),

$$I(R) = I_e \times exp[-b(n) \times \{(R/R_e)^{1/n} - 1\}], \tag{1.1}$$

where the Sérsic index, n, determines the shape of the light profile, and the the value of $b(n)$ is determined purely by n, such that the effective radius, R_e, contains half of the integrated light of the galaxy; last, the value of I_e is simply the intensity [erg cm^{-2} sr^{-1} s^{-1}] at the effective radius. In this way, the light profile (sans the scaling factor of I_e) of a galaxy can be purely determined by only two parameters, n and R_e. The Sérsic profile is able to encapsulate the light profiles of both spirals and elliptical galaxies through variations of the Sérsic index n, with $n = 4$ and $n = 1$ being classically associated with elliptical and spiral galaxies, respectively. In practice, most non-irregular galaxies can be fit with a Sérsic profile, with Sérsic indices between 0.5 and 10.

Another key aspect of galaxies is hidden in the idea of a galaxy's "color". As was discussed above, elliptical galaxies are typically redder in color, and spiral galaxies are typically bluer. This color comes from the stellar populations associated with each type. The blue color of galaxies is associated with large populations of short-lived blue O and B stars, while a reddish color denotes a dearth of these young, hot stars and the dominance of longer-lived, red stars such as types G, K, and M. Further, the lack of O and B type stars indicates that there is little ongoing star formation in a galaxy. The tendency for elliptical galaxies to be red and have little ongoing star formation is due to the fact that they typically do not have large reserves of gas that can form stars, while spiral galaxies with ongoing star formation do. This is why elliptical galaxies are often referred to as "red and dead". This dichotomy of ellipticals (sometimes referred to as early type) and spirals (sometimes referred to as late type) and their respective typical colors and specific star formation rates (sSFR; SFR divided by galaxy stellar mass) can be seen in Figure 1.2. Upon examining this color-mass diagram, it is clear that ellipticals (Figure 1.2, top right) occupy a redder color space and have lower sSFRs on average, while spiral galaxies (Figure 1.2, bottom right) are bluer and

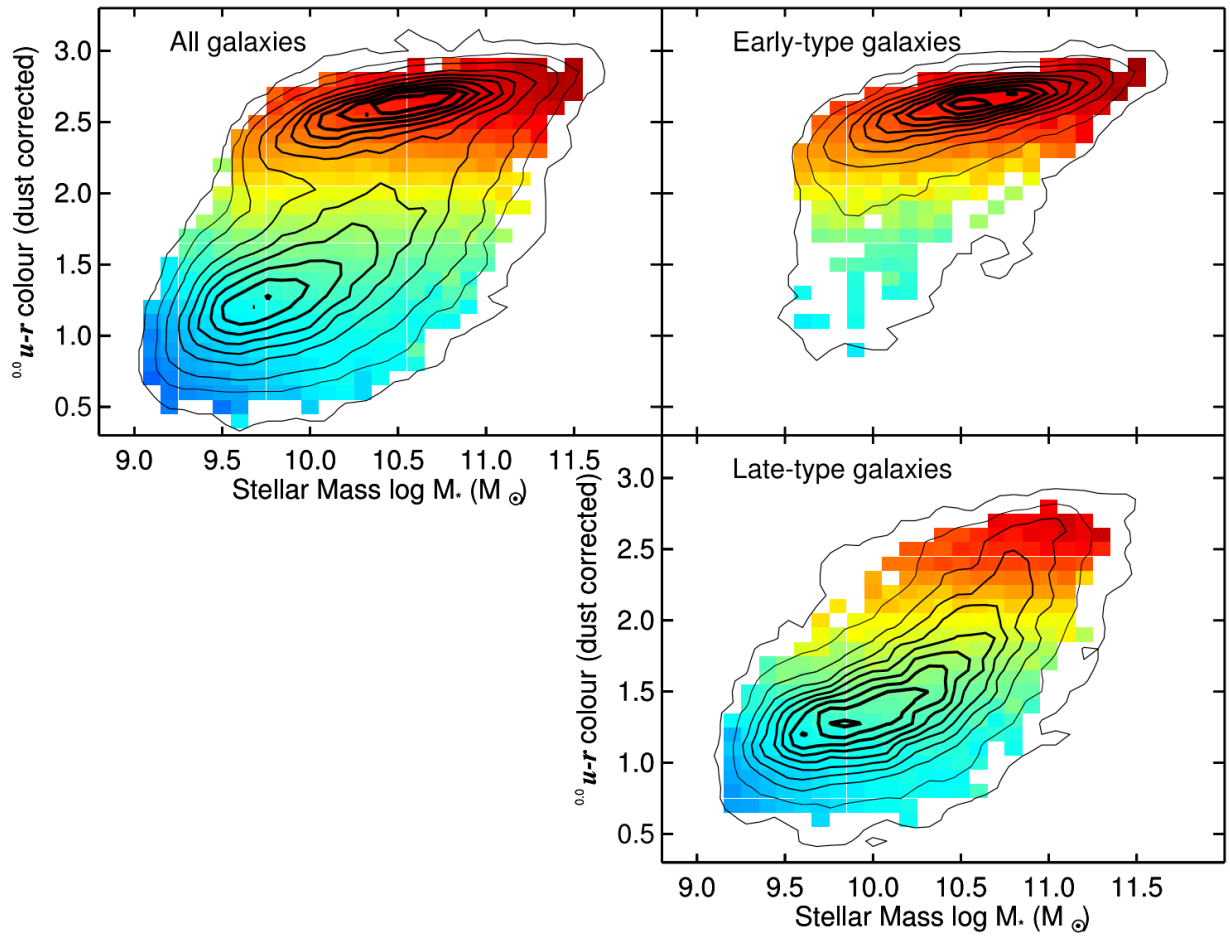

Figure 1.2: A color-mass diagram of SDSS galaxies from Schawinski et al. (2014). Each 0.1×0.1 dex bin is colored by its mean sSFR (bluer being higher sSFR and redder being lower sSFR). Top left shows all galaxies, while early-types galaxies are shown in the top right and late-type galaxies are shown in the bottom right. This diagram shows quite clearly the dichotomy between elliptical (early-type) and spiral (late-type) galaxies in color space and sSFRs.

have higher sSFRs on average. When both populations are looked at together (Figure 1.2, left), we can see the classic bimodal distribution of what is known as the blue cloud (consisting primarily of spiral and irregular galaxies) and the red sequence (consisting primarily of ellipticals). Using this knowledge, galaxies' SFRs and colors have been frequently used as a classifier of galaxy type (e.g. van den Bergh, 1976; Elmegreen and Elmegreen, 1987).

However, by studying large populations of galaxies, we know that galaxies are not static;

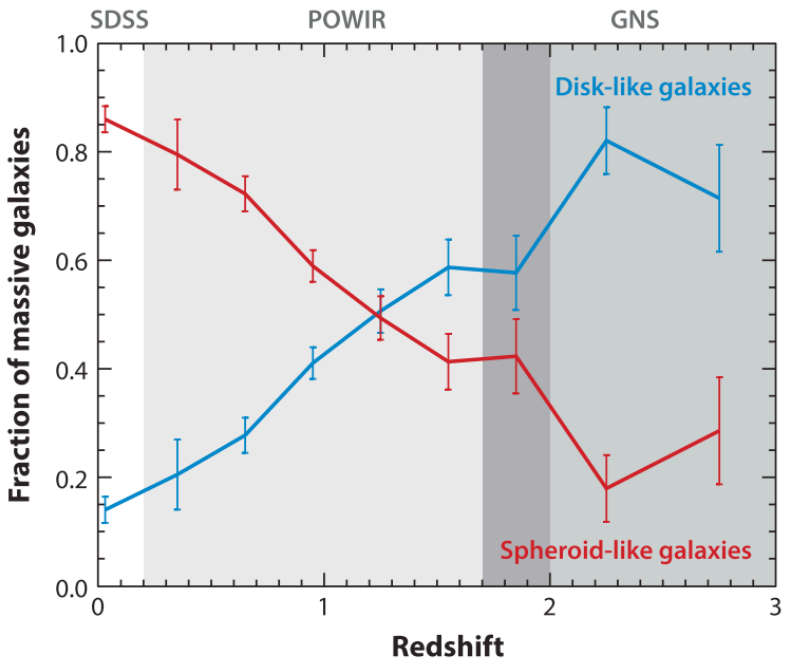

Figure 1.3: The evolution of apparent galaxy morphology with redshift from Buitrago et al. (2013). The sample seen here is restricted to galaxies with $M_* > 10^{11}\mathrm{M}_\odot$. While disk-like (spiral) galaxies dominate in the early universe, as the universe increases in age (decreases in redshift), the populations of galaxies evolve, becoming predominantly spheroidal (elliptical).

instead they evolve — changing their structure and properties over large timescales. The current prevailing framework for structure formation in the universe, Λ cold dark matter, predicts that galaxies form as gas coalesces and cools within a dark matter halo (e.g. White and Rees, 1978; White and Frenk, 1991). They then grow through secular processes, such as gas accretion from cosmic filaments, and merger events, evolving from small, high SFR, irregular galaxies, through spiral galaxies, and eventually to large, low SFR, elliptical galaxies (e.g. Lilly et al., 1995; Giavalisco et al., 1996; Dekel et al., 2009; Ciotti et al., 2010); this shift from spiral galaxies to elliptical galaxies can be seen in Figure 1.3. Further, in this framework, Figure 1.2, left could also be thought of as showing an evolutionary sequence of galaxies, migrating from the blue cloud in the lower left to the red sequence in the upper right.

As galaxies evolve, their morphology, gas supply, and stellar population all undergo processes

which work to eventually shift them towards the "red and dead" properties of a large elliptical galaxy. The key interplay of a galaxy's gas and its star formation, and how star formation can be shut down or enhanced during different stages of galaxy evolution is of particular interest. Star formation can be shut down by any process that inhibits the presence or collapse of cold molecular gas in a galaxy. A galaxy's morphology can accomplish this; for example, both bars and bulges can restrict star formation in the central regions of a galaxy (e.g. Sheth and Van De Weygaert, 2004; Bluck et al., 2014). Supernova feedback can also quench star formation in galaxies, essentially acting as a self-regulating process (e.g. Peng et al., 2010, 2012). A galaxy's own SMBH may provide a strong negative feedback mechanism on star formation, but this scenario is typically limited to SMBHs that are strongly accreting and observable as an AGN.

1.2 Active Galactic Nuclei and Selection Techniques

When the first AGN were observed by Seyfert (1943), the importance of the discovery was relatively unrecognized until further work by Burbidge et al. (1959) and Schmidt (1963); like many things in astronomy, their observational characteristics were understood before the physical mechanisms that caused them were known. We now know that AGN are actively accreting SMBHs, and that SMBH growth primarily occurs during this AGN phase (e.g. Lynden-Bell, 1969; Shakura and Sunyaev, 1973; Rees, 1984). But there are still many unanswered questions related to SMBHs and AGN, such as how AGN coevolve with their host galaxies; this topic specifically is discussed more in Section 1.3.

AGN are powered through the conversion of gravitational energy into radiative and/or kinetic energy; since a SMBH's gravitational well is exceedingly deep, AGN can be extremely energetic. There are two primary modes of AGN: radiative-mode AGN and jet-mode AGN. Radiative-mode AGN are AGN that primarily convert the gravitational energy of accreting gas into electromagnetic radiation. This mode of energy conversion is very efficient, and radiative-mode AGN luminosities can be simply calculated as a function of the SMBH's mass accretion rate ($\dot{m}_{BH}$) and efficiency

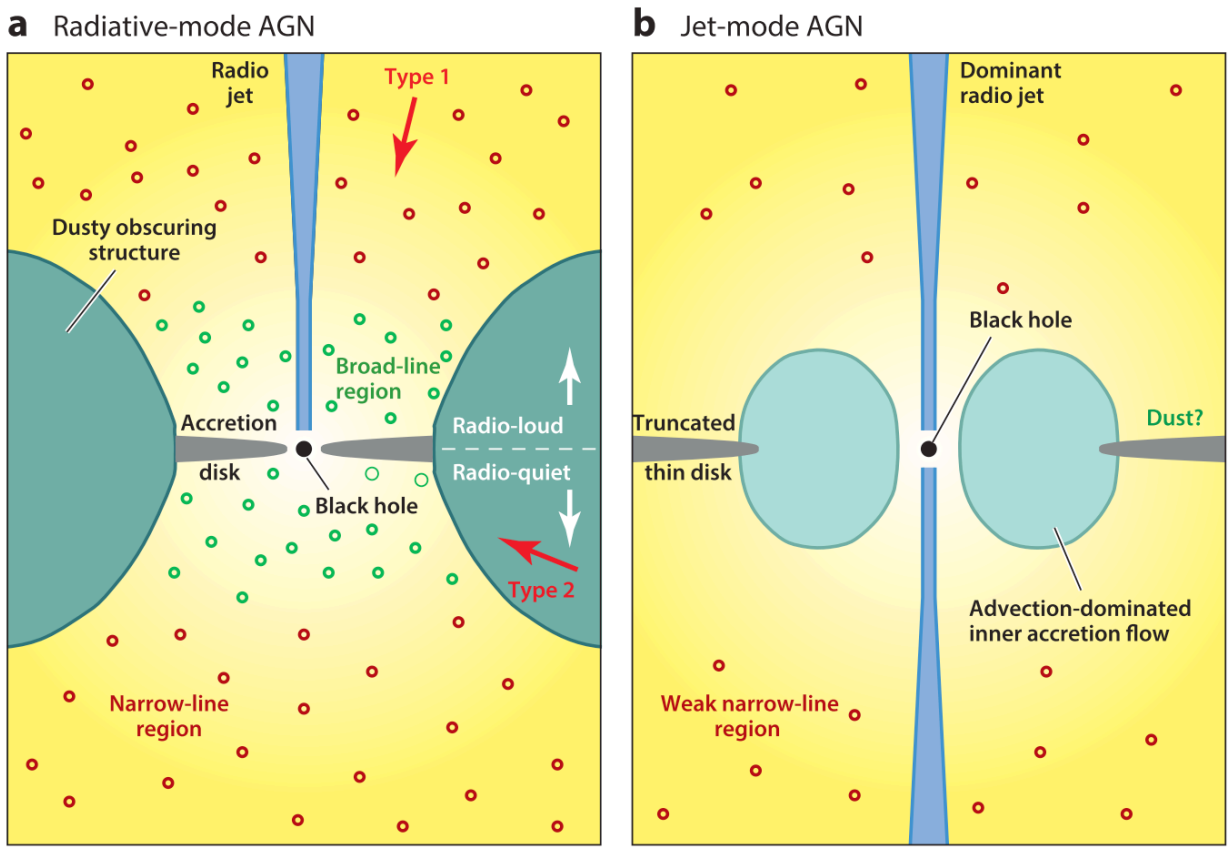

Figure 1.4: Schematic drawings of near-accretion regions of radiative-mode AGN (left) and jet-mode AGN (right) from Heckman and Best (2014). Full descriptions of these diagrams are included in that work, while summaries are included here.

(ϵ), which is typically assigned a value of $\epsilon \sim 10\%$,

$$L_{bol} = 1.5\epsilon \left(\frac{\dot{m}_{BH}}{\mathrm{M}_\odot \ \mathrm{yr}^{-1}} \right) 10^{45} \ \mathrm{erg \ s}^{-1}. \tag{1.2}$$

Radiative-mode AGN are also referred to as Seyferts or quasi-stellar objects (QSOs), depending on the source and context. In contrast, jet-mode AGN produce very little radiation, but instead convert gravitational energy into the bulk kinetic flow of bipolar collimated jets. These jet-mode AGN are also frequently referred to as radio-mode AGN, or radio-loud AGN, since these jets strongly emit synchrotron radiation in the radio regime.

The geometries and makeup of the near-accretion region of these two modes of AGN differ slightly, and we include schematic drawings of both from Heckman and Best (2014) in Figure

1.4. Here I will present summary descriptions, but encourage the reader to examine Heckman and Best (2014), and the references therein, for further information. Radiative-mode AGN possess a geometrically thin, optically thick accretion disk, that extends down to near the event horizon of the SMBH. This hot accretion disk thermally radiates photons with wavelengths in the visible regime, up to the extreme UV. The corona surrounds the accretion disk, and inverse Compton scatters photons from the disk into the X-ray regime. The light from the corona and accretion disk can be partially absorbed by nearby dense clouds and re-emitted as emission lines – as these lines are Doppler broadened on the order of thousands of kilometers per second, this is called the broad-line region. The last leg of the journey for escaping radiation depends on the angle of escape. If the light is sufficiently near the poles of the system, it can be further partially absorbed by low-density clouds of gas and re-emitted as emission lines, but as these lines are only Doppler-broadened on the order of hundreds of kilometers per second, this area is called the narrow-line region. However, if instead the light travels along a path that is near the plane of the disk, it will encounter the dusty obscuring structure (aka torus). This is a dense region of dusty molecular gas, with column densities from 10^{23} to 10^{25} cm^{-2}, that can absorb even the most energetic photons from the corona when column densities exceed 1.5×10^{24} (Compton-thick). This absorbed energy is then re-emitted in the infrared regime. Because of this dependence on angle, radiative-mode AGN can appear substantially different depending on the angle of observation. Observations with lines of sight near the polar axis can see light from the disk, corona, broad-line region, and narrow-line region, while observations in-plane with the disk may only see narrow emission lines or light emanating from the dusty torus, or in some cases, hard X-rays that pass through the torus; these are differentiated, and called Type 1 and Type 2, respectively (Antonucci, 1993). While radiative-mode AGN may also possess jet(s), it is not always the case.

There are key differences in the geometry of jet-mode AGN that cause them to be radiatively inefficient. There is no geometrically thin accretion disk in the inner regions, instead this is replaced by a geometrically thick advection dominated accretion flow region (e.g. Narayan and Yi, 1994). It is these types of flows that can launch the titular jets. Once these jets leave the launching region

near the SMBH, they can remain collimated until they reach the circumgalatic or intergalactic medium.

Many works in the last few decades have focused on finding AGN using a multitude of different observational instruments and techniques. Here we will briefly discuss methods for AGN identification in the optical, infrared, and X-ray regimes; due to the nature of the work in this thesis, we will focus our discussion to techniques typically used in large-scale surveys.

The identification of AGN in the optical regime in large-scale surveys has primarily been through the use of spectroscopy. One of the primary diagnostics used in optical emission-line surveys has been that of Baldwin-Philip-Terlevich diagrams (BPT; Baldwin et al., 1981). BPT diagnostics compare specific emission lines in order to isolate the spectroscopic signature of AGNs, while avoiding contamination by stellar emission (e.g. that of O type stars). The primary diagnostic is a comparison of the flux ratio of [OIII]/Hβ to that of [NII]/Hα, but additional flux ratio pairs have been found to be successful in identifying AGN when compared to the flux ratio of [OIII]/Hβ (e.g. Kewley et al., 2006); specifically, the ratios of [OI]/Hα and [SII]/Hα. Examples from Kewley et al. (2006) of these diagnostics being used to classify Sloan galaxies are shown in Figure 1.5. These diagrams are designed to split likely star-formation dominated galaxies (bottom left of the BPT diagram) from AGN dominated galaxies (upper right of the BPT diagram). The middle and right diagrams of Figure 1.5 also include a designated area for "LINER" type galaxies; these are galaxies with strong low-ionization emission associated with their nuclear regions (Heckman, 1980). However, many works have presented evidence that many LINER type galaxies may not necessarily be fueled by AGN (e.g. Stasińska et al., 2008; Sarzi et al., 2010; Belfiore et al., 2016).

While optical diagnostics focus on examining emission from the narrow-line region around an AGN, infrared selection techniques are designed to detect the reprocessed light associated with the dusty torus surrounding many AGN. Because the light signature of this torus can be dominated by dust associated with star-formation in the far-infrared (e.g. Hatziminaoglou et al., 2010), infrared AGN selection methods focus on the mid-infrared (MIR) regime, where stellar contamination is less prevalent. However, care must still be taken to avoid stellar contamination (see Figure 1.6, left);

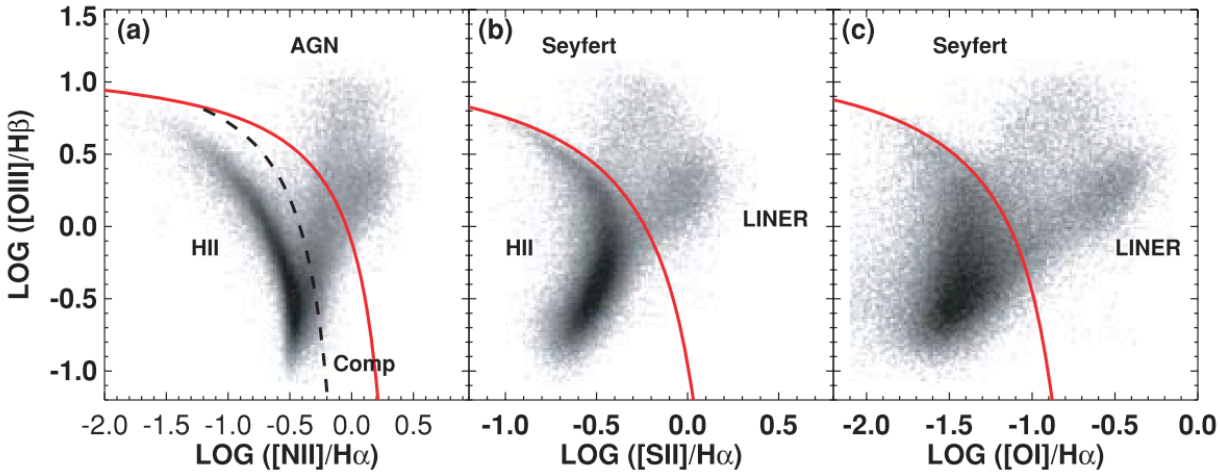

Figure 1.5: BPT diagrams of Sloan galaxies (small gray dots) from Kewley et al. (2006). These diagrams split the observed galaxies into star forming (lower left), AGN (upper right), and in the case of the middle and right BPT diagrams, LINER (lower right). The red line is used to denote the maximum extent of star-forming galaxies.

this is accomplished through highly specific selection criteria (sometimes called wedges) in the MIR color space. A strength of MIR selection techniques is that they are able to detect heavily obscured AGN — a regime in which X-ray selection techniques struggle. With many infrared missions and surveys taking place over the last few decades (e.g. *IRAS*, *Spitzer*, *AKARI*, *WISE*), many AGN selection techniques have been developed to take advantage of these data. These selection techniques examine flux ratios and/or colors in the MIR in order to select AGN and avoid contamination from star formation; due to the wide range of MIR selection criteria available, I will not list them all here, but instead direct the reader to the excellent review by Padovani et al. (2017) on the subject. Some specific MIR AGN selection criteria of importance for the work in this thesis include MIR AGN selection criteria for *Spitzer* data by Stern et al. (2005) (Figure 1.6, right), and Donley et al. (2012).

The last set of AGN selection techniques that will be discussed here are those that take advantage of observations in the X-ray regime. X-ray selection techniques are able to provide very complete samples of AGN with low contamination. This is primarily due to the fact that almost

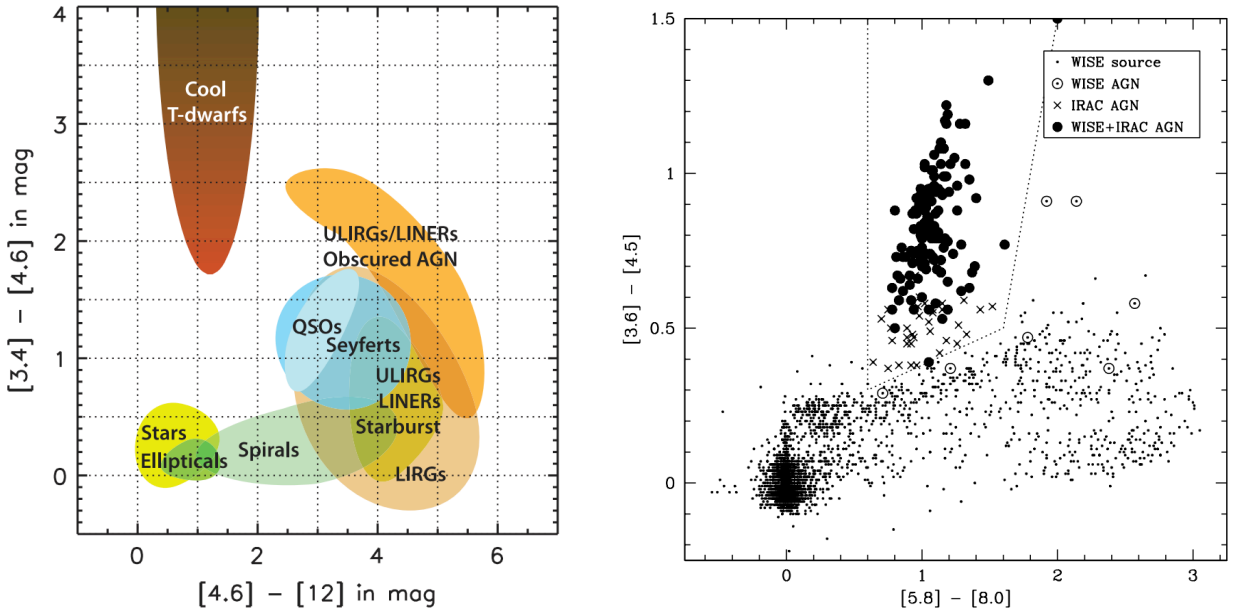

Figure 1.6: Mid-Infrared color-color diagrams that outline AGN selection methods in this regime. The left color-color diagram (from Wright et al. 2010), with axes in terms of *WISE* bands, shows how AGN occupy a unique region of parameter space in the MIR, while the right color-color diagram (from Stern et al. 2012), with axes in terms of *Spitzer* bands, shows the *Spitzer* based AGN selection wedge of Stern et al. (2005); this wedge is specifically designed to avoid stellar contamination while still retaining a highly complete sample of AGN.

all AGN emit X-rays that are able to pass through all but the most dense obscuring material, and AGN typically dominate their host galaxy's X-ray emission (see Brandt and Alexander 2015 for a review). As discussed above, X-ray emission from AGN originates from inverse Compton scattering of photons in the AGN's corona, so it is this signature that X-ray AGN selection techniques use to identify AGN. In particular, two common methods of identifying AGN in the X-ray regime are the use of an X-ray luminosity cut, and through the analysis of the X-ray spectral shape. The first method takes advantage of the fact that AGN X-ray luminosities are typically much greater than those of their host galaxies; this is especially true when looking at high energy (hard) X-rays. Requiring an observed X-ray luminosity in the 2 – 10 keV band of $L_{2-10} > 10^{42}$ erg s^{-1} is a typical AGN selection technique; this ensures that all but the most vigorously star-forming galaxies are excluded, while still including moderate luminosity AGN (Ranalli et al., 2003). Another method

used to select AGN is to examine the X-ray spectrum of a candidate AGN source. AGN spectra in the X-ray regime follow a power-law relation that is typically flat in comparison to that of stellar X-ray binaries.

With the impressive array of AGN selection techniques outlined above, large samples of AGN and their host galaxies can be identified and studied. This type of examination is what is needed in order to understand the environments that AGN are found in and how AGN and their host galaxies grow together.

1.3 AGN – Galaxy Coevolution

Some of the most intriguing unanswered questions in galaxy evolution are related to the discovery of correlations that strongly link SMBH properties with the properties of their host galaxies. Within the last 20 years, multiple works have found that the mass of a galaxy's SMBH is not only proportional to the mass of the galaxy's central bulge, but also the stellar velocity dispersion of the central bulge, and the luminosity of the central bulge (e.g. Kormendy and Richstone, 1995; Magorrian et al., 1998; Ferrarese and Merritt, 2000; Gebhardt et al., 2000; Tremaine et al., 2002; Marconi and Hunt, 2003; Gültekin et al., 2009). These tight correlations (seen in Figure 1.7) seem to imply a currently poorly understood connection between the growth and evolution of SMBHs, and that of their host galaxies. The environmental factors and methods by which the coevolution of SMBHs and their host galaxies take place is the primary focus of this thesis. It is known that both secular processes and merger events drive the evolution of SMBHs and their host galaxies; we first discuss secular coevolution, and then merger-driven coevolution.

In order to understand the processes that drive coevolution, first we must address how SMBHs grow. The mechanisms of SMBH accretion and growth is an ongoing field of study. SMBH growth depends on the accretion of gas that is at much larger scales than not only the accretion disk, but also the SMBH's gravitational area of influence ($\sim$1 – 100 pc). Since the majority of gas in a galaxy exists at radii on the scale of kpc, there must be methods by which the gas is driven down to parsec scales so that it can eventually be accreted and drive SMBH growth and AGN activity.

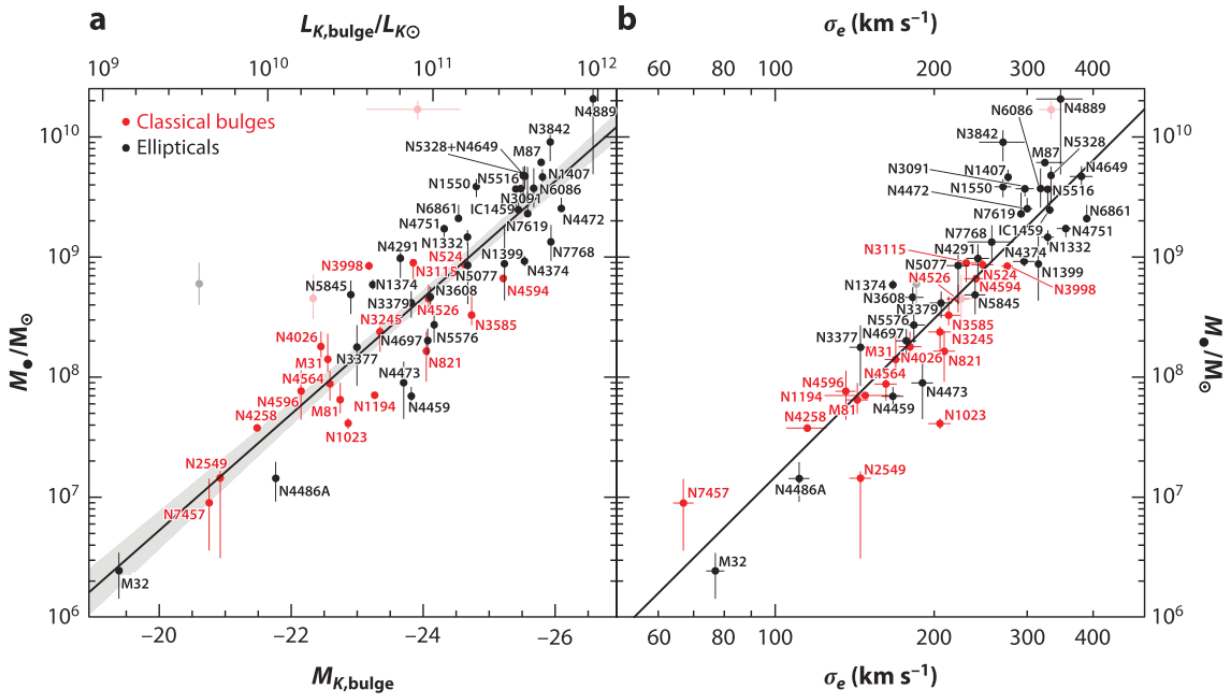

Figure 1.7: Correlations between SMBH and host bulge properties from Kormendy and Ho (2013). Left (a) shows how SMBH mass correlates with the host galaxy bulge luminosity (top axis), while right (b) shows how the SMBH mass correlates with the stellar velocity dispersion of the host galaxy bulge.

In secular processes, this inward driving of gas can be started by large-scale gravitational torques from galaxy structures, such as spiral bars (e.g. Bournaud and Combes, 2002). However, these processes may not be responsible for significant inward driving of gas at sub-kpc scales. Instead, more localized processes must take effect at these scales, such as nested bars, nuclear spirals, or clumpy circumnuclear regions (e.g. Englmaier and Shlosman, 2004; Maciejewski, 2004; Hopkins and Quataert, 2010). Once the gas is driven to radii <10 pc, the gravitational effects of the SMBH begin to dominate those of the host galaxy; however, the actual processes that finish the migration of gas onto the SMBH's accretion disk in this region are complex and still being studied (see Hopkins and Quataert, 2010; Power et al., 2011).

As for the secular growth of galaxies, most star-forming galaxies lie along a star-forming main sequence, where the galaxy's star formation rate is tightly correlated with galaxy mass (e.g.,

Noeske et al., 2007; Daddi et al., 2007; Elbaz et al., 2011; Whitaker et al., 2012; Schreiber et al., 2015). This tight correlation is thought to be the result of slow and continuous fueling of star formation in these galaxies through inflows of cold gas from cosmic filaments (e.g., Dekel et al., 2009; Ciotti et al., 2010). This cold molecular gas can then gather into star-forming regions through dynamical processes, and collapse under self-gravitation to form stars. But the same gas that fuels star formation can also be driven inwards to fuel AGN and grow SMBHs. A prime example of this link is work by Müller-Sánchez et al. (2009) that finds that some AGN host galaxies have comparatively large reservoirs of cold circumnuclear gas, which is perfect for use in star formation.

Because of the similarities in predicted high-growth environments for both SMBH growth and star formation, the coevolution of SMBHs and their host galaxies has been a topic of recent interest. While previous work has found that cosmic star formation and black hole accretion history behave similarly (e.g. Boyle and Terlevich, 1998; Silverman et al., 2008; Shankar et al., 2009; Aird et al., 2010), a direct connection between SFR and AGN activity in samples of AGN host galaxies is less certain. Specifically, many works have found that AGN activity is correlated with the SFR of their host galaxies (e.g. Mullaney et al., 2012; Chen et al., 2013; Delvecchio et al., 2015; Harris et al., 2016; Lanzuisi et al., 2017), while others have found that there is no correlation, or only a shallow correlation (e.g. Azadi et al., 2015; Stanley et al., 2015, 2017; Shimizu et al., 2017). However, much of this disagreement may rely on redshift and host galaxy mass dependencies of both AGN luminosity and SFR (e.g. Lutz et al., 2010; Mullaney et al., 2012). These dependencies can be seen very clearly in the studies of Delvecchio et al. (2015), as shown in Figure 1.8. While it is apparent that SFR is evolving with the black hole accretion rate (BHAR) in Figure 1.8, top, we can see that the majority of any correlation between AGN growth and SFR is actually due to redshift and host galaxy mass dependencies; this is similar to the findings of Stanley et al. (2017). Therefore, any future studies of AGN – galaxy coevolution in these systems must include methods that account for these biases, while attempting to find deeper nuance or disprove further underlying connections.

While secular processes are thought to be the key drivers of SMBH and host galaxy growth over cosmic time, galaxy merger events are thought to cause rapid growth over shorter time periods.

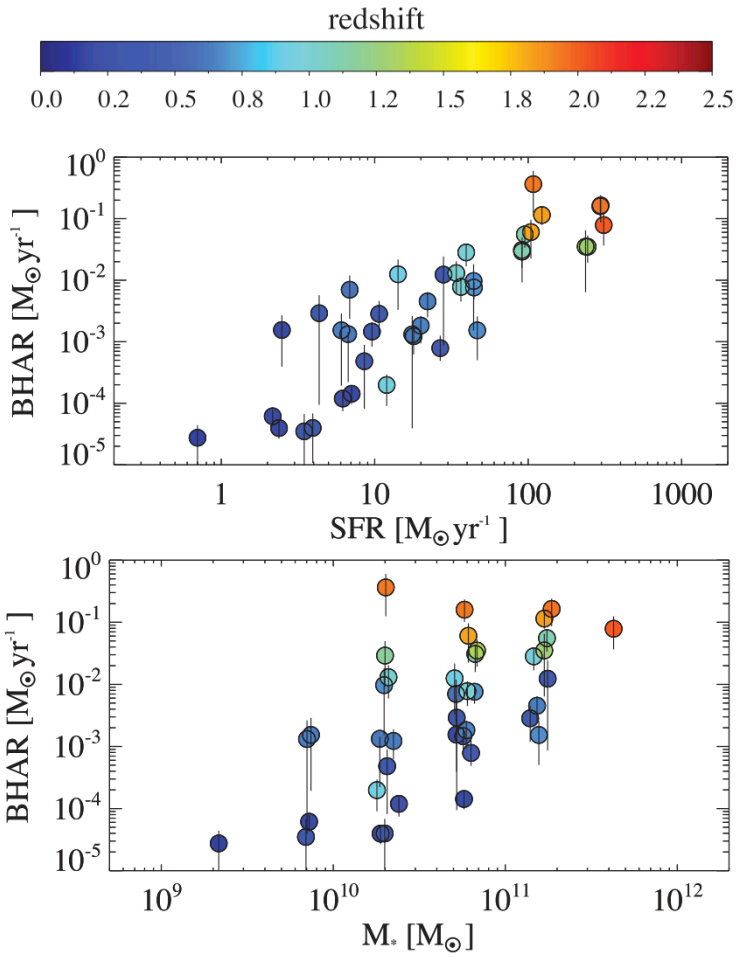

Figure 1.8: Correlations between BHAR and SFR from Delvecchio et al. (2015). The top figure shows how BHAR behaves as a function of SFR, where the color of the circle indicates the redshift of the system. The bottom figure shows BHAR as a function of galaxy stellar mass. Together, these figures show that while AGN activity is correlated with SFR in the host galaxy, these correlations are primarily due to mutual dependencies on redshift and host galaxy stellar mass.

Unlike secular processes which rely primarily on fueling from intergalactic filaments and lengthy dynamical processes to drive gas inward, mergers take advantage of the dynamical processes of the merger itself to drive gas inward and trigger AGN and enhanced star formation. Simulations have shown that galaxy mergers introduce and disturb large volumes of gas, drive it inwards through dynamical processes, and enable rapid star formation (e.g. Hopkins and Hernquist, 2009; Veilleux et al., 2009). Since SMBHs are typically found in the central bulges of their host galaxies, galaxy

mergers also create pairs of SMBHs that slowly draw closer over the timescale of the merger. It is thought that these SMBHs pairs remain at separations of 1 – 20 kpc for ∼100 Myr before they eventually fall inward and become a gravitationally bound SMBH binary (Begelman et al., 1980; Milosavljevic and Merritt, 2001). A generalized outline of a gas-rich major galaxy merger is shown in Figure 1.9, including simulated predictions as to how SFR is enhanced in the interaction (c) and coalescence (d) phases (Figure 1.9, middle top). During these phases, the large amounts of disturbed gas and dust that is enhancing star formation can also be driven inward, and triggering the resident SMBHs to become observable as AGN; this enhances AGN luminosity, and therefore SMBH growth (e.g. Joseph and Wright, 1985; Hopkins et al., 2008; Hopkins and Hernquist, 2009; Knapen et al., 2015). This enhancement of AGN luminosity occurs at similar times in the merger to that of SFR enhancement (see Figure 1.9, middle bottom), which indicates strong AGN – galaxy coevolution during these phases of galaxy mergers. Because of this, studies that examine these phases of galaxy mergers (mergers with SMBH pair separations <20 kpc) are very important for understanding SMBH – galaxy coevolution in mergers. When studying these mergers, we call galaxy mergers hosting two AGN at pair separations <20 kpc "dual AGN" systems, and galaxy mergers hosting one AGN and one quiescent SMBH at pair separations <20 kpc "offset AGN" systems.

Due to the importance of late-stage galaxy mergers in SMBH – galaxy coevolution, the study of galaxy mergers hosting AGN has become an important topic in the last two decades. Here I will detail a non-exhaustive list of recent work and open questions related to AGN host galaxies in late-stage mergers. Work by Van Wassenhove et al. (2012) and Blecha et al. (2013) has focused on simulating galaxy mergers in order to identify the peak of SMBH growth, with Van Wassenhove et al. (2012) finding a peak at SMBH separations of 1 – 10 kpc, and Blecha et al. (2013) finding a peak at SMBH separations of 0.1 – 2 kpc. While observations have not been able to test these predictions due to the limited number of systems with SMBH separations <10 kpc currently known, multiple works do confirm the trend that SMBH growth increases as SMBH pair separation decreases from 100 kpc to 10 kpc (e.g. Ellison et al., 2011; Van Wassenhove et al., 2012;

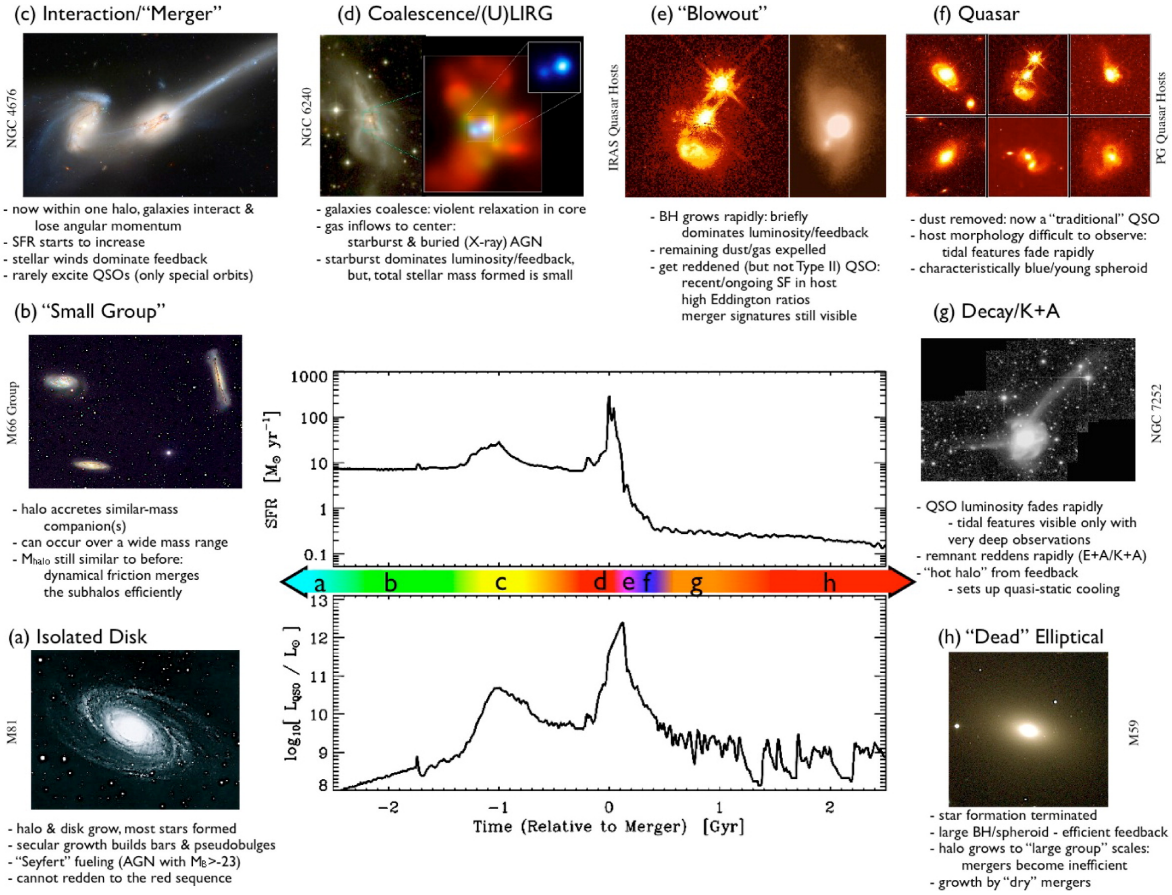

Figure 1.9: Schematic outline of the phases of a gas-rich major merger from Hopkins et al. (2008). Middle shows diagrams of AGN luminosity and star formation as a function of time until/from coalescence (denoted as 0). Note how phases (c) and (d) coincide with enhancements of SFR and AGN luminosity; these phases relate to SMBH pair separations <20 kpc.

Koss et al., 2012; Blecha et al., 2013; Barrows et al., 2017a; Capelo et al., 2017; Foord et al., 2020). Other work has focused on studying the impact of merger mass ratio (the ratio of galaxy masses in a merger) on AGN triggering and luminosity. Simulations predict that major mergers (mergers with a mass ratio <4) should trigger the most luminous AGN (Hopkins and Hernquist, 2009), but observational studies have not agreed on the subject, with some finding that they do (e.g. Treister et al., 2012), and others that they do not (e.g. Kocevski et al., 2012; Villforth et al., 2017). Still other simulations predict that major mergers should preferentially trigger dual AGN (e.g. Volonteri

et al., 2003; Hopkins et al., 2005; Steinborn et al., 2016), and observational work appears to support that prediction (e.g. Ellison et al., 2008; Comerford et al., 2015; Barrows et al., 2017a), but these observational studies have been limited to very small samples.

The fundamental problem with previous observational studies of these systems is the limited number of known dual and offset AGN. While many works have sufficient samples at SMBH pair separations >20 kpc, the number of known systems between 10 and 20 kpc decreases sharply, while the number of known systems with SMBH pair separations <10 kpc is less than 40 across all works, and no one work has a sample of more than 5 dual AGN (not including those found in the works detailed in this thesis; see Rubinur et al. 2018 for a review of dual AGN studies). This is due to the fact that dual and offset AGN systems are difficult to find and observe.

Early discoveries of dual AGN systems were serendipitous (e.g. Komossa et al., 2003; Bianchi et al., 2008), but more recent studies have attempted to identify them with more systematic methods. One recently developed observational technique tries to identify the spectroscopic signatures of dual and offset AGN, including double-peaked emission lines or single-peaked emission lines with a velocity offset relative to the host galaxy. This method has had mixed success, with some identified galaxies being confirmed as offset and dual AGN (Fu et al., 2011; Liu et al., 2013; Müller-Sánchez et al., 2015; Comerford et al., 2015), but many were ultimately found not to be dual or offset AGN. The contamination of this method stems from the fact that AGN outflows and gas kinematics can produce velocity shifted and double-peaked emission lines that can sufficiently mimic the signatures of offset and dual AGNs (Rosario et al., 2010; Shen et al., 2011; Comerford et al., 2012; Fu et al., 2012; Barrows et al., 2013; McGurk et al., 2015; Nevin et al., 2016). Other work focuses on using surveys to search for the tell-tale morphological features of mergers, followed by spectroscopy, radio, or X-ray observations to verify their candidates (Koss et al., 2012; Fu et al., 2015; Satyapal et al., 2017; Silverman et al., 2020), but sample sizes remain small due to the multiwavelength observational needs of this method. Still other work has searched for offset and dual AGNs by identifying X-ray sources offset from their optical counterpart host galaxies, though this approach has found only limited success (Barrows et al., 2016, 2018; Foord et al., 2019, 2020, 2021). All of the above

studies accentuate the problems in finding these systems — observations of offset and dual AGNs are difficult because of the high resolution imaging and/or spectroscopy needed to differentiate pairs of AGN, or the stellar bulges associated with a SMBH, at these separations; this is also why currently known offset and dual AGNs are mostly limited to the low-redshift Universe ($z \lesssim 0.2$).

It is important to note that the coevolution of SMBHs and their host galaxies also encompasses processes related to the inhibition of star formation or AGN activity. In these cases, we refer to the limiting processes as negative feedback. In the context of this thesis, the two main forms of negative feedback of note are stellar feedback and AGN feedback. Stellar feedback, as discussed briefly above, is primarily accomplished via supernovae explosions that heat the interstellar medium, stopping it from condensing; a process that is necessary for both star formation and accretion onto AGN (e.g. Peng et al., 2010, 2012). AGN feedback on the other hand may be different depending on AGN mode. Radiative-mode AGN tend to drive strong winds that work to expel the cold gas reservoir of the host galaxy, removing the fuel of future star-formation and AGN growth; while the relativistic jets associated jet-mode AGN are thought to heat gas in the galaxy, inhibiting star formation and future AGN activity (e.g. Silk and Rees, 1998; Bower et al., 2006). These feedback processes can take place during both secular and merger-driven coevolution of AGN and their host galaxies. In this way, AGN – galaxy coevolution works to drive correlated growth not only through similar growth mechanisms, but also through linked negative feedback processes.

1.4 Overview of This Dissertation

Work that can successfully find and study large samples of AGN host galaxies in late-stage mergers may be able to address many of the open questions related to the coevolution of AGN and their host galaxies. The work of this thesis focuses on solving the observational difficulties of finding and studying dual and offset AGN, and then analyzing samples of AGN host galaxies in various phases of evolution in order to better understand the environmental factors and methods by which AGN coevolve with their host galaxies in isolation and in mergers.

I begin by creating and analyzing a sample of AGN host galaxies in Chapter 2. This work includes the identification of AGN in large survey fields that have multiwavelength coverage. The large amount of multiwavelength coverage also enables the estimation of many AGN and host galaxy properties, including AGN luminosity, host galaxy mass, and star formation rate. This large sample of AGN host galaxies along with important AGN and galaxy properties enables the study of AGN – galaxy coevolution in the general AGN population, including the study of how AGN activity and host galaxy star formation is correlated (e.g. Mullaney et al., 2012; Chen et al., 2013; Delvecchio et al., 2015; Azadi et al., 2015; Stanley et al., 2015; Harris et al., 2016; Lanzuisi et al., 2017; Shimizu et al., 2017; Stanley et al., 2017).

In Chapter 3, I then identify over 200 AGN in late-stage mergers from that sample. The identification of a large sample of AGN in late-stage mergers has been a very difficult observational task, as discussed above. The work in Chapter 3 is able to create such a large sample by taking advantage of the excellent spatial resolution of *Hubble* observations, and the power of the galaxy morphological fitting software `GALFIT`. With a final sample of 204 AGN in mergers with SMBH pair separations <20 kpc, I am able to address questions related to AGN – galaxy coevolution in mergers, with special interest in studying AGN activation as a function of SMBH pair separation (e.g. Ellison et al., 2011; Van Wassenhove et al., 2012; Koss et al., 2012; Blecha et al., 2013; Barrows et al., 2017a; Capelo et al., 2017; Foord et al., 2020), and as a function of galaxy merger mass ratio (e.g. Volonteri et al., 2003; Hopkins et al., 2005; Ellison et al., 2008; Comerford et al., 2015; Steinborn et al., 2016; Barrows et al., 2017a), in addition to examining how the population of AGN host galaxies in late-stage mergers differs from a general population of AGN host galaxies.

I build upon that work by creating subsamples of dual AGN and offset AGN in Chapter 4. By examining *Chandra* observations of X-ray selected AGN host galaxies in late-stage mergers using the Bayesian analysis tool `BAYMAX`, I create samples of 10 dual AGN and 103 offset AGN in mergers at SMBH pair separations <20 kpc. These are the largest samples of verified dual and offset AGN at separations <20 kpc selected and examined in a single systematic study to-date, and enable further studies of AGN – galaxy coevolution in late-stage mergers. Specifically, it allows nuance to

be added to AGN activation trends as functions of SMBH pair separation and merger mass ratio, and provides a direct observational test of predictions by Van Wassenhove et al. (2012) and Blecha et al. (2013). Further, it also is able to address questions about whether the most luminous AGN are found in major mergers (e.g. Hopkins and Hernquist, 2009; Kocevski et al., 2012; Treister et al., 2012; Villforth et al., 2017).

Finally, in Chapter 5 I discuss future projects that can build upon these works and address remaining open questions related to AGN – galaxy coevolution in late-stage mergers. The first project I discuss builds directly on the work in Chapter 4, and involves increasing the sample sizes of my confirmed dual and offset AGN at SMBH pair separations <10 kpc via new observations by *Chandra*. This would enable statistically stronger confirmations or refutations of predictions related to AGN – galaxy coevolution in the crucial 1 – 10 kpc range, where both AGN activity and SFR is thought to peak in mergers. The second project I outline is focused on creating samples of AGN in late-stage mergers with sample sizes in the thousands and tens of thousands — orders of magnitude increases from currently available samples — by leveraging the power of machine learning against the huge datasets of current and upcoming surveys.

Chapter 2

A Catalog of AGN Host Galaxies Observed with HST/ACS: Correlations between Star Formation and AGN Activity

Abstract

We present the Advanced Camera for Surveys Active Galactic Nuclei (ACS-AGN) Catalog, a catalog of 2585 active galactic nucleus (AGN) host galaxies that are at redshifts $0.2 < z < 2.5$ and that were imaged with the *Hubble Space Telescope's* Advanced Camera for Surveys (ACS). Using the ACS General Catalog (ACS-GC) as our initial sample, we select an AGN subsample using *Spitzer* and *Chandra* data along with their respective established AGN selection criteria. We then gather further multi-wavelength photometric data in order to construct spectral energy distributions (SEDs). Using these SEDs we are able to derive multiple AGN and host galaxy properties, such as star formation rate, AGN luminosity, stellar mass, and nuclear column density. From these data, we show that AGN host galaxies tend to lie below the star-forming main sequence, with X-ray-selected AGN host galaxies being more offset than IR-selected AGN host galaxies. This suggests that there is some process, possibly negative feedback, in AGN host galaxies causing decreased star formation. We also demonstrate that there is a positive trend between star formation rate and AGN luminosity in AGN host galaxies, in individual redshift bins and across all redshift bins, and that both are correlated with the stellar mass of their galaxies. This points towards an underlying link between the stellar mass, stellar growth, and SMBH growth in a galaxy.

This chapter was originally published as a paper in the January 2020 issue of *The Astrophysical Journal* (Volume 888, page 78), and is reproduced here with the permission of the AAS.

2.1 Introduction

Supermassive black holes (SMBHs) are thought to exist at the centers of all massive galaxies, and there is evidence of these central SMBHs being coupled to their host galaxies. In particular, there are strong correlations between observed properties of the SMBH and host galaxy properties; for example, the relations between SMBH mass and host galaxy bulge mass (M_{BH} – M_{Bulge} relation), luminosity (M_{BH} – L_{Bulge} relation), and velocity dispersion (M_{BH} – σ_{Bulge} relation) (e.g., Magorrian et al., 1998; Ferrarese and Merritt, 2000; Gebhardt et al., 2000; Marconi et al., 2004; Greene and Ho, 2006; Gültekin et al., 2009; Kormendy and Ho, 2013). Further, the cosmic star formation history and black hole accretion history appear to behave similarly, peaking near $z \sim 2$ and declining to local values (e.g., Boyle and Terlevich, 1998; Silverman et al., 2008; Shankar et al., 2009; Aird et al., 2010; Madau and Dickinson, 2014). These relations point towards a connection between SMBH growth and host galaxy growth, even though the spatial scales of active SMBH accretion (i.e., an active galactic nucleus, AGN) and host galaxy star formation differ by up to 9 orders of magnitude.

Despite the large separations in spatial scales, both SMBH growth and star formation require a cold gas supply. This alludes to a connection that may lie in coincident feeding mechanisms. There are two primary modes of star formation: via the star-forming main sequence, or merger driven star formation. Most star-forming galaxies lie along a star-forming main sequence, where the star formation rate is tightly correlated with stellar mass (e.g., Noeske et al., 2007; Daddi et al., 2007; Elbaz et al., 2011; Whitaker et al., 2012; Schreiber et al., 2015). It is thought that this tight correlation is created by the presence of slow and continuous inflows of cold gas streams from cosmic filaments that feed star formation in these galaxies (e.g., Dekel et al., 2009; Ciotti et al., 2010). Mergers, on the other hand, can have much larger star formation rates for their stellar mass. Galaxy merger events introduce and disturb large volumes of gas, driving it inwards, and enabling the rapid creation of a large number of stars (e.g., Hopkins and Hernquist, 2009; Veilleux et al., 2009). While the supply of gas available in both of these modes can be driven inwards to

the AGN through the loss of angular momentum via gravitational torque processes (García-Burillo et al., 2005), it is still not apparent that these two modes lead to correlated SMBH growth and star formation (see Alexander and Hickox 2012, for a review).

Therefore, much recent work has focused on studying the link, or lack thereof, between star formation and SMBH growth. Several studies have found that the star formation rate (SFR) of a galaxy is correlated with its AGN's luminosity (e.g Mullaney et al., 2012; Chen et al., 2013; Delvecchio et al., 2015; Harris et al., 2016; Lanzuisi et al., 2017), while others have found either a shallow SFR to AGN luminosity correlation or no correlation (e.g., Azadi et al., 2015; Stanley et al., 2015, 2017; Shimizu et al., 2017). A few works examine the relation in bins of AGN luminosity and find that the relation is luminosity and redshift dependent, with only higher luminosity AGN ($L_{\rm AGN} > 10^{44}$ erg s^{-1}) and lower redshift ($z < 1$) galaxies exhibiting a steep correlation, while lower luminosities or higher redshifts produce flattened relations (e.g., Shao et al., 2010; Rosario et al., 2012; Harrison et al., 2012); these findings were also supported by later semi-analytic work by Gutcke et al. (2015).

Further theoretical work found that the disagreement could arise from the method of analysis used; specifically, that the bivariate distribution of SFR and AGN luminosity gives differing results dependent on the whether the data is binned by SFR or AGN luminosity (Volonteri et al., 2015a,b). Earlier work by Hickox et al. (2014) found that this disagreement could be caused by the differences in timescales between the two processes, with measurable SFR being averaged over $\sim$100 Myr while AGN X-ray luminosity varies on much shorter timescales. Therefore using AGN luminosity measurements taken at one point in time would introduce scatter.

Another prediction of Volonteri et al. (2015b) is that SMBH growth is better correlated with nuclear SFR ($r < 5$ kpc), and that a relation between AGN luminosity and SFR weakens or disappears for SFR integrated over larger areas, i.e. "global" SFR. This idea was supported by earlier observations by Diamond-Stanic and Rieke (2012).

Still other works focus less on the direct connection between SMBH growth and star formation, but instead compare AGN host galaxies to general samples of star-forming galaxies. Some

of these find that AGN host galaxies tend to lie primarily along the star-forming main sequence (e.g., Rosario et al., 2013; Stanley et al., 2017), while others find that they tend to lie below the main sequence, having a lower SFR on average for a fixed galaxy mass (e.g., Shimizu et al., 2015; Mullaney et al., 2015). This points to an uncertainty as to whether AGNs are primarily found in quiescent or star-forming galaxies and, importantly, whether star formation and AGNs are similarly triggered.

This work addresses some of these lingering observational conflicts. By using a systematic AGN selection method and deriving all AGN and host galaxy properties from spectral energy distributions (SEDs), we create the Advanced Camera for Surveys Active Galactic Nuclei (ACS-AGN) Catalog. This is a catalog of 2585 AGN host galaxies imaged by the Advanced Camera for Surveys (ACS) on the *Hubble Space Telescope* (*HST*) with redshifts of $0.2 < z < 2.5$, along with uniformly derived AGN and galaxy properties. Typically, AGN and star formation contributions can be difficult to disentangle, but we avoid this problem by fitting AGN and galaxy SED components simultaneously. This approach also enables us to average out AGN variability and decrease its effect on AGN luminosity measurements due to the broadband nature of our photometric input. Further, by deriving all properties from the same SED fit, we ensure that they are self-consistent.

Here we present and make publicly available the ACS-AGN Catalog along with analysis examining the relation between AGN host galaxies and the star formation main sequence and the relation between AGN luminosity and SFR. The paper is organized as follows: Section 2.2 presents our initial sample of galaxies; Section 2.3 discusses the AGN selection; in Section 2.4 we discuss the fitting of SED components to our AGN host galaxies using multi-band photometric data; in Section 2.5 we discuss the derivation of our AGN and host galaxy properties; in Section 2.6 we present our findings from statistical analysis of the AGN and host galaxy properties; and finally, in Section 2.7 we discuss our conclusions. Throughout this paper, we use the Planck 2015 cosmology of $H_0 = 67.8$ km s^{-1} Mpc^{-1}, $\Omega_M = 0.308$, and $\Omega_\Lambda = 0.692$ (Planck Collaboration et al., 2016).

2.2 Parent Galaxy Sample

Our input galaxy sample was the Advanced Camera for Surveys General Catalog (ACS-GC; Griffith et al., 2012). The ACS-GC is a photometric and morphological catalog of 469,501 galaxies imaged by the ACS on *HST* in four surveys: the Galaxy Evolution from Morphologies and SEDs (GEMS) survey, the Cosmological Evolutionary Survey (COSMOS), the Great Observatories Origins Deep Survey (GOODS), and the All-wavelength Extended Groth Strip International Survey (AEGIS). The ACS-GC provides photometric and/or spectroscopic redshifts for 345,783 (74%) of its galaxies, spanning a redshift range of $z \lesssim 6$ with a median redshift of $\langle z \rangle = 0.885$. This subsample of ACS-GC galaxies with redshifts is our parent galaxy sample.

The GEMS survey (Caldwell et al., 2008) uses the F606W and F850LP filters, has a coverage area of 0.21 deg^2, and a 5σ limiting AB magnitude of 25.7. COSMOS (Scoville et al., 2007) uses the F814W filter, has a coverage area of 1.8 deg^2, and a 5σ limiting AB magnitude of 26.0. GOODS (Dickinson and Giavalisco, 2003) uses the F606W, F775W, and F850LP filters, has a coverage area of 0.14 deg^2, and a 5σ limiting AB magnitude of 25.7. The GOODS survey is split into the GOODS-N (North) field and GOODS-S (South) field, with the GEMS field enveloping the GOODS-S field. Lastly, AEGIS (Davis et al., 2007) uses the F606W and F850LP filters, has a coverage area of 0.20 deg^2, and a 5σ limiting AB magnitude of 26.2. The ACS-GC is dominated by COSMOS galaxies due to its large field; COSMOS galaxies are 65% of all ACS-GC galaxies while GEMS + GOODS-S, AEGIS, and GOODS-N galaxies constitute 15%, 15%, and 5% of ACS-GC galaxies, respectively.

2.3 Active Galaxy Selection

Infrared (IR) and X-ray data are commonly used to identify galaxies containing an AGN (e.g. Stern et al., 2005; Brusa et al., 2010). During AGN accretion, gas is accreted and heated in the accretion disk, emitting strongly in the ultraviolet (UV). Some of these UV photons can interact with the AGN's hot compact plasma corona and undergo inverse Compton scattering, shifting them into the X-ray regime. This makes AGNs an ideal target for detection in the X-ray if they are

unobscured, or even moderately obscured (Brandt and Alexander, 2015). A common criterion for selecting AGNs in the X-ray regime is a rest-frame luminosity cut in the 2 – 10 keV band (Brandt and Alexander, 2015). In addition to interacting with the corona, some of the UV light from the AGN accretion disk is reprocessed into lower energy wavelengths as it heats nearby material, e.g. a torus (see Brandt and Alexander (2015) for an in-depth review of AGN physics and selection techniques). Some IR AGN selection techniques focus on the mid-IR regime and compare flux in different bands (color cuts) in the mid-IR, selecting for the spectral signature of an AGN torus-like structure that has been heated by its host AGN (e.g. Lacy et al., 2004; Stern et al., 2005; Donley et al., 2012). The mid-IR emission from the AGN torus is largely unattenuated by dust, making IR AGN selection complementary to X-ray AGN selection (Assef et al., 2013). The most common color cuts used to select AGNs in the mid-IR are from Lacy et al. (2004, 2007), Stern et al. (2005, 2012), and Donley et al. (2012).

In this Section we create our active galaxy sample using IR and X-ray AGN selection criteria, finding 3955 AGN host galaxies. In Section 2.3.1 we select AGNs using data from the *Spitzer Space Telescope*. In Section 2.3.2 we select AGNs using data from the *Chandra X-ray Observatory*. In Section 2.3.3 we compare the different AGN samples obtained from each telescope.

2.3.1 Infrared AGN Selection

In the IR regime, we created our active galaxy sample using data from the Infrared Array Camera (IRAC) on *Spitzer* (Fazio et al., 2004). IRAC has observed all four of the ACS-GC *HST* fields in four bands, channel 1: 3.6 μm, channel 2: 4.5 μm, channel 3: 5.8 μm, and channel 4: 8.0 μm, with a resolution of $\sim 2\farcs5$ for all channels.

We conducted a spatial crossmatch between the ACS-GC and the NASA/IPAC Infrared Science Archive (IRSA)[1] source catalog for *Spitzer* (the *Spitzer* Enhanced Imaging Products (SEIP) Source List), using the IRSA Gator search tool. We used an initial conical search radius of $3\farcs0$ for each source in order to fully understand the distribution of spatial separations between

[1] `http://irsa.ipac.caltech.edu`

Table 2.1: Systematic offsets in source matching

ACS-GC Field	IR / X-ray Catalog	RA Offset [arcsec]	Dec Offset [arcsec]
GEMS +	SEIP	$+0.058 \pm 0.001$	-0.213 ± 0.002
GOODS-S	CSC	-0.070 ± 0.016	$+0.282 \pm 0.024$
COSMOS	SEIP	-0.053 ± 0.001	$+0.092 \pm 0.001$
	CSC	$+0.027 \pm 0.006$	$+0.032 \pm 0.007$
GOODS-N	SEIP	-0.009 ± 0.003	-0.288 ± 0.005
	CSC	$+0.068 \pm 0.015$	-0.118 ± 0.023
AEGIS	SEIP	-0.029 ± 0.002	-0.200 ± 0.002
	CSC	-0.082 ± 0.011	$+0.156 \pm 0.117$

Systematic offsets based on Gaussian fits to positional differences between the ACS-GC and SEIP/CSC catalogs for each field (offset $\equiv$ SEIP/CSC $-$ ACS-GC).

sources from the ACS-GC and the SEIP. We then found the 3σ radius of this distribution of source separations. This 3σ radius should encompass nearly all true matches (99.7% if Gaussian) while minimizing false matches between sources from each catalog. We found that the 3σ radius of the SEIP crossmatches in these fields was $0\farcs5$. We redid the crossmatch, requiring the source separations to be less than or equal to this value.

The matched source separations were approximately Gaussian distributed, as expected from small random differences in position between the optical and IR sources and/or statistical fluctuations in measured source positions. The distributions also had small systematic offsets for each extragalactic field (i.e., GEMS + GOODS-S, COSMOS, GOODS-N, AEGIS). We calculated these systematic offsets by fitting a Gaussian profile to each distribution of source separations, and present the astrometric offsets for each field in Table 2.1.

We then adjusted the *HST* coordinates for these systematic offsets and did a final crossmatch, using a radius of $0\farcs5$ for SEIP sources. We retain the original ACS-GC coordinates in our catalog. Correcting for the systematic astrometric offsets increased the number of matched sources within our search cone by 2.7% for SEIP sources.

We then identified galaxies hosting AGNs using the established Donley et al. (2012) IR AGN selection criteria. Implicit with these criteria, each source was required to have data in

all four IRAC channels; approximately 43% of matched *Spitzer* sources met this requirement. Most incompleteness was in the 5.8 μm and 8.0 μm bands, which are approximately an order of magnitude less sensitive than the 3.6 μm and 4.5 μm bands of *Spitzer*. Our selection resulted in 1861 IR-selected AGN host galaxies (2.3% of all matched *Spitzer* sources with four channel flux data).

2.3.2 X-Ray AGN Selection

To create our active galaxy selection in the X-ray regime, we used data from the Advanced CCD Imaging Spectrometer (ACIS) on *Chandra*, presented in the *Chandra* Source Catalog (CSC) v2.0 (Evans and Civano, 2018) preliminary detection list (pd1).

We repeated our aforementioned crossmatching procedure, conducting an initial spatial crossmatch between the ACS-GC catalog and the CSC 2.0 pd1 using a $2\farcs0$ matching radius, finding the 3σ radius of the resulting distribution ($1\farcs5$), and redoing the crossmatch using this value. We then repeated our procedure of Gaussian fitting and removal of systematic offsets in the positional differences between matched sources as outlined in Section 2.3.1; the offsets for each field can be found in Table 2.1. Correcting the systematic astrometric offsets increased the number of matched sources within our *Chandra* search cone by 0.21%.

The AGN selection criterion we used for the X-ray regime was a rest-frame X-ray luminosity cut in the 2 – 10 keV band of $L_{2-10} > 10^{42}$ erg s^{-1}; this criterion ensures the exclusion of all but the most vigorously star-forming galaxies – those with SFR $\geq 200\ M_{\odot}\ \mathrm{yr}^{-1}$ (Ranalli et al., 2003). In order to obtain a rest-frame luminosity in the 2 – 10 keV band, we first converted the observed 2 – 7 keV photon flux from the CSC to energy flux using an effective energy[2] of 3.8 keV. We then assumed a power law X-ray spectrum with a photon index of 1.7, the mean value found for a comparable AGN sample by Brightman et al. (2014), in order to model the observed 2 – 10 keV energy flux. Finally, we used galaxy redshift data from the ACS-GC catalog in order to apply a K-correction to the observed 2 – 10 keV energy flux and calculate the rest-frame 2 – 10 keV

[2] `http://cxc.harvard.edu/csc/columns/ebands.html`

luminosity for each object. We then selected AGN as galaxies that had restframe 2 – 10 keV band luminosity 1σ lower bounds greater than our luminosity cutoff of 10^{42} erg s^{-1}.

Our selection resulted in 2624 X-ray-selected AGN host galaxies (83.5% of all matched *Chandra* sources with flux data in the 2 – 10 keV band), with a significant number of these also selected as AGN in the IR. This overlap is discussed further in Section 2.3.3.

2.3.3 AGN Selection Comparison

X-ray and IR selection techniques uncover different samples of AGNs that have some overlap. Eckart et al. (2010) found that X-ray AGNs that lack high-ionization and/or broad lines in the optical were less likely to be selected as IR AGNs, and further suggest that IR-selected AGNs that are not selected in the X-ray are primarily high-luminosity AGNs that are obscured and/or at high redshift. Based on a sample of 55 AGNs in the COSMOS, GOODS-N, and EGS fields, Azadi et al. (2017) find many selection biases in X-ray and IR-selected AGNs, including a bias towards high-mass galaxies in X-ray-selected AGNs and a bias towards moderate-mass galaxies in IR-selected AGNs. They attribute this to the fact that X-ray selection techniques can identify AGNs at low specific accretion rates, while IR selection techniques are biased towards finding high specific accretion rate AGNs. Azadi et al. (2017) also finds that IR-selected AGNs are biased towards lower dust content than X-ray-selected galaxies, which they attribute to the stellar mass selection bias of IR-selected AGNs. Specifically, IR-selected AGNs are found in lower stellar mass galaxies, which tend to be dustier than higher mass galaxies. Further, Hainline et al. (2016) found that an IR-selected AGNs sample can be contaminated by star-forming dwarf galaxies that are capable of mimicking the IR colors of more luminous AGNs.

Through our selection process, we narrowed our initial sample of 345,783 ACS-GC galaxies with redshifts to 3955 unique active galaxies identified by IR and/or X-ray methods. Of these, 2094 and 1331 were uniquely identified by *Chandra* and *Spitzer*, respectively, while 530 were identified by both telescopes (Figure 2.1). With the wide redshift range and galaxy parameter space covered by the deep *Spitzer* and *Chandra* observations in these fields, we see the benefit of using X-ray and

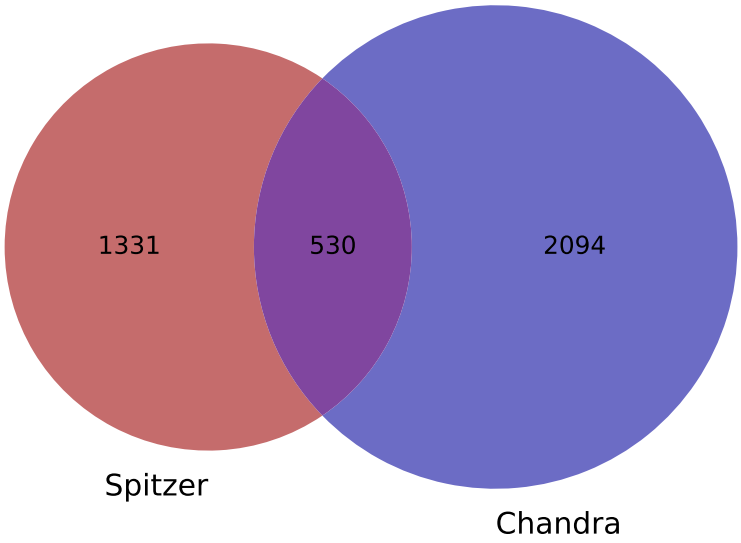

Figure 2.1: Venn diagram of identified AGN host galaxies: IR-selection by *Spitzer* and X-ray-selection by *Chandra*.

IR selection techniques in tandem as their biases work to complement each other.

Examining the COSMOS field — our largest field, with an area of $\sim$1.6 deg^2 — we find number densities of 1154 X-ray-selected AGNs per deg^2 and 818 IR-selected AGNs per deg^2. We can compare these numbers to those of Mendez et al. (2013), a study that compares X-ray and IR AGN selection techniques in the COSMOS field. We find the number density of X-ray-selected AGNs to be in good agreement (1154 vs 1176), while our IR-selected AGNs number density disagrees significantly (818 vs 443). This may be due to the increase in *Spitzer* observation depth since that work, with Mendez et al. (2013) reporting flux limits of $\gtrsim$20 μJy in the 5.8 μm channel while the SEIP data typically have flux densities ($3\sigma+$) as low as 0.01-1 μJy in the 5.8 μm channel.

2.4 Obtaining Galaxy SEDs

We use SEDs in order to create self-consistent models based on photometric data to derive AGN and galaxy properties. Since observations that span a large portion of a galaxy's spectrum

are difficult to obtain, fitting SED templates to available photometric data is often necessary. The Low-Resolution Templates (`LRT`) program (Assef et al., 2008, 2010) is one such template fitting package that fits galaxy and AGN templates at the same time.

In this Section we model our AGN host galaxies' SEDs and employ Monte Carlo technique error modeling, resulting in 2873 AGN host galaxies with well fit SEDs. In Section 2.4.1 we discuss the multi-band photometric data we obtained and used to model our SEDs. In Section 2.4.2 we discuss how we fit galaxy and AGN SED templates to the multi-band photometric data of our active galaxies. Finally, in Section 2.4.3 we discuss the method by which we estimated errors on our SED-derived galaxy parameters through the use of Monte Carlo techniques.

2.4.1 Photometric Data

We first obtained multi-band photometric data for our AGN host galaxies, requiring flux data in at least seven bands for each galaxy. This is because `LRT` requires flux data in at least seven photometric bands from 0.03 μm – 30 μm in order to properly fit SED templates and an extinction parameter and maintain at least 1 degree of freedom in the model.

For most galaxies in the COSMOS field, we used the COSMOS2015 catalog from Laigle et al. (2016). This catalog includes flux and/or magnitude data from the X-ray to radio; however, we only used data in 22 of the bands, from the mid-UV to the mid-IR, due to the 0.03 – 30 μm wavelength range of our SED fitting software. These data came from instruments on *GALEX*, Subaru, CFHT, VISTA, and *Spitzer*. Of the 2639 galaxies we selected as active in the COSMOS field, the COSMOS2015 catalog contained at least seven bands of photometric data for 2587 (98.0%) of them.

Unlike the COSMOS survey, the other three surveys included in this work do not have large, complete, multi-band photometric catalogs publicly available. For the remaining 1316 non-COSMOS galaxies we selected as active, we obtained photometry for 576 (43.7%) of them in 18 bands, ranging from the near-UV to the mid-IR. These data came from the CFHT and VISTA telescopes (data provided by Dan Masters, private correspondence), as well as *WISE* and *Spitzer*

(data from the AllWISE Source Catalog and the SEIP Source List). In total, we obtained at least seven bands of photometric data for 3163 of the 3955 (79.9%) galaxies we selected as active.

2.4.2 SED Fitting

We use the multi-band photometric data to fit SED templates to our active galaxies with the `LRT` software. `LRT` models a galaxy's SED as a non-negative linear combination of an AGN and three galaxy SED components: elliptical, SBc spiral, and irregular. The AGN SED component is a Type 1 AGN to which an extinction law is applied (Cardelli et al., 1989; Gordon and Clayton, 1998). The extinction term E_{B-V} is fit by `LRT` and mimics nuclear obscuration when applied, allowing for the AGN template to resemble an obscured AGN. The low-resolution templates were empirically derived from over 16,000 galaxies in the Boötes field with spectroscopic redshifts and photometry, and are limited to the wavelength range of 0.03 – 30 μm (Assef et al., 2008, 2010). These templates are simultaneously fit to the observed photometric data points, accounting for the associated error on the flux measurements.

The creation of empirically derived templates involves condensing a large dataset with intrinsic scatter into a singular SED template. This process creates uncertainty in the template itself, and may be one of the largest sources of error in SED modeling (Abrahamse et al., 2011). In order to account for template uncertainty, we instituted an error floor of 10% on all of our photometric data (i.e., if the associated error on a given flux measurement was <10%, we fixed it to 10%). This practice is also used by other studies to account for known errors (e.g. instrument calibration errors, Donley et al., 2012).

In addition, the number of inaccurate photometric data points increases as the size of the data set increases. Anomalous photometric data can come from multiple sources, encompassing both instrumental and astrophysical errors (e.g. variability, foreground/background). The presence of anomalous data points will lead to poor SED fits. A method used to minimize the impact of anomalous data points is to iteratively exclude individual photometric data points, fit the SED templates, and calculate whether the fit is substantially improved from its parent using the F ratio

statistic, which compares the improvement in χ^2 with the change in degrees of freedom (e.g., Chung et al., 2014). We used this method in our SED fitting, allowing up to two photometric data points to be excluded for each galaxy being modeled, as long as there was at least seven data points still being fit, requiring a p-value ≤ 0.05 in the F ratio test, as well as a χ^2_ν goodness of fit cutoff. The model was only found satisfactory if $\chi^2_\nu < 1 + \sqrt{2/\nu}$, where ν is the degrees of freedom (ν = data points – fit parameters – 1) and $\sqrt{2/\nu}$ is the 1σ error, assuming Gaussian uncertainties (Chung et al., 2014).

2.4.3 Monte Carlo Error Estimation

In order to model errors for the AGN and host galaxy properties that we extract from the SED fit (Section 2.5), we used Monte Carlo techniques. Specifically, after eliminating any anomalous data points (Section 2.4.2), we resampled the remaining photometric data, drawing new values from a Gaussian distribution centered on the known value, with standard deviation equal to the associated flux error. After doing this for all data points, we reran `LRT`, creating a new SED model fit. We repeated this process 1000 times for each galaxy, keeping only those SED model fits that obeyed the goodness of fit criterion outlined in Section 2.4.2. We removed from further analysis the galaxies in which fewer than 10 of the 1000 iterations met the goodness of fit criterion.

This process created an SED model fit distribution with up to 1000 individual fits for each AGN host galaxy, propagating the uncertainty from the photometric data to the SED model fits. This allowed us to obtain uncertainty values for the AGN and host galaxy properties derived in the following Section. In total, we were able to satisfactorily model and create SED model fit distributions for 2873 of the 3163 (88.0%) active galaxies for which we obtained multi-band photometric data.

2.5 Galaxy Properties

All of the AGN and host galaxy properties we use in our analysis, save for the redshifts included in the ACS-GC, are derived from the aforementioned SED model fits. By obtaining all

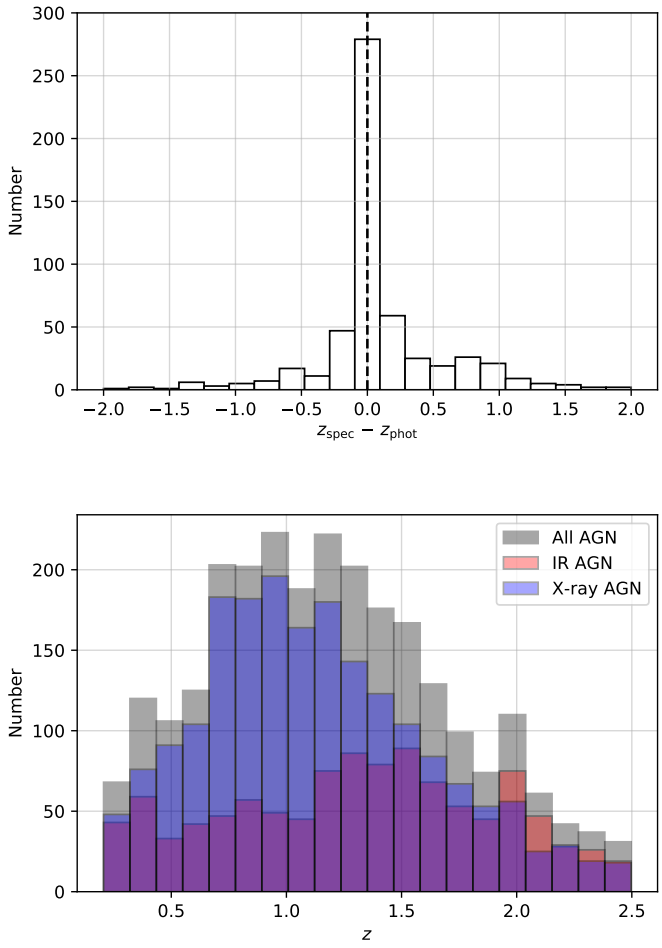

Figure 2.2: Histogram of the differences between spectroscopic and photometric redshift values for the subsample of our galaxies that have both and exist between $0.2 < z_{\rm spec} < 2.5$ (top); the dashed line is the $z_{\rm spec} = z_{\rm phot}$ line. Histogram of the redshifts for our active galaxy sample (bottom); note how the X-ray-selected distribution peaks at a lower redshift value than the IR-selected distribution. The All AGN sample (gray) is included in addition to the two subpopulations that make it up (IR AGN [Red] and X-ray AGN [Blue]) because the two selection techniques create an overlapping sample of AGNs.

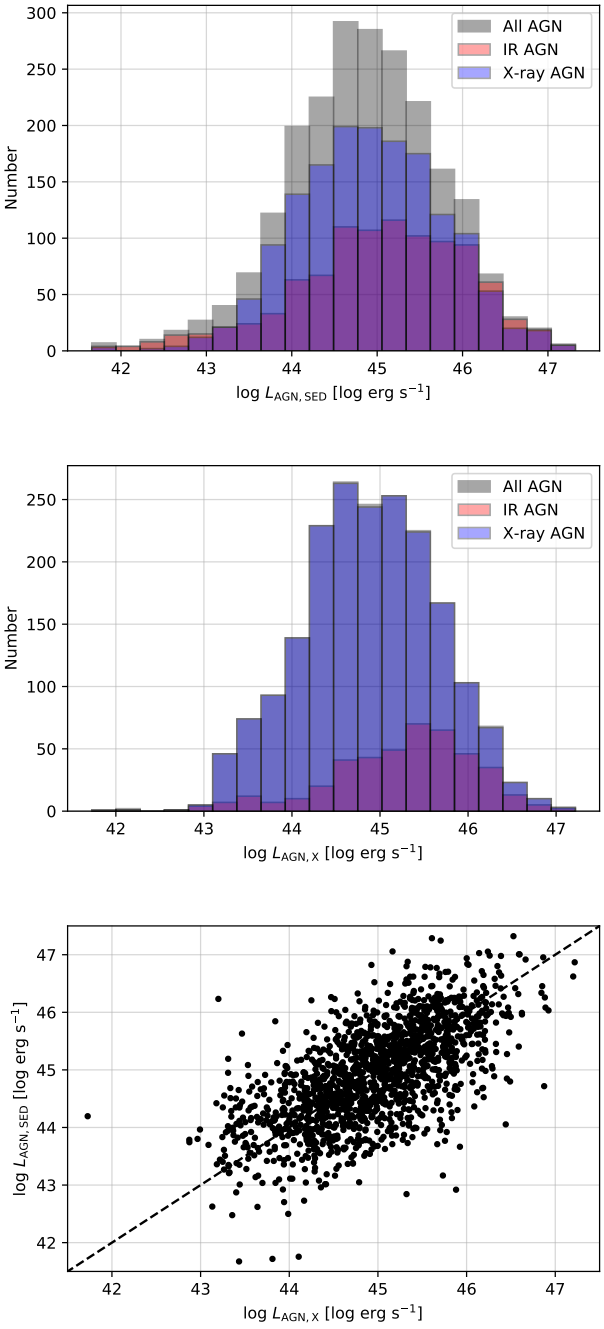

Figure 2.3: Histogram of the $L_{\mathrm{AGN,SED}}$ values for our active galaxy sample (top); note the similar peaks of the IR and X-ray-selected distributions. Histogram of the $L_{\mathrm{AGN,X}}$ values for our X-ray-selected subsample (middle); note the higher luminosity peak for those selected with both IR and X-ray methods. $L_{\mathrm{AGN,SED}}$ as a function of $L_{\mathrm{AGN,X}}$ for the subsample of galaxies which have both luminosity measurements (bottom); the dashed line is the $L_{\mathrm{AGN,X}} = L_{\mathrm{AGN,SED}}$ line. Note that the scatter is evenly distributed across the $L_{\mathrm{AGN,X}} = L_{\mathrm{AGN,SED}}$ line for all luminosities, and therefore there is no dependence on AGN luminosity.

properties from the same SED model, we ensure they are self-consistent, free from biases introduced when using different filters or observations to calculate different AGN or host galaxy properties, and decrease the effect of AGN variability on measured properties.

In this Section we discuss the derivation of AGN and host galaxy properties. In Section 2.5.1 we discuss our sample's redshift distribution, and the selection of our final sample of 2585 AGN host galaxies included in the catalog. In Section 2.5.2 we discuss the derivation of AGN bolometric luminosity from both the SED model and X-ray data, and we compare the two resulting datasets. In Section 2.5.3 we discuss the derivation of stellar mass from the SED model. In Section 2.5.4 we discuss the derivation of SFR from the SED model, and in Section 2.5.5 we discuss the derivation of column density from the SED model. All of these properties are included in the ACS-AGN catalog, as shown in Table 2.2. Finally, in Section 2.5.6 we examine our derived properties in comparison with other recent work.

2.5.1 Redshift (z)

We selected our initial sample to only be galaxies that the ACS-GC provides redshift values for, either photometric or spectroscopic. All but 11 galaxies in our final sample have photometric redshifts, and approximately 20% of our galaxies also have spectroscopic redshifts. When a galaxy has both photometric and spectroscopic redshifts, we us the spectroscopic redshift, except in rare cases when the error on the spectroscopic redshift is large, as indicated in the ACS-GC.

We then examine the subsample of our galaxies for which we have both photometric and spectroscopic redshifts. The ACS-GC also provides errors for their photometric redshifts; using these, and again instituting a 10% error floor on the error values similar to the one discussed in Section 2.4.2 for photometric flux errors, we find that the majority (75%) of spectroscopic and photometric redshifts agree to within 3σ. However, there is significant deviation when examining the distributions of our lowest ($z_{\rm spec} < 0.2$) and highest ($z_{\rm spec} > 2.5$) redshift galaxies (median $z_{\rm spec} - z_{\rm phot} = 1.0$ and 2.3, respectively). Therefore, for the rest of this paper we only study the 2585 galaxies with redshifts of $0.2 < z < 2.5$. The distribution of differences between spectroscopic

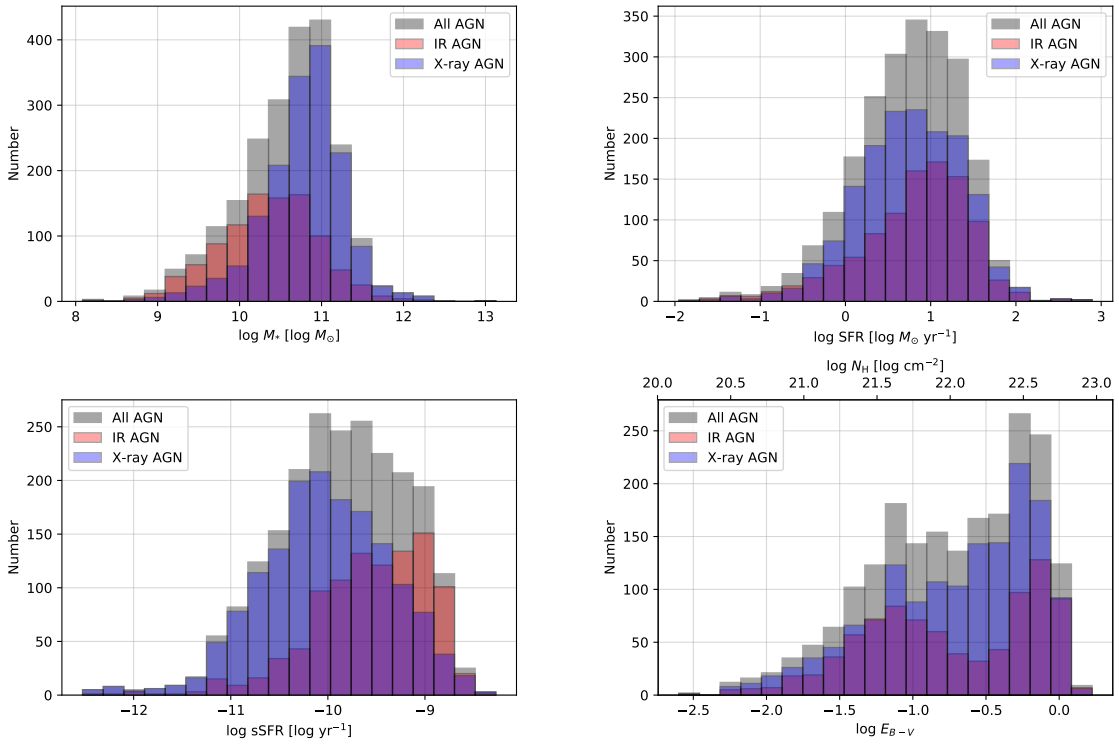

Figure 2.4: Histogram of the M_* values for our active galaxy sample (top left), histogram of the SFR for our active galaxy sample (top right), and histogram of the sSFR values for our active galaxy sample (bottom left); note the lower peak M_* value of the IR-selected AGN host galaxy distribution compared to the X-ray-selected AGN host galaxy distribution, and the slightly higher SFR peak of the IR-selected AGN host galaxy distribution compared to that of the X-ray-selected AGN host galaxy distribution. These effects combine to produce the two subsamples' sSFR distributions, with the IR-selected AGN host galaxy distribution peaking at a higher value than the X-ray-selected AGN host galaxy distribution. Histogram of the E_{B-V} and $N_{\rm H}$ values for our active galaxy sample (bottom right); note the double peaked nature of the distributions.

and photometric redshift for the galaxies that fall within this range can be seen in Figure 2.2, top. The distribution is approximately a Gaussian with enhanced tails, centered on zero, and with a standard deviation of $\sigma = 0.1$

The full redshift distribution of our galaxy sample is shown in Figure 2.2, bottom. When examining our AGN subsamples, we find that our IR-selected AGNs display a flat distribution of redshifts, while the X-ray-selected AGNs display a positively skewed (longer tail towards higher redshifts) distribution and peaks at a lower redshift value than the IR-selected distribution. These distributions coincide with the previously discussed findings of Eckart et al. (2010) (see Section 2.3) that X-ray AGNs not selected in the IR tend to have lower redshifts on average. They attribute this to the fact that X-ray selection techniques are able to select low-luminosity AGNs missed by IR selection techniques.

2.5.2 AGN Bolometric Luminosity ($L_{\rm AGN}$)

In order to examine SMBH growth, we need to measure AGN bolometric luminosity. Commonly, other works use the X-ray luminosity, either directly or converted to a bolometric luminosity, of the AGN when comparing SMBH growth to a host galaxy's SFR. While this attempts to avoid possible contamination added by star formation, and error added through any bolometric correction when using X-ray luminosity directly, this measurement is susceptible to AGN variability in the X-ray (e.g., Hickox et al., 2014; Volonteri et al., 2015b,a). Deriving AGN bolometric luminosity by integrating an AGN SED model that has been simultaneously fit alongside a galaxy SED model, including any star formation components, allows us to avoid star formation contamination and bolometric correction error, while also being less susceptible to AGN variability due to the broadband nature of the SED.

In order to calculate the bolometric luminosity from the SED fits ($L_{\rm AGN,SED}$) we integrate the best fit rest-frame unextincted AGN SED component template for each galaxy from 0.1 μm – 30 μm. This range dominates the integrated luminosity of the AGN and can be used as a good estimate of the AGN bolometric luminosity (Assef et al., 2011). The distribution of these

bolometric luminosities are shown in Figure 2.3, top. Both IR and X-ray-selected AGN distributions are roughly symmetric and peak near luminosities of 10^{45} erg s^{-1}.

For the subsample of our galaxies for which we had X-ray data, we calculate an alternate bolometric luminosity ($L_{\mathrm{AGN,X}}$) from the previously calculated L_{2-10} (Section 2.3.2) using the relation found in Marconi et al. (2004). This work improves upon earlier work by Elvis et al. (1994) and applies a larger bolometric correction for higher luminosity values. The distribution of these bolometric luminosities are shown in Figure 2.3, middle. The IR-selected AGN subsample distribution peaks at a higher luminosity than that of the total X-ray-selected AGN distribution, indicating that AGNs selected in both the IR and X-ray have higher luminosities on average than AGNs selected in only one regime.

We also compared these two methods of calculating AGN bolometric luminosity for the 1676 (58%) AGN host galaxies that had *Chandra* data. To compare them, we examined $L_{\mathrm{AGN,SED}}$ as a function of $L_{\mathrm{AGN,X}}$ (Figure 2.3, bottom); from this we find that the data are evenly distributed across the $L_{\mathrm{AGN,X}} = L_{\mathrm{AGN,SED}}$ line for all luminosities, and therefore the difference distribution has no dependence on AGN luminosity. We find that the distribution of log-differences in AGN bolometric luminosity between the two methods is a Gaussian centered at zero with a standard deviation of 0.6. This indicates that the integrated luminosity of the modeled AGN SED is a comparable measure to traditional X-ray bolometric correction methods on average. The spread of the distribution may be due to the assumption of a uniform photon index value when calculating $L_{\mathrm{AGN,X}}$, causing obscuration, and therefore luminosity, to be under or overestimated in specific cases.

This can be further investigated by examining reported hardness ratios (HR) for our galaxies. HR is a metric which roughly quantifies the X-ray spectral shape of an X-ray source, specifically the intrinsic absorption (Marchesi et al., 2016), where low values of HR represent less absorption and higher values represent more absorption. The photon index used when calculating X-ray luminosity in Section 2.3.2 also assumes an X-ray spectral shape and intrinsic absorption, with a value of 1.9 being an accepted value for an unabsorbed AGN (Corral et al., 2011). Therefore, our choice of 1.7

is an assumption of slight absorption in our AGN.

To investigate whether the scatter could be due to the uniform photon index assumption, we examined the differences in AGN bolometric luminosity as a function of HR for the subset of our sample which had HR values reported in the COSMOS-Legacy catalog (Civano et al., 2016), and find that there is only partial correlation between the two. Specifically, when binning by HR, we find that at low HR (HR < -0.4) our SED model AGN luminosity is greater when compared to the X-ray calculated AGN bolometric luminosity by approximately 0.2 dex (with a standard deviation of 0.4 dex). This follows with our assumptions, as at low HR our choice of photon index was too low, causing an overestimation of X-ray absorption. But at higher HR (HR > -0.4) the two calculations for AGN bolometric luminosity are in agreement (no difference but with standard deviations up to 0.6 dex). If the scatter in our two methods was purely due to the use of a single photon index, at the highest HR values we would expect the SED model AGN luminosity to be less than the X-ray calculated AGN bolometric luminosity as our chosen photon index should be underestimating X-ray absorption in these cases. Since we do not see this, this is either a selection effect in the comparison sample (we do note a lack of high HR sources, with only 7% of the comparison sample having values of HR > 0.4) or there must be further scatter intrinsic in the X-ray calculation of AGN bolometric luminosity than can be accounted for solely by the use of a single photon index. The lack of X-ray data for a significant portion of our sample and the scatter introduced from the assumption of a uniform photon index when calculating AGN luminosities from X-ray data led us to choose $L_{\mathrm{AGN,SED}}$ as the AGN luminosity metric used in our analysis for the rest of this paper.

2.5.3 Stellar Mass (M_*)

We used a color to specific luminosity relation in order to derive our galaxy stellar masses. First, we obtained the modeled g' and r' band galaxy magnitudes as well as the restframe luminosity in the r band (L_r), not including the contribution from the AGN component, from the SED model. We then used these to calculate galaxy stellar mass using the relation between $g' - r'$ color and M/L_r from Bell et al. (2003): $\log_{10}(M/L_r) = -0.499 + 1.519(g' - r')$, where the M/L_r ratio is in

solar units.

The stellar mass distribution of our active galaxy sample is shown in Figure 2.4, top left. We see that the X-ray-selected AGN host galaxy distribution peaks at a higher stellar mass than that of the IR-selected AGN host galaxy distribution. These findings are in line with the previously discussed findings of Azadi et al. (2017), that X-ray-selected AGN host galaxies are biased towards higher stellar mass values, while IR-selected AGN host galaxies are biased towards moderate mass values (see Section 2.3).

2.5.4 Star Formation Rate (SFR)

There are multiple methods used to calculate a galaxy's SFR, including emission line diagnostics, monochromatic luminosities, and integrated IR luminosity. Since we have modeled our galaxy SEDs, we opt to use a monochromatic luminosity conversion to estimate SFRs. This approach has the added benefit of not having contamination from the AGN, since each SED model included separate AGN and galaxy components. We used the 2800 Å monochromatic luminosity conversion, assuming a Salpeter IMF, described in Madau et al. (1998) in order to calculate our host galaxy SFRs: $\mathrm{SFR}/(M_\odot\ \mathrm{yr}^{-1}) = L_{2800}/(7.9 \times 10^{27}\ \mathrm{erg\ s^{-1}\ Hz^{-1}})$. The distribution of these derived values is shown in Figure 2.4, top right. Comparing the two AGN selection methods, it appears that galaxies hosting IR-selected AGNs have slightly higher SFR values on average than galaxies hosting X-ray-selected AGNs (we discuss this further in Section 2.6.1): IR-selected AGN host galaxy median SFR $= 8.5 \pm 0.6\ M_\odot\ \mathrm{yr}^{-1}$ and X-ray-selected AGN host galaxy median SFR $= 5.9 \pm 0.3\ M_\odot\ \mathrm{yr}^{-1}$.

By combining our stellar mass and SFR measurements, we also examine specific star formation rates ($\mathrm{sSFR} \equiv \mathrm{SFR}/M_*$). Figure 2.4, bottom left, shows that the two selection methods are significantly diverged, with the IR-selected AGN host galaxy distribution having a strong negative skew and peaking more than an order of magnitude higher in sSFR values than the X-ray-selected AGN host galaxy distribution.

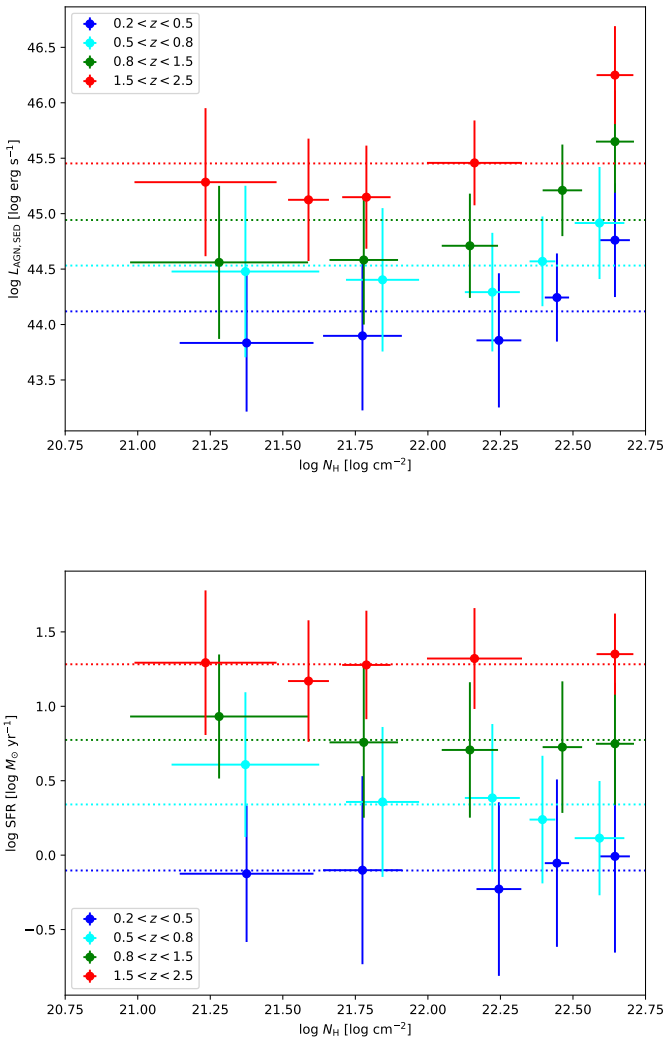

Figure 2.5: A plot of AGN bolometric luminosity as a function of nuclear column density for our active galaxy sample (top), binned by redshift (blue = $0.2 < z < 0.5$, cyan = $0.5 < z < 0.8$, green = $0.8 < z < 1.5$, and red = $1.5 < z < 2.5$) and then by nuclear column density such that each column density bin has an equal number of galaxies for a given redshift bin; the horizontal dashed lines are powerlaw slopes of zero (constant). Note that the points are consistent with zero slope, but appear to begin to show a positive correlation above column densities of $\sim 10^{22}$ cm^{-2}. A plot of host galaxy star formation rate as a function of nuclear column density, binned by redshift and then nuclear column density, for our active galaxy sample (bottom), where the horizontal dashed lines are powerlaw slopes of zero (constant); note that the points are consistent with zero slope throughout.

2.5.5 Nuclear Column Density ($N_{\rm H}$)

One of the parameters fit by `LRT` is an extinction value, E_{B-V}, that is applied to the AGN template. The E_{B-V} extinction parameter can be converted to column density via a conversion derived from two studies (Maiolino et al., 2001; Burtscher et al., 2016) that found a ratio between the two for approximately 40 AGN host galaxies. By computing a weighted average of all galaxies presented in the two works, we find a conversion factor of $E_{B-V}/N_{\rm H} = 1.80 \pm 0.15 \times 10^{-23}$ cm^2. After applying this conversion, we find the distribution shown in Figure 2.4, bottom right. We find that our IR-selected AGN distribution is significantly bimodal, with our X-ray-selected AGN distribution also showing a secondary peak at the same location as that of the IR-selected AGN distribution. This bimodal nature of column density values for a population of AGNs was observed previously by Civano et al. (2016), which used the hardness ratio in place of column density. Civano et al. (2016) interpreted this bimodal feature as the result of the galaxy population containing both obscured and unobscured AGNs.

Further, we analyze trends in the comparison of our column density values as a function of known HR values from Civano et al. (2016). As discussed in Section 2.5.2, low HR values correspond with less intrinsic absorption (low column densities) and high HR values correspond to more intrinsic absorption (high column densities). Therefore as HR values increase, we should expect to see column densities increase as well. When examining our AGN host galaxies, we find that while our column densities do increase as HR becomes more positive, there is considerable scatter, with standard deviations in column density of approximately 0.5 dex across all HR bins.

We also examine the relationship between nuclear column density and AGN luminosity (Figure 2.5, top), as well as host galaxy SFR (Figure 2.5, bottom). First, we find both the $L_{\rm AGN,SED}-N_{\rm H}$ and SFR – $N_{\rm H}$ relations are consistent with a powerlaw slope of zero (constant) for all redshift bins (none of the eight powerlaw fits resulted in a p-value < 0.01, and only one with a p-value < 0.05). However, we do note that at higher nuclear column densities ($N_{\rm H} \gtrsim 10^{22}$ cm^{-2}), the AGN bolometric luminosity seems to increase with nuclear column density. This behavior seems to be apparent

at all redshifts, but is not significant in any (none of the eight powerlaw fits using only data points with $N_{\rm H} \gtrsim 10^{22}$ cm^{-2} resulted in a p-value < 0.01, and only one with a p-value < 0.05). This may indicate that nuclear column density is not a critical tracer of AGN fueling until reaching higher values or could be a result of the flux-limited nature of our sample; possible future work could explore whether this trend is significant at higher column densities and into the Compton thick regime ($N_{\rm H} \geq 10^{24}$ cm^{-2}) for a sample which is not flux-limited.

The lack of correlation between nuclear column density and host galaxy star formation has been observed before (e.g., Rosario et al., 2012), and may point to a difference in fueling processes or timescales between SMBH growth and host galaxy star formation. This is surprising however given that models by Sanders et al. (1988) predict that most SMBH growth occurs when the AGN is surrounded by a dense, dusty, obscuring envelope, and models by Somerville et al. (2008) predict that AGN obscuration should trend with a galaxy's global SFR.

2.5.6 Comparison to Other Work

The variety and depth of observations in the COSMOS field has enabled a significant number of works and catalogs to be built from them. The catalog produced by Jin et al. (2018) (hereafter J18) is one such work; galaxy properties within this catalog, including SFR and M_*, are derived from SED fits to "super-deblended" photometric observations ranging in wavelength from the far-IR (FIR) to the submillimeter (sub-mm). Matching AGN host galaxies from our catalog to that of J18 using a search cone of radius $0\farcs25$, and requiring a difference in redshift of $\Delta z < 0.1$, results in 1197 galaxies with which we can compare derived SFR and M_* values.

When comparing our galaxy properties to those derived by J18, we find that our $\log(M_*)$ values are systematically higher than those of J18, with a median difference of 0.25 dex, and that our log(SFR) values are systematically lower, with a median difference of -0.71 dex. These disagreements are due to differences in methods between this work and J18. The first significant difference is the bands used to create the SEDs in each work, with J18 using FIR to sub-mm bands and this work using mid-UV to mid-IR bands. This results in minimal overlap in the observational

wavelength regime used to build the underlying SEDs and derive galaxy properties. Secondly, J18 derive their SFR via a two-step process. First an initial SED fit is used to calculate an initial SFR, which is then used to choose whether a starburst or main-sequence galaxy type stellar component is used in the final SED fit. This final SED fit, based on the preliminary SFR measurement, is then used to determine the final SFR. This approach limits the range of stellar component fits while the method described in Section 2.4.2 of this work allows for a large range of stellar component SEDs by using a linear combination of three diverse galaxy templates for all SED fits. This could explain the lower SFR values found in this work when compared to the values found in J18.

Further, our SED fitting method and derivation of galaxy properties has been tested by Barrows et al. (2017b). They examine four SDSS galaxies and compare SFR and M_* values derived using the same method as this work to measurements made with SDSS optical fiber spectra and included in the MPA-JHU catalog (Kauffmann et al., 2003; Brinchmann et al., 2004). Barrows et al. (2017b) find their derived values of SFR and M_* to be consistent within their uncertainties to those of the MPA-JHU catalog and they find no systematic offset between the two (see Barrows et al. (2017b) for a more in-depth discussion).

Therefore, we find it difficult to make a direct comparison to J18 because of significant differences in methods between our two works. We believe our approach to be more appropriate due to our use of a more diverse wavelength range and a more diverse set of SED stellar components when creating the SED models from which we calculate SFR and M_* values. Our approach is also consistent with SFR and M_* values in SDSS as shown in Barrows et al. (2017b).

2.6 Results

In this Section we discuss the primary results from statistical analysis of the properties of our AGNs and their host galaxies. In Section 2.6.1 we examine the location of our AGN host galaxies with respect to the star-forming main sequence, and in Section 2.6.2 we examine an SFR – AGN luminosity relation, accounting for redshift.

Table 2.2: Data Fields in the ACS-AGN Catalog

No.	Field	Note
1	ID	catalog specific unique identifier
2	RA	right ascension [J2000, decimal degrees]
3	DEC	declination [J2000, decimal degrees]
4	Z	redshift used
5	SPECZ	spectroscopic redshift
6	PHOTOZ	photometric redshift
7	Spitzer_AGN	if AGN was selected in *Spitzer* [Boolean]
8	Chandra_AGN	if AGN was selected in *Chandra* [Boolean]
9	L_bol_sed_md	AGN bolometric luminosity derived from SED, median [erg s^{-1}]
10	L_bol_sed_lo	AGN bolometric luminosity derived from SED, lower bound [erg s^{-1}]
11	L_bol_sed_hi	AGN bolometric luminosity derived from SED, upper bound [erg s^{-1}]
12	L_x_md	2 – 10 keV restframe luminosity, median [erg s^{-1}]
13	L_x_lo	2 – 10 keV restframe luminosity, lower bound [erg s^{-1}]
14	L_x_hi	2 – 10 keV restframe luminosity, upper bound [erg s^{-1}]
15	L_bol_x_md	AGN bolometric luminosity derived from X-ray, median [erg s^{-1}]
16	L_bol_x_lo	AGN bolometric luminosity derived from X-ray, lower bound [erg s^{-1}]
17	L_bol_x_hi	AGN bolometric luminosity derived from X-ray, upper bound [erg s^{-1}]
18	M_star_md	galaxy stellar mass, median [$M_\odot$]
19	M_star_lo	galaxy stellar mass, lower bound [$M_\odot$]
20	M_star_hi	galaxy stellar mass, upper bound [$M_\odot$]
21	SFR_md	star formation rate, median [$M_\odot$ yr^{-1}]
22	SFR_lo	star formation rate, lower bound [$M_\odot$ yr^{-1}]
23	SFR_hi	star formation rate, upper bound [$M_\odot$ yr^{-1}]
24	Nh_md	nuclear column density, median [cm^{-2}]
25	Nh_lo	nuclear column density, lower bound [cm^{-2}]
26	Nh_hi	nuclear column density, upper bound [cm^{-2}]
27	SFR_norm_md	normalized star formation rate, median
28	SFR_norm_lo	normalized star formation rate, lower bound
29	SFR_norm_hi	normalized star formation rate, upper bound

Field numbers 2 – 6 are taken from the ACS-GC catalog (Griffith et al., 2012). AGN selection and derivations of AGN and host galaxy properties are described throughout this paper. The lower bound and upper bound are defined as the 16th and 84th percentiles of the distribution, respectively. A "999" value in the table represents no data. This table is available in its entirety in FITS format from the original publisher.

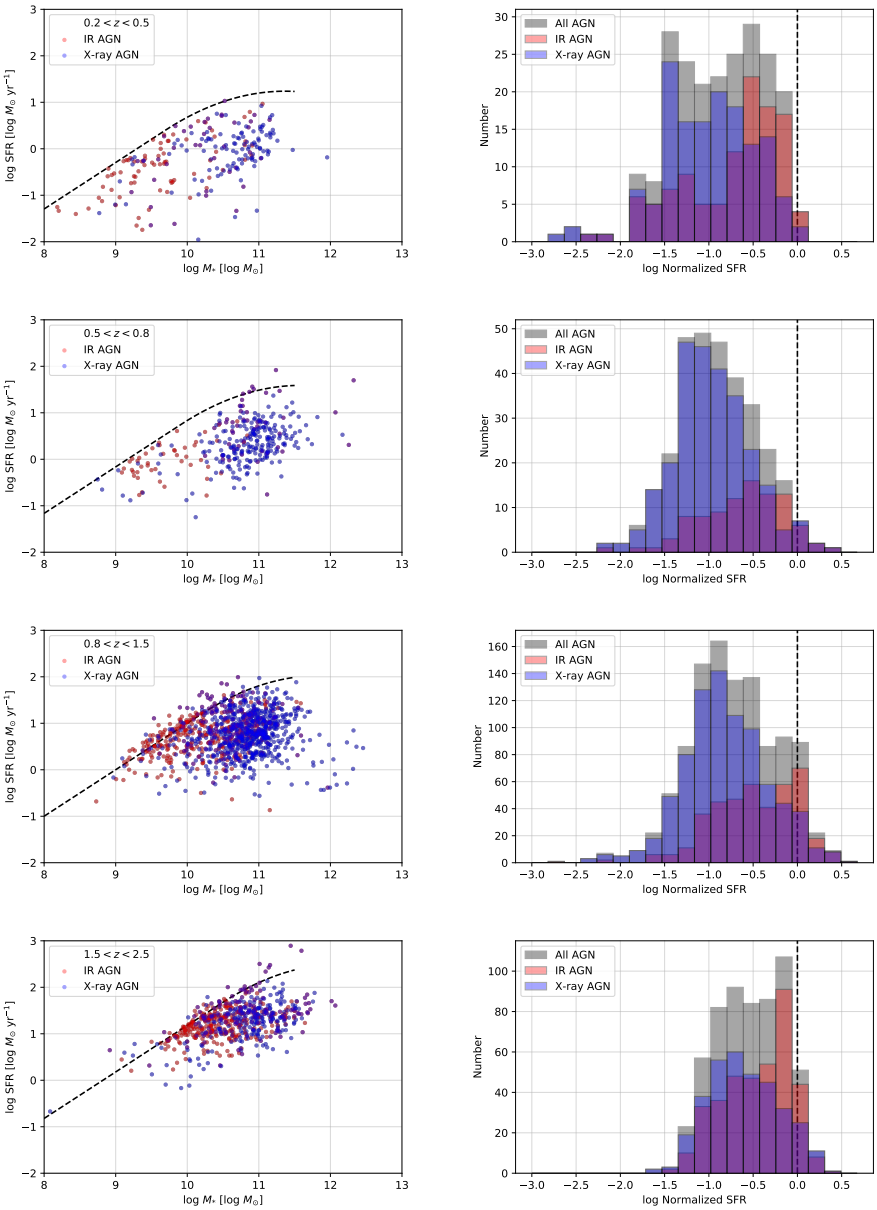

Figure 2.6: SFR as a function of stellar mass (left column) and histograms of normalized SFR $\equiv$ SFR/SFR$_{\rm MS}$ (right column) for our AGN host galaxies; each row depicts a redshift bin — from top to bottom they are: $0.2 < z < 0.5$, $0.5 < z < 0.8$, $0.8 < z < 1.5$, and $1.5 < z < 2.5$. The dashed lines on the left plots are the star-forming main sequence from Schreiber et al. (2015) for the median redshift value in each bin, while the dashed lines on the right plots are the SFR = SFR$_{\rm MS}$ line. Note that the majority of the active galaxies lie below the median star-forming main sequence for their redshift bin. This is further shown in the right plots, which show that very few of our galaxies have SFRs at or above their comparative star-forming main sequence values. We see that IR-selected AGN host galaxies have higher normalized SFR values on average than our X-ray-selected AGN host galaxies, with the two distributions' peaks typically separated by 0.5 – 1.0 dex. Further, we find a gradual shift towards higher normalized SFRs as the galaxies increase in redshift.

2.6.1 Galaxies Hosting AGNs Have Lower SFRs

Previous studies have observed and reported on relations between a galaxy's redshift, stellar mass, and its star formation rate (e.g., Noeske et al., 2007; Whitaker et al., 2012; Schreiber et al., 2015). This relation between the star formation rate of a galaxy and its stellar mass is typically called the star-forming main sequence. This metric is a useful tool in conjunction with observed galaxy SFR in order to determine whether a given galaxy has a normal, above, or below average SFR given its redshift and mass. These relations are empirical and have been iteratively improved over the last decade (e.g. Whitaker et al., 2012; Schreiber et al., 2015). We use the Schreiber et al. (2015) relation to determine the main sequence star formation rates ($\mathrm{SFR_{MS}}$) for our AGN host galaxies, defined as: $\log_{10}(\mathrm{SFR_{MS}}[M_\odot\ \mathrm{yr}^{-1}]) = m - m_0 + a_0 r - a_1[max(0, m - m_1 - a_2 r)]^2$, where $r \equiv \log_{10}(1+z)$, $m \equiv \log_{10}(M_*/10^9 M_\odot)$, $m_0 = 0.5 \pm 0.07$, $a_0 = 1.5 \pm 0.15$, $a_1 = 0.3 \pm 0.08$, $m_1 = 0.36 \pm 0.3$, and $a_2 = 2.5 \pm 0.6$.

We use this relation to test whether a general population of star-forming galaxies with SFRs calculated using the methods presented in this paper lies on the star-forming main sequence defined by Schreiber et al. (2015). To do this, we randomly selected, created SEDs, and extracted galaxy properties for 2245 star-forming ACS-GC galaxies in the COSMOS field, where we use the Schreiber et al. (2015) definition of star-forming galaxies. These galaxies were randomly selected spatially from the same parent sample as our AGN sample, and have similar distributions for all measured parameters. In order to examine an individual galaxy's SFR in relation to the star-forming main sequence value, we also calculated a normalized SFR (normalized SFR $\equiv$ SFR/$\mathrm{SFR_{MS}}$). We find that these star-forming galaxies do lie predominantly on the star formation main sequence, with median (standard deviation) log normalized SFR values of -0.23 (0.29), -0.30 (0.34), -0.14 (0.39), and -0.11 (0.27) for redshift bins of $0.2 < z < 0.5$, $0.5 < z < 0.8$, $0.8 < z < 1.5$, and $1.5 < z < 2.5$, respectively.

In contrast we find that our AGN host galaxies lie, on average, below the star-forming main sequence, as can be seen in Figure 2.6. Specifically we find that our AGN host galaxies lie below the

star-forming main sequence with median (standard deviation) log normalized SFR values of: -0.54 (0.55), -0.57 (0.48), -0.47 (0.48), and -0.39 (0.38) for IR-selected AGN host galaxies; -0.98 (0.52), -1.01 (0.44), -0.85 (0.47), and -0.62 (0.40) for X-ray-selected AGN host galaxies; and -0.84 (0.54), -0.95 (0.45), -0.75 (0.50), and -0.52 (0.39) for the total AGN host galaxy sample, for redshift bins of $0.2 < z < 0.5$, $0.5 < z < 0.8$, $0.8 < z < 1.5$, and $1.5 < z < 2.5$, respectively.

If we account for the systematic offset of the matched inactive star-forming galaxies below the main sequence as discussed above, we find that our AGN host galaxies lie below the star-forming main sequence with median (standard deviation) log normalized SFR values of: -0.31 (0.62), -0.27 (0.59), -0.33 (0.62), and -0.28 (0.47) for IR-selected AGN host galaxies; -0.75 (0.60), -0.71 (0.56), -0.71 (0.61), and -0.51 (0.48) for X-ray-selected AGN host galaxies; and -0.61 (0.61), -0.65 (0.56), -0.61 (0.63), and -0.41 (0.47) for the total AGN host galaxy sample, for the respective redshift bins.

Examining the normalized SFRs of our galaxies seen in Figure 2.6, we find a similar but distinct trend to that of sSFR (see Sections 2.5.3 and 2.5.4). Because our X-ray-selected AGN host galaxies have higher masses and similar to lower SFRs in comparison to IR-selected AGN host galaxies, we find a compound effect when examining normalized SFR. While both AGN subpopulations, on average, lie below their comparative star-forming main sequence values, the IR-selected AGN host galaxies tend to be closer to the main sequence — with median normalized SFR values lying within one standard deviation of the main sequence for all redshift bins — than the X-ray-selected AGN host galaxies. We find this for all redshift bins, with higher redshift bins producing normalized SFRs that are closer to 1 and less discrepancy between the two AGN subpopulations.

Recent work by Bernhard et al. (2019) finds that galaxies hosting higher luminosity AGNs lie closer to the star formation main sequence than galaxies hosting lower luminosity AGNs; however our IR and X-ray-selected AGN host galaxies have similar AGN luminosities (see Figure 2.3, top), ruling this out as a possible explanation. Instead, the differences between these two selection techniques can be attributed to the selection biases described in Azadi et al. (2017) and discussed in Section 2.3.3. Specifically, that IR selection techniques favor galaxies that are moderate mass,

dusty, and have higher SFRs, while X-ray selection techniques favor galaxies that are high mass, less dusty, and quiescent. These selection biases cause IR-selected AGN host galaxies to shift up (higher SFR) on the galaxy mass – SFR plane, while X-ray-selected AGN host galaxies are shifted right (higher mass) and down (quiescent). This separates the two populations, with IR-selected AGN host galaxies lying closer to the star formation main sequence than X-ray-selected AGN host galaxies.

Previous work has examined the location of AGN host galaxies in relation to the star-forming main sequence. Work by Stanley et al. (2017) find that on, on average, galaxies hosting AGNs lie along the star-forming main sequence, while work by Shimizu et al. (2015) and Mullaney et al. (2015) find that AGN host galaxies tend to lie below the star-forming main sequence, i.e., have less star formation than other galaxies of similar mass.

This disagreement may stem from the wavelength regimes used to select the AGNs and measure the SFRs. Specifically, Stanley et al. (2017) select AGNs using visible observations from SDSS, and find that their AGN sample lies on or near the star-forming main sequence. In contrast to Stanley et al. (2017), studies by Shimizu et al. (2015) and Mullaney et al. (2015) select their AGNs using X-ray observations from *Swift*/BAT and *Chandra*, respectively. Their findings using X-ray selection coincides with ours, that X-ray selected AGN host galaxies lie significantly below the star-forming main sequence on average.

However, it is also possible that the disagreements in the findings of previous works arise from differing derivation techniques for both stellar mass and SFR. For example, Stanley et al. (2017) uses SED models to find SFRs, and then uses emission line derived SMBH mass values in order to then extract galaxy stellar mass values using a $M_{BH} - M_*$ relation. Our work avoids any discrepancies introduced in using multiple observation methods to determine galaxy properties by deriving all of them using self-consistent SED fitting techniques that reproduce the Schreiber et al. (2015) star-forming main sequence when examining a general population of star-forming galaxies.

Our findings that AGN host galaxies are, on average, offset below the star-forming main sequence seem to indicate that there is a mechanism that precludes the maximal or even average

formation rate of stars in AGN dominated systems. This may provide some evidence for the presence of negative feedback on star formation in these systems.

2.6.2 SFR and SMBH Growth are Correlated

Previous studies examining an SFR – AGN luminosity relation have found conflicting results. Many observational works find that SFR is correlated to AGN luminosity (e.g., Mullaney et al., 2012; Chen et al., 2013; Hickox et al., 2014; Delvecchio et al., 2015; Harris et al., 2016; Lanzuisi et al., 2017), some find that SFR is not correlated with AGN luminosity, or at least only with a shallow relation (e.g., Stanley et al., 2015; Azadi et al., 2015; Stanley et al., 2017; Shimizu et al., 2017), while some find limited correlations. Specifically, Diamond-Stanic and Rieke (2012) finds that a galaxy's nuclear ($r < 1$ kpc) SFR is well correlated with its AGN, but that the relation disappears when using total SFR. This is similar to results from simulations done by Volonteri et al. (2015b) examining the relation between a galaxy's SFR and the luminosity of its AGN; these simulations also predict that a galaxy's global SFR and the growth of its AGN are most strongly correlated during mergers.

In addition, observational work by Rosario et al. (2012) finds that the dependence of a galaxy's SFR with its AGN luminosity varies, with a steep relation only existing for moderate to high luminosity AGNs ($L_{\rm AGN} > 10^{44}$ erg s^{-1}) and low redshifts ($z < 1$), with the relation flattening outside of those regimes; these findings are similar to theoretical work by Gutcke et al. (2015). Gutcke et al. (2015) created semi-analytic models that predict that an SFR – AGN luminosity relation evolves with AGN luminosity. Specifically, they find that the relation is flat, or even slightly negative, at low AGN luminosities and becomes steeper at higher AGN luminosities.

While some of the previous work has attempted to account for the co-dependence of SFR and AGN luminosity with redshift and stellar mass (e.g., Rosario et al., 2012; Stanley et al., 2015; Azadi et al., 2015; Stanley et al., 2017), none have done so while creating a common SED from which all AGN and galaxy parameters are derived, as this work does.

The goal of examining an SFR – AGN luminosity relation is to understand the connection

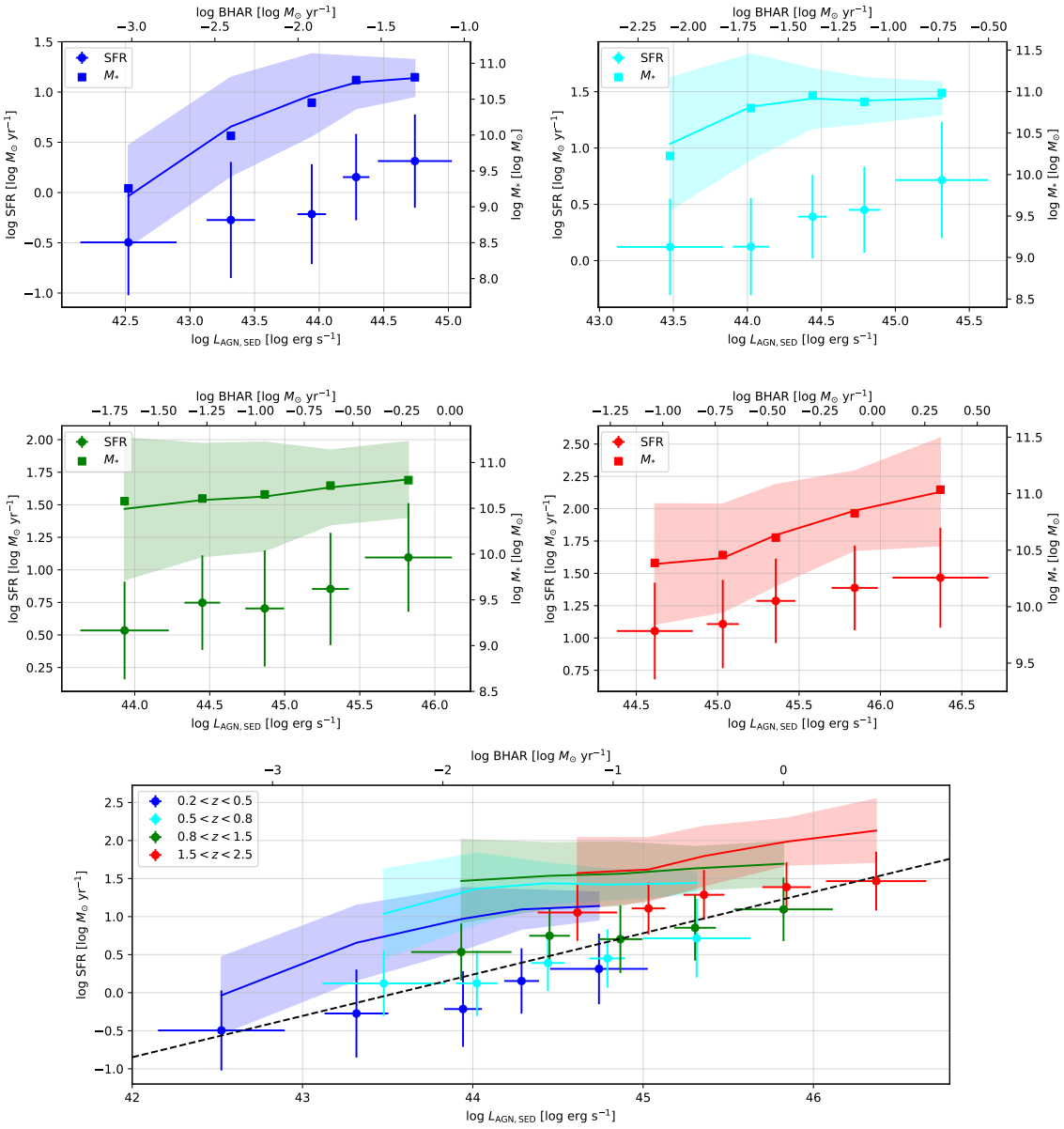

Figure 2.7: SFR as a function of AGN luminosity (BHAR) for our active galaxy sample, paneled by redshift bin and further binned by AGN luminosity; the circular markers are the data with associated errors while the solid line with shading is the calculated star-forming main sequence values (line), with SFR values calculated using the Schreiber et al. (2015) relation for star-forming main sequence galaxies with similar redshifts and stellar masses to those of our sample, and 1σ error (shading) for each data point, while the square markers are the median stellar mass values: top left is $0.2 < z < 0.5$, top right is $0.5 < z < 0.8$, middle left is $0.8 < z < 1.5$, middle right is $1.5 < z < 2.5$; note the similar slopes between the observed and main sequence SFRs as well as the significant negative offset of the active galaxy SFRs from the main sequence. Also note the tight correlation between the median stellar mass in each bin and the main sequence SFRs. The bottom panel shows the active galaxy SFRs and main sequences for all redshift bins as a function of AGN luminosity (BHAR) as well as the line of best fit (dashed) for our data; note that redshift evolution of the relevant properties results in a steeper slope than any individual bin.

between SMBH growth and stellar mass growth in a galaxy. A more intuitive parameter for this is black hole accretion rate (BHAR) rather than AGN bolometric luminosity. We calculate BHAR for an AGN from its bolometric luminosity using the mass-energy conversion equation from Alexander and Hickox (2012): $\mathrm{BHAR} = \epsilon L_{\mathrm{AGN}} * 1.5 \times 10^{-45}$ $[(M_{\odot}\ \mathrm{yr}^{-1})/(\mathrm{erg\ s}^{-1})]$, where ϵ is the mass-energy conversion efficiency, assigned a value of 10% ($\epsilon = 0.1$) (Marconi et al., 2004). Since this is a linear scaling relation, any powerlaw slopes are equivalent between relations of SFR – AGN luminosity and SFR – BHAR.

In order to account for redshift evolution of the relevant galaxy properties we binned our sample by redshift, choosing similar bins to those of previous works (e.g., Rosario et al., 2012; Stanley et al., 2015, 2017): $0.2 < z < 0.5$, $0.5 < z < 0.8$, $0.8 < z < 1.5$, and $1.5 < z < 2.5$. We further binned our sample by AGN bolometric luminosity in order to minimize the effect of our sample's flux-limited selection bias. We find that the SFR of an AGN host galaxy is significantly positively correlated with its AGN's bolometric luminosity, in all redshift bins and across all bins, i.e. combining all bins (see Figure 2.7).

Specifically we find powerlaw slopes relating SFR to AGN bolometric luminosity (and equivalently, BHAR) of 0.36 ± 0.07, 0.34 ± 0.06, 0.27 ± 0.05, and 0.25 ± 0.03 for the redshift bins, in ascending order. These slope values are in rough agreement with the slopes of the comparative star-forming main sequence values (the shaded lines in Figure 2.7), with all measured SFR slopes being within 3σ of the star-forming main sequence slope. Further, we find that the comparative star-forming main sequence tightly follows the increasing median stellar mass in each AGN bolometric luminosity bin (square datapoints in Figure 2.7), as expected from the Schreiber et al. (2015) relation. This indicates that an active galaxy's star formation is correlated to AGN bolometric luminosity, but may be due to a mutual dependence on galaxy stellar mass.

We do not find a slope dependence on AGN luminosity such as that found by Rosario et al. (2012) and predicted by Gutcke et al. (2015). Instead we find that the relations are approximately linear throughout the luminosity range of our sample. Further, while these slopes show less than a one-to-one relation between SFR and BHAR, they are still significantly non-zero and are more

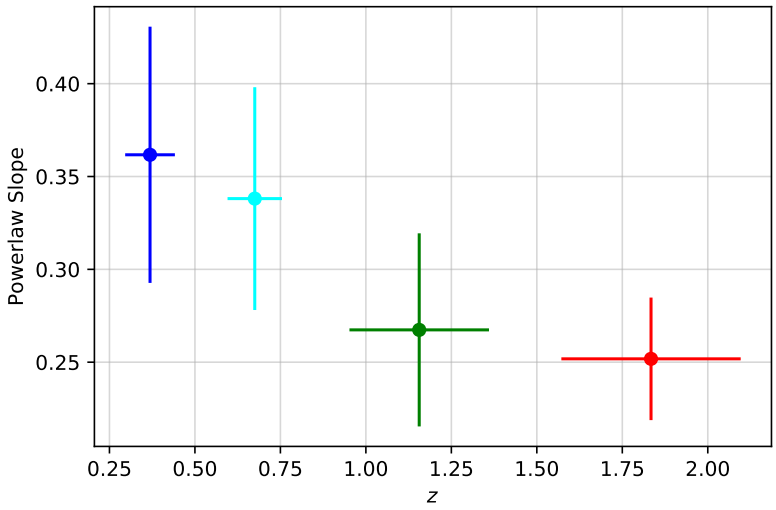

Figure 2.8: Powerlaw slope of the SFR – AGN luminosity relation as a function of redshift.

steep than the relations seen in Stanley et al. (2015), Azadi et al. (2015), and Shimizu et al. (2017).

We also find that the relation between SFR and AGN luminosity evolves with redshift, with the powerlaw slope of the relation flattening as redshift increases, as seen in Figure 2.8. The decrease in slope is gradual, with the powerlaw slope decreasing by 0.08 per unit increase in redshift. Further, with only the four redshift bins, this finding is not significant (p-value = 0.054); however, this is an effect of underbinning our data. Examining this same evolution when using 10 equally populated redshift bins finds a similar decrease at a significant level (p-value = 0.007). This gradual flattening of powerlaw slope with redshift is in contrast to the trend found by Stanley et al. (2017) of slope increasing as redshift increased, but agrees with findings by others (e.g., Rosario et al., 2012; Azadi et al., 2015) that the relation is strongest for low redshift galaxies and flattens at higher redshifts. Rosario et al. (2012) attributes this behavior to the greater importance of major mergers, which trigger both AGNs and star formation, for galaxy and AGN growth at lower redshifts.

If we examine the relation across all the redshift bins, we find a significant powerlaw relation between SFR and AGN luminosity with a slope of 0.54 ± 0.06 and intercept of 1.23 ± 0.10. This slope is shallower than to that of Netzer (2009), which found a powerlaw relation with a slope of

~ 0.8 for AGN-dominated systems. This disagreement could be caused by differences in the sample arising from the observational wavelength used to select AGNs and measure SFR as was discussed in Section 2.6.1, or could arise from differences in measurements of both SFR and AGN luminosity. The work by Netzer (2009) uses Oxygen emission line measurements ([OIII] and [OI]) to acquire AGN luminosity and an IR indicator, νL_ν at 60 μm, to determine SFR, while this work derives both from the same self-consistent SED model, ensuring no contamination between the SFR and AGN components.

Our findings that SFR is positively correlated with BHAR in AGN host galaxies and that AGN host galaxies are, on average, offset below the star-forming main sequence seem to indicate that the process of AGN growth is linked to the process of global star formation in AGN host galaxies. AGN feedback is one such mechanism that could correlate these two processes.

2.7 Conclusions

We present a systematic method of deriving AGN and galaxy properties by fitting multiple components to the SEDs of galaxies in multi-wavelength surveys. Using this approach on galaxies found in the ACS-GC, we create a catalog of 2585 AGN host galaxies and their properties. We analyze the AGN and host galaxy properties of this sample, with findings summarized below.

(1) We find that AGN host galaxies lie significantly below the star-forming main sequence, with lower SFRs than star-forming galaxies of similar mass. This offset shrinks as redshift increases. Further, we find that X-ray-selected AGN host galaxies have greater offsets from the star-forming main sequence than IR-selected AGN host galaxies. This could resolve discrepancies between previous studies about the location of AGN host galaxies relative to the star-forming main sequence, since each study selected its AGNs using different observations.

(2) We find that the SFRs of AGN host galaxies increase with AGN luminosity (and therefore BHAR) when binned by redshift, but that this may be due to a mutual dependence on

galaxy stellar mass. We also find that the slope of this relation flattens as redshift increases.

These findings suggest that a galaxy's SMBH and stellar population co-evolve, but that a process, such as AGN feedback, may restrict the SFRs of AGN host galaxies from reaching that of star-forming main sequence galaxies on average. In order to determine whether this is the case, follow-up observations are needed that identify AGN outflows and determine whether they heat or remove cool molecular gas from the host galaxy. These are both feedback effects that could inhibit global star formation in the host galaxy.

Acknowledgments

Support for this work was provided by NASA's Astrophysics Data Analysis program, grant number NNX15AI69G, the CU Boulder / JPL Strategic University Research Partnership program, and the National Science Foundation's Graduate Research Fellowship program. The work of DS was carried out at the Jet Propulsion Laboratory, California Institute of Technology, under a contract with NASA. RJA was supported by FONDECYT grant number 1191124. This work utilized the RMACC Summit supercomputer, which is supported by the National Science Foundation (awards ACI-1532235 and ACI-1532236), the University of Colorado Boulder, and Colorado State University. The Summit supercomputer is a joint effort of the University of Colorado Boulder and Colorado State University. The authors would also like to thank Murray Brightman, Daniel Masters, and Rebecca Nevin for providing data and support to this work.

Chapter 3

A Catalog of 204 Offset and Dual AGNs: Increased AGN Activation in Major Mergers and Separations under 4 kpc

Abstract

During galaxy mergers, gas and dust is driven towards the centers of merging galaxies, triggering enhanced star formation and supermassive black hole (SMBH) growth. Theory predicts that this heightened activity peaks at SMBH separations <20 kpc; if sufficient material accretes onto one or both of the SMBHs for them to become observable as active galactic nuclei (AGNs) during this phase, they are known as offset and dual AGNs, respectively. To better study these systems, we have built the ACS-AGN Merger Catalog, a large catalog ($N = 204$) of uniformly selected offset and dual AGN observed by *HST* at $0.2 < z < 2.5$ with separations <20 kpc. Using this catalog, we answer many questions regarding SMBH – galaxy coevolution during mergers. First, we confirm predictions that the AGN fraction peaks at SMBH pair separations <10 kpc; specifically, we find that the fraction increases significantly at pair separations of <4 kpc. Second, we find that AGNs in mergers are preferentially found in major mergers and that the fraction of AGNs found in mergers follows a logarithmic relation, decreasing as merger mass ratio increases. Third, we do not find that mergers (nor the major or minor merger subpopulations) trigger the most luminous AGNs. Finally, we find that nuclear column density, AGN luminosity, and host galaxy star formation rate have no dependence on SMBH pair separation or merger mass ratio in these systems, nor do the distributions of these values differ significantly from that of the overall AGN population.

This chapter is currently accepted for publication in the *The Astrophysical Journal*, and is reproduced here with the permission of the AAS.

3.1 Introduction

Mergers between two galaxies, each with a supermassive black hole (SMBH) at its center, result in a pair of SMBHs in the merger remnant. The paired SMBHs slowly spiral toward the center of mass of the newly merged system and remain in a <20 kpc separation "dual" phase for ∼100 Myr (Begelman et al., 1980; Milosavljevic and Merritt, 2001), before dynamical friction drives them into a sub-pc gravitationally bound binary and they eventually coalesce. During this dual phase, significant gas can be driven inward towards the center of the merger remnant and onto the SMBHs, fueling their growth, and making them observable as active galactic nuclei (AGNs); this should also enhance star formation in the host galaxy (e.g. Joseph and Wright, 1985; Hopkins et al., 2008; Hopkins and Hernquist, 2009; Knapen et al., 2015)

When one or both of the SMBHs are accreting in this dual phase, they are known as offset AGNs (e.g. Comerford and Greene, 2014) or dual AGNs (e.g. Gerke et al., 2007; Comerford et al., 2009), respectively. During this phase, the outer stars are tidally stripped away, but the merging galaxies retain their central stellar bulges (Liu et al., 2010; Fu et al., 2011; Rosario et al., 2011); these stellar bulges contain the SMBHs. Therefore, offset AGNs are merging galaxy systems where one stellar bulge hosts an AGN and one does not; presumably the latter hosts a quiescent SMBH. Similarly, dual AGNs are merging galaxy systems in which both stellar bulges host an AGN.

There are strong correlations between observed properties of the SMBH and host galaxy properties, such as the M-σ relation (e.g. Magorrian et al., 1998; Ferrarese and Merritt, 2000; Gebhardt et al., 2000; Greene and Ho, 2006), which seems to indicate a connection between SMBH growth and the evolution of its host galaxy. In order to understand this connection, studies of systems hosting AGNs during periods of growth are necessary. Offset and dual AGNs are powerful observational tools for studies of SMBH and galaxy co-evolution as they are direct probes of the state of a SMBH and its host galaxy during a merger event. However, their utility has been limited because the number of known systems is small.

A large sample of offset and dual AGNs could address open questions in the field of SMBH

and galaxy co-evolution. For example, some simulations predict that major mergers trigger the most luminous AGNs (Hopkins and Hernquist, 2009). However, observational studies have found conflicting results about whether the most luminous AGNs are preferentially triggered in mergers, primarily due to the lack of a large, clean sample of AGNs in merging galaxy systems (e.g. Kocevski et al., 2012; Treister et al., 2012; Villforth et al., 2014, 2017). Other simulations predict that the peak of SMBH growth in mergers occurs when the paired SMBHs are separated by 1 – 10 kpc (Van Wassenhove et al., 2012) or 0.1 – 2 kpc (Blecha et al., 2013). Observations have not yet been able to test these predictions due to the limited number of known systems with SMBH pair separations <10 kpc, but they do verify the trend in the 10 – 100 kpc range (Ellison et al., 2011; Koss et al., 2012). Lastly, a large sample of these systems could test whether findings of increased star formation in mergers (e.g. Cox et al., 2008; Ellison et al., 2008; Patton et al., 2013) also apply to merging systems hosting AGN at small separations.

Since offset and dual AGNs are a promising avenue of approach to study SMBH and galaxy co-evolution, there have been many searches recently to find them. While most initial findings of these systems were serendipitous (e.g. Komossa et al., 2003; Bianchi et al., 2008), recent studies have attempted a more systematic approach. One such method is looking for the spectroscopic signatures of the AGNs in these systems, including double-peaked emission lines or single-peaked emission lines with a velocity offset relative to the host galaxy. While some of the galaxies identified in these studies have been confirmed as offset and dual AGNs (Fu et al., 2011; Liu et al., 2013; Müller-Sánchez et al., 2015; Comerford et al., 2015), many have not; this is because in most galaxies, AGN outflows and gas kinematics produce velocity shifted and double-peaked emission lines that mimic the signatures of offset and dual AGNs (Rosario et al., 2010; Shen et al., 2011; Comerford et al., 2012; Fu et al., 2012; Barrows et al., 2013; McGurk et al., 2015; Nevin et al., 2016). Work by Barrows et al. (2016) found offset and dual AGNs by searching for X-ray sources offset from their optical counterpart host galaxies, but the number able to be found using this method was limited due to the spatial resolution limits of the X-ray and optical observations. Still other work has focused on using surveys to search for morphological signatures of mergers, followed

by spectroscopy, radio, or X-ray observations to verify their sample (Koss et al., 2012; Fu et al., 2015; Satyapal et al., 2017; Silverman et al., 2020). This accentuates a problem in finding these systems — observations of offset and dual AGNs are difficult because of the high spatial resolution imaging and/or spectroscopy needed to differentiate the stellar bulges associated with a SMBH pair at these separations; this is also why currently known offset and dual AGNs are mostly limited to the low-redshift Universe ($z \lesssim 0.2$).

The Advanced Camera for Surveys (ACS) on the *Hubble Space Telescope* (*HST*) has an angular resolution of $0\farcs05$. This makes it ideal for observations requiring high resolution, such as detecting the multiple stellar bulges associated with offset and dual AGNs. By choosing *HST* galaxies in deep survey fields, such as GEMS, COSMOS, GOODS, and AEGIS, multi-wavelength data can be used to select AGNs, while galaxy morphological fitting can select galaxy mergers. This provides an approach for detecting offset and dual AGNs in greater numbers and at higher redshifts than ever before, enabling them to be used for statistical studies of AGN activation and SMBH – galaxy coevolution for the first time.

Here we present a catalog and analysis of 204 offset and dual AGNs identified using a new systematic method for finding offset and dual AGNs in large, multi-wavelength *HST* galaxy surveys. Section 3.2 discusses our initial sample of galaxies. In Section 3.3 we present the methods by which we modeled and selected our offset and dual AGN sample from the ACS-AGN Catalog, while Section 3.4 discusses the biases in our methods and how we corrected for them. Section 3.5 discusses the AGN and host galaxy properties of our offset and dual AGNs, both in comparison to a general AGN population and in relation to their merger parameters, and Section 3.6 presents our findings on AGN triggering in mergers. Finally, in Section 3.7 we discuss our conclusions. Throughout this paper, we use the Planck 2015 cosmology of $H_0 = 67.8$ km s^{-1} Mpc^{-1}, $\Omega_M = 0.308$, and $\Omega_\Lambda = 0.692$ (Planck Collaboration et al., 2016).

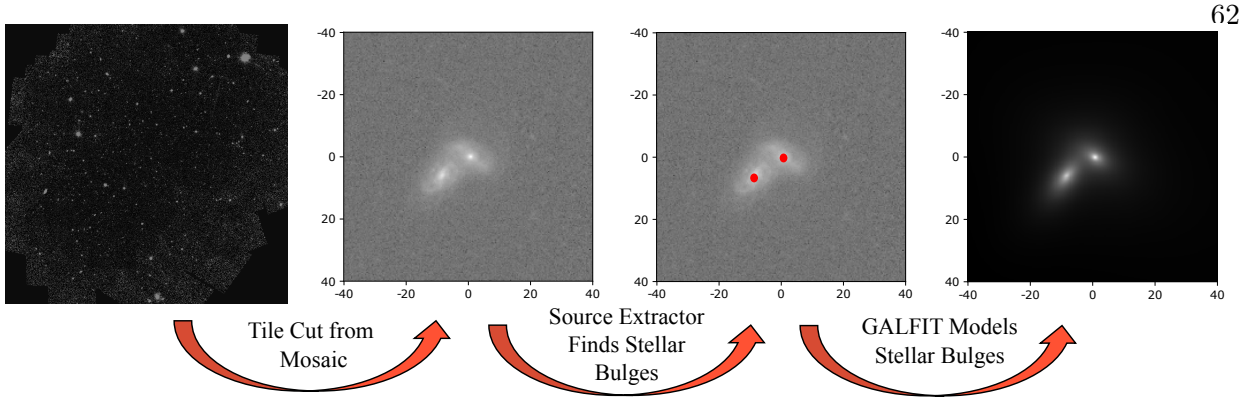

Figure 3.1: A flowchart summarizing the steps that we use to identify and model offset and dual AGNs. The axes of the tiles are in units of kpc, with the origin centered on the AGN host galaxy. We purposefully choose a simple galaxy system to show here as an example; a typical galaxy tile would have more sources found by Source Extractor, some of which may be removed after they fail to meet our modeling criteria, and there would be many iterations of GALFIT modeling (Section 3.3.2). The system shown here has a merger mass ratio of 4 and a bulge separation of 11 kpc.

3.2 Initial Galaxy Sample

Our parent galaxy sample was the Advanced Camera for Surveys Active Galactic Nuclei Catalog (ACS-AGN; Stemo et al., 2020, hereafter referred to as S20). The ACS-AGN is a catalog of 2585 AGN host galaxies that were imaged with *HST*/ACS and span a redshift range of $0.2 < z < 2.5$. These AGN host galaxies are located in four deep survey fields: the Galaxy Evolution from Morphologies and SEDs (GEMS) survey (Caldwell et al., 2008), the Cosmological Evolutionary Survey (COSMOS) (Scoville et al., 2007), the Great Observatories Origins Deep Survey (GOODS) (Dickinson and Giavalisco, 2003), and the All- wavelength Extended Groth Strip International Survey (AEGIS) (Davis et al., 2007).

These AGNs were selected by applying mid-infrared and X-ray AGN selection criteria to *Spitzer* and *Chandra* data available in these survey fields. The mid-infrared color cut described by Donley et al. (2012) was used for *Spitzer* observed galaxies and a rest-frame X-ray luminosity cut in the 2–10 keV band of $L_{2-10} > 10^{42}$ erg s^{-1} was used for *Chandra* observed galaxies. Of the 2585 AGN host galaxies in the ACS-AGN Catalog, 1065 are infrared selected and 1945 are X-ray selected.

While redshift data was already available for these galaxies (Griffith et al., 2012), AGN and host galaxy properties were not. These properties were calculated from SEDs created for each galaxy from multi-wavelength photometric data using the SED template fitting software `LRT` (Assef et al., 2010). Specifically, AGN bolometric luminosity ($L_{\rm AGN}$) was calculated by integrating the AGN component of the SED model. Stellar mass (M_*) was calculated using the relation between the SED modeled (excluding the AGN component) $g' - r'$ color and M/L_r from Bell et al. (2003). Host galaxy star formation rate (SFR) was calculated from the SED modeled (excluding the AGN component) 2800 Å monochromatic luminosity as described in Madau et al. (1998). Finally, the nuclear neutral hydrogen column density ($N_{\rm H}$) was calculated from the SED modeled extinction value (E_{B-V}) using a conversion factor derived from Maiolino et al. (2001) and Burtscher et al. (2016).

The parent galaxy sample has a median redshift of $\langle z \rangle \approx 1.15$, and contains AGN host galaxies that cover a significant parameter space: $L_{\rm AGN}$ [erg s^{-1} cm^2] has a range of $10^{42} \lesssim L_{\rm AGN} \lesssim 10^{47}$, with a median of $10^{44.7}$; M_* [$M_\odot$] has a range of $10^9 \lesssim M_* \lesssim 10^{12}$, with a median of $10^{10.6}$; SFR [$M_\odot$ yr^{-1}] has a range of $10^{-1} \lesssim {\rm SFR} \lesssim 10^2$, with a median of $10^{0.55}$; while $N_{\rm H}$ [cm^{-2}] has a range of $10^{20.5} \lesssim N_{\rm H} \lesssim 10^{23}$, with a median of $10^{21.4}$. This sample is found to lie generally below the star-forming main sequence and also shows correlated behavior between SFR and $L_{\rm AGN}$, most likely due to a mutual dependence on galaxy mass.

The AGN selection process, SED creation, AGN and host galaxy property calculation, and analysis is described in more detail in S20.

3.3 Galaxy Modeling & Merger Identification

The utility of computers in identifying, classifying, and decomposing galaxies in astronomical images has been growing as the effectiveness of image analysis software has increased. We use two such software packages, `Source Extractor` (Bertin and Arnouts, 1996) and `GALFIT` (Peng et al., 2002), to identify and model multiple stellar bulge components in *HST* images of the ACS-AGN galaxies in order to identify offset and dual AGN candidates.

In Section 3.3.1, we create tiles of the ACS-AGN galaxies. We then use `Source Extractor` and `GALFIT` to model the morphology of the ACS-AGN galaxies in Section 3.3.2. Finally, in Section 3.3.3, we eliminate false positives and select our offset and dual AGN sample.

3.3.1 Galaxy Tiling

In order to best select stellar bulges associated with SMBHs, we chose to examine them in the F814W filter of *HST*/ACS — the reddest available ACS filter that has been used to observe the entire ACS-AGN sample. This band peaks at 8333 Å, with a FWHM of 2511 Å, and is well-suited for tracing a galaxy's stellar component in our sample's redshift range. Specifically, the F814W band outperforms available shorter wavelength bands, such as the F438W and F606W, at this task because those bands tend to be dominated by light from ionized gas, not stellar emission, which peaks further into the infrared (e.g. Comerford et al., 2017).

Of the four surveys from which our sample is drawn, only the AEGIS and COSMOS surveys were observed and have mosaics in the F814W filter. Fortunately, the CANDELS survey (Grogin et al., 2011) observed the remaining fields (GEMS and GOODS) in the F814W and provide mosaics of these observations. It also observed parts of the COSMOS and AEGIS fields, but not in their entirety (for further detail, see Grogin et al. 2011). Therefore, where multiple surveys' observations exist for our sample, the CANDELS mosaics are the deepest available, but only marginally so — where they are available, CANDELS Wide observations increase the depth in the COSMOS field from a 5σ AB magnitude of 27.2 to 27.7 and from a 5σ AB magnitude of 28.1 to 28.2 in the AEGIS field. The F814W 5σ depth of the CANDELS Deep + Wide observations in the GEMS and GOODS fields are AB magnitude 28.8.

We gathered *HST*/ACS publicly available F814W mosaics from the COSMOS (Scoville et al., 2007), AEGIS (Davis et al., 2007), and CANDELS (Grogin et al., 2011) surveys. These mosaics are science products that have undergone significant processing, including calibration (e.g., bias and dark subtraction, gain correction, flat-fielding, bad pixel rejection, and low-level background removal), astrometric registration, cosmic ray cleaning, and have been co-added with MultiDrizzle

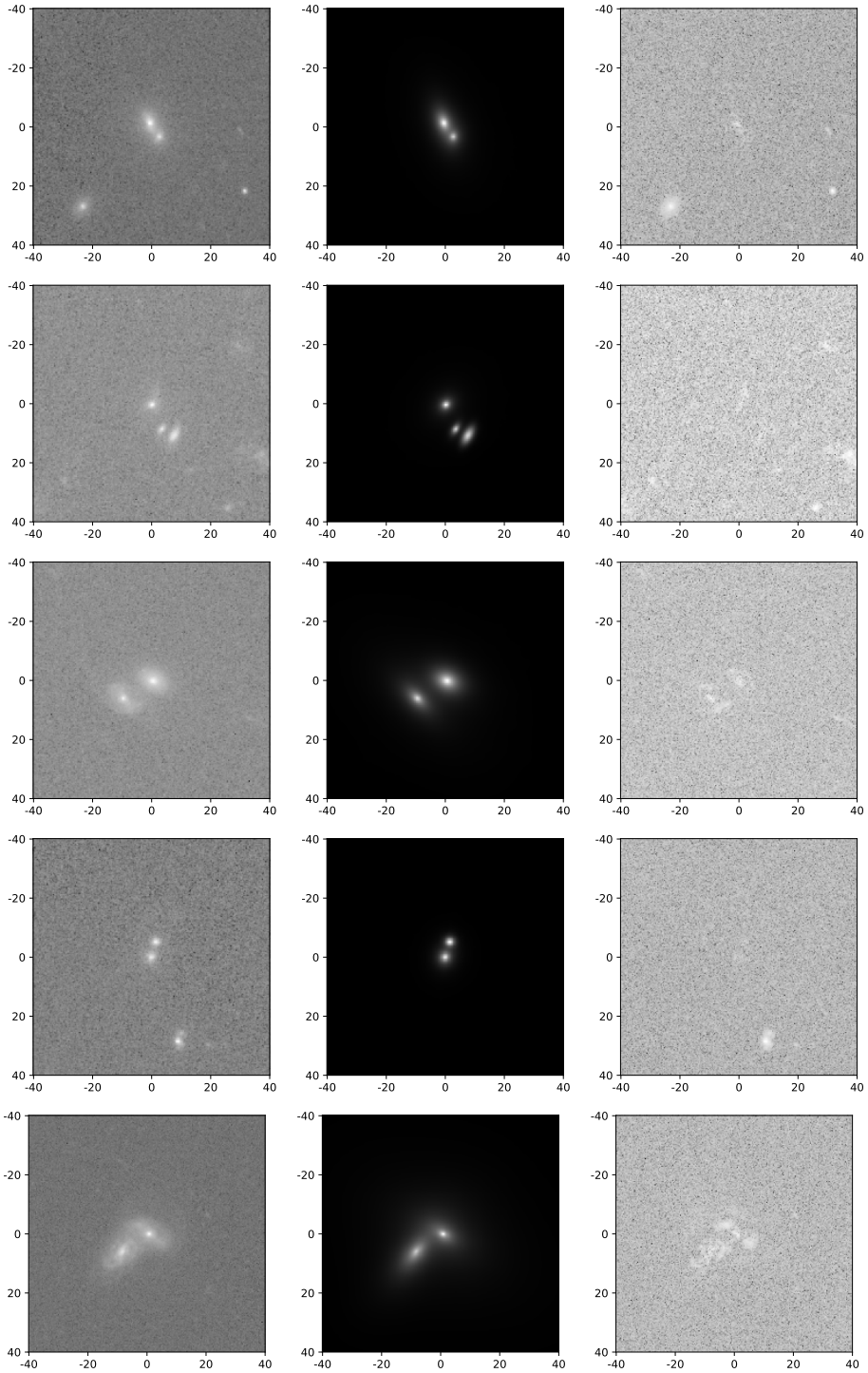
-40
-20
0
20
40

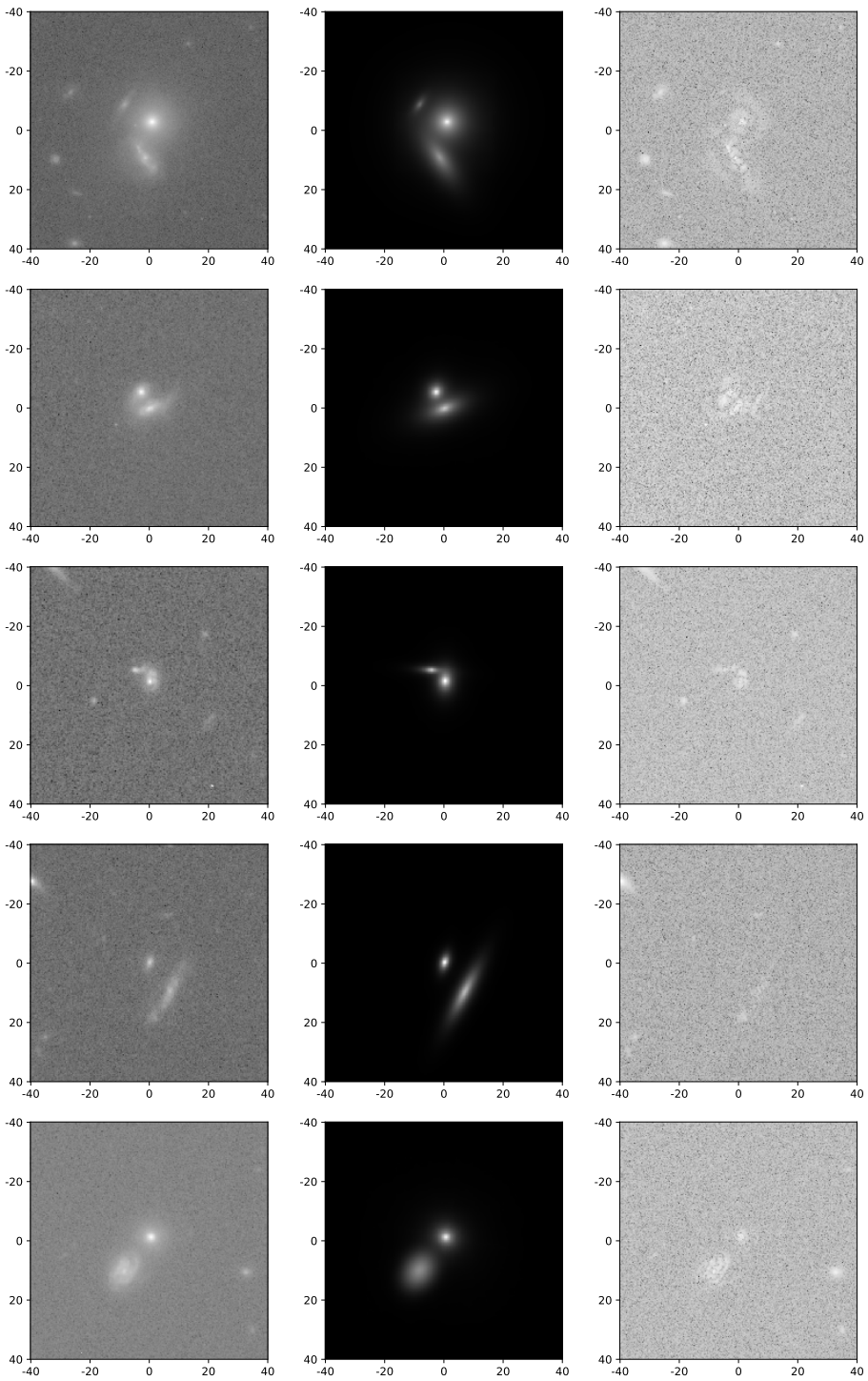

Figure 3.2: Examples of offset and dual AGNs identified and included in the ACS-AGN Merger Catalog. The axes of the tiles are in units of kpc, with the origin centered on the AGN host galaxy. Each row presents a merger candidate and is organized as follows: *HST* F814W image (left), GALFIT model (middle), and residual (right). The Catalog IDs of the systems shown are, from top to bottom: 169, 633, 1194, 1195, 1372, 1689, 1966, 2316, 2381, 2477.

(Koekemoer et al., 2007).

From these mosaics we created 80 kpc × 80 kpc tiles centered on the ACS-AGN galaxies. This size is significantly larger than the maximum 20 kpc separation radius we are allowing for our offset and dual AGN candidates, but allows for more accurate background estimation and subsequent fitting by `GALFIT`. For our galaxies that were observed in the F814W by CANDELS, we created tiles from the CANDELS mosaics; for those not within the boundaries of the CANDELS mosaics, we created tiles from the original survey mosaics in the F814W.

Of the 2585 ACS-AGN galaxies, we could not create tiles for 19 of them. These galaxies were in a region of the AEGIS field where no F814W mosaics were available at the time of publication. This left 2566 active galaxies that we created tiles for and could be analyzed for multiple stellar bulges.

3.3.2 Source Identification and Fitting

Offset and dual AGNs exist in galaxy mergers. In order to find them, we search our active galaxy sample for signs of multiple stellar bulges, which should only exist in galaxy mergers. The dual phase (1 – 20 kpc stellar bulge separation) of galaxy mergers is especially important because at separations greater than 20 kpc, the galaxies should only be minimally interacting, while at separations less than ∼1 kpc, a significant portion of stellar bulges may be coalescing. Therefore, we specifically search for multiple stellar bulges within this range in order to identify offset and dual AGNs.

We can identify which AGN host galaxies contain multiple stellar bulges by modeling them with `Source Extractor` (Bertin and Arnouts, 1996) and `GALFIT` (Peng et al., 2002). Since these galaxies are already known to host at least one AGN, if we identify them as having multiple stellar bulges, we can deduce that these galaxies are undergoing a merger and host an offset or dual AGN.

In practice, we identified multiple stellar bulges in our active galaxy sample by fitting Sérsic surface brightness profiles to bright sources in the galaxy tiles. Specifically, we passed the active galaxy tiles through `Source Extractor`; this identifies bright groupings of pixels in the image as

Table 3.1: Data Fields in the ACS-AGN Merger Catalog

No.	Field	Note
1	ID	catalog specific unique identifier
2	RA	right ascension [J2000, decimal degrees]
3	DEC	declination [J2000, decimal degrees]
4	Z	redshift used
5	SPECZ	spectroscopic redshift
6	PHOTOZ	photometric redshift
7	Spitzer_AGN	if AGN was selected in *Spitzer* [Boolean]
8	Chandra_AGN	if AGN was selected in *Chandra* [Boolean]
9	L_bol_sed_md	AGN bolometric luminosity derived from SED, median [erg s^{-1}]
10	L_bol_sed_lo	AGN bolometric luminosity derived from SED, lower bound [erg s^{-1}]
11	L_bol_sed_hi	AGN bolometric luminosity derived from SED, upper bound [erg s^{-1}]
12	L_x_md	2 – 10 keV restframe luminosity, median [erg s^{-1}]
13	L_x_lo	2 – 10 keV restframe luminosity, lower bound [erg s^{-1}]
14	L_x_hi	2 – 10 keV restframe luminosity, upper bound [erg s^{-1}]
15	L_bol_x_md	AGN bolometric luminosity derived from X-ray, median [erg s^{-1}]
16	L_bol_x_lo	AGN bolometric luminosity derived from X-ray, lower bound [erg s^{-1}]
17	L_bol_x_hi	AGN bolometric luminosity derived from X-ray, upper bound [erg s^{-1}]
18	M_star_md	galaxy stellar mass, median [$M_\odot$]
19	M_star_lo	galaxy stellar mass, lower bound [$M_\odot$]
20	M_star_hi	galaxy stellar mass, upper bound [$M_\odot$]
21	SFR_md	star formation rate, median [$M_\odot$ yr^{-1}]
22	SFR_lo	star formation rate, lower bound [$M_\odot$ yr^{-1}]
23	SFR_hi	star formation rate, upper bound [$M_\odot$ yr^{-1}]
24	Nh_md	nuclear column density, median [cm^{-2}]
25	Nh_lo	nuclear column density, lower bound [cm^{-2}]
26	Nh_hi	nuclear column density, upper bound [cm^{-2}]
27	SFR_norm_md	normalized star formation rate, median
28	SFR_norm_lo	normalized star formation rate, lower bound
29	SFR_norm_hi	normalized star formation rate, upper bound
30	Sep_12	separation between primary and secondary components [kpc]
31	Ratio_12	galaxy merger mass ratio between primary and secondary components
32	Sep_13	separation between primary and tertiary components [kpc]
33	Ratio_13	galaxy merger mass ratio between primary and tertiary components

Field numbers 1 – 29 are taken from the ACS-AGN catalog (Stemo et al., 2020); AGN selection and derivation of AGN host galaxy properties are found therein. Merger selection and derivations of merger properties are described throughout this paper; note that for field numbers 31 and 33 reported values are integrated flux ratios that are used as proxies for merger mass ratio. Lower bound and upper bound are defined as the 16th and 84th percentiles of the distribution, respectively. A "-999" value in the table represents no data. The ACS-AGN Merger Catalog is available in its entirety in fits format from the original publisher.

possible sources, fits an elliptical profile to them, and outputs basic information such as the source location, its flux, and its position angle. Given the high redshifts in our sample, `Source Extractor` is ideal as it detects sources via a threshold method, which is more suited to the detection of low surface brightness objects than peak finding methods (Yee, 1991). When detecting sources using `Source Extractor`, we used a detection threshold of 3σ above background and a minimum source area of 7 pixels.

We then used the outputs of `Source Extractor` as initial parameters (source position, source position angle) for fitting with `GALFIT`. `GALFIT` minimizes χ^2_ν (reduced χ^2) by fitting various modeled surface brightness profiles convolved with a PSF to an input galaxy image. We allowed `GALFIT` to fit Sérsic surface brightness profiles to the sources in our tiles. By varying the Sérsic index and effective radius, the Sérsic profile can accurately model an extended bulge structure as well as more compact objects, such as AGNs, when convolved with a PSF.

While `GALFIT` includes many other surface brightness profiles and can fit highly complex galaxy structure, the limited nature of our method keeps our computational load down while still satisfactorily modeling our science targets (stellar bulges). We recognize that galaxies can be more complex than a single Sérsic profile; however, for this work, we are only concerned with `GALFIT` detecting merging systems, and accurately modeling the bulges' separation and relative integrated flux (discussed in Section 3.5.1). In practice, the centroid of a properly modeled Sérsic profile will coincide with the light center of a galaxy component (i.e. the central bulge); therefore, the separations of our merging systems should be well measured. As well, unless there is significant surface brightness profile asymmetry in the merger components, flux should be correctly proportioned between them according to their physical structure. Significant deviations in the relative flux assignment would require uncommon geometries to occur (e.g. a primary galaxy starburst near the secondary galaxy bulge), and therefore should not have a significant impact on the overall results. Specifically, we found that our methods very accurately modeled most galaxy components except those with significant, large-scale spiral or asymmetric structure — a minority of our sample; Figure 3.2 shows this quite well. These outliers may cause some scatter in our data (specifically

merger mass ratio), and should be carefully considered when examining individual systems instead of the sample en masse, but should not significantly affect any findings based on the entire sample, such as those discussed in this paper.

The speed at which `GALFIT` can simultaneously fit multiple profiles to a given image is highly dependent on image size, convolution size, and number of fits. In order to manage the computational load, the sources from `Source Extractor` were only used as inputs for `GALFIT` if the source position was within 22 kpc of the center of the image and the source flux was at least 1% of the maximal source flux within the innermost 10 kpc of the image. The position limitation is reasonable as the AGN host galaxy is approximately centered on our image tile and our goal is to identify offset and dual AGNs separated by 20 kpc or less — the extra 2 kpc acts as a buffer in case of non-centered tiles. The flux limitation compares possible companions to the central galaxy and is used to reduce the amount of galaxy structure (e.g. spiral arms, star-forming regions, etc.), background galaxies, and other spurious objects fit by `GALFIT`; this limitation should only restrict selection of the most minor mergers (merger mass ratio $\gtrsim 100$). While `GALFIT` could reproduce nearly all features of a galaxy image given sufficient components and parameters, only stellar bulges are needed to be identified for this work. Lastly, we limited the maximum number of sources being simultaneously modeled to three, as the likelihood of finding systems with four or more stellar bulges is very low and increasing the number of simultaneous fits would result in a large increase in false positives and computation time. Even with all of these restrictions in place, some AGN host galaxies were still fit with over 2600 unique `GALFIT` models due to the high number of sources present that needed to be fit in all combinations.

Other restrictions were also put in place to avoid over fitting. Specifically, we restricted our `GALFIT` components to be centered within 2.5 kpc of its `Source Extractor` source. This is in addition to default `GALFIT` restrictions on model parameters that are unphysical (e.g. effective radius < 0.01 pixel, Sérsic indices <0.01 or >20, etc.). This forced `GALFIT` to model only the sources we wanted to model and to only model those sources with realistic bulge profiles. For our process, this meant that adding spurious Sérsic components typically resulted in worse fits than

modeling with fewer Sérsic components. Therefore, for each tile we selected the model with the minimum χ^2_ν as the best fit.

Of the 2566 galaxies selected as active for which tiles could be made, 6 could not be modeled due to too many sources being identified by `Source Extractor` than would be reasonable to computationally model using our methods, with some having as many as 20 sources identified by `Source Extractor`. These were inspected visually and 2 were selected to be fit using a subset of the sources identified by `Source Extractor` that appeared to be possible stellar bulges. In all, 350 active galaxies were best fit by a `GALFIT` model with two or three components, while the rest were either best fit with a single Sérsic component or with no Sérsic component (i.e. only a background component); the ones best fit with no Sérsic component typically had extremely dim surface brightness profiles.

3.3.3 False Positive Reduction

Not all 350 galaxies that were best fit with two or three components by `GALFIT` truly contain multiple stellar bulges. Even with the initial source limitations imposed prior to `GALFIT` modeling, there were still a significant number of models with components fit to non-bulge features (e.g. spiral arms, star-forming regions, etc.). In order to reduce these false positives, we put in place further restrictions on our `GALFIT` component parameters: a centroid separation limit, an integrated flux ratio limit, and a significance above background restriction.

When `GALFIT` models an image, there is no inherent lower limit to component separation and it is only restricted in its upper limit to the size of the image. These limits are unrealistic on the low end and not useful for this work on the high end. Since our goal is to identify offset and dual AGNs, the separation of possible stellar bulges containing SMBHs should be inherently limited to <20 kpc. However, there must also be a lower limit; an absolute lower limit would be the angular resolution of the observing instrument ($0\farcs05$ for *HST*/ACS), but the lower limit of typical bulge sizes is actually the more restrictive lower separation in this case. For example, the nearby ($z = 0.02$) active dwarf galaxy RGG 118 has a bulge diameter of approximately 1.5 kpc (Baldassare

et al., 2017). This 1.5 kpc lower limit is a conservative estimate for possible bulge sizes identifiable in our sample; the moderate to massive galaxies of the ACS-AGN should contain similar or larger bulges, and 1.5 kpc is above the resolution limit of *HST* for all redshifts present in our sample. Therefore we impose a separation limit for our modeled stellar bulges of >1.5 kpc and <20 kpc.

In addition, the automated nature of our bulge fitting method frequently results in additional components being fit to non-bulge features such as spiral arms, star-forming regions, and occasionally low-surface brightness, extended features. In order to address these issues, we put in place two further restrictions on the modeled `GALFIT` components. First, we required that the integrated fluxes of any paired components must be within 5 magnitudes of each other (1%). If we take the integrated flux ratio as a proxy for the stellar mass ratio (see Section 3.5.1), this constraint limits the possible merger mass ratios of our candidates to <100. This restriction is successful at eliminating many false positives typically related to star-forming regions and some spiral arms and only eliminates the most minor of mergers. Our second restriction is a significance above background criterion; specifically, we require that the modeled flux at the centroid of any fit component must be at least 5σ above the background, as modeled by `GALFIT`. This restriction is excellent at eliminating more extended, low-surface brightness false positive fits, such as those typically associated with diffuse gas features and some spiral arms.

After we removed a large number of false positives through automated means, 280 active galaxies were still identified as hosting multiple stellar bulges. Due to the automated nature of our approach, there were still some false positives included in this set. Therefore, as a final check, this reduced sample was visually examined independently by the three lead authors of this work, with any split determinations resulting in the conservative decision of removal from the sample. We also used this opportunity to refit individual stellar bulge models as needed in order to more accurately model the offset and dual AGN system; this was typically slightly adjusting the centroid of the bulge fit, the axis ratio, or the Sérsic index and effective radius to better reflect the observed data. This final verification and refit resulted in 204 unique systems identified as offset and dual AGNs — 187 of these being two-bulge systems and 17 being three-bulge systems. Some examples

of offset and dual AGNs that we identified are shown in Figure 3.2, including the original *HST* F814W image, the GALFIT model, and the resulting residual.

For the rest of this paper, we will analyze the two-bulge systems and the galaxy pairs containing the AGN host galaxy and the brightest secondary galaxy in the three-bulge systems. While this choice of analyzing only the brightest pairs in triple systems could theoretically lead to a bias in our analysis, we verified that none of the analyses or results presented in the remainder of the paper would be significantly altered if we were to examine all pairs (i.e. both sets of pairs containing the AGN host galaxy in triple systems) or if we were to completely exclude triple systems from any analysis. Differentiating offset from dual AGNs in our sample and analysis of the individual sub-populations, as well as the triple bulge systems, will be the focus of a future paper (Stemo et al., in prep).

3.4 Bias Analysis & Correction

All methods of identifying galaxy mergers are prone to significant selection biases. The process outlined in Section 3.3 is purposefully conservative and designed to minimize false positives; this in itself is a selection bias. Further, our methods rely upon the ability to properly detect and separate the stellar bulges associated with the AGNs or SMBHs of each merger component, which can be extremely challenging and result in false negatives. Both of these effects need to be accounted for.

As a merging systems bulges near each other, their surface brightness profiles can overlap significantly; but as was discussed in Section 3.3.3, bulges can be as close as 1.5 kpc before they physically begin to coalesce. This means that physically distinct stellar bulge pairs at small separations can be especially difficult to detect even with *HST*/ACS 's spatial resolution. This is exacerbated by the high redshift nature of our sample, with a 1.5 kpc separation corresponding to less than 6 pixels in the most extreme region of our redshift range.

In addition to the challenge in resolving small separations, the higher the merger mass ratio (the more dissimilar the masses), the more likely the system is to be modeled as a single component

rather than as multiple stellar bulges. As the merger mass ratio increases, the integrated flux ratio also increases. This leads to one surface brightness profile dominating the other; therefore, the model of the lower integrated flux (lower mass) component is less important to the goodness of fit of the overall model.

Both of these factors cause our merger identification pipeline to frequently incorrectly model closely separated and high merger mass ratio galaxy mergers with a single component. This means that our galaxy merger sample is biased towards major mergers (low mass ratio) and mergers at large separations. In order to correct for this, we simulated and modeled 377,000 galaxy mergers across a large swath of parameter space. Examining the resulting `GALFIT` models of these simulated mergers allowed us to correct for the aforementioned separation and merger mass ratio selection biases.

In Section 3.4.1, we discuss the creation of the galaxy merger models and the parameter space they cover. In Section 3.4.2, we detail the `GALFIT` modeling of the simulated mergers and report the regions of success and failure of our merger identification pipeline. Lastly, in Section 3.4.3, we discuss the quantification of our selection biases and the process we used to correct for them.

3.4.1 Simulating Galaxy Mergers

Our merger identification pipeline relies on modeling multiple stellar bulges with Sérsic profiles. Ignoring position, Sérsic profiles only need three variables to be fully defined; these are typically the Sérsic index, effective radius, and intensity at the effective radius. However, we choose to define integrated flux (i.e. total flux) as the last variable instead of intensity at the effective radius for our simulations. Since we are modeling mergers, we also need to define a merger mass ratio and a separation.

In order to properly estimate the biases involved with our approach to identifying galaxy mergers, we created a large number of simulated Sérsic pairs with parameter values that span the expected parameter space, as estimated by our observed *HST* galaxies, convolved them with an appropriate PSF for the ACS instrument on *HST*, and then added noise to the data which mimicked

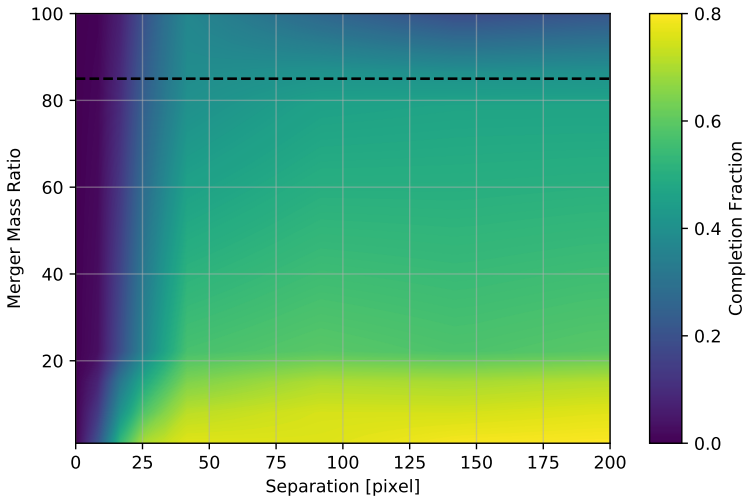

Figure 3.3: The bias map of our merger identification pipeline as determined by simulating and fitting Sérsic pairs across a large span of parameter space. The black dashed line is the upper merger mass ratio limit (= 85) where this bias map is accurate. Note how quickly and severely the selection becomes biased at small separations.

the observed background of our galaxy tiles.

We simulated all combinations of the following parameter arrays: Sérsic index = [0.25, 0.5, 1, 3, 6, 10], effective radius = [2, 5, 10, 15, 30, 60, 100], integrated flux = [10^3, 10^4, 10^5, 10^6, 10^7, 10^8], merger flux ratio = [1, 2, 4, 8, 16, 40, 100], and separation = [3.5, 10, 15, 25, 50, 100, 150, 196]. Here we are using the merger flux ratio as a proxy for the merger mass ratio. The effective radius and separation are in units of pixels (*HST*/ACS has a pixel scale of 0.″03 per pixel), while the integrated flux is in units of ADUs. The separations were chosen to span the range of 1 to 20 kpc across our entire sample redshift range, while the integrated fluxes were chosen to fully span the range of our observed sample integrated fluxes. We restricted our simulated mergers by limiting the ratio of effective radius to Sérsic index to being less than 40; this was done because galaxy parameters outside of that are not physical. To best mimic the observed background of our galaxy tiles, we added Poisson noise from our simulated models as well as Gaussian noise with a mean of 1200 and standard deviation of 400; these values were estimated from the distribution of our sample's `GALFIT` modeled backgrounds.

In total we created 376,992 simulated galaxies to model, consisting of 11,088 simulated single galaxies and 365,904 simulated galaxy pairs.

3.4.2 Modeling the Simulated Mergers

We then ran these simulated galaxies through our merger identification pipeline as detailed in Sections 3.3.2 & 3.3.3. Of the 11,088 simulated single galaxies, 5565 were correctly modeled, 5443 were not modeled at all, and 80 were incorrectly modeled with only a background component. The 5443 that were not modeled had low intensity levels; specifically they had intensities (in units of ADUs) at their effective radius of $I_e < 10^0$ and central intensities of $I_0 < 10^{2.7}$. The 80 that were incorrectly modeled had $I_e > 10^0$ and $I_0 > 10^{2.7}$, and therefore can be classified as false negatives. Of the 5565 true positives, all had $I_e > 10^0$ and $I_0 > 10^{2.7}$.

Of the 365,904 simulated galaxy pairs, 64,979 were correctly modeled, 180,724 were not modeled at all, and 120,188 were incorrectly modeled with either a single galaxy component or only a background component. There were only 13 simulated pairs that were modeled with more than two galaxy components. The 180,724 that were not modeled had $I_e < 10^0$ and $I_0 < 10^{2.7}$, while 69,526 of the 120,188 that were incorrectly modeled had $I_e > 10^0$ and $I_0 > 10^{2.7}$, and therefore can be classified as false negatives. Of the 64,979 true positives, all had $I_e > 10^0$ and $I_0 > 10^{2.7}$.

3.4.3 Correcting for Selection Biases

In order to properly account for the biases in our selection pipeline, we calculated the fraction of true positives to true positives plus false negatives; there were 70,544 true positives out of 140,150 true positives and false negatives; we define this as the completion fraction. We calculated the completion fraction at all points across the separation and merger mass ratio axes, which gave us a sparse two-dimensional bias map that we interpolated (Figure 3.3) in order to allow us to correct our results across the entire separation and merger mass ratio range of our sample. The simulations with $I_e < 10^0$ and $I_0 < 10^{2.7}$ were considered true negatives (i.e. accurately not found due to being too faint for the background noise — this mirrors a sensitivity limit for true data), while the 13

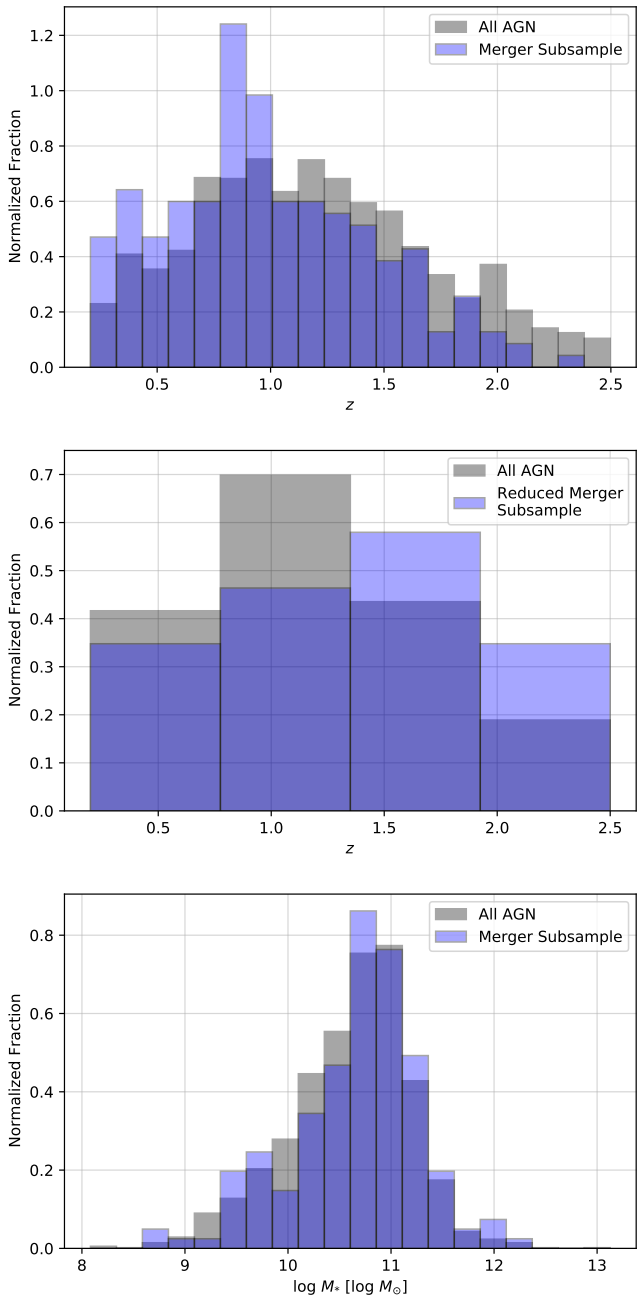

Figure 3.4: Histogram of the redshifts (top) of our merger subsample in comparison to the general AGN population of the ACS-AGN Catalog; note that the histograms are normalized to an area of 1 for comparison purposes. The over-representation of offset and dual AGNs at low redshift and under-representation at high redshift is due to selection effects. Once these effects have been accounted for, the expected distribution of mergers as a function of redshift is found, as seen in the histogram of the bias-corrected merger subsample (middle, Section 3.5.2). Below these we see the histogram of the stellar masses (bottom) of our merger subsample in comparison to the general AGN population of the ACS-AGN Catalog: the merger subsample distribution does not differ significantly from that of the general AGN population.

false positives were ignored as their contribution is trivial to the overall statistics (i.e. less than a 0.001 contribution to the completion fraction).

While examining our biases across our parameter space, we found that when the separation exceeded 50 pixels at the highest merger mass ratio (1:100), our pipeline's accuracy dropped significantly. This is due to the `Source Extractor` source flux limitation we used. Since `Source Extractor` limits the flux ratio between multiple sources to 1:100 prior to modeling by `GALFIT`, our pipeline becomes insensitive to merger mass ratios $\gtrsim 85$. This does not affect our analysis since we have no offset or dual AGNs with merger mass ratios greater than 85, but we include this discussion for completeness.

We applied corrections for these biases to our sample. When examining how AGN activation behaves as a function of bulge separation (see Section 3.6.1), we first binned by redshift in order to assign pixel separations to our kpc separation bins, then binned into our kpc bins, and lastly binned by merger mass ratio. We then applied a correction factor, the reciprocal of the completion factor calculated at the mean separation and merger mass ratio values of our bins, to offset our biases; we also estimated error values by calculating this correction at the minimum and maximum separation and mass ratio values in each bin.

We repeated this process to examine how AGN activation relates to merger mass ratio (see Section 3.6.2); the only difference was the binning order, with merger mass ratio first, followed by bulge separation. Lastly, if the error in a bin was less than the Poisson statistic of $\sqrt{N}$, where N was the number added as a correction in that bin, we set the error to $\sqrt{N}$; this was done to account for any errors associated with our assumptions as well as unknown errors so as to not overestimate the accuracy of our methods.

During the `GALFIT` modeling and bias correction process of this work, strictly Sérsic profiles were used. While we discuss how the use of only Sérsic profiles should not significantly impact the estimated merger properties of our sample in Section 3.3.2, the use of only Sérsic type simulated galaxies in our bias correction process means that any biases against non-Sérsic type galaxies is hard to detect and account for. This would not necessarily affect any separations or merger mass

ratios more than others, but it could result in an overall lower detection rate of mergers. While we did not notice a dearth of spiral or irregular type galaxies while examining our sample by eye as part of our false positive reduction measures (Section 3.3.3), this should be thought of as a selection bias and considered while examining the data and during any future use of this sample.

3.5 Merging Galaxy Properties & Comparison to ACS-AGN Sample

The ACS-AGN Catalog contains AGN and host galaxy properties, most derived from SED template fits to photometric data; these data include: redshift (z), AGN bolometric luminosity ($L_{\rm AGN}$), galaxy mass (M_*), star formation rate (SFR), and column density ($N_{\rm H}$). The process by which these properties are derived from observations or from SED template fits is explored in depth in S20. The selection and modeling of our offset and dual AGN sample in this work allows us to derive some merger specific properties, such as bulge separation and merger mass ratio.

In Section 3.5.1, we discuss how we calculate these merger specific properties. We then examine the AGN and host galaxy properties of offset and dual AGNs in comparison to the general AGN sample of the ACS-AGN Catalog in Section 3.5.2. Lastly, we search for any correlations between the AGN, host galaxy, and merger properties of offset and dual AGNs in Section 3.5.3.

All of the properties discussed in this section, and more, are included in the ACS-AGN Merger Catalog, presented in Table 3.1. This catalog is also available in its entirety in fits format from the original publisher.

3.5.1 Obtaining Merger Parameters

Two important merger parameters can be obtained from the `GALFIT` models: component separation and the integrated flux of each component. The centroid locations of all fit components are given by `GALFIT` in image units (pixel values). Using these centroid locations, and knowledge of the pixel scale of the galaxy tiles, we back out the angular separation of the stellar bulges for our candidates. The angular separation is then transformed into a projected physical separation using the angular distance calculated from each galaxy's redshift.

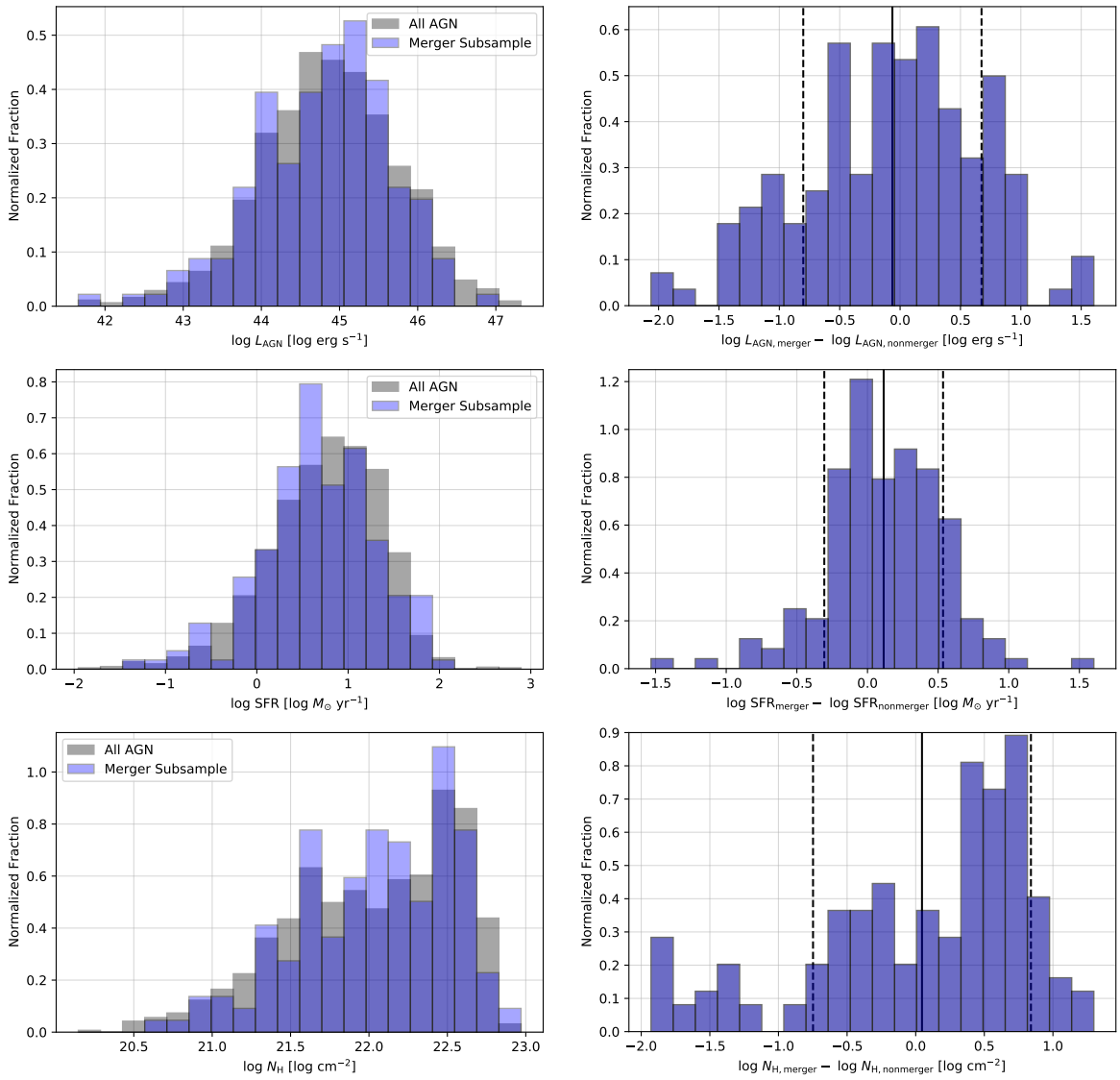

Figure 3.5: Histograms of the AGN and host galaxy property values of our merger subsample in comparison to the general AGN population of the ACS-AGN Catalog (left) alongside histograms of the difference in AGN and host galaxy properties of our merger subsample in comparison to non-merging AGN host galaxies matched in redshift and galaxy stellar mass (right); the vertical solid lines indicate the mean difference values while the vertical dashed lines indicate the difference distributions' standard deviations. Note that the merger subsample distributions mimic that of the general AGN population and that the means of the difference distributions are approximately zero.

The second significant merger parameter that can be obtained from the GALFIT model is merger mass ratio. GALFIT measures and reports an integrated flux measurement for each component during its fitting process. We take the ratio of integrated fluxes between bulge pairs as a proxy for their stellar mass ratio.

As was discussed in Section 3.3.2, our choice to use Sérsic profiles to model our merger components should result in accurate measurements of these properties in most cases, but may cause scatter in their distributions (specifically merger mass ratio), and caution should be taken when attempting to examine individual systems instead of the sample en masse. The distributions of these parameters are shown in Figures 3.8 & 3.9, respectively, and will be discussed further in Section 3.6.

3.5.2 Comparison to the General AGN Sample

With this being the largest catalog of offset and dual AGNs yet assembled, we examine how this population behaves and relates to more general populations, such as the population of all AGN host galaxies.

At first glance, it seems that our merger subsample is over-represented at lower redshifts (and under-represented at higher redshifts) when compared with the general AGN population of the ACS-AGN, as seen in Figure 3.4. Specifically, we find that our offset and dual AGN distribution increases until $z \sim 1$ and then decreases. This is surprising given that the merger fraction is thought to increase with redshift, peaking at redshifts near $z = 1.5$ (e.g. Carlberg, 1990), with work studying deep surveys confirming those predictions (e.g. Ryan et al., 2008; Stott et al., 2013). However, our distribution is in agreement with the merger fraction for massive galaxies in the UltraVISTA/COSMOS catalog, as shown in Man et al. (2016). They explain that the reason for the drop in merger fraction above $z = 1$ in their sample is due to being incomplete at higher redshifts as low surface brightness partners become undetectable.

Therefore, we test whether the trends seen in our offset and dual AGNs' redshift distribution are also due to this selection bias. In order to do this, we adjusted the surface brightnesses and

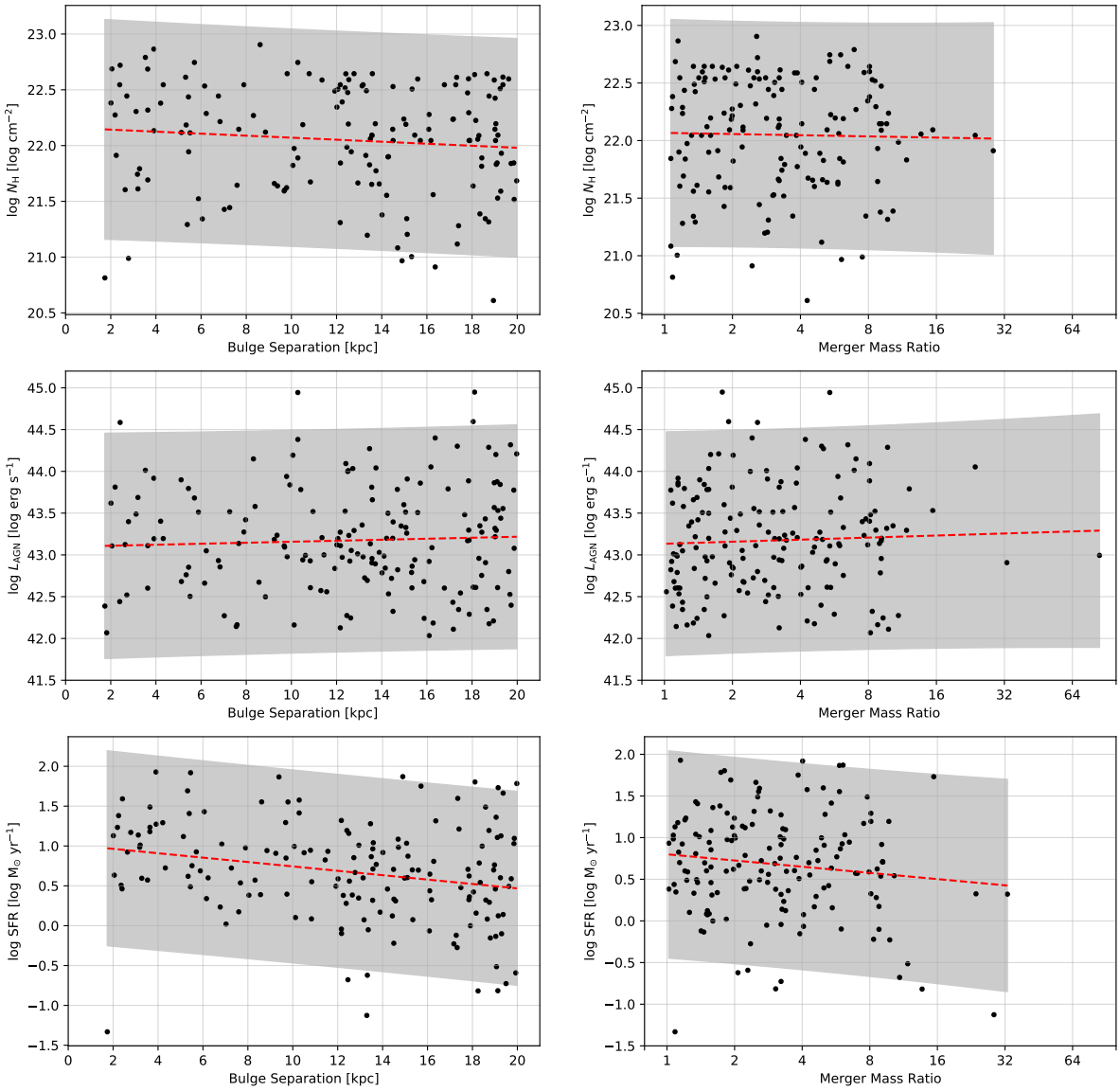

Figure 3.6: Relations between AGN and host galaxy properties with the merger parameters of bulge separation (left) and merger mass ratio (right); from top to bottom, the AGN and host galaxy properties examined are: nuclear column density, AGN luminosity, and SFR. The overlaid red dashed lines and gray regions are linear fits to the data and the fits' 95% confidence regions, respectively. None of the linear fits show any significant correlations except for SFR as a function of separation; this is due to correlations with galaxy mass (see Section 3.5.3 and Figure 3.7). Note that the scale for the merger mass ratio axis is Log_2.

pixel separations of our sample to what would be observed if they were at the highest redshift in our sample, $z = 2.5$; specifically, for surface brightness we multiplied by a factor of $(d_L(z)/d_L(z = 2.5))^2$, where $d_L(z)$ is the luminosity distance at the given redshift, z; this follows the known relation of surface brightness being proportional to $(1 + z)^{-4}$ (e.g. Tolman, 1930; Hubble and Tolman, 1935; Sandage, 1961). We found that the bulge separations of our offset and dual AGNs were not a limiting factor, with all being able to be detected even when adjusted to a $z = 2.5$ frame. However, only 16 out of the 204 dual and offset AGNs in our sample had sufficient surface brightness to be able to be detected using the methods outlined in Section 3.3 when adjusted to a $z = 2.5$ frame.

Therefore, we are heavily biased towards selecting only the brightest bulges at high redshifts. If we only examine the subsample of offset and dual AGNs that could be observed even when adjusted to the $z = 2.5$ frame (as seen in Figure 3.4), we find that our distribution peaks near $z = 1.5$, falling off at low redshift due to the decrease in survey volume observed as redshift decreases and dropping off rapidly at high redshift due to surface brightness dimming and survey depth limits. Therefore, we find that the redshift distribution of our offset and dual AGN sample recovers the expected merger fraction distribution with redshift of previous works (e.g. Carlberg, 1990; Ryan et al., 2008; Stott et al., 2013), once this has been corrected for.

The distributions of the rest of the AGN and host galaxy properties (M_*, $L_{\rm AGN}$, SFR, and $N_{\rm H}$) for the offset and dual AGNs closely mirror that of the general AGN population of the ACS-AGN Catalog. This can be seen in Figures 3.4 & 3.5, and is verified by Kolmogorov-Smirnov (KS) tests for each.

We also examined the AGN and host galaxy properties of our offset and dual AGNs in comparison to samples of non-merging AGN host galaxies matched by redshift and galaxy stellar mass. To do this, we matched each offset and dual AGN in our sample to a set of non-merging AGN host galaxies from the ACS-AGN catalog that had redshifts within 0.1 and galaxy stellar masses within 0.25 dex of the offset or dual AGN system. We required that each dual and offset AGN had a matched sample of at least 10 systems in order to be analyzed. In total, we examined 161 of the 204 dual and offset AGNs along with their matched samples, with the minimum, median, and

maximum number of ACS-AGN galaxies in the matched samples being 10, 60, and 133, respectively. We then calculated how the offset and dual AGNs' $L_{\rm AGN}$, SFR, and $N_{\rm H}$ values differed from their matched non-merging sample's mean $L_{\rm AGN}$, SFR, and $N_{\rm H}$ values. The distribution of the differences between the offset and dual AGNs and their matched samples $L_{\rm AGN}$, SFR, and $N_{\rm H}$ values are shown in Figure 3.5. We find that the means of the difference distributions of these properties are all approximately zero, and therefore that the $L_{\rm AGN}$, SFR, and $N_{\rm H}$ values of the offset and dual AGNs do not significantly differ from that of non-merging AGN host galaxies, even when matched in redshift and galaxy stellar mass.

From these results, we specifically find that at high AGN luminosities, offset and dual AGNs are not overrepresented compared to the general AGN population of the ACS-AGN. Therefore we find that mergers do not preferentially trigger the most luminous AGN, but instead host AGN with similar luminosities to AGN not in mergers; this is true not only when examining the total sample, but also for the minor mergers (merger mass ratio > 4) and major mergers (merger mass ratio < 4) separately. This is in disagreement with theoretical predictions made by Hopkins and Hernquist (2009) and observations by Treister et al. (2012), but is in agreement with observational work by Kocevski et al. (2012) and Villforth et al. (2014). Further, recent studies by Ricarte et al. (2019) of the `ROMULUS` simulations (Tremmel et al., 2017) predict that there is no enhancement of SMBH growth in mergers, but instead that SMBH growth approximately follows host galaxy SFR. These findings, along with trends found by S20, are in agreement with those predictions.

We also do not find any evidence that SFR is enhanced in offset and dual AGNs, instead finding that offset and dual AGNs do not exhibit any shift towards higher SFRs when compared to the overall active galaxy population. Other works have found that star formation is enhanced in mergers in general (e.g. Joseph and Wright, 1985; Knapen et al., 2015). Our results indicate that the presence of offset and dual AGNs makes these merging systems unique in this regard. The lack of a shift to higher SFRs in offset and dual AGNs may indicate that the presence of an AGN in the merging system inhibits the increase in SFR seen in non-AGN host mergers. If this is so, then this is a key piece of observational evidence pointing toward the ability of AGNs to impart negative

feedback during galaxy mergers and shut down star formation in their host galaxies.

Lastly, we find that the nuclear column densities of offset and dual AGNs are similar on average to those of the overall active galaxy population and that there is no enhancement present in offset and dual AGNs even when matched in redshift and galaxy stellar mass. However, the distribution is highly asymmetric, showing a longer tail of less obscured systems out to -2 dex, while the distribution peaks at the moderately increased obscuration value of +0.5 dex.

3.5.3 AGN and Host Galaxy Properties Are Not Correlated with Merger Parameters

Lastly, we examine the AGN and host galaxy properties of offset and dual AGNs as a function of their merger properties. We specifically examine relations between nuclear column density, AGN luminosity, and SFR to search for correlations in our data.

Merger events should drive significant material inwards towards the center of the merging system; this material can fuel star formation and SMBH growth (e.g. Hopkins et al., 2008; Hopkins and Hernquist, 2009). There has been a substantial amount of work done predicting and searching for evidence of increased star formation, and increased SMBH growth in mergers. Star formation is expected to increase as separation decreases in merging systems (e.g. Ellison et al., 2008; Patton et al., 2013), as well as increase as merger ratio approaches unity (e.g. Somerville et al., 2001; Cox et al., 2008; Ellison et al., 2008). Since SMBHs are thought to be fed by the same material that is enhancing star formation in these scenarios, it is also predicted that AGN triggering increases as separation decreases to small separations (e.g. Ellison et al., 2011; Van Wassenhove et al., 2012; Koss et al., 2012; Blecha et al., 2013; Satyapal et al., 2014); whether the most luminous AGN are found in mergers with mass ratios near unity is debated (e.g. Kocevski et al., 2012; Treister et al., 2012; Villforth et al., 2014, 2017). If true, this increase would follow from the expected increase in available material near the center of the merging system; this has been hinted, with observations suggesting that obscured AGN are more likely to reside in mergers Kocevski et al. (2015); Ricci et al. (2017); Donley et al. (2018); Pfeifle et al. (2019), but the sample sizes have been limited in

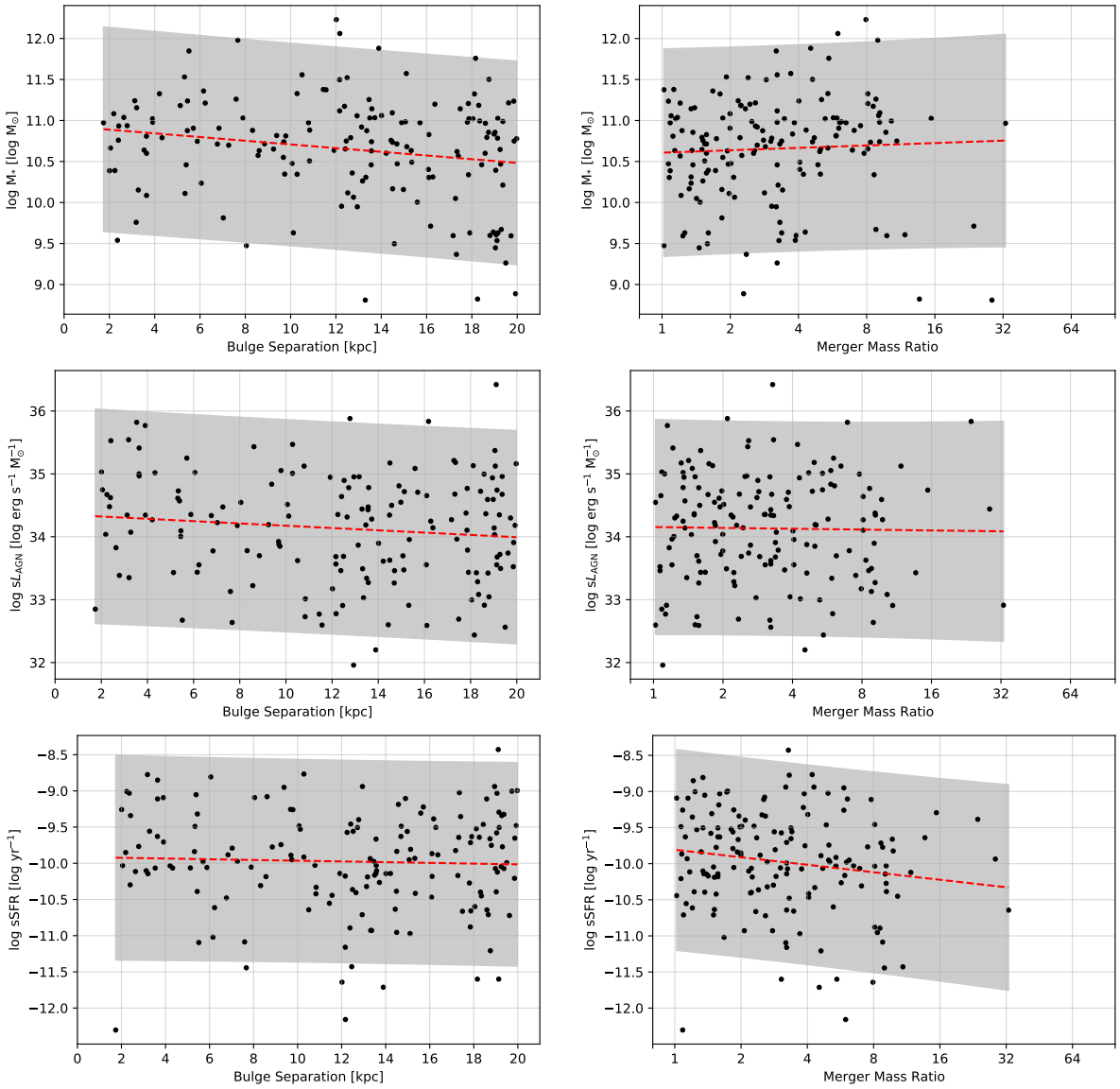

Figure 3.7: Relations between specific SFR and specific AGN luminosity ($L_{\rm AGN}/M_*$) with the merger parameters of bulge separation (left) and merger mass ratio (right). The overlaid red dashed lines and gray regions are linear fits to the data and the fits' 95% confidence regions, respectively. We see that by accounting for known correlations with galaxy mass, neither specific SFR or specific AGN luminosity show any significant correlations with bulge separation or merger mass ratio.

these studies.

When looking at our relations shown in Figure 3.6, it is apparent that there is a large amount of scatter in the data, with no tight correlations emerging. Overlaid on top of the data are linear fits; these correspond to exponential and logarithmic fits when examining these properties as functions of bulge separation and merger mass ratio, respectively. Excluding SFR as a function of bulge separation, we find that none of the fits have slopes that are significantly non-zero (p-value < 0.05) and that no pair is significantly correlated, as determined by its Spearman rank-order correlation coefficient (p-value < 0.05).

However, we know that the ACS-AGN galaxies show correlations between galaxy mass and SFR as well as galaxy mass and AGN luminosity (see S20 for more detail); this relation has also been shown to exist for galaxies in mergers (Barrows et al., 2017b). As we can see in Figure 3.7, galaxy mass is significantly inversely correlated with separation in our sample; this is verified by examining the significance of its fit and Spearman rank-order correlation coefficient. Therefore we examine the specific SFR (sSFR; i.e. SFR divided by galaxy stellar mass) and AGN luminosity divided by galaxy stellar mass ($sL_{\rm AGN}$), in order to correct for any galaxy mass – separation correlation and galaxy mass – merger ratio correlation.

While SFR is significantly correlated with bulge separation, we find that this is due to the correlation between galaxy mass and separation. When examining sSFR and specific AGN luminosity, we find that neither have significant linear trends nor are they correlated at significant levels to bulge separation or merger mass ratio. This can be seen in Figure 3.7. Where Barrows et al. (2018) find that AGN luminosity increases as merger mass ratio decreases, this work does not find such a relationship. It is possible that nuclear star formation correlates with separation (e.g. U et al., 2019), however due to the limitations of our methods, we cannot decompose nuclear and global star formation in our sample in order to investigate this.

From these data, we find that there is no observational evidence that nuclear column density, AGN luminosity, or SFR is correlated with bulge separation or merger mass ratio for offset and dual AGNs. We also examined these data by redshift and found that no correlations exist in any

redshift bin examined ($0.2 < z < 0.5$, $0.5 < z < 0.8$, $0.8 < z < 1.5$, or $1.5 < z < 2.5$). This stands in contrast to many of the findings outlined above related to SFR increasing as separation decreases and as merger ratio approaches unity in the general population of mergers. Since the primary difference between these two populations is the presence of AGNs, this finding provides another piece of evidence supporting the hypothesis that an AGN can impart negative feedback on its host galaxy, maintaining a lower level of star formation than would be expected in a merger without AGN. We also find that the most luminous AGN are not preferentially triggered by major mergers; this is in agreement with previous findings by Kocevski et al. (2012) and Villforth et al. (2014, 2017).

3.6 Results

3.6.1 AGN Activation Peaks at the Smallest Bulge Separations

One of the major open questions that this sample of offset and dual AGNs can address is whether the fraction of AGNs in mergers peaks at separations below 10 kpc. Theoretical work predicts that SMBH growth peaks at separations of either 1 – 10 kpc (Van Wassenhove et al., 2012) or 0.1 – 2 kpc (Blecha et al., 2013). While observations have found that AGN fraction increases from 100 – 10 kpc, the trend could not be constrained below 10 kpc due to the limited samples at small separations (Ellison et al., 2011; Koss et al., 2012; Barrows et al., 2017a).

We find that AGN activation increases significantly below 10 kpc. In Figure 3.8, we see that the AGN activation is mostly flat from 20 – 14 kpc, has a bump from 14 – 11 kpc, drops slightly from 11 – 4 kpc, and then increases significantly and peaks at our smallest separation bin, 3 – 2 kpc. This distribution is in qualitative agreement with previous work examining simulations of dual AGNs by Rosas-Guevara et al. (2019) that shows a bump in dual AGN fraction near 14 kpc and a rise as separations near 5 kpc. It should be noted that we had one system observed between 1.5 and 2 kpc, which is not included in this analysis because it is the only system in that bin.

We also analyze both the major and minor merger sub-populations of our sample in Figure

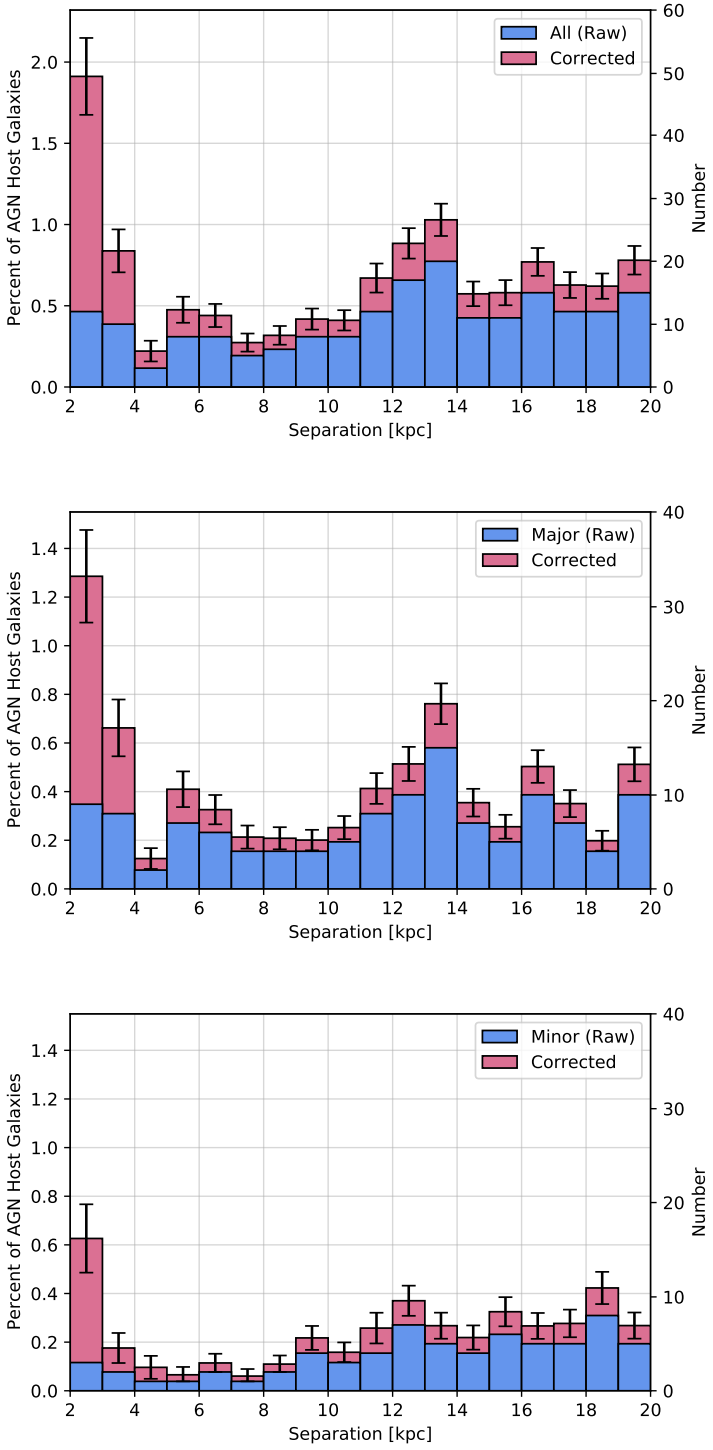

Figure 3.8: Histogram of percentage of AGNs in mergers as a function of separation; raw numbers are reported as well as bias corrected values. The top plot shows all of our sample, while the middle shows only major mergers (ratio < 4) and the bottom shows only minor mergers (ratio > 4). Note that AGN activation peaks at separations less than 4 kpc and that there is a bump, more apparent in the major merger subsample than minor merger subsample, near separations 11 – 14 kpc.

3.8; we define major mergers as those with merger mass ratios <4 and minor mergers as those with merger mass ratios >4. We see similar distributions as the total sample, with the exception that the bump near 14 kpc is only found in our major merger sample. This bump coincides with separations corresponding to the merger's first pericenter passage, typically seen at separations from 10 – 20 kpc in simulations, when significant gas would be driven inwards, triggering AGN activation (Van Wassenhove et al., 2012; Blecha et al., 2013; Rosas-Guevara et al., 2019). This explains why this bump is only seen in our major merger sample, as first pericenter passage in major mergers should be more dynamic, driving more gas inwards than minor mergers, and more readily triggering AGN activation.

Therefore, we confirm the theoretical predictions of Van Wassenhove et al. (2012) and Blecha et al. (2013), and are able to extend the trends seen by Ellison et al. (2011), Koss et al. (2012), and Barrows et al. (2017a). Further, we find that we are in good agreement with the smallest separation bin of Koss et al. (2012), which studied a small sample of moderate-luminosity, ultra-hard X-ray selected AGN at low redshifts. They find that 7.8±1.8% of AGN are found in mergers at separations < 15 kpc, while we find that 9.3±1.3% of AGN are found in mergers at those separations, after accounting for biases.

It is uncertain whether AGN activation and SMBH growth continues to increase below 2 kpc. As was discussed in Section 3.3.2, a reasonable estimate of the physical size of a stellar bulge is approximately 1.5 kpc. Further, 1.5 kpc is very close to the limit at which we can accurately resolve two bulges, if they are even physically small enough to exist discretely at those separations. Therefore, we cannot reliably use offset and dual AGN discovered by selecting multiple stellar bulges to study AGN activation and SMBH growth below 2 kpc.

3.6.2 AGN are Preferentially Found in Major Mergers

The second primary question that can be addressed with our sample of offset and dual AGNs is whether merger mass ratio affects AGN activation. Many others have examined whether major mergers trigger the most luminous AGN. As previously discussed, theoretical work by Hopkins and

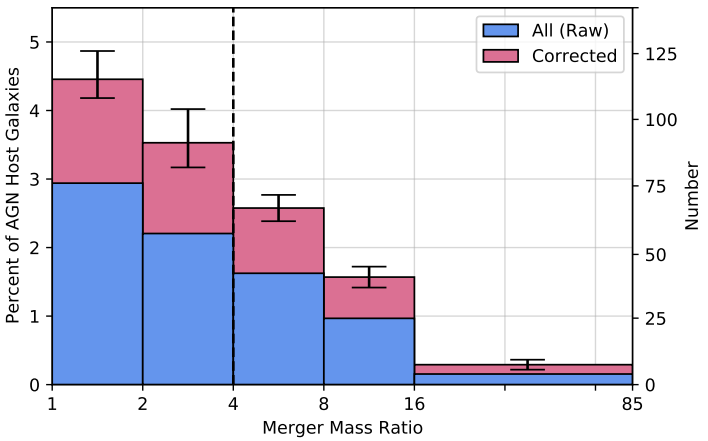

Figure 3.9: Histogram of percentage of AGNs in mergers as a function of merger mass ratio; raw numbers are reported in addition to the bias corrected values. Note that the scale for the merger mass ratio axis is Log_2, and that the last bin spans merger mass ratio values from 16 to 85 due to the small number of galaxies in that range.. The dashed vertical line at merger mass ratio = 4 separates major mergers to the left and minor mergers to the right. Note that AGNs in mergers at separations < 20 kpc are preferentially found in major mergers and that the percent of AGNs decreases as ratio increases as a log base 2 function with slope ≈ -1 from merger mass ratio values of 1 to 16.

Hernquist (2009) predicts that major mergers trigger the most luminous AGN, while observational studies on the subject are not in agreement, with some in finding they do (e.g. Treister et al., 2012), and some finding no relation (e.g. Kocevski et al., 2012; Villforth et al., 2014, 2017).

While we also find that there is no relation between merger mass ratio and AGN luminosity (as discussed in Section 3.5.3), we do find that AGNs are preferentially found in major mergers; this can be seen in Figure 3.9. Using our corrected values and a merger mass ratio cutoff value of 4:1 between major and minor mergers, we find that 8.0±0.8% of all AGNs are found in major mergers at separations <20 kpc and 4.5±0.4% of all AGNs are found in minor mergers (with merger mass ratios greater than 4 and less than 85) at separations <20 kpc. In total we find that 12.5±1.2% of all AGNs are found in mergers at separations <20 kpc. The overabundance of AGN in major mergers compared to minor mergers is especially significant because it is thought that minor mergers outnumber major mergers three to one (e.g. Bertone and Conselice, 2009; Lotz et al.,

2011); this means that AGN are overrepresented in major mergers by approximately a factor of six when compared to what would be expected if AGN activation had no dependence on merger mass ratio.

We also find that the fraction of AGNs in mergers at separations < 20 kpc follows a logarithmic relationship from ratios of 1 to 16 — we find a relationship of: percent of AGN in merger mass ratio bin $= -\mathrm{Log}_2(\mathrm{MassRatio})+5$, where MassRatio is the center value of the bin. Note that due to the nature of a histogram, this specific relation only applies when using bin widths of powers of two, but a logarithmic relation would remain regardless.

Last, we can compare our fractions of AGN activation in the lowest merger mass ratio bins to that found by Koss et al. (2012). They find that the fraction of their AGNs in each bin is 4.2±1%, 1.8±0.6%, and 1.8±0.6% for merger mass ratio bins from 1 – 2, 2 – 4, and 4 – 8, respectively; they did not have any systems with merger mass ratios greater than 8. In comparison we find that the fraction of AGNs in each bin is 4.5±0.3%, 3.6±0.4%, and 2.6±0.2%, respectively. Comparing these values, we find that while we are in good agreement for mergers with mass ratios nearest unity, our approach finds more offset and dual AGNs at higher merger mass ratio values than the Koss et al. (2012) sample. We note that the fraction of AGN that we find to be in mergers is significantly higher than values predicted by Yu et al. (2011) and Rosas-Guevara et al. (2019); this is most likely due to those works focusing on dual AGN specifically, while this work includes offset AGN as well.

3.7 Conclusions

Here we have detailed the identification and analysis of 204 offset and dual AGNs observed with *HST*/ACS at $0.2 < z < 2.5$ and with stellar bulge separations <20 kpc. These offset and dual AGNs are a subsample of the AGN host galaxies in the ACS-AGN Catalog and were selected as AGN using mid-infrared and X-ray selection criteria applied to *Spitzer* and *Chandra* data. This sample and their associated AGN, AGN host galaxy, and merger properties are made available in the ACS-AGN Merger Catalog. We have analyzed this sample, with our main findings summarized below.

(1) We find that AGN activation increases significantly at bulge separations from 4 to 2 kpc. We also note a bump at separations from 14 to 11 kpc that is present in major mergers, but not minor mergers. This is likely attributable to first pericenter passage occurring near these separations, which is more likely to trigger AGN activation in major mergers than minor mergers.

(2) We find that AGNs in mergers at separations <20 kpc are preferentially found in major mergers. Specifically, using values corrected for selection effects related to bulge separation and merger mass ratio, we find that 8.0±0.8% of all AGNs are found in major mergers (merger mass ratios from 1 to 4) and 4.5±0.4% of all AGNs are found in minor mergers (merger mass ratios from 4 to 85), bringing the total percent of AGNs found in mergers to 12.5±1.2%. We also find that the percentage of AGNs found at different merger mass ratios follows a logarithmic relation, decreasing as merger mass ratio increases.

(3) We find that mergers do not trigger the brightest AGNs, but instead mergers at separations <20 kpc trigger AGNs with a similar distribution of luminosities as that of the general AGN population. This is true of all mergers, including the major and minor merger subpopulations.

(4) We find that SFR, AGN luminosity, and nuclear column density have no significant correlations or dependencies on bulge separation or merger mass ratio, once known correlations with galaxy mass have been accounted for. Further, we find that the distributions of these values for AGNs and AGN host galaxies in mergers at separations <20 kpc do not significantly differ from the distributions of AGNs and AGN host galaxies in general.

These findings show that in mergers where the stellar bulges are separated by <20 kpc, bulge separation and merger mass ratio play an important role in the activation of AGNs, but do not significantly enhance star formation or the luminosity of AGNs in galaxy mergers. This implies that there may be AGN feedback involved in these systems that heats and/or blows out excess material,

inhibiting AGN growth and slowing star formation rapidly after AGN activation, returning the system to AGN luminosity and star formation rates typically seen in non-mergers.

Acknowledgments

Support for this work was provided by NASA's Astrophysics Data Analysis program, grant number NNX15AI69G, the CU Boulder / JPL Strategic University Research Partnership program, the National Science Foundation's Graduate Research Fellowship program, and a Chance Irick Cooke Fellowship. The work of DS was carried out at the Jet Propulsion Laboratory, California Institute of Technology, under a contract with NASA. RJA was supported by FONDECYT grant number 1191124. This work utilized the RMACC Summit supercomputer, which is supported by the National Science Foundation (awards ACI-1532235 and ACI-1532236), the University of Colorado Boulder, and Colorado State University. The Summit supercomputer is a joint effort of the University of Colorado Boulder and Colorado State University. The authors would also like to thank Rebecca Nevin and Hayley Roberts for providing support to this work.

Chapter 4

Observational Evidence for a Transition from Offset to Dual AGN Predominance in Late Stage Mergers

Abstract

Galaxy merger events are thought to be key phases of supermassive black hole growth (SMBH) and galaxy evolution. Theory predicts that the dynamical processes present in mergers can trigger SMBHs to become observable as active galactic nuclei (AGNs) as well as enhance star formation. To better study these systems, we identify and analyze 10 dual AGN systems (merging systems hosting 2 AGNs at separations <20 kpc) and 103 offset AGN (similar systems hosting 1 AGN and 1 quiescent SMBH at separations <20 kpc) observed with *Chandra* using the Bayesian analysis tool `BAYMAX`. We then study these systems in order to understand the environments in which they are found as well as their AGN and host galaxy properties in relation to non-merging AGN host galaxies and each other. First, we find that dual AGN systems host AGNs with luminosities significantly higher than those found in non-merging AGN host galaxies as well as offset AGN systems matched in galaxy mass and redshift. Second, we find that dual AGN systems strongly prefer the most major of mergers (merger mass ratios less than 2), while offset AGN systems only mildly prefer major mergers. Finally, we find that dual AGN systems are preferentially found at the smallest separations studied (2 – 4 kpc), while offset AGN systems are preferentially found at larger separations. This suggests that offset AGN transition to dual AGN as galaxy mergers progress to the smallest separations.

This chapter is in preparation and nearing submission for publication as a letter in the *The Astrophysical Journal*.

4.1 Introduction

As galaxies undergo merger events, their respective supermassive black holes (SMBHs) exist at separations of 1 – 20 kpc for ∼100 Myr before being driven toward the center of mass of the soon-to-be merger remnant (Begelman et al., 1980; Milosavljevic and Merritt, 2001). Similarly, gas and dust is thought to be driven inwards during this phase, enhancing star formation, and in some cases, causing one or both of the paired SMBHs to be observable as active galactic nuclei (AGNs, e.g. Joseph and Wright, 1985; Hopkins et al., 2008; Hopkins and Hernquist, 2009; Knapen et al., 2015). When one of the merging system's SMBHs is observable as an AGN, it is known as an offset AGN system, while a dual AGN system is when both are observable as AGN during this 1 – 20 kpc separation phase.

The timing and environmental factors that trigger dual AGN have been the focus of many recent works. It is predicted that major mergers (those with mass ratios <4) favor the dual AGN scenario (e.g. Volonteri et al., 2003; Hopkins et al., 2005; Steinborn et al., 2016), and multiple observational studies have found this as well (e.g. Ellison et al., 2008; Comerford et al., 2015; Barrows et al., 2017a). In addition, both simulations and observations have found that AGN fraction increases as the separation between the merging SMBHs decreases (Ellison et al., 2011; Van Wassenhove et al., 2012; Koss et al., 2012; Blecha et al., 2013; Barrows et al., 2017a; Capelo et al., 2017; Foord et al., 2020). However, observational studies of these systems have been limited to low redshifts and very small samples at separations <20 kpc.

Recent work by Stemo et al. (2021) has produced the ACS-AGN Merger Catalog: the largest catalog of dual and offset AGN to date (N = 204), consisting of systems at intermediate redshift (median $z \sim 1$) in four deep *Hubble Space Telescope* (*HST*) survey fields that include full *Chandra X-Ray Observatory* coverage. However, this catalog does not distinguish offset AGN from dual AGN systems. The Bayesian analysis tool `BAYMAX` has had recent success in identifying and separating close X-ray pairs in *Chandra* observations (Foord et al., 2019, 2020), and is an ideal tool to classify the X-ray AGN merger systems in the ACS-AGN Merger Catalog as either dual or offset AGN

systems.

In this letter we discuss the methods we use to identify 10 dual AGN and 103 offset AGN systems in the ACS-AGN Merger Catalog through the use of `BAYMAX`, and our findings related to the AGN triggering in those systems. These samples are the largest samples of verified dual and offset AGN at separations <20 kpc selected and examined in a single systematic study to-date.

4.2 Methods

While many works have serendipitously found dual AGN systems, there have only been a few successful systematic studies of offset and dual AGN systems at separations <20 kpc; in total, there are approximately 40 known dual AGN systems, with the majority of them being at redshifts of $z < 0.2$ and in sample sizes of four or less (see Rubinur et al. 2018 for a review of these studies). Fortunately, as the field pushes towards larger and deeper multiwavelength surveys, we continue to be presented with opportunities to find and study rare systems such as dual AGN. This work is one such example, where we use new computational techniques to identify and study dual and offset AGN systems present in deep multiwavelength survey field observations.

In Section 4.2.1 we discuss the parent merger sample from which we will select our dual and offset AGN, the ACS-AGN Merger Catalog. We then present the Bayesian analysis software `BAYMAX` in Section 4.2.2, and explain how we use it to select dual and offset AGN from the parent sample of X-ray AGN host mergers. Lastly, we discuss the resultant dual and offset AGN samples and their properties in comparison to the parent sample and matched samples in Section 4.2.3.

4.2.1 ACS-AGN Merger Catalog

Our parent merger sample was the Advanced Camera for Surveys Active Galactic Nuclei Merger Catalog (ACS-AGN Merger; Stemo et al., 2021). The ACS-AGN Merger Catalog is a catalog of 204 AGN host merging galaxy systems with SMBH separations under 20 kpc located in four deep survey fields: the Galaxy Evolution from Morphologies and SEDs (GEMS) survey (Caldwell et al., 2008), the Cosmological Evolutionary Survey (COSMOS) (Scoville et al., 2007),

the Great Observatories Origins Deep Survey (GOODS) (Dickinson and Giavalisco, 2003), and the All- wavelength Extended Groth Strip International Survey (AEGIS) (Davis et al., 2007). These 204 merging systems galaxies have been observed by *HST*/ACS, *Chandra*/ACIS, *Spitzer*/IRAC, along with further multiwavelength coverage, and span a redshift range of $0.2 < z < 2.3$.

Work by Stemo et al. (2020) identified these systems as AGN hosts by applying mid-infrared and X-ray AGN selection criteria to *Spitzer* and *Chandra* data available in these survey fields. Specifically, they used the Donley et al. (2012) mid-infrared color cut for *Spitzer* observed galaxies and a rest-frame X-ray luminosity cut in the 2–10 keV band of $L_{2-10} > 10^{42}$ erg s^{-1} for *Chandra* observed galaxies. Further, Stemo et al. (2020) also derived key AGN and host galaxy properties from spectral energy distribution (SED) models for these systems; properties such as redshift (z), host galaxy mass (M_*), AGN luminosity ($L_{\rm AGN}$), star formation rate (SFR), and nuclear column density ($N_{\rm H}$) were included in the catalog of Stemo et al. (2020). This process, as well as the AGN selection process, is described in detail in that work.

The ACS-AGN Merger Catalog was built by selecting merging systems from the catalog of 2585 AGN host galaxies in Stemo et al. (2020). Stemo et al. (2021) used an iterative process to identify multiple stellar bulges at close separations in *HST* F814W images; these are thought to coincide with the merging galaxies' respective SMBHs. They used `Source Extractor` to identify bright sources in the *HST* tiles, and then iteratively fit Sérsic surface brightness profiles to those sources using `GALFIT`, looking for models which favored pairs or triplets of stellar bulges. They also performed significant false-positive reduction, including a visual examinations of all merger candidates, in order to eliminate non-mergers from the sample. The ACS-AGN Merger Catalog also includes projected separation values for the SMBH pairs, as well as estimated merger mass ratio values for the merging system; these were derived from the `GALFIT` models of the systems. This merger selection and derivation of merger properties is described in detail in Stemo et al. (2021).

Analysis conducted by Stemo et al. (2021) on the 204 AGN host mergers at separations under 20 kpc included in the ACS-AGN Merger Catalog revealed that AGN activation was enhanced in

major mergers and at the smallest SMBH pair separations (<4 kpc). Further, they found that there were no significant correlations between merger properties (i.e. separation or merger mass ratio) and galaxy properties (e.g. $L_{\rm AGN}$, SFR, $N_{\rm H}$). However, Stemo et al. (2021) did not separate these mergers into distinct samples of dual and offset AGN, and therefore did not address the question of whether offset and dual AGN preferentially exist in different merger environments or at different merger stages.

4.2.2 Identification of Dual AGN Using BAYMAX

We have built on the work of Stemo et al. (2021) by analyzing the 173 X-ray AGN host mergers in the ACS-AGN Merger Catalog — identifying 10 dual AGN systems and 103 offset AGN systems which we can study separately and in comparison with each other. This was made possible through the use of a `BAYMAX`, a new tool for analyzing *Chandra* observations.

Classically, identifying dual X-ray point sources can be very difficult in the low-count regime and at small separations, which is the expected case for many dual AGN systems not in the local universe. `BAYMAX` (Foord et al., 2019) addresses this issue by using a Bayesian framework to quantitatively evaluate whether a given *Chandra* observation is more likely a single or dual point source. Specifically, `BAYMAX` takes calibrated *Chandra* events and compares them to models of single and multiple point sources. A Bayes factor is calculated to determine the preferred model, and the code calculates posterior distributions for the separations and count ratios (ratio between a given point source and the primary point source). Lastly, `BAYMAX` fits spectra to each point source component. With at least 20 counts between 0.5–7 keV, `BAYMAX` can successfully identify dual AGN at sub-PSF separations and count ratios $\sim$0.1, as seen in Foord et al. (2019, 2020, 2021).

The ACS-AGN Merger Catalog includes 173 X-ray AGN host merger systems that have been observed by *Chandra*, with total observation times ranging from 50 ksec – 7.5 Msec; however, due to the survey nature of those observations, many are significantly off-axis. Off-axis observations quickly degrade the PSF of *Chandra*, in some cases making the identification of dual X-ray sources at small separations impossible, even with the power of `BAYMAX`. Luckily, the size of the PSF of

Chandra as a function of off-axis angle is well known, and we can exclude observations that are too extreme for successful analysis.

Of the 173 X-ray AGN host merger systems in the ACS-AGN Merger Catalog, 113 have at least one *Chandra* observation with a PSF that is smaller than the modeled SMBH separation. These are the systems for which we can reliably use `BAYMAX` to classify them as either a single X-ray source (offset AGN) or dual X-ray source (dual AGN). While some systems have as many as 85 *Chandra* observations, the computation time of `BAYMAX` can be as long as 10 hours for a single observation, and computation time increases as N^2 in number of observations. Therefore in order to best balance computational time with model accuracy, we limited `BAYMAX` to analyzing the five most on-axis *Chandra* observations of each system, and that these observations could not be more than 10 arcmin off-axis. In general, the median off-axis angle of these observations was 5 arcmin, but ranged from 0.2 – 9.9 arcmin. `BAYMAX` analyzes each of these observations individually and then combines into a final analysis.

As discussed above, `BAYMAX` calculates a Bayes factor (BF) for its dual X-ray source models. In theory, a Bayes factor of $\mathrm{Log}_{10}(\mathrm{BF}) > 0$ favors the model, while a Bayes factor of $\mathrm{Log}_{10}(\mathrm{BF}) < 0$ does not. However, a Bayes factor of $\mathrm{Log}_{10}(\mathrm{BF}) \geq 3$ has been used in literature as a strong indicator of a strong dual model (see Foord et al. 2019 and references therein). To be conservative, we choose to use a Bayes factor that is 5σ above $\mathrm{Log}_{10}(\mathrm{BF}) = 3$ to select our dual AGN. Any system that does not meet this threshold is considered a single X-ray source and is classified as an offset AGN. This resulted in 29 systems selected as dual AGN and 84 selected as offset AGN systems. However, because `BAYMAX` analyzes a much larger field of view to select X-ray sources than the modeled separations in the ACS-AGN Merger Catalog, we then visually inspected the `BAYMAX` models alongside the `GALFIT` models of Stemo et al. (2021) to verify that the modeled dual X-ray sources matched with the modeled galaxy merger components. This left us with verified final samples of 10 dual and 103 offset AGN systems; these 10 dual AGN systems are shown in Table 4.1. We note that the dual AGN fraction that we find ($\sim$0.6%) is in good agreement with predictions made by Rosas-Guevara et al. (2019) based on dual AGN abundance in the EAGLE simulations.

Table 4.1: Verified Dual X-Ray AGN in the ACS-AGN Merger Catalog

ID	RA	Dec	z	M_* $[M_\odot]$	SFR $[M_\odot\ \mathrm{yr}^{-1}]$	L_{AGN} [erg s^{-1}]	N_{H} [cm^{-2}]	Separation [kpc]	Mass Ratio
51	53.1048	-27.705	1.62	-999	-999	-999	-999	10.4	1.5
292	149.5864	1.769	0.79	4.35×10^{10}	3.74	2.87×10^{46}	6.17×10^{22}	3.5	6.9
346	149.6242	2.181	1.19	6.00×10^{10}	60.8	8.68×10^{45}	4.83×10^{21}	19.9	1.7
410	149.6626	1.749	0.83	5.20×10^{10}	8.76	2.60×10^{44}	1.32×10^{22}	8.9	1.5
1041	150.0286	2.210	0.66	6.17×10^{10}	2.43	1.27×10^{45}	8.80×10^{21}	12.7	2.2
1249	150.1579	2.139	1.63	5.15×10^{9}	2.12	3.51×10^{45}	1.11×10^{22}	16.2	23
1288	150.1798	2.110	0.36	1.09×10^{11}	8.39	7.30×10^{44}	4.02×10^{21}	2.6	1.2
1685	150.4183	2.085	0.43	7.17×10^{10}	2.89	9.93×10^{44}	2.66×10^{22}	19.0	1.4
1694	150.4222	2.175	0.30	6.09×10^{10}	0.15	2.18×10^{44}	3.38×10^{21}	19.1	3.0
1927	150.5395	1.874	0.71	-999	-999	-999	-999	5.1	1.4

The ID number corresponds to the system ID in the ACS-AGN Merger Catalog (Stemo et al., 2021); AGN selection and derivation of AGN and AGN host galaxy properties can be found in Stemo et al. (2020), while merger selection and derivations of merger properties can be found in Stemo et al. (2021); note that reported mass ratios are integrated flux ratios that are used as proxies for merger mass ratio. A "-999" value in the table represents no data, and in the above instances specifically indicates that there was no satisfactory SED model from Stemo et al. (2020). The ACS-AGN Merger Catalog is available in its entirety, including more parameters and error estimations, in fits format from the original publisher.

4.2.3 Dual and Offset AGN Sample

We find that these samples have similar distributions of host galaxy mass, star formation rate, AGN luminosity, and nuclear column density as those seen in the general AGN host galaxy sample of Stemo et al. (2020) that these systems are ultimately drawn from; this is verified by Kolmogorov-Smirnov (KS) tests. Further, we do not find any significant differences between the M_*, SFR, $L_{\rm AGN}$, and $N_{\rm H}$ distributions of the dual and offset AGN samples as verified by KS tests. However, as AGN and host galaxy properties are known to have dependencies on redshift and host galaxy mass (e.g. Stanley et al., 2015, 2017; Stemo et al., 2020), a more accurate comparison should account for this.

Therefore, we examine the AGN and host galaxy properties of the offset and dual AGN samples in comparison to samples of non-merging AGN host galaxies matched in galaxy mass and redshift, as well as each other. To do this, we matched each offset AGN system in our sample with a set of non-merging AGN host galaxies from Stemo et al. (2020) that had redshifts within 0.3 and galaxy stellar masses within 0.5 dex of the offset AGN system. We also did this with the dual AGN systems, with the addition of similarly matching them with offset AGN systems as well. We then examined the differences in three key AGN and host galaxy properties: SFR, $L_{\rm AGN}$, and $N_{\rm H}$; this can be seen in Figure 4.1.

When examining the offset and dual AGN samples in comparison to their matched samples, we find that offset AGN and dual AGN have enhanced SFR and $N_{\rm H}$ values when compared to non-merging AGN host galaxies. Specifically, we find that the medians of the log differences (i.e. Δ log SFR, Δ log $\rm N_H$) are significantly above zero. We also find that the distribution of the log differences significantly overlap with 0, showing that while there is an overall enhancement, there are still systems found at values below those of matched non-merging AGN host galaxies. Further we find that dual AGN systems are similarly enhanced above matched offset AGN systems. This may be evidence that the specific environmental factors that trigger dual AGN also enhance star formation and drive excess gas and dust inwards at levels even greater than that of offset AGN; we

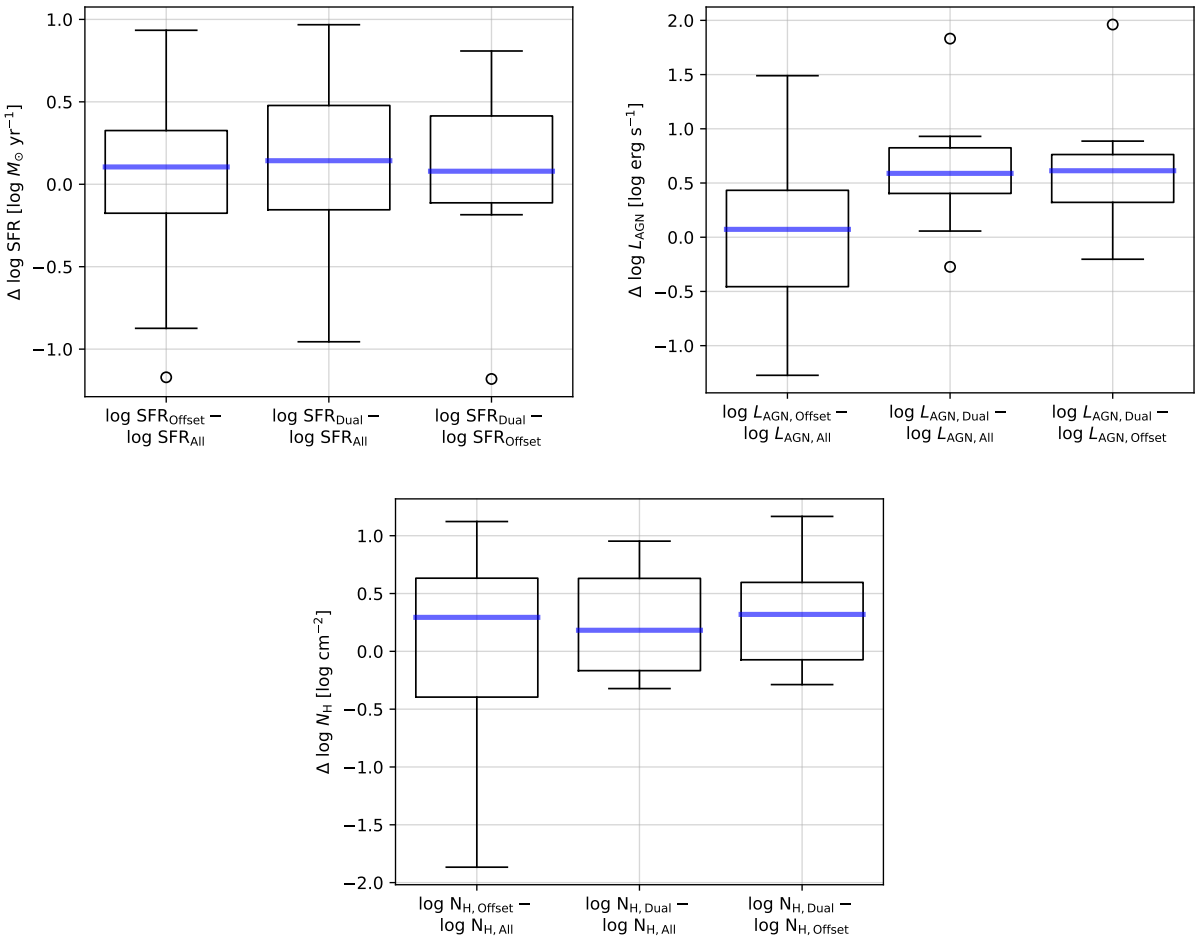

Figure 4.1: Boxplots showing the distributions of differences in galaxy parameters between the offset and dual AGN samples and systems matched in redshift and galaxy mass. An explanation of boxplots: boxplots describe distributions; these show the median (blue line), the 25th percentile to 75th percentile range (also called the interquartile range, or IQS; this is the box surrounding the median), include whiskers that either encompass the remaining data points or extend up to 1.5 times the IQS, and finally show any outliers that exist beyond the whisker (circles). In each subfigure there are three boxplots — from left to right these are: the difference of the offset AGN sample with matched AGN host galaxies, the difference of the dual AGN sample with matched AGN host galaxies, and the difference of the dual AGN sample with matched offset AGN systems. Note that both the offset and dual AGN sample lie slightly above 0 when compared to matched AGN host galaxies (and when examining dual AGN in comparison to offset AGN), indicating a slight enhancement of SFR, $L_{\rm AGN}$, and $N_{\rm H}$. Further, we see a more significant enhancement of $L_{\rm AGN}$ in the dual AGN sample, but not statistically above a factor of 2.

explore some environmental factors that may be responsible in Section 4.3.

We also find that offset AGN galaxies have $L_{\rm AGN}$ values nearly equal to those of matched non-merging AGN host galaxies. This is somewhat surprising as both SFR and N_H are enhanced in these systems, and one would expect AGN luminosity to trend similarly as it is thought that similar processes affect all three of these in merging systems, as discussed in Section 4.1. Rather, dual AGN systems have significantly higher median luminosities in comparison to non-merging AGN host galaxies — well above even the expected factor of 2 (as the stated values of $L_{\rm AGN}$ encompass both AGN in the system, see Stemo et al. 2020). In fact, the AGN luminosities of the dual AGN systems in comparison to non-merging AGN hosts and offset AGN only barely overlap with 0, telling us that dual AGN systems have AGN luminosities greater than almost all other AGN host systems with similar galaxy mass and at similar redshift.

This is a significant finding as theoretical predictions find that the most luminous AGN should be associated with mergers (Hopkins and Hernquist, 2009; Treister et al., 2012), while some observational studies have not found this (Kocevski et al., 2012; Villforth et al., 2014). Why we are in agreement with these theoretical predictions while other observational works are not may be explained by inherent differences in the AGN host merger population and the limits of previous works. First, we find that dual AGN systems host the most luminous AGN when matched in galaxy mass and redshift, while offset AGN systems are not significantly enhanced in comparison to non-mergers, Second, we find that there are many more offset AGN than dual AGN found at these separations using modern observational techniques (103 and 10, respectively, in our samples). Therefore, observational studies that do not (or cannot) separate their AGN host merger sample into dual and offset AGN subsamples, may have findings dominated by the offset AGN population, which does not appear to host AGN with significantly higher AGN luminosity values than matched non-merging systems.

4.3 Results

When examining offset and dual AGN, the most influential merger parameters related to SMBH – galaxy coevolution are believed to be the merger mass ratio and the separation, which acts as an indicator of merger stage (i.e. the smaller the separation, the further into the merger the system is). As was discussed at the beginning of this letter, many works have found that dual AGN are more likely to be found in major mergers (e.g. Volonteri et al., 2003; Hopkins et al., 2005; Ellison et al., 2008; Comerford et al., 2015; Steinborn et al., 2016; Barrows et al., 2017a) and that AGN fraction increases as the separation decreases (Ellison et al., 2011; Van Wassenhove et al., 2012; Koss et al., 2012; Blecha et al., 2013; Barrows et al., 2017a; Capelo et al., 2017; Foord et al., 2020), but these works have limited samples at small separations. Therefore, using the largest samples of offset and dual AGN found systematically in a single work to-date, we examine how the merger mass ratio of a merger affects the prevalence of offset and dual AGN (Section 4.3.1), and how merger stage (via SMBH separation) impacts the presence of offset and dual AGN (Section 4.3.2).

When analyzing our samples of dual and offset AGN in this section, we will include corrections stemming from the merger selection process of Stemo et al. (2021). These corrections are derived from a large Monte Carlo bias estimation and error correction process meant to correct for selection effects stemming from biases against identifying small separation and large merger mass ratio mergers. See Stemo et al. (2021) for an in-depth discussion of this process.

4.3.1 Dual AGN Prefer the Most Major Mergers

When examining offset and dual AGN presence in relation to merger parameters, the AGN fraction as a function of merger mass ratio is often studied. Stemo et al. (2021) found that the AGN fraction of the systems in the ACS-AGN Merger Catalog followed a Log_2 relation with merger mass ratio. That is, AGN fraction was highest for the smallest (most major) merger mass ratio, and then decreased linearly as merger mass ratio increased in powers of 2, up to a cutoff of merger

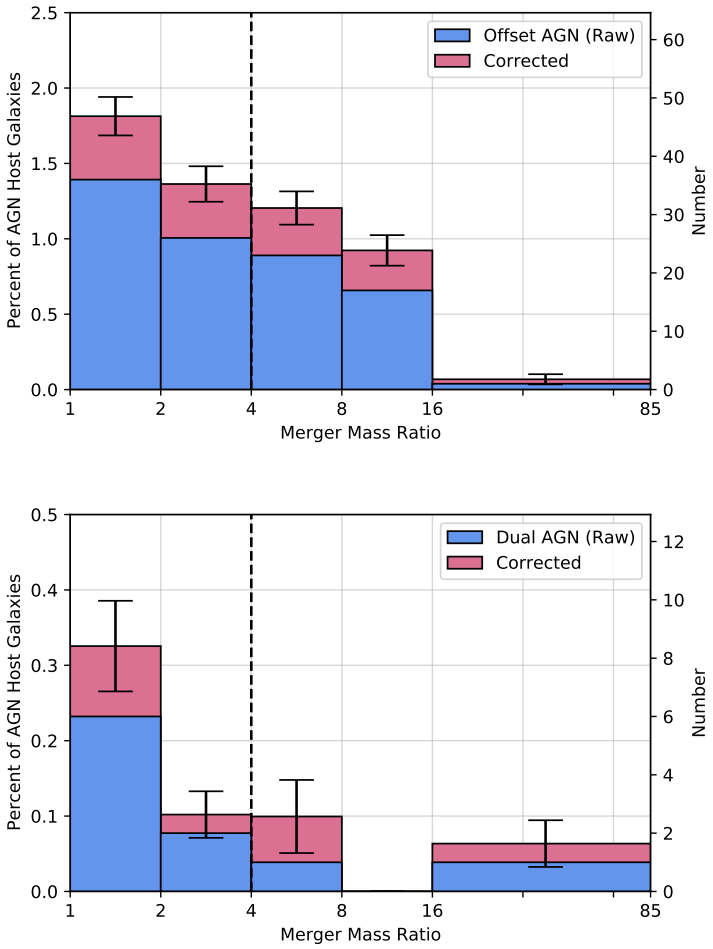

Figure 4.2: Histogram of percentage of AGNs in mergers as a function of merger mass ratio; raw numbers are reported in addition to the bias corrected values (see Stemo et al. 2021 for further information). Note that the scale for the merger mass ratio axis is Log_2, and that the last bin spans merger mass ratio values from 16 to 85 due to the small number of galaxies in that range. The dashed vertical line at merger mass ratio = 4 separates major mergers to the left and minor mergers to the right. We find that while the offset AGN sample closely follows the trend of the overall merger sample found in Stemo et al. (2021), the dual AGN sample is found predominantly in the most major of mergers and is equally less likely (within error) beyond merger mass ratios of 2.

mass ratio of 16 where the number of AGN host mergers decreased to near-zero.

We find a similar trend for our sample of offset AGN (see Figure 4.2, top); the fraction of offset AGN also follows a Log_2 relation, albeit at a shallower slope than that of the full ACS-AGN Merger Catalog. However, when examining the fraction of dual AGN as a function of merger mass ratio (Figure 4.2, bottom), we find a very different relation to that of the ACS-AGN Merger Catalog. While the AGN fraction of the ACS-AGN Merger sample and the offset AGN sample both peaked at merger mass ratios near unity and slowly decreased, the dual AGN sample seems to show a much stronger preference for the most major of mergers (merger mass ratios from 1 – 2). Outside of this small window, the fraction of dual AGN plummets to a third of its peak value and remains relatively unchanged, within error, out to the most minor of mergers.

These findings are in agreement with the general trends predicted by Volonteri et al. (2003); Hopkins et al. (2005); Steinborn et al. (2016) and observational studies by Ellison et al. (2008); Comerford et al. (2015); Barrows et al. (2017a), that dual AGN are preferentially found in major mergers. Further this work builds on those by showing that not only are dual AGN preferentially found in the most major of mergers (mass ratio < 2), but also that while offset AGN prefer major mergers as well, they do not see as sharp of a decline when moving into the minor regime.

4.3.2 As a Population, Offset AGN Transition to Dual AGN at Small Separations

Theory predicts SMBH growth peaks at separations under 10 kpc (e.g. Van Wassenhove et al., 2012; Blecha et al., 2013; Capelo et al., 2017), and as SMBH growth increases, AGN activation should increase. With that, past observational work has found that AGN activation does in fact increase as separation decreases, but these studies have not been able to fully constrain the relation below 10 kpc due to the limited number of systems in their samples at small separations (Ellison et al., 2011; Koss et al., 2012; Barrows et al., 2017a; Foord et al., 2020). Stemo et al. (2021) was able to confirm this trend down to separations of 2 kpc, with AGN activation increasing as separation decreased from 10 – 2 kpc. But, they were not able to independently analyze offset and dual AGN systems in order to examine whether intra-system AGN activation increased as separation

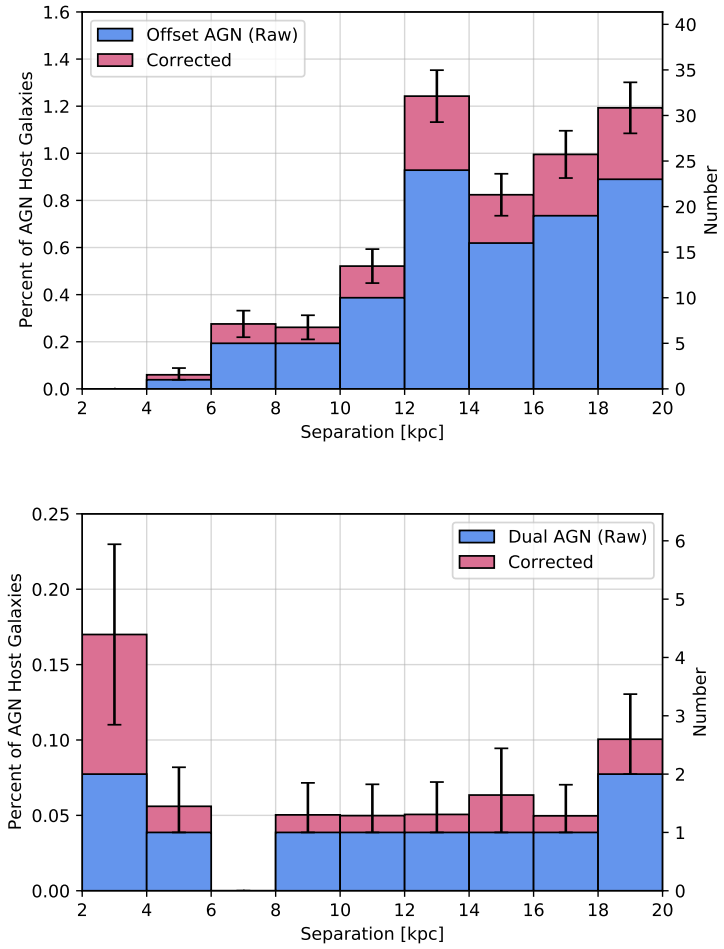

Figure 4.3: Histogram of percentage of AGNs in mergers as a function of SMBH separation; raw numbers are reported as well as bias corrected values (see Stemo et al. 2021 for further information). We find that the offset AGN sample generally follows the trends of the overall merger sample found in Stemo et al. (2021) until separations of ∼5 kpc, where they rapidly drop off to zero. In contrast, we find that dual AGNs are found roughly equally at all separations until the smallest separations, where they quickly increase in number. This may point towards a transition from offset AGN to dual AGN as mergers progress to smaller separations.

decreased (i.e. a shift from offset to dual AGN as separation decreased), as is predicted in the simulations of Van Wassenhove et al. (2012) and Blecha et al. (2013).

The large sample size of our offset and dual AGN samples allows us to address this specific question. Examining the offset AGN fraction as a function of separation (Figure 4.3, top), we find that it generally decreases as separation decreases, except for a noticeable bump near 13 kpc which is thought to be associated with increased activation due to first pericenter passage (Stemo et al., 2021), and then drops to 0 near $\sim$5 kpc. This is slightly different than the trend Stemo et al. (2021) found for the overall AGN host merger population of the ACS-AGN Merger Catalog. They found that AGN activation was mostly flat from 20 – 10 kpc, except for the first pericenter passage bump, then decreased from 10 – 4 kpc before increasing sharply as separation decreased down to 2 kpc. The most prominent difference is the decrease to near zero at $\sim$5 kpc, instead of a sharp increase at the smallest separations. Similar to the trends related to merger mass ratio discussed above, this difference can be accounted for when examining the dual AGN sample.

The dual AGN fraction as a function of separation (Figure 4.3, bottom) is very different than that of offset AGN and the overall ACS-AGN Merger sample. We find that the dual AGN fraction is relatively flat as separation decreases from 20 kpc to the very smallest separations, where we see it increase by a factor of 3 in the 4 – 2 kpc bin. This tells us that while dual AGN can be found at all separations in this merger phase, they see a strong increase in fraction at the smallest separations. While previous works tracked general AGN activation trends, we are able to see a more nuanced picture of AGN activation in mergers. Specifically, we show that dual AGN fraction peaks as offset AGN fraction reaches a minimum, both at the smallest separations. This is strong evidence that supports the hypothesis that not only does AGN fraction increase as separation decreases in mergers, but also that offset AGN transition to dual AGN as the merger progresses to the smallest separations. This confirms theoretical predictions by Van Wassenhove et al. (2012) and Blecha et al. (2013), and is the strongest observational evidence for this aspect of SMBH – galaxy coevolution to date.

4.4 Conclusions

In this letter we have detailed the identification and analysis of 10 dual AGN and 103 offset AGN in late-stage galaxy mergers with SMBH separations <20 kpc. These samples were selected from the ACS-AGN Merger Catalog through analysis of *Chandra* observations using the Bayesian analysis tool `BAYMAX`. We have analyzed these samples and our main findings are summarized below:

(1) We find that dual AGN systems have AGN luminosity values that are significantly higher than those of non-merging AGN host galaxies matched in galaxy mass and redshift, as well as similarly matched offset AGN systems; we do not find this for offset AGN systems matched with non-merging AGN host galaxies. We also find that both dual and offset AGN systems have SFR and nuclear column density values that are, on average, slightly elevated above matched non-merging AGN host galaxies, and in the case of dual AGN, matched offset AGN systems as well.

(2) We find that dual AGN strongly prefer the most major of mergers, with the dual AGN fraction peaking at merger mass ratios <2, before falling to a third of the peak value and remaining unchanged out to the most minor of mergers. We also find that the offset AGN fraction follows a Log_2 relation in merger mass ratio, slowly decreasing down to merger mass ratios of 16.

(3) We find that dual AGN systems are preferentially found at the smallest separations, while offset AGN systems are preferentially found at larger separations. Specifically, we find that the offset AGN fraction decreases as separation decreases from 20 kpc to ∼5 kpc, where it then drops to near-zero; this is in contrast with the dual AGN fraction, which is largely flat until the smallest separations (4 – 2 kpc), where it then increases by a factor of 3.

These findings show that the presence of dual AGN and offset AGN is very sensitive to the merger environment. While offset AGN are only mildly sensitive to merger mass ratios <16, dual AGN are very sensitive, and strongly prefer the most major of mergers. Further, the trends of offset

AGN fraction and dual AGN fraction as functions of separation seems to strongly indicate that, as a population, offset AGN transition to dual AGN as mergers progress to the smallest separations.

Acknowledgments

Support for this work was provided by NASA's Astrophysics Data Analysis program, grant number NNX15AI69G, the CU Boulder / JPL Strategic University Research Partnership program, the National Science Foundation's Graduate Research Fellowship program, and a Chance Irick Cooke Fellowship. The work of DS was carried out at the Jet Propulsion Laboratory, California Institute of Technology, under a contract with NASA. RJA was supported by FONDECYT grant number 1191124. This work utilized the RMACC Summit supercomputer, which is supported by the National Science Foundation (awards ACI-1532235 and ACI-1532236), the University of Colorado Boulder, and Colorado State University. The Summit supercomputer is a joint effort of the University of Colorado Boulder and Colorado State University.

Chapter 5

How to Expand Our Understanding of the Coevolution of AGN and Their Host Galaxies

Preface

In this chapter I wish to discuss and briefly outline a couple of projects that I consider very promising as future research paths. The first of these is directly related to the previous chapter, and is focused on expanding the number of dual and offset AGN systems known at separations under 10 kpc. While 10 dual and 103 offset AGN systems were identified and studied with SMBH separations under 20 kpc in Chapter 4, due to the limitations of current *Chandra* observations, only 4 dual AGN and 11 offset AGN were found at separations under 10 kpc, the phase thought to be where AGN activity and star formation peaks. Therefore, a quick and useful follow-up project would be to obtain new *Chandra* observations of systems with separations <10 kpc in order to increase the sample sizes in that regime and enable us to answer relevant science questions with statistical confidence.

The second project is much more ambitious, but also has the potential to be very impactful to the field. As observational astronomy moves towards larger and deeper surveys (e.g. Hyper Suprime-Cam (HSC), Vera Rubin Observatory (VRO)), astronomers will be inundated with petabytes of survey data. In order to analyze these data in a timely and effective manner, a shift to machine learning may be necessary. Through the use of machine learning techniques, I estimate that over 4000 AGN in mergers at separations under 15 kpc could be identified in current HSC data, and over 60,000 in VRO data when its survey mission is complete. This could allows us to answer key questions related to AGN – host galaxy coevolution with unrivaled statistical accuracy.

5.1 Using New On-Axis *Chandra* Observations to Find Dual AGN in Late-Stage Mergers

5.1.1 Introduction

Understanding how and when supermassive black holes (SMBHs) grow with their host galaxies is a central problem in the study of galaxy evolution. Observations suggest that major galaxy mergers are effective mechanisms for triggering accretion onto SMBHs and hence active galactic nuclei (AGN; e.g. Sanders et al., 1988; Canalizo and Stockton, 2001; Glikman et al., 2015), but the role of mergers in SMBH – galaxy coevolution is unclear. Many works suggest that secular processes or minor mergers may be the dominant routes of SMBH growth (e.g. Kocevski et al., 2012; Simmons et al., 2012; Villforth et al., 2017). However, recent numerical simulations have suggested a more nuanced picture in which major galaxy mergers play a significant role under certain conditions (e.g. Van Wassenhove et al., 2012; Capelo et al., 2015; Steinborn et al., 2016; Capelo et al., 2017).

Moreover, while observations have shown that the fraction of AGN in mergers increases toward small galaxy pair separations (e.g. Ellison et al., 2011; Koss et al., 2012; Satyapal et al., 2014; Stemo et al., 2021), the distinction between how this evolution affects the growth of one versus both SMBHs (offset AGN versus dual AGN) has yet to be definitively made. In particular, simulations predict that dual AGN are more common than offset AGN by a factor of 2 or 3 at small nuclear separations (Van Wassenhove et al., 2012; Steinborn et al., 2016; Capelo et al., 2017). This numerical prediction is also consistent with a transition from single to dual AGN triggering as a merger progresses toward smaller pair separations, such as the trend seen at in Chapter 4.

To understand how galaxy mergers build up SMBH mass, we also require a clear picture of which SMBH is growing the fastest or the most efficiently. While several independent simulations have made specific predictions about which SMBH in a galaxy merger has the highest Eddington ratio, there is currently no consensus. For example, numerical work from Capelo et al. (2015)

predicts that the more massive SMBH grows faster than the less massive SMBH in major mergers. On the other hand, simulations from Steinborn et al. (2016) predict that in dual AGN systems the less massive SMBH grows more efficiently and that in offset AGN systems the more massive SMBH grows more efficiently. Testing these numerical predictions is a fundamental step toward forming a comprehensive picture of SMBH-galaxy co-evolution. However, previous studies of dual and offset AGN have suffered from limited samples and nonuniform methods, prohibiting a systematic analysis of the triggering mechanisms for each sample.

5.1.2 How To Build Upon Previous Work

A large, uniformly selected sample of mergers in which each SMBH is observationally determined to be either quiescent or active is needed to address these questions. The first piece of this is currently available: the Advanced Camera for Surveys AGN (ACS-AGN) Merger Catalog (see Chapter 3 and Stemo et al. 2021) consists of 204 AGN host galaxies in late-stage mergers imaged by the *Hubble Space Telescope* (*HST*) at $0.2 < z < 2.5$ and includes crucial galaxy properties, such as AGN luminosity, galaxy mass, star formation rate, SMBH separation, and merger mass ratio. The second requirement is high resolution X-ray observations of these systems in order to classify them as offset (single AGN) or dual AGN mergers.

Since simulations predict that the peak of AGN activation and growth in mergers occurs at SMBH separations <10 kpc (e.g. Hopkins et al., 2008; Hopkins and Hernquist, 2009), we need to spatially resolve AGN at these small separations in order to understand SMBH – galaxy coevolution in mergers. Even at moderate redshift ranges, resolving these separations requires high resolution X-ray or radio data. However, with only ∼10% of AGN being radio-loud (Müller-Sánchez et al., 2015), X-ray observations are the most complete approach. The excellent angular resolution of the *Chandra X-ray Observatory* is ideal for identifying and studying AGN in SMBH pairs at small separations during galaxy mergers, and no other X-ray telescope has the ability to do so for this sample.

Of the 204 mergers hosting AGN in the ACS-AGN Merger Catalog, archival *Chandra* ob-

servations show that 49 host at least one X-ray AGN (using a luminosity cutoff of 10^{42} erg/s in the 2–10 keV band) in a SMBH pair at separations <10 kpc. However, due to the high redshifts, small SMBH separations, and the point spread function (PSF) of the existing (off-axis) *Chandra* observations, previous work has only been able to confirm 4 dual AGN and 11 offset AGN from this sample (see Chapter 4). This is statistically insufficient to answer open science questions related to AGN – galaxy coevolution at these separations. An ideal solution would be to build a sample combining these 15 dual and offset AGN systems at separations <10 kpc, with new on-axis *Chandra* observations for 8 other candidate systems. This sample would enable us to answer, with unprecedented statistical significance, open questions related to the triggering and growth of offset and dual AGN in mergers.

5.1.2.1 Archival Sample Selection

To reiterate, a readily available sample could be drawn from the offset and dual AGN candidates selected and identified in the ACS-AGN Merger Catalog, as it provides a large and reliable sample of uniformly selected offset and dual AGN candidates observed in the AEGIS, GOODS, GEMS, and COSMOS fields by *HST* at $0.2 < z < 2.5$ with separations <10 kpc. To build our AGN sample in Stemo et al. (2021), we selected 1945 active galaxies using data from the *Chandra* Source Catalog (CSC) 2.0 (Evans et al., 2020), with the criterion $L_{2-10\mathrm{keV}} > 10^{42}$ erg s^{-1}. We also measured galaxy properties (e.g. SFR, galaxy mass, etc.) from SEDs constructed using multi-wavelength photometric data (see Stemo et al. 2020 for further information on methods).

Finally, we selected our offset and dual AGN candidates as AGN host galaxies that displayed two stellar bulges (each associated with a SMBH) with separations <20 kpc in *HST* I-band imaging, as determined by multi-component galaxy morphological modeling using `GALFIT`. In addition, our models allowed them to calculate a luminosity ratio between the stellar bulges, which was used as a proxy for the merger mass ratio.

But, in order to address pertinent science questions using *Chandra*, we can only study offset and dual AGN candidates that are separated by more than the *Chandra* spatial resolution limit, so

Target Name	Red-shift (z)	Merger Mass Ratio	Bulge Sep.[a]	Current 68% ECF PSF[a]	Off Axis Angle[b]	Count Rate[c]	Exp Time [ks]
2CXO J095810.2+022232	0.9	2.2	1.1 (8.6)	1.5 (12)	4.1	0.6	30
2CXO J095839.0+014455	0.8	1.5	1.1 (8.9)	1.7 (14)	4.6	0.9	20
2CXO J100043.1+020637	0.4	1.2	0.6 (2.7)	1.2 (5)	3.4	2.3	10
2CXO J100201.5+020329	0.6	4.0	0.8 (5.4)	1.0 (7)	3.0	0.5	40
2CXO J100209.4+015225	0.7	1.4	0.7 (5.1)	2.0 (15)	4.8	2.0	15
2CXO J100216.3+015008	0.6	1.7	0.9 (6.2)	1.1 (8)	3.1	0.4	35
2CXO J100227.9+023258	1.0	1.1	1.2 (9.9)	1.9 (16)	4.4	0.6	20
2CXO J100241.7+013549	0.7	1.2	0.8 (5.4)	5.9 (40)	8.7	2.5	15

Table 1: [a] In units of arcsec (kpc)
[b] In units of arcmin
[c] 0.5-7 keV count rate in units of 10^{-3} photons s^{-1}

that two X-ray AGN can be resolved. Of the 49 X-ray offset and dual AGN candidates with SMBH separations under 10 kpc in the ACS-AGN Merger Catalog, only 15 have *Chandra* observations with PSF values smaller than their SMBH separations. For these 15, we were already able to parameterize them as either dual or offset AGN systems (see Chapter 4).

5.1.2.2 New *Chandra* Observations Are Needed

AGN host galaxies in late-stage mergers are rare. The available sample (N=15) of mergers at separations <10 kpc classifiable as either offset or dual AGN as described above is not sufficient to address science questions related to AGN triggering and growth in late-stage mergers with statistical significance.

While the work described in Chapter 4 is sufficient for studies of dual and offset AGN out to SMBH separations of 20 kpc, this approach finds very few systems at small separations when the *Chandra* PSF is too large due to off-axis observations. This is the case for most of remaining 34 offset and dual AGN candidates in the ACS-AGN Merger Catalog with separations under 10 kpc. However, on-axis *Chandra* observations would have 68% ECF PSFs (∼0.5 arcsec) smaller than the bulge separations of 18 of them, which would allow us to distinguish between the offset and dual AGN scenarios in these cases.

Therefore, in order to address open questions related to SMBH growth and galaxy coevolution

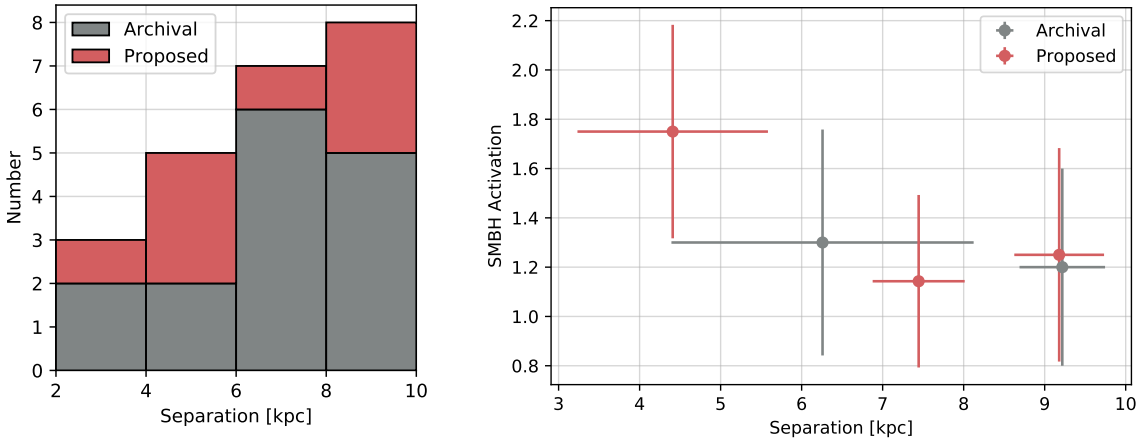

Figure 5.1: Left: Histogram of a possible final sample, consisting of the 4 dual and 11 offset AGN systems discussed in Chapter 4 and 8 new *Chandra* targets (red); the proposed sample would enable examination at lower separations than ever before. Right: Example of a possible examination of dual AGN fraction evolution (Section 5.1.3); while the known sample of 15 systems (gray) is not sufficient to find any significant correlation at separations under 10 kpc, the full possible sample (red) could find a correlation with significance of 3σ.

in mergers, new, on-axis observations of 8 offset and dual AGN candidate galaxies with bulge separations <10 kpc would be ideal (Table 5.1.2.1). These observations would provide the needed angular resolution and signal-to-noise levels to resolve each bulge and determine which host an AGN and classify them as either an offset or dual AGN. These systems would span the parameter space required to address the science questions outlined below (e.g. Figure 5.1, left), as well as have 0.5–7 keV count rates that provide sufficient signal-to-noise observations in reasonable observation times. The exposure times listed in Table 5.1.2.1 would be sufficient to determine whether each system is an offset or dual AGN at the $>3\sigma$ level.

5.1.3 Science Questions That Could Be Addressed

The new observations discussed here would increase the sample sizes of dual and offset AGN with SMBH separations under 10 kpc seen in Chapter 4 by 50%, and could more than double the dual AGN sample size as dual AGN are expected to dominate at the smallest separations. These samples could allow for an examination of prominent outstanding questions in the field of AGN – galaxy coevolution with unprecedented statistical significance. Below, I briefly discuss two such

science questions.

5.1.3.1 How Does Separation Affect the Dual AGN Fraction in Galaxy Mergers?

Simulations have predicted that the instantaneous SMBH growth rate increases below SMBH pair separations of 20 kpc, peaking at separations <10 kpc (Van Wassenhove et al., 2012; Blecha et al., 2013; Steinborn et al., 2016). This peak in SMBH growth should coincide with increased AGN activation. Observations have shown that the AGN fraction does indeed increase as the separation between two SMBHs in merging galaxies decreases from 100 kpc to 10 kpc (Ellison et al., 2011; Koss et al., 2012; Stemo et al., 2021), but the trend is not yet strongly shown at smaller separations because of the limited number of AGN currently known in <10 kpc separation SMBH pairs. Analysis of the full sample of 23 systems discussed here could prove that the dual AGN fraction increases as SMBH pair separation decreases below 10 kpc at the 3σ level. This estimate is based on preliminary investigations of the known sample (Chapter 4) and hypothesized classifications of the proposed targets based on dual fraction estimates from previous work by Steinborn et al. (2016), Capelo et al. (2017), and the work outlined in Chapter 4. Figure 1 (Right) shows this possibility, including both the known sample and new observations of the possible targets (red), in comparison to analysis of only the known sample (gray). As can be seen, the inclusion of new observations would allow an underlying trend to be seen if predictions from simulations are correct.

5.1.3.2 Where Does the Most Efficient SMBH Growth Occur in Galaxy Mergers?

The physical conditions that lead to accretion onto SMBHs are poorly understood. In particular, it is currently unclear if accretion occurs more efficiently onto the SMBH in the more or less massive merger component (Steinborn et al., 2016; Capelo et al., 2017). Additionally, numerical results suggest that the location of the most efficient SMBH growth evolves with the merger itself, transitioning from the less massive to more massive component (Van Wassenhove et al., 2012). Putting constraints on this process is fundamental to both our understanding of the growth tracks

of SMBHs and for informing cosmological simulations of hierarchical growth. `BAYMAX` enables us to estimate the X-ray flux ratio between two X-ray sources, allowing us to properly measure the X-ray luminosity of both when combined with known system X-ray luminosities. Therefore, with new observations we could confirm or deny the predictions of Van Wassenhove et al. (2012) that AGN efficiency transitions with merger stage with unprecedented statistical significance.

5.2 Understanding AGN and Star Formation Triggering During Mergers Using Machine Learning

5.2.1 Introduction

We know that SMBHs and their host galaxies must coevolve in order to result in the tight correlations seen between them (e.g. the $M_{BH} - \sigma$ relation, see Heckman and Best 2014 for a review); however, one of the mysteries of astrophysics today is understanding how that coevolution takes place. Galaxy mergers are known to be key events in the evolution of not only galaxies, but also their SMBHs, and may be the mechanism that connects their evolution. During galaxy mergers, gas is disturbed and driven inwards; these inflows can trigger both star formation and cause the SMBH to become visible as an AGN (Begelman et al., 1980). These inflows are typically so significant that theory predicts that merger events are periods of peak star formation and AGN activity for a galaxy (Springel et al., 2005; Hopkins and Hernquist, 2009; Van Wassenhove et al., 2012; Blecha et al., 2013).

However, there is still disagreement in observational works as to whether AGN activity and star formation rates (SFRs) are correlated in mergers, whether AGN are preferentially found in galaxy mergers, and whether AGN in mergers can shut down star formation in their host galaxies effectively (Canalizo and Stockton, 2001; Dunlop et al., 2003; Cisternas et al., 2011; Villar-Martín et al., 2011; Ellison et al., 2016a; Stemo et al., 2021). These disagreements may lie in the fact that SFR and AGN luminosity are predicted to evolve throughout the merger event (Cox et al., 2008; Hopkins et al., 2008; Torrey et al., 2012; Hopkins et al., 2013; Moreno et al., 2015, 2019). Specifically, previous work has shown that AGN and host galaxy properties, especially AGN activation, can vary significantly in mergers with bulge separations under 20 kpc (Stemo et al., 2021). Understanding the evolution of these properties throughout the stages of a merger event is crucial in understanding the coevolution of SMBHs and their host galaxies. Therefore, being able to observationally select and differentiate mergers by stage is key in exploring the processes and timeline of SMBH – galaxy

coevolution in mergers.

Obtaining a large, clean sample of galaxies spanning all the stages of merging with which we can examine this evolution is a very challenging observational task however, and many different approaches to identifying mergers in observational data have been attempted. Mergers can be selected visually based on morphological features such as tidal tails, streams, and nearby companions (e.g. Darg et al., 2010; Kartaltepe et al., 2015; Simmons et al., 2017); however, this method is subjective and can be inaccurate at coarse resolutions and at low surface-brightnesses. Other methods try to use morphological parameters and criteria in order to avoid having to examine each system by eye. These methods focus on using measures such as asymmetry and concentration (e.g. Conselice, 2003; Lotz et al., 2004; Pawlik et al., 2016; Rodriguez-Gomez et al., 2019). These methods can be faster and less subjective than visual inspection, but the criteria are based on observations and can therefore be limited by observational biases. A better solution to this is to use these same morphological parameters, but use simulation data instead of observational data to create criteria for assigning galaxy morphologies (e.g. Lotz et al., 2008, 2010a,b; Nevin et al., 2019).

However, the most robust and unbiased approach is not automating the identification of mergers through the use of classic merger predictor criteria, but rather automating the creation of the merger predictors themselves. This is what some machine learning does; specifically, this is what a convolutional neural network (CNN) does. Given a sufficient amount of "training" data, a CNN can accurately classify mergers by stage, and the accuracy of these classifications is quantifiable (see Section 5.2.2.2). The use of CNNs in galaxy morphology classification has been rapidly gaining use in the last five years or so (e.g. Huertas-Company et al., 2015; Ackermann et al., 2018; Nelson et al., 2018; Huertas-Company et al., 2019; Rodriguez-Gomez et al., 2019; Snyder et al., 2019).

By training CNNs with simulation data that have been modified to look observationally realistic, we can identify mergers in large surveys and classify them by stage quickly and accurately. Some preliminary success has been achieved in using simulation snapshots from the original Illustris simulations to create mock *HST* and *JSWT* images that were then used to train a CNN for merger identification (Snyder et al., 2019). Still other work has used a random forest technique, another

machine learning approach, to identify mergers in a subsection of the Hyper Suprime-Cam (HSC) wide field and study AGN growth in mergers (Goulding et al., 2018).

As shown in previous chapters, much of my work has focused on understanding SMBH – galaxy coevolution. Therefore, an ideal future project would be to build on my previous works and those of others by training a merger identification CNN on mock HSC images, and later mock Vera Rubin Observatory (VRO) images, of galaxies from the IllustrisTNG simulations (Nelson et al., 2019). A CNN can be used to identify mergers and classify by them by stage in the complete HSC wide survey field, and then initial VRO data. IllustrisTNG is the 'next generation' of the Illustris simulations, and its main improvements are: it includes new physics that improve the modeling of, e.g., star formation, black hole accretion, and feedback; it reproduces known observational results better than the original Illustris; and it has higher spatial resolution than the original Illustris (Nelson et al., 2019). The medium resolution simulation, IllustrisTNG100, is ideal because its median resolution meets or exceeds that of HSC and VRO imaging. The choice of the HSC wide and VRO surveys are perfect for this approach because the large areas (1400 and 18,000 deg^2, respectively), moderate depths ($\sim$26 mag), and sub-arcsecond resolutions ($\sim$0.5 arcsec) of these surveys would yield very large and detailed samples of galaxy mergers. These samples, once refined into sub-samples by merger stage, would be perfect to address open questions regarding the timing of AGN activity and star formation in mergers, such as: what is the timeline for AGN and star formation triggering in mergers?

5.2.2 Using Machine Learning Techniques to Identify Mergers in HSC and VRO Data

Machine learning in its most simple form is just an algorithm that can 'learn' from data. Typically this involves an iterative process where the algorithm self adjusts in order to minimize some predetermined metric. CNNs are a type of machine learning algorithm. They are a form of supervised learning, meaning that they need to know some ground truth. In this case, it means that the known merger stage classification data must be in included in the training set; this can be

thought of as pointing the algorithm toward what we want it to focus on. But more importantly, CNNs are a form of deep learning, meaning that they extract the most important information needed to correctly minimize the metric themselves. This means that CNNs are very powerful and highly accurate, but also that they need significant amounts of training data; luckily the use of IllustrisTNG can provide a large and diverse training set, more than sufficient to train a CNN.

While a small aspect of this work could include evaluating and comparing a CNN approach to other approaches (e.g. Goulding et al., 2018), the primary goal would be to understand the timing and environment of AGN growth and star formation in galaxy mergers. The key to accomplishing this is creating a large, diverse, and observationally realistic set of galaxy mergers in order to train a CNN to identify and classify mergers in observational data quickly and accurately. This Section will explain how we can accomplish this. I will discuss how to create observationally realistic galaxy mergers from simulation data (Section 5.2.2.1), use it to train a CNN (Section 5.2.2.2), and then apply the CNN to HSC data, and later VRO data (Section 5.2.2.3), in order to create a large sample of mergers and non-mergers to answer the science question. Then, I discuss how to identify AGN using MIR selection techniques, how to create SEDs for the sample galaxies, and how to estimate AGN and host galaxy properties for the sample galaxies in Section 5.2.2.4. Throughout this Section I will primarily discuss the application of these techniques to HSC data, as it is already available to be analyzed, but please note that this process would be identical for VRO data with minor changes for filter and instrument differences.

5.2.2.1 Using IllustrisTNG Data to Create Observationally Realistic Training Sets

Unlike many other fields, it is very difficult in astrophysics to calibrate observed data to known truth. We see this problem arise when considering how to create a pure training sample for a CNN. There is no large, clean sample of uniformly selected merging systems available to use to train this proposed CNN. Therefore, we can instead use merging galaxies drawn from the highly realistic IllustrisTNG simulations to create a training set.

The IllustrisTNG cosmological simulations are ideal as they combine high resolutions, large

box sizes, and they have been shown to reliably reproduce properties of galaxy populations in the local Universe (Nelson et al., 2019). The IllustrisTNG simulations come in three size scales, 300, 100, and 50; these correspond to the box lengths in units of Mpc, and they also correspond to inversely related spatial resolutions. The TNG100 simulation is currently public and suits this project well, with the median spatial resolution of TNG100 ($\sim$350 pc) meeting or exceeding that of HSC and VRO observations at redshifts of $z > 0.025$. While IllustrisTNG has snapshots up to redshifts of 20, the depth and angular resolution of HSC and VRO limit the redshift range at which low surface brightness and late stage mergers can be detected. Therefore, we would only draw galaxies from the 60 snapshots that span simulated redshift ranges of $0.05 < z < 2$. While the exact number of galaxies and mergers in TNG100 changes as the simulation progresses through its redshift evolution, the number of galaxies with stellar masses $>10^{8.5} M_{\odot}$ is in the tens of thousands at low redshifts (Pillepich et al., 2018). This ensures that we would have a very large and diverse set of galaxies to train the CNN with.

The use of observationally realistic images when training CNNs is extremely important; one recent work found that CNNs trained on observationally realistic data had median overall performance values near 90%, while those trained on idealized images never exceed 60% (Bottrell et al., 2019). This means that in order to have an effective CNN, we need to create observationally realistic images from simulation data.

To create realistic galaxy images, we can first process the TNG100 galaxies through the dust radiative transfer code SKIRT (Baes et al., 2011), which has been applied to IllustrisTNG galaxies previously (e.g. Rodriguez-Gomez et al., 2015; Huertas-Company et al., 2019). Then, we can create mock rest-frame HSC images of the simulated galaxies with the five filters used in the HSC wide field (g, r, i, z, y). Luckily, we can follow a similar procedure as that in Nevin et al. (2019) to create realistic mock HSC images; specifically, convolve the raw broadband images with PSFs drawn from the HSC PSF map, re-bin to the correct instrument pixel scale, and add residual background noise typical appropriate to the filter. The results of using this procedure to simulate an *HST* image from a TNG50 galaxy can be seen in Figure 5.2 (image credit to Becky Nevin).

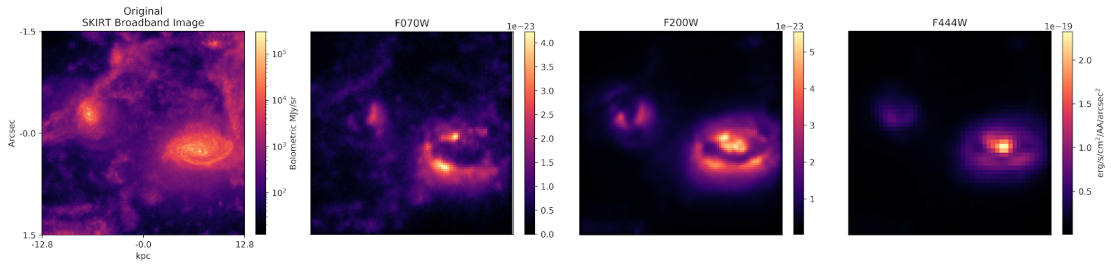

Figure 5.2: A broadband image of an early stage merger in TNG50 at $z = 2$ (left); (right) mock *HST* images created in different bands using the process outlined in Section 5.2.2.1 (image credit to Becky Nevin). This project would create similar mock images for the training of a galaxy merger classifying CNN, but they would be created for the HSC (and later VRO) filters and would be at marginally lower spatial resolutions.

The goal of this project would be to study AGN and star formation triggering by merger stage because AGN and host galaxy properties are known to vary significantly by across the lifetime of a merger (Cox et al., 2008; Hopkins et al., 2008; Torrey et al., 2012; Hopkins et al., 2013; Moreno et al., 2015, 2019; Stemo et al., 2021). Therefore, we would need to separate the training set into 5 subsets: isolated galaxies (galaxies not merging and have not merged within the last 0.5 Gyr), early stage mergers (projected stellar bulge separations from 15 – 40 kpc), intermediate stage mergers (projected stellar bulge separations from 5 – 15 kpc), late stage mergers (projected stellar bulge separations <5 kpc, but not yet coalesced), and post-coalescence mergers (galaxies ranging from coalescence to 0.5 Gyr post-coalescence). We can identify the merging systems using the IllustrisTNG merger trees and select isolated galaxies randomly to match the parameter space of the merging galaxies.

Since galaxy morphology classification can vary depending on redshift (e.g. Guo et al., 2015), it would be best to create 15 CNNs, each associated with multiple snapshots and redshift ranges of $\Delta z = 0.2$ or less, that span the full redshift range ($0.05 < z < 2$). This would ensure that even if the merger predictors shift across these redshift bins, the CNN remains accurate. Due to the large box size of TNG100, I estimate that we would produce training sets with N in the thousands for each redshift bin — ideal numbers for CNN training.

5.2.2.2 Training My CNN to Identify and Classify Mergers in Real Data

The heart of any neural network is the 'neurons'. These neurons exist in layers and the neurons and layers can be thought of as forming a matrix. Information is passed to the neurons by neurons from the previous layer, where that information is operated on and then passed forward. The convolutional part of CNN comes from the fact that the information passed forward is actually a convolution of the neurons before it. This technique has been shown to be very effective for analyzing and classifying images (e.g. Fukushima et al., 1980).

When using a CNN, the choice of layers and convolutions is important, but satisfactory arrangements are arrived at through testing. Previous works have explored this for galaxy morphology classifications (e.g. Huertas-Company et al., 2015, 2019; Bottrell et al., 2019). Therefore, an initial CNN architecture could be based on those works and slightly altered as needed in order to optimize the CNNs.

When one trains and optimizes a CNN, they can choose which metrics to prioritize. Common metrics used in machine learning are precision, recall, and accuracy; the first two are analogous to purity (aka 1-contamination) and completeness, while accuracy can be thought of as how well your CNN performs at correctly classifying things in general. Further, since these values are reported when running the algorithm, they allow us to calculate statistical errors and corrections to the classified datasets. This is very useful for understanding general trends in the data, e.g. merger fraction, as it allows for known errors and biases to be corrected for, while also providing quantifiable uncertainties to any findings.

Previous work has used a bootstrap method of machine learning training with great success (Goulding et al., 2018). A similar bootstrap method could be used here to create multiple training sets for each redshift and filter combination; the CNNs could then be trained on these bootstrapped sets. This would allow us to assign a probability to each classification when the CNNs are applied to real survey data.

5.2.2.3 Identifying Galaxy Mergers in Real Survey Data

After training this CNN, it could be applied to the HSC wide survey data, which is currently available in its entirety, and later to VRO data, in order identify mergers and create a merger stage sub-samples. These merger stage classifications could be assigned based on the probability measurements as described in Section 5.2.2.2. If the probability is above 50% (i.e. more than half of the bootstrapped CNNs assign that classification), the galaxy would be assigned that classification, otherwise the galaxy would not be given a classification nor included in any analysis.

Based on the size and depth of HSC, along with similar work using smaller regions of HSC surveys (Goulding et al., 2018), we could expect to find tens of thousands of mergers, and many more isolated galaxies, with exact numbers depending on depth limits put in place to ensure completeness. When these methods are applied to VRO data of similar depth as they become available, we could expect these numbers to increase by at least an order of magnitude, due to the increased survey area — possibly increasing them into the hundreds of thousands.

5.2.2.4 Selecting AGN Using *WISE* Color Cuts

We could then use mid-infrared (MIR) color cuts in order to select AGN in the sample. While no one wavelength regime is perfect at identifying all AGN (Alexander et al., 2008; Donley et al., 2008; Hickox et al., 2009; Juneau et al., 2011; Mendez et al., 2013; Goulding et al., 2014; Trump et al., 2015; Azadi et al., 2017; Stemo et al., 2020), MIR AGN selection techniques can detect luminous AGN, even in the presence of significant dust attenuation. This is because MIR techniques select for the signatures of a dusty torus re-emitting the higher energy light produced by the AGN's accretion disk or corona, and this reprocessed light is relatively unaffected by dust further from the AGN. MIR AGN selection techniques do tend to select higher luminosity AGN with lower host galaxy stellar masses and star formation rates (Stemo et al., 2020); but the bias is not extreme, and since it is known, it can be accounted for during analysis.

Many different MIR AGN selection techniques have been developed for *Spitzer* and *WISE*

observations (e.g. Lacy et al., 2004; Stern et al., 2005; Donley et al., 2012; Stern et al., 2012; Mateos et al., 2012). An excellent choice would be to follow previous work on identifying AGN in the HSC wide field (Goulding et al., 2018) and use *WISE* AGN selection criteria because *WISE* observations cover the entire HSC field. The longer wavelength bands of *WISE* are much less sensitive than the shorter wavelength bands. Therefore, where data in the necessary bands exist, we could use the three-band WISE color cut AGN selection criteria from Mateos et al. (2012) along with the single band *WISE* color cut from Stern et al. (2012) for those galaxies where data do not exist in the longer wavelength bands of *WISE*. Using this method, I estimate from previous work (Goulding et al., 2018; Stemo et al., 2020) that we could find approximately 30,000 AGN in the HSC wide field, with approximately 4000 of these being AGN in mergers with bulge separations under 15 kpc; this is more than an order of magnitude increase in the number of observed systems of this type (Stemo et al., 2020). Once VRO achieves similar depth to HSC, we could apply these techniques to the full VRO field and expect these numbers to increase by another order of magnitude, to an estimated 400,000 AGN identified and 60,000 in mergers with bulge separations under 15 kpc.

5.2.2.5 Selecting AGN and Estimating Galaxy Properties

In order to understand the interplay of AGN activity and star formation during mergers, one first needs to estimate the properties of the AGN and host galaxies in the sample. In order to do that, we can create SEDs for each galaxy in the sample that these properties can be estimated from. Following my previous work on creating SEDs as discussed in Chapter 2 and Stemo et al. (2020), we could use the Low-Resolution Template (LRT) SED fitting tool (Assef et al., 2010). LRT generates basic galaxy properties like stellar mass and star formation rate, with minimal input assumptions, while fitting galaxy and AGN SED templates simultaneously and obtaining basic galaxy properties with as few assumptions as possible.

LRT fits the rest-frame wavelength range 0.03 – 30 μm and uses a linear combination of three empirical galaxy templates (elliptical, spiral, and irregular; intergalactic medium absorption is included as a free parameter) and an AGN template that includes a freely varying extinction

term (E(B-V)$_{AGN}$) to account for nuclear obscuration. This simple combination of templates has been shown to provide very good fits for galaxies with and without AGN (e.g. Assef et al., 2010; Stemo et al., 2020). Therefore, we could construct SEDs with LRT from HSC photometry data (and/or VRO photometry as available) along with the *WISE* and *GALEX* photometry that exists for the HSC Wide field. These data cover the full rest-frame wavelength range that is explored by the SED models, for all of the proposed galaxy redshifts.

While LRT outputs the best-fit SED model for a galaxy, it does not provide errors on the best-fit parameters. For this, we could use an iterative approach to estimate errors using a Monte-Carlo process, where we resample the photometric data by drawing new values from a Gaussian distribution centered on the known value, with standard deviation equal to the associated flux error. A good practice would be to resample the photometric data 1000 times and refit the SED with LRT each time, in order to get errors on the galaxy properties derived from the SED fits (Stemo et al., 2020). Below are some galaxy properties that we could measure from the SED fits:

Redshift. Whenever spectroscopic redshifts are available, we could use them as inputs to the SED fitting procedure since the spectroscopic redshifts are generally more precise than photometric redshifts (e.g. Momcheva et al., 2016). Since the HSC wide field is so large, it includes many surveys with catalogs of spectroscopic redshifts (e.g. 3D-HST, zCOSMOS, VIPERS, GAMA, PRIMUS, etc.). Where spectroscopic redshifts are not available, we could use the photometric redshifts fit by LRT during the creation of the galaxy SED fits.

Galaxy Stellar Mass. Excluding the AGN component (if present) of each best-fit SED model, we could extract the g' and r' band magnitudes as well as the rest-frame luminosity in the r band, L_r. From those, one can estimate the galaxy stellar mass M using the relation between color and M/L_r from Bell et al. (2003).

Star Formation Rate. Excluding the AGN component (if present) of each best-fit SED model, we could extract the 2800 Å monochromatic luminosity and convert it to a SFR using the ultraviolet-based relation of Madau et al. (1998) and a Salpeter initial mass function. Since dust may affect measurements of ultraviolet luminosities, it would be best to compute dust cor-

rection terms for the ultraviolet fluxes based on the K-corrected slope $B - z$ (Daddi et al., 2007), where B and z are magnitudes from the SED model, and report the dust-corrected SFRs.

AGN Bolometric Luminosity. The AGN bolometric luminosity can be derived from the from the MIR luminosity or from the SED model. Both could be included for completeness. First, we could estimate the rest-frame 6 μm luminosity from the *WISE* data, convert it to a rest-frame 2 – 10 keV luminosity (Lanzuisi et al., 2009; Stern, 2015), and then convert that to a bolometric luminosity via Marconi et al. (2004). While, with the SED approach, one can simply integrate the unextincted AGN component of the best-fit SED model to estimate the AGN bolometric luminosity, as in Assef et al. (2011).

5.2.3 Addressing Open Science Questions

After completing all of these technical steps, we would have a sample that consist of tens of thousands of HSC galaxies (and later hundreds of thousands of VRO galaxies) at redshifts $0.05 < z < 2$, that would be subdivided into groups of early stage mergers, intermediate stage mergers, late stage mergers, post-coalescence mergers, and isolated galaxies. This would include approximately 30,000 AGN (400,000 in VRO), 4000 (60,000 in VRO) of which are AGN in mergers at separations <15 kpc. This would be very exciting as never before have galaxy mergers containing AGN been studied in these numbers. We could then use the full sample to explore the coevolution of SMHBs and their host galaxies during merger events and answer questions related to the timeline of AGN and star formation triggering in mergers.

Both AGN activity and star formation require a cold gas supply, and AGN feedback can regulate star formation, which suggests that AGN and star formation may be linked in galaxies. However, the observational studies are in disagreement: some find a correlation between AGN and SFR (e.g. Stemo et al., 2020; Mullaney et al., 2015; Shimizu et al., 2015) while others do not (e.g. Kartaltepe et al., 2015; Stanley et al., 2017). The reason for this observational tension may be that the correlation between AGN and SFR depends on whether the host galaxy is undergoing a merger, which can drive inflows of gas that boost both AGN luminosity and SFR (Ellison et al.,

2016b). Numerical simulations predict that SFR and AGN luminosity peak at different stages in a galaxy merger, with SFR peaking earlier in the merger and AGN luminosity peaking later in the merger (e.g. Capelo et al., 2015; Hopkins et al., 2008; Stickley and Canalizo, 2014; Volonteri et al., 2015b). While some observations have indeed shown SFR enhancements in early stage mergers (e.g. Ellison et al., 2008; Patton et al., 2013), observational tests in the late stage regime have been limited due to the challenge of identifying these late stage mergers. While I have created the largest observational study (N=204) of AGN activity and star formation in late stage mergers to date (Stemo et al., 2021), it is still insufficient to address some questions. The project outlined here would build and expand on that with successive order of magnitudes increase in sample size and could be the first observational study of the connection between AGN and SFR that examines these connections by merger stage from bulge separations of 40 kpc to down to post-coalescence.

To determine what the timeline for AGN and star formation triggering in mergers is, we could compare the SFRs and AGN luminosities of 1) early stage active mergers to early stage inactive mergers; 2) intermediate stage active mergers to intermediate stage inactive mergers; 3) late stage active mergers to late stage inactive mergers; 4) post-coalescence active mergers to post-coalescence inactive mergers; and 5) isolated active galaxies to isolated inactive galaxies. In each case, since SFRs and AGN luminosities are also dependent on host galaxy stellar mass and redshift, and it would be necessary to match the active galaxies and inactive galaxies in stellar mass and redshift. If we did find that SFRs peak in earlier stage mergers while AGN luminosities peak in later stage mergers when compared to matched systems, it would show that there is a connection between star formation and AGN in mergers, and that this connection has a temporal delay (e.g. Schawinski et al., 2009; Wild et al., 2010; Hopkins, 2012).

Chapter 6

Conclusions

Here I have presented a body of works focused on understanding the environmental factors that lead to AGN – galaxy coevolution and the correlations present therein, with a specific interest in these processes during late stage galaxy mergers.

I began this work by creating and analyzing the Advanced Camera for Surveys Active Galactic Nuclei (ACS-AGN) Catalog, which included 2585 active galactic nucleus (AGN) host galaxies at redshifts $0.2 < z < 2.5$ (Chapter 2). These AGN were selected using *Spitzer* and *Chandra* data along with well established AGN selection criteria. Since these AGN host systems were found in large survey fields, I then gathered multi-wavelength photometric data and constructed spectral energy distributions (SEDs) for these systems. Using these SEDs, I was able to derive multiple AGN and host galaxy properties. I then showed that AGN host galaxies tend to lie below the star-forming main sequence, which hints at the presence of negative feedback in AGN host galaxies that causes decreased star formation. I also found that there is a positive trend between star formation rate and AGN luminosity in AGN host galaxies, and that both are correlated with the stellar mass of their galaxies. This points towards an underlying link between the stellar mass, stellar growth, and SMBH growth in a galaxy.

In Chapter 3, I built upon my previous work by identifying systems in the ACS-AGN Catalog that were undergoing mergers through an iterative process of galaxy component modeling. This enabled me to create the ACS-AGN Merger Catalog, which included 204 uniformly selected offset and dual AGN with SMBH separations <20 kpc. Using this sample I was able to confirm predictions

that the AGN fraction peaks at SMBH pair separations <10 kpc; specifically, I found it increases significantly at separations under 4 kpc. I also found that AGNs in mergers are preferentially found in major mergers and that the fraction of AGNs found in mergers decreases as merger mass ratio increases in a log-linear fashion. Third, I found that, as a whole, mergers do not necessarily trigger the most luminous AGNs. Finally, I also found that nuclear column density, AGN luminosity, and host galaxy star formation rate are not correlated with merger parameters in these systems as a whole. However, this work studied both dual AGN and offset AGN as a combined population.

Therefore, in Chapter 4, I worked to isolate the subpopulations of dual AGN and offset AGN in order to study them separately. In total, I identified and analyzed 10 dual AGN and 103 offset AGN systems using the Bayesian analysis tool `BAYMAX` to verify single or dual X-ray AGN sources in their *Chandra* observations. Upon examination of these samples, I found that dual AGN systems host AGNs with luminosity values significantly higher than those found in matched non-merging AGN host galaxies as well as matched offset AGN systems matched. I also found that dual AGN systems strongly prefer the most major of mergers (merger mass ratios less than 2), while offset AGN systems only mildly prefer major mergers. Finally, I found that dual AGN systems are preferentially found at the smallest separations studied (between 2 and 4 kpc), while offset AGN systems are preferentially found at larger separations. I plan on finishing this work with a study of AGN luminosity as a function of relative merger component mass (i.e. testing whether the less massive galaxy component hosts the brighter AGN or vice versa), prior to its submission for publication.

Work that could build on this in the immediate future includes acquiring new *Chandra* observations of 8 X-ray AGN host systems in the ACS-AGN Merger Catalog with merger separations under 10 kpc (Chapter 5, Section 5.1). This would increase the number of known dual AGN and offset AGN in the ACS-AGN Merger Catalog at separations under 10 kpc by 50%, and could more than double the known number of dual AGN. The increase in sample size could enable for a much stronger statistical significance to be found for the trends hinted at in Chapter 4, and answer key questions such as: how separation affect the dual AGN fraction in galaxy mergers, and where does

the most efficient SMBH growth occur in galaxy mergers?

Finally, I outlined a very exciting future project that could use machine learning techniques to identify and study AGN host galaxy systems and classify them by merger stage (Chapter 5, Section 5.2). This project would leverage the power of machine learning against the large amounts of data produced by current and next-generation surveys (e.g. Hyper Suprime-Cam and the Vera Rubin Observatory). I estimate that this project would produce samples of AGN host systems in various stages of merging that are order of magnitudes larger in size than currently available samples. This project could be the first observational study of the connection between AGN and SFR that examines these connections by merger stage from bulge separations of 40 kpc to down to post-coalescence. Analysis of the samples produced in this project could test whether star formation peaks in the earlier stages of mergers and AGN luminosity peaks in the later stages of mergers, as predicted by simulations. This would prove that there is a connection between star formation and AGN in mergers, and that this connection has a temporal delay.

Bibliography

Augusta Abrahamse, Lloyd Knox, Samuel Schmidt, Paul Thorman, J. Anthony Tyson, and Hu Zhan. Characterizing and propagating modeling uncertainties in photometrically derived redshift distributions. The Astrophysical Journal, 734:36, 2011.

Sandro Ackermann, Kevin Schawinski, Ce Zhang, Anna K. Weigel, and M. Dennis Turp. Using transfer learning to detect galaxy mergers. Monthly Notices of the Royal Astronomical Society, 479(1):415, 2018.

J. Aird, K. Nandra, E. S. Laird, A. Georgakakis, M. L.N. Ashby, P. Barmby, A. L. Coil, J. S. Huang, A. M. Koekemoer, C. C. Steidel, and C. N.A. Willmer. The evolution of the hard X-ray luminosity function of AGN. Monthly Notices of the Royal Astronomical Society, 401:2531–2551, 2010.

D. M. Alexander and R. C. Hickox. What drives the growth of black holes? New Astronomy Reviews, 56:93, 2012.

D. M. Alexander, R.R. Chary, A. Pope, F. E. Bauer, W. N. Brandt, E. Daddi, M. Dickinson, D. Elbaz, and N. A. Reddy. Reliable Identification of Comptonthick Quasars at z 2: Spitzer MidInfrared Spectroscopy of HDFoMD49 . The Astrophysical Journal, 687(2):835–847, 2008.

Robert Antonucci. Unified Models for Active Galactic Nuclei and Quasars. Annual Review of Astronomy and Astrophysics, 31:473, 1993.

R. J. Assef, C. S. Kochanek, M. Brodwin, M. J. I. Brown, N. Caldwell, R. J. Cool, P. Eisenhardt, D. Eisenstein, A. H. Gonzalez, B. T. Jannuzi, C. Jones, E. McKenzie, S. S. Murray, and D. Stern. LowResolution Spectral Templates for Galaxies from 0.2 to 10 μm. The Astrophysical Journal, 676(1):286–303, 2008.

R. J. Assef, C. S. Kochanek, M. Brodwin, R. Cool, W. Forman, A. H. Gonzalez, R. C. Hickox, C. Jones, E. Le Floc'h, J. Moustakas, S. S. Murray, and D. Stern. Low-Resolution Spectral Templates for Active Galactic Nuclei and Galaxies From 0.03 to 30 μm. The Astrophysical Journal, 713(2):970–985, 2010.

R. J. Assef, C. S. Kochanek, M. L.N. Ashby, M. Brodwin, M. J.I. Brown, R. Cool, W. Forman, A. H. Gonzalez, R. C. Hickox, B. T. Jannuzi, C. Jones, E. Le Floc'h, J. Moustakas, S. S. Murray, and D. Stern. The mid-IR-and X-ray-selected QSO luminosity function. The Astrophysical Journal, 728:56, 2011.

R. J. Assef, D. Stern, C. S. Kochanek, A. W. Blain, M. Brodwin, M. J. I. Brown, E. Donoso, P. R. M. Eisenhardt, B. T. Jannuzi, T. H. Jarrett, S. A. Stanford, C.-W. Tsai, J. Wu, and L. Yan. Mid-Infrared Selection of Active Galactic Nuclei With the Wide-Field Infrared Explorer. II. Properties of WISE-Selected Active Galactic Nuclei in the NDWFS Bootes Field. The Astrophysical Journal, 772(1):26–43, 2013.

Mojegan Azadi, James Aird, Alison L. Coil, John Moustakas, Alexander J. Mendez, Michael R. Blanton, Richard J. Cool, Daniel J. Eisenstein, Kenneth C. Wong, and Guangtun Zhu. Primus: The Relationship Between Star Formation and AGN Accretion. The Astrophysical Journal, 806: 187, 2015.

Mojegan Azadi, Alison L. Coil, James Aird, Naveen Reddy, Alice Shapley, William R. Freeman, Mariska Kriek, Gene C. K. Leung, Bahram Mobasher, Sedona H. Price, Ryan L. Sanders, Irene Shivaei, and Brian Siana. The MOSDEF survey: AGN multi-wavelength identification, selection biases and host galaxy properties. The Astrophysical Journal, 835(1):27–48, 2017.

Maarten Baes, Joris Verstappen, Ilse De Looze, Jacopo Fritz, Waad Saftly, Edgardo Vidal Pérez, Marko Stalevski, and Sander Valcke. Efficient three-dimensional NLTE dust radiative transfer with skirt. The Astrophysical Journal Supplement Series, 196(2):22, 2011.

Vivienne F Baldassare, Amy E Reines, Elena Gallo, and Jenny E Greene. Hubble Space Telescope Imaging of the Active Dwarf Galaxy RGG 118. The Astrophysical Journal, 850(2):196, 2017.

A. Baldwin, M. M. Phillips, and R. Terlevich. Classification Parameters for the Emission-Line Spectra of Extragalactic Objects. Publications of the Astronomical Society of the Pacific, 93:5, 1981.

R. Scott Barrows, Claud H.Sandberg Lacy, Julia Kennefick, Julia M. Comerford, Daniel Kennefick, and Joel C. Berrier. Identification of outflows and candidate dual active galactic nuclei in SDSS quasars at z = 0.8-1.6. The Astrophysical Journal, 769(2), 2013.

R. Scott Barrows, Julia M. Comerford, Jenny E. Greene, and David Pooley. Spatially Offset Active Galactic Nuclei. I. Selection and Spectroscopic Properties. The Astrophysical Journal, 829(1): 37–59, 2016.

R. Scott Barrows, Julia M. Comerford, Jenny E. Greene, and David Pooley. Spatially Offset Active Galactic Nuclei. II. Triggering in Galaxy Mergers. The Astrophysical Journal, 838(2):129, 2017a.

R. Scott Barrows, Julia M. Comerford, Nadia L. Zakamska, and Michael C. Cooper. Observational Constraints on Correlated Star Formation and Active Galactic Nuclei in Late-Stage Galaxy Mergers. The Astrophysical Journal, 850(1):27, 2017b.

R. Scott Barrows, Julia M Comerford, and Jenny E Greene. Spatially Offset Active Galactic Nuclei . III . Discovery of Late-stage Galaxy Mergers with the Hubble Space Telescope. The Astrophysical Journal, 869:154, 2018.

M.C. Begelman, Roger D. Blandford, and M.J. Rees. Massive Black Hole Binaries in Active Galactic Nuclei. Nature, 287:307, 1980.

Francesco Belfiore, Roberto Maiolino, Claudia Maraston, Eric Emsellem, Matthew A. Bershady, Karen L. Masters, Renbin Yan, Dmitry Bizyaev, ederic Boquien, Joel R. Brownstein, Kevin

Bundy, Niv Drory, Timothy M. Heckman, David R. Law, Alexandre Roman-Lopes, Kaike Pan, Letizia Stanghellini, Daniel Thomas, Anne Marie Weijmans, and Kyle B. Westfall. SDSS IV MaNGA-spatially resolved diagnostic diagrams: A proof that many galaxies are LIERs. Monthly Notices of the Royal Astronomical Society, 461(3):3111, 2016.

Eric F. Bell, Daniel H. McIntosh, Neal Katz, and Martin D. Weinberg. The Optical and Near-Infrared Properties of Galaxies: I. Luminosity and Stellar Mass Functions. The Astrophysical Journal Supplement Series, 149:289–312, 2003.

E. Bernhard, L. P. Grimmett, J. R. Mullaney, E. Daddi, C. Tadhunter, and S. Jin. Inferring a difference in the star-forming properties of lower versus higher X-ray luminosity AGNs. Monthly Notices of the Royal Astronomical Society: Letters, 483:L52, 2019.

E. Bertin and S. Arnouts. SExtractor: Software for source extraction. Astronomy and Astrophysics Supplement Series, 117:393–404, 1996.

Serena Bertone and Christopher J. Conselice. A comparison of galaxy merger history observations and predictions from semi-analytic models. Monthly Notices of the Royal Astronomical Society, 396(4):2345–2358, 2009.

Stefano Bianchi, Marco Chiaberge, Enrico Piconcelli, Matteo Guainazzi, and Giorgio Matt. Chandra unveils a binary active galactic nucleus in Mrk 463. Monthly Notices of the Royal Astronomical Society, 386(1):105–110, 2008.

Laura Blecha, Abraham Loeb, and Ramesh Narayan. Double-peaked narrow-line signatures of dual supermassive black holes in galaxy merger simulations. Monthly Notices of the Royal Astronomical Society, 429(3):2594, 2013.

Asa F.L. Bluck, J. Trevor Mendel, Sara L. Ellison, Jorge Moreno, Luc Simard, David R. Patton, and Else Starkenburg. Bulge mass is king: The dominant role of the bulge in determining the fraction of passive galaxies in the sloan digital sky survey. Monthly Notices of the Royal Astronomical Society, 441(1):599–629, 2014.

Connor Bottrell, Maan H. Hani, Hossen Teimoorinia, Sara L. Ellison, Jorge Moreno, Paul Torrey, Christopher C. Hayward, Mallory Thorp, Luc Simard, and Lars Hernquist. Deep learning predictions of galaxy merger stage and the importance of observational realism. Monthly Notices of the Royal Astronomical Society, 490(4):5390–5413, 2019.

F. Bournaud and F. Combes. Gas accretion on spiral galaxies: Bar formation and renewal. Astronomy and Astrophysics, 392(1):83–102, 2002.

R. G. Bower, A. J. Benson, R. Malbon, J. C. Helly, C. S. Frenk, C. M. Baugh, S. Cole, and C. G. Lacey. Breaking the hierarchy of galaxy formation. Monthly Notices of the Royal Astronomical Society, 370(2):645–655, 2006.

B. J. Boyle and Roberto J. Terlevich. The cosmological evolution of the QSO luminosity density and of the star formation rate. Monthly Notices of the Royal Astronomical Society, 293:L49–L51, 1998.

W. N. Brandt and D. M. Alexander. Cosmic X-ray surveys of distant active galaxies: The demographics, physics, and ecology of growing supermassive black holes. Astronomy and Astrophysics Review, 23(1):1, 2015.

Murray Brightman, Kirpal Nandra, Mara Salvato, Li Ting Hsu, James Aird, and Cyprian Rangel. Compton thick active galactic nuclei in Chandra surveys. Monthly Notices of the Royal Astronomical Society, 443(3):1999–2017, 2014.

J. Brinchmann, S. Charlot, S. D.M. White, C. Tremonti, G. Kauffmann, T. Heckman, and J. Brinkmann. The physical properties of star-forming galaxies in the low-redshift Universe. Monthly Notices of the Royal Astronomical Society, 351(4):1151, 2004.

M. Brusa, F. Civano, A. Comastri, T. Miyaji, M. Salvato, G. Zamorani, N. Cappelluti, F. Fiore, G. Hasinger, V. Mainieri, A. Merloni, A. Bongiorno, P. Capak, M. Elvis, R. Gilli, H. Hao, K. Jahnke, A. M. Koekemoer, O. Ilbert, E. Le Floc'H, E. Lusso, M. Mignoli, E. Schinnerer, J. D. Silverman, E. Treister, J. D. Trump, C. Vignali, M. Zamojski, T. Aldcroft, H. Aussel, S. Bardelli, M. Bolzonella, A. Cappi, K. Caputi, T. Contini, A. Finoguenov, A. Fruscione, B. Garilli, C. D. Impey, A. Iovino, K. Iwasawa, P. Kampczyk, J. Kartaltepe, J. P. Kneib, C. Knobel, K. Kovac, F. Lamareille, J. F. Leborgne, V. Le Brun, O. Le Fevre, S. J. Lilly, C. Maier, H. J. McCracken, R. Pello, Y. J. Peng, E. Perez-Montero, L. De Ravel, D. Sanders, M. Scodeggio, N. Z. Scoville, M. Tanaka, Y. Taniguchi, L. Tasca, S. De La Torre, L. Tresse, D. Vergani, and E. Zucca. The XMM-newton wide-field survey in the cosmos field (XMM-COSMOS): Demography and multiwavelength properties of obscured and unobscured luminous active galactic nuclei. The Astrophysical Journal, 716(1):348, 2010.

Fernando Buitrago, Ignacio Trujillo, Christopher J. Conselice, and Boris Häußler. Early-type galaxies have been the predominant morphological class for massive galaxies since only z ˜ 1. Monthly Notices of the Royal Astronomical Society, 428(2):1460–1478, 2013.

E. Margaret Burbidge, G. R. Burbidge, and Kevin H. Prendergast. Mass Distribution and Physical Conditions in the Inner Region of NGC 1068. The Astrophysical Journal, 130:26, 1959.

L. Burtscher, R. I. Davies, J. Gracia-Carpio, M. J. Koss, M. Y. Lin, D. Lutz, P. Nandra, H. Netzer, G. Orban de Xivry, C. Ricci, D. J. Rosario, S. Veilleux, A. Contursi, R. Genzel, A. Schnorr-Mueller, A. Sternberg, E. Sturm, and L. J. Tacconi. On the relation of optical obscuration and X-ray absorption in Seyfert galaxies. Astronomy and Astrophysics, 586:A28, 2016.

John A. R. Caldwell, Daniel H. McIntosh, HansWalter Rix, Marco Barden, Steven V. W. Beckwith, Eric F. Bell, Andrea Borch, Catherine Heymans, Boris Häußler, Knud Jahnke, Shardha Jogee, Klaus Meisenheimer, Chien Y. Peng, Sebastian F. Sánchez, Rachel S. Somerville, Lutz Wisotzki, and Christian Wolf. GEMS Survey Data and Catalog. The Astrophysical Journal Supplement Series, 174(1):136–144, 2008.

Gabriela Canalizo and Alan Stockton. QuasiStellar Objects, Ultraluminous Infrared Galaxies, and Mergers. The Astrophysical Journal, 555(2):719, 2001.

Pedro R. Capelo, Marta Volonteri, Massimo Dotti, Jillian M. Bellovary, Lucio Mayer, and Fabio Governato. Growth and activity of black holes in galaxy mergers with varying mass ratios. Monthly Notices of the Royal Astronomical Society, 447(3):2123–2143, 2015.

Pedro R. Capelo, Massimo Dotti, Marta Volonteri, Lucio Mayer, Jillian M. Bellovary, and Sijing Shen. A survey of dual active galactic nuclei in simulations of galaxy mergers: Frequency and properties. Monthly Notices of the Royal Astronomical Society, 469(4):4437–4454, 2017.

J. Cardelli, G. Clayton, and J. Mathis. The Relationship Between Infrared, Optical, and Ultraviolet Extinction. The Astrophysical Journal, 345:245–256, 1989.

R. G. Carlberg. Mergers as an Omega estimator. The Astrophysical Journal Letters, 359(1):L1, 1990.

Chien-Ting J. Chen, Ryan C. Hickox, Stacey Alberts, Mark Brodwin, Christine Jones, Stephen S. Murray, David M. Alexander, Roberto J. Assef, Michael J. I. Brown, Arjun Dey, William R. Forman, Varoujan Gorjian, Andrew D. Goulding, Emeric Le Floc'h, Buell T. Jannuzi, James R. Mullaney, and Alexandra Pope. a Correlation Between Star Formation Rate and Average Black Hole Accretion in Star-Forming Galaxies. The Astrophysical Journal, 773:3, 2013.

Sun Mi Chung, Christopher S. Kochanek, Roberto Assef, Michael J I Brown, Daniel Stern, Buell T. Jannuzi, Anthony H. Gonzalez, Ryan C. Hickox, and John Moustakas. A UV to mid-IR study of AGN selection. The Astrophysical Journal, 790:54, 2014.

Luca Ciotti, Jeremiah P. Ostriker, and Daniel Proga. Feedback from central black holes in elliptical galaxies. III. Models with both radiative and mechanical feedback. The Astrophysical Journal, 717:708, 2010.

Mauricio Cisternas, Knud Jahnke, Katherine J. Inskip, Jeyhan Kartaltepe, Anton M. Koekemoer, Thorsten Lisker, Aday R. Robaina, Marco Scodeggio, Kartik Sheth, Jonathan R. Trump, René Andrae, Takamitsu Miyaji, Elisabeta Lusso, Marcella Brusa, Peter Capak, Nico Cappelluti, Francesca Civano, Olivier Ilbert, Chris D. Impey, Alexie Leauthaud, Simon J. Lilly, Mara Salvato, Nick Z. Scoville, and Yoshi Taniguchi. The bulk of the black hole growth since z 1 occurs in a secular universe: No major merger-AGN connection. Astrophysical Journal, 726(2), 2011.

F. Civano, S. Marchesi, A. Comastri, M. C. Urry, M. Elvis, N. Cappelluti, S. Puccetti, M. Brusa, G. Zamorani, G. Hasinger, T. Aldcroft, D. M. Alexander, V. Allevato, H. Brunner, P. Capak, A. Finoguenov, F. Fiore, A. Fruscione, R. Gilli, K. Glotfelty, R. E. Griffiths, H. Hao, F. A. Harrison, K. Jahnke, J. Kartaltepe, A. Karim, S. M. LaMassa, G. Lanzuisi, T. Miyaji, P. Ranalli, M. Salvato, M. Sargent, N. J. Scoville, K. Schawinski, E. Schinnerer, J. Silverman, V. Smolcic, D. Stern, S. Toft, B. Trakhenbrot, E. Treister, and C. Vignali. The Chandra COSMOS Legacy Survey: Overview and Point Source Catalog. The Astrophysical Journal, 819(1):62, 2016.

Julia M. Comerford and Jenny E. Greene. Offset Active Galactic Nuclei As Tracers of Galaxy Mergers and Supermassive Black Hole Growth. The Astrophysical Journal, 789(2):112, 2014.

Julia M Comerford, Roger L Griffith, Brian F Gerke, Michael C Cooper, Jeffrey A Newman, Marc Davis, and Daniel Stern. 1.75 kpc Separation Dual Active Galactic Nuclei at z=0.36 in the COSMOS Field. The Astrophysical Journal Letters, 702(1):L82–L86, 2009.

Julia M. Comerford, Brian F. Gerke, Daniel Stern, Michael C. Cooper, Benjamin J. Weiner, Jeffrey A. Newman, Kristin Madsen, and R. Scott Barrows. Kiloparsec-Scale Spatial Offsets in Double-Peaked Narrow-Line Active Galactic Nuclei. I. Markers for Selection of Compelling Dual Active Galactic Nucleus Candidates. The Astrophysical Journal, 753(1):42–52, 2012.

Julia M. Comerford, David Pooley, R. Scott Barrows, Jenny E. Greene, Nadia L. Zakamska, Greg M. Madejski, and Michael C. Cooper. Merger-driven Fueling of Active Galactic Nuclei: Six Dual and Offset Active Galactic Nuclei Discovered with Chandra and Hubble Space Telescope Observations. The Astrophysical Journal, 806(2):219–238, 2015.

Julia M. Comerford, R. Scott Barrows, Francisco Müller-Sánchez, Rebecca Nevin, Jenny E. Greene, David Pooley, Daniel Stern, and Fiona A. Harrison. An Active Galactic Nucleus Caught in the Act of Turning Off and On. The Astrophysical Journal, 849(2):102, 2017.

Christopher J Conselice. the Relationship Between Stellar Light Distributions of Galaxies and Their. The Astrophysical Journal Supplement Series, 147:1–28, 2003.

Christopher J. Conselice. The evolution of galaxy structure over cosmic time. Annual Review of Astronomy and Astrophysics, 52:291–337, 2014.

A. Corral, R. Della Ceca, A. Caccianiga, P. Severgnini, H. Brunner, F. J. Carrera, M. J. Page, and A. D. Schwope. The X-ray spectral properties of the AGN population in the XMM-Newton bright serendipitous survey. Astronomy and Astrophysics, 530:A42, 2011.

T. J. Cox, Patrik Jonsson, Rachel S. Somerville, Joel R. Primack, and Avishai Dekel. The effect of galaxy mass ratio on merger-driven starbursts. Monthly Notices of the Royal Astronomical Society, 384(1):386–409, 2008.

E Daddi, M Dickinson, G Morrison, R Chary, A Cimatti, D Elbaz, D Frayer, A Renzini, A Pope, D M Alexander, F E Bauer, and M Giavalisco. Multiwavelength Study of Massive Galaxies at z ˜ 2. I. Star Formation and Galaxy Growth. The Astrophysical Journal, 670:156, 2007.

D. W. Darg, S. Kaviraj, C. J. Lintott, K. Schawinski, M. Sarzi, S. Bamford, J. Silk, D. Andreescu, P. Murray, R. C. Nichol, M. J. Raddick, A. Slosar, A. S. Szalay, D. Thomas, and J. Vandenberg. Galaxy Zoo: The properties of merging galaxies in the nearby Universe - Local environments, colours, masses, star formation rates and AGN activity. Monthly Notices of the Royal Astronomical Society, 401(3):1552–1563, 2010.

M Davis, P Guhathakurta, N P Konidaris, J A Newman, M L N Ashby, A D Biggs, P Barmby, K Bundy, S C Chapman, A L Coil, C J Conselice, M C Cooper, D J Croton, P R M Eisenhardt, R S Ellis, S M Faber, T Fang, G G Fazio, A Georgakakis, B F Gerke, W M Goss, S Gwyn, J Harker, A M Hopkins, J Huang, R J Ivison, S A Kassin, E N Kirby, A M Koekemoer, D C Koo, E S Laird, E Le Floc'h, L Lin, J M Lotz, P J Marshall, D C Martin, A J Metevier, L A Moustakas, K Nandra, K G Noeske, C Papovich, A C Phillips, R M Rich, G H Rieke, D Rigopoulou, S Salim, D Schiminovich, L Simard, I Smail, T A Small, B J Weiner, C N A Willmer, S P Willner, G Wilson, E L Wright, and R Yan. The All-Wavelength Extended Groth Strip International Survey (AEGIS) Data Sets. The Astrophysical Journal Letters, 660:L1, 2007.

Gerard de Vaucouleurs. Recherches sur les Nebuleuses Extragalactiques. Annales d'Astrophysique, 11:247, 1948.

A. Dekel, Y. Birnboim, G. Engel, J. Freundlich, T. Goerdt, M. Mumcuoglu, E. Neistein, C. Pichon, R. Teyssier, and E. Zinger. Cold streams in early massive hot haloes as the main mode of galaxy formation. Nature, 457:451, 2009.

I. Delvecchio, D. Lutz, S. Berta, D. J. Rosario, G. Zamorani, F. Pozzi, C. Gruppioni, C. Vignali, M. Brusa, A. Cimatti, D. L. Clements, A. Cooray, D. Farrah, G. Lanzuisi, S. Oliver, G. Rodighiero, P. Santini, and M. Symeonidis. Mapping the average AGN accretion rate in the SFR-M* plane for Herschel-selected galaxies at $0 < z$ 2.5. Monthly Notices of the Royal Astronomical Society, 449(1):373–389, 2015.

Aleksandar M. Diamond-Stanic and George H. Rieke. The relationship between black hole growth and star formation in seyfert galaxies. The Astrophysical Journal, 746(2):168–181, 2012.

Mark Dickinson and Mauro Giavalisco. The Great Observatories Origins Deep Survey. In R. Bender and A. Renzini, editors, The Mass of Galaxies at Low and High Redshift, page 324, Venice, Italy, 2003.

J. L. Donley, G. H. Rieke, P. G. PérezGonzález, and G. Barro. Spitzer's Contribution to the AGN Population . The Astrophysical Journal, 687(1):111–132, 2008.

J. L. Donley, A. M. Koekemoer, M. Brusa, P. Capak, C. N. Cardamone, F. Civano, O. Ilbert, C. D. Impey, J. S. Kartaltepe, T. Miyaji, M. Salvato, D. B. Sanders, J. R. Trump, and G. Zamorani. Identifying Luminous Active Galactic Nuclei in Deep Surveys: Revised Irac Selection Criteria. The Astrophysical Journal, 748(2):142–163, 2012.

J. L. Donley, J. Kartaltepe, D. Kocevski, M. Salvato, P. Santini, H. Suh, F. Civano, A. M. Koekemoer, J. Trump, M. Brusa, C. Cardamone, A. Castro, M. Cisternas, C. Conselice, D. Croton, N. Hathi, C. Liu, R. A. Lucas, P. Nair, D. Rosario, D. Sanders, B. Simmons, C. Villforth, D. M. Alexander, E. F. Bell, S. M. Faber, N. A. Grogin, J. Lotz, D. H. McIntosh, and T. Nagao. Evidence for Merger-Driven Growth in Luminous, High-z, Obscured AGN in the CANDELS/COSMOS Field. The Astrophysical Journal, 853(1):63, 2018.

J. S. Dunlop, R. J. McLure, M. J. Kukula, S. A. Baum, C. P. O'Dea, and D. H. Hughes. Quasars, their host galaxies and their central black holes. Monthly Notices of the Royal Astronomical Society, 340(4):1095–1135, 2003.

Megan E. Eckart, Ian D. McGreer, Daniel Stern, Fiona A. Harrison, and David J. Helfand. A Comparison of X-Ray and Mid-Infrared Selection of Obscured Active Galactic Nuclei. The Astrophysical Journal, 708(1):584–597, 2010.

David Elbaz, M. Dickinson, H. S. Hwang, T. Díaz-Santos, G. Magdis, B. Magnelli, D. Le Borgne, F. Galliano, M. Pannella, P. Chanial, L. Armus, V. Charmandaris, E. Daddi, H. Aussel, P. Popesso, J. Kartaltepe, B. Altieri, I. Valtchanov, D. Coia, H. Dannerbauer, K. Dasyra, R. Leiton, J. Mazzarella, D. M. Alexander, V. Buat, D. Burgarella, R.-R. Chary, R. Gilli, R. J. Ivison, S. Juneau, E. Le Floc'h, D. Lutz, G. E. Morrison, J. R. Mullaney, E. Murphy, A. Pope, D. Scott, M. Brodwin, D. Calzetti, C. Cesarsky, S. Charlot, H. Dole, P. Eisenhardt, H. C. Ferguson, N. Förster Schreiber, D. Frayer, M. Giavalisco, M. Huynh, A. M. Koekemoer, C. Papovich, N. Reddy, C. Surace, H. Teplitz, M. S. Yun, and G. Wilson. GOODS Herschel : an infrared main sequence for star-forming galaxies. Astronomy and Astrophysics, 533:A119, 2011.

Sara L. Ellison, David R. Patton, Luc Simard, and Alan W. McConnachie. Galaxy pairs in the sloan digital sky survey. I. Star formation, active galactic nucleus fraction, and the luminosity/mass-metallicity relation. The Astronomical Journal, 135(5):1877–1899, 2008.

Sara L. Ellison, David R. Patton, J. Trevor Mendel, and Jillian M. Scudder. Galaxy pairs in the Sloan Digital Sky Survey - IV. Interactions trigger active galactic nuclei. Monthly Notices of the Royal Astronomical Society, 418(3):2043–2053, 2011.

Sara L. Ellison, Hossen Teimoorinia, David J. Rosario, and J. Trevor Mendel. The star formation rates of active galactic nuclei host galaxies. Monthly Notices of the Royal Astronomical Society: Letters, 458(1):L34–L38, 2016a.

Sara L. Ellison, Hossen Teimoorinia, David J. Rosario, and J. Trevor Mendel. The star formation rates of active galactic nuclei host galaxies. Monthly Notices of the Royal Astronomical Society: Letters, 458(1):L34–L38, 2016b.

Debra Meloy Elmegreen and Bruce G. Elmegreen. Arm Classification for Spiral Galaxies. The Astrophysical Journal, 314:3, 1987.

Martin Elvis, Belinda J Wilkes, Jonathan C Mcdowell, Richard F Green, Jill Bechtold, S P Willner, M S Oey, Elisha Polomski, and Roc Cutri. Atlas of Quasar Energy Distributions. The Astrophysical Journal Supplement Series, 95:1, 1994.

Peter Englmaier and Isaac Shlosman. Dynamical Decoupling of Nested Bars: Self-gravitating Gaseous Nuclear Bars. The Astrophysical Journal, 617(2):L115–L118, 2004.

I. N. Evans, F. A. Primini, J. B. Miller, J. D. Evans, C. E. Allen, C. S. Anderson, G. Becker, J. A. Budynkiewicz, D. Burke, J. C. Chen, F. Civano, R. D'Abrusco, S. M. Doe, G. Fabbiano, J. Martinez Galarza, II Gibbs, D. G., K. J. Glotfelty, D. E. Graessle, Jr. Grier, J. D., R. M. Hain, D. M. Hall, P. N. Harbo, J. C. Houck, J. L. Lauer, O. Laurino, N. P. Lee, M. L. McCollough, J. C. McDowell, W. McLaughlin, D. L. Morgan, A. E. Mossman, D. T. Nguyen, J. S. Nichols, M. A. Nowak, C. Paxson, M. Perdikeas, D. A. Plummer, A. H. Rots, A. L. Siemiginowska, B. A. Sundheim, S. Thong, M. S. Tibbetts, D. W. Van Stone, S. L. Winkelman, and P. Zografou. The Chandra Source Catalog - A Billion X-ray Photons. American Astronomical Society, 52(154.05), 2020.

Ian N Evans and Francesca Civano. The Chandra Source Catalog release 2.0. Astronomy and Geophysics, 59(2):2.17, 2018.

G. G. Fazio, J. L. Hora, L. E. Allen, M. L. N. Ashby, P. Barmby, L. K. Deutsch, J.S. Huang, S. Kleiner, M. Marengo, S. T. Megeath, G. J. Melnick, M. a. Pahre, B. M. Patten, J. Polizotti, H. a. Smith, R. S. Taylor, Z. Wang, S. P. Willner, W. F. Hoffmann, J. L. Pipher, W. J. Forrest, C. W. McMurty, C. R. McCreight, M. E. McKelvey, R. E. McMurray, D. G. Koch, S. H. Moseley, R. G. Arendt, J. E. Mentzell, C. T. Marx, P. Losch, P. Mayman, W. Eichhorn, D. Krebs, M. Jhabvala, D. Y. Gezari, D. J. Fixsen, J. Flores, K. Shakoorzadeh, R. Jungo, C. Hakun, L. Workman, G. Karpati, R. Kichak, R. Whitley, S. Mann, E. V. Tollestrup, P. Eisenhardt, D. Stern, V. Gorjian, B. Bhattacharya, S. Carey, B. O. Nelson, W. J. Glaccum, M. Lacy, P. J. Lowrance, S. Laine, W. T. Reach, J. a. Stauffer, J. a. Surace, G. Wilson, E. L. Wright, A. Hoffman, G. Domingo, and M. Cohen. The Infrared Array Camera (IRAC) for the Spitzer Space Telescope. The Astrophysical Journal Supplement Series, 154:10–17, 2004.

Laura Ferrarese and David Merritt. A Fundamental Relation Between Supermassive Black Holes and Their Host Galaxies. The Astrophysical Journal Letters, 539(1):L9–L12, 2000.

Adi Foord, Kayhan Gültekin, Mark T. Reynolds, Edmund Hodges-Kluck, Edward M. Cackett, Julia M. Comerford, Ashley L. King, Jon M. Miller, and Jessie C. Runnoe. A Bayesian Analysis of SDSS J0914+0853, a Low-mass Dual AGN Candidate. The Astrophysical Journal, 877(1):17, 2019.

Adi Foord, Kayhan Gültekin, Rebecca Nevin, Julia M. Comerford, Edmund Hodges-Kluck, R. Scott Barrows, Andrew D. Goulding, and Jenny E. Greene. A Second Look at 12 Candidate Dual AGNs Using BAYMAX. The Astrophysical Journal, 892(1):29, 2020.

Adi Foord, Kayhan Gültekin, Jessie C. Runnoe, and Michael J. Koss. AGN Triality of Triple Mergers: Multiwavelength Classifications. The Astrophysical Journal, 907(2):72, 2021.

Hai Fu, Adam D. Myers, S. G. Djorgovski, and Lin Yan. Mergers in Double-Peaked [O III] Active Galactic Nuclei. The Astrophysical Journal, 733(2):103–109, 2011.

Hai Fu, Lin Yan, Adam D. Myers, Alan Stockton, S. G. Djorgovski, G. Aldering, and Jeffrey A. Rich. the Nature of Double-Peaked [O Iii] Active Galactic Nuclei. The Astrophysical Journal, 745(1):67–84, 2012.

Hai Fu, A. D. Myers, S. G. Djorgovski, Lin Yan, J. M. Wrobel, and A. Stockton. Radio-selected binary active galactic nuclei from the very large array Stripe 82 survey. Astrophysical Journal, 799(1):1–10, 2015.

T. Fukushima, Y. Eriguchi, D. Sugimoto, and G. S. Bisnovatyi-Kogan. Concave Hamburger Equilibrium of Rotating Bodies. Progress of Theoretical Physics, 63(6):1957–1970, 1980.

S. García-Burillo, F. Combes, E. Schinnerer, F. Boone, and L. K. Hunt. Molecular gas in NUclei of GAlaxies (NUGA). Astronomy and Astrophysics, 441:1011, 2005.

Karl Gebhardt, John Kormendy, Luis C. Ho, Ralf Bender, Gary Bower, Alan Dressler, S. M. Faber, Alexei V. Filippenko, Richard Green, Carl Grillmair, Tod R. Lauer, John Magorrian, Jason Pinkney, Douglas Richstone, and Scott Tremaine. Black Hole Mass Estimates from Reverberation Mapping and from Spatially Resolved Kinematics. The Astrophysical Journal Letters, 543(1): L5–L8, 2000.

B F Gerke, J A Newman, J Lotz, R Yan, P Barmby, A L Coil, C J Conselice, R J Ivison, L Lin, D C Koo, K Nandra, S Salim, T Small, B J Weiner, M C Cooper, M Davis, S M Faber, and P Guhathakurta. The DEEP2 Galaxy Redshift Survey: AEGIS Observations of a Dual AGN at z = 0.7. The Astrophysical Journal Letters, 660:L23–L26, 2007.

Mauro Giavalisco, Charles C. Steidel, and F. Duccio Macchetto. Hubble Space Telescope Imaging of Star-Forming Galaxies at Redshifts z>3. The Astrophysical Journal, 470:189, 1996.

Eilat Glikman, Brooke Simmons, Madeline Mailly, Kevin Schawinski, C. M. Urry, and M. Lacy. Major Mergers Host the Most-Luminous Red Quasars at z 2: A Hubble Space Telescope WFC3/IR Study. The Astrophysical Journal, 806(2):218, 2015.

K. Gordon and G. Clayton. Starburst-Like Dust Extinction in the Small Magellanic Cloud. The Astrophysical Journal, 500:816–824, 1998.

A. D. Goulding, W. R. Forman, R. C. Hickox, C. Jones, S. S. Murray, A. Paggi, M. L.N. Ashby, A. L. Coil, M. C. Cooper, J. S. Huang, R. Kraft, J. A. Newman, B. J. Weiner, and S. P. Willner. Tracing the evolution of active galactic nuclei host galaxies over the last 9 Gyr of cosmic time. Astrophysical Journal, 783(1), 2014.

Andy D. Goulding, Jenny E. Greene, Rachel Bezanson, Johnny Greco, Sean Johnson, Alexie Leauthaud, Yoshiki Matsuoka, Elinor Medezinski, and Adrian M. Price-Whelan. Galaxy interactions trigger rapid black hole growth: An unprecedented view from the Hyper Suprime-Cam survey. Publications of the Astronomical Society of Japan, 70:1–27, 2018.

Jenny E. Greene and Luis C. Ho. The MBH-Sigma* Relation in Local Active Galaxies. The Astrophysical Journal Letters, 641(1):L21–L24, 2006.

Roger L. Griffith, Michael C. Cooper, Jeffrey A. Newman, Leonidas A. Moustakas, Daniel Stern, Julia M. Comerford, Marc Davis, Jennifer M. Lotz, Marco Barden, Christopher J. Conselice, Peter L. Capak, S. M. Faber, J. Davy Kirkpatrick, Anton M. Koekemoer, David C. Koo, Kai G. Noeske, Nick Scoville, Kartik Sheth, Patrick Shopbell, Christopher N. A. Willmer, and Benjamin Weiner. The Advanced Camera for Surveys General Catalog: Structural Parameters for Approximately Half a Million Galaxies. The Astrophysical Journal Supplement Series, 200(1): 9–21, 2012.

Norman A Grogin, Dale D Kocevski, S M Faber, Henry C Ferguson, Anton M Koekemoer, Adam G Riess, Viviana Acquaviva, David M Alexander, Omar Almaini, Matthew L N Ashby, Marco Barden, Eric F Bell, Marco Castellano, Peter Challis, Ranga-ram Chary, Edmond Cheung, Michele Cirasuolo, F De Mello, Avishai Dekel, Mark Dickinson, Timothy Dolch, Jennifer L Donley, Romeel Dav, Patrick J Mccarthy, Elizabeth J Mcgrath, Daniel H Mcintosh, Ross J Mclure, Bahram Mobasher, Leonidas A. Moustakas, Mark Mozena, Kirpal Nandra, Jeffrey A. Newman, Sami-Matias Niemi, Kai G. Noeske, Casey J. Papovich, Laura Pentericci, Alexandra Pope, Joel R. Primack, Abhijith Rajan, Swara Ravindranath, Naveen A. Reddy, Alvio Renzini, Hans-Walter Rix, Aday R. Robaina, Steven A. Rodney, David J. Rosario, Piero Rosati, Sara Salimbeni, Claudia Scarlata, Brian Siana, Luc Simard, Joseph Smidt, Rachel S. Somerville, Hyron Spinrad, Amber N. Straughn, Louis-Gregory Strolger, Olivia Telford, Harry I. Teplitz, Jonathan R. Trump, Arjen van der Wel, Carolin Villforth, Risa H. Wechsler, Benjamin J. Weiner, Tommy Wiklind, Vivienne Wild, Grant Wilson, Stijn Wuyts, Hao-Jing Yan, and Min S. Yun. CANDELS: The Cosmic Assembly Near-Infrared Deep Extragalactic Legacy Survey. The Astrophysical Journal Supplement Series, 197:35, 2011.

Kayhan Gültekin, Douglas O. Richstone, Karl Gebhardt, Tod R. Lauer, Scott Tremaine, M. C. Aller, Ralf Bender, Alan Dressler, S. M. Faber, Alexei V. Filippenko, Richard Green, Luis C. Ho, John Kormendy, John Magorrian, Jason Pinkney, and Christos Siopis. The M-σ and M-L relations in galactic bulges, and determinations of their intrinsic scatter. The Astrophysical Journal, 698:198, 2009.

Yicheng Guo, Henry C. Ferguson, Eric F. Bell, David C. Koo, Christopher J. Conselice, Mauro Giavalisco, Susan Kassin, Yu Lu, Ray Lucas, Nir Mandelker, Daniel M. McIntosh, Joel R. Primack, Swara Ravindranath, Guillermo Barro, Daniel Ceverino, Avishai Dekel, Sandra M. Faber, Jerome J. Fang, Anton M. Koekemoer, Kai Noeske, Marc Rafelski, and Amber Straughn. Clumpy galaxies in candels. I. the definition of UV clumps and the fraction of clumpy galaxies at $0.5 < z < 3$. Astrophysical Journal, 800(1), 2015.

Thales A. Gutcke, Nikos Fanidakis, Andrea V. Macciò, and Cedric Lacey. The star formation and AGN luminosity relation: Predictions from a semi-analytical model. Monthly Notices of the Royal Astronomical Society, 451(4):3759–3767, 2015.

Kevin N. Hainline, Amy E. Reines, Jenny E. Greene, and Daniel Stern. Mid-Infrared Colors of Dwarf Galaxies: Young Starbursts Mimicking Active Galactic Nuclei. The Astrophysical Journal, 832(2):119–132, 2016.

Kathryn Harris, Duncan Farrah, Bernhard Schulz, Evanthia Hatziminaoglou, Marco Viero, Nick Anderson, Matthieu Béthermin, Scott Chapman, David L. Clements, Asantha Cooray, Andreas

Efstathiou, Anne Feltre, Peter Hurley, Eduardo Ibar, Mark Lacy, Sebastian Oliver, Mathew J. Page, Ismael Pérez-Fournon, Sara M. Petty, Lura K. Pitchford, Dimitra Rigopoulou, Douglas Scott, Myrto Symeonidis, Joaquin Vieira, and Lingyu Wang. Star formation rates in luminous quasars at $2 < z < 3$. Monthly Notices of the Royal Astronomical Society, 457(4):4179–4194, 2016.

C. M. Harrison, D. M. Alexander, J. R. Mullaney, B. Altieri, D. Coia, V. Charmandaris, E. Daddi, H. Dannerbauer, K. Dasyra, A. Del Moro, M. Dickinson, R. C. Hickox, R. J. Ivison, J. Kartaltepe, E. Le Floc'H, R. Leiton, B. Magnelli, P. Popesso, E. Rovilos, D. Rosario, and A. M. Swinbank. No clear submillimeter signature of suppressed star formation among X-ray luminous active galactic nuclei. The Astrophysical Journal Letters, 760:L15, 2012.

E. Hatziminaoglou, A. Omont, J. A. Stevens, A. Amblard, V. Arumugam, R. Auld, H. Aussel, T. Babbedge, A. Blain, J. Bock, A. Boselli, V. Buat, D. Burgarella, N. Castro-Rodríguez, A. Cava, P. Chanial, D. L. Clements, A. Conley, L. Conversi, A. Cooray, C. D. Dowell, E. Dwek, S. Dye, S. Eales, D. Elbaz, D. Farrah, M. Fox, A. Franceschini, W. Gear, J. Glenn, E. A. González Solares, M. Griffin, M. Halpern, E. Ibar, K. Isaak, R. J. Ivison, G. Lagache, L. Levenson, N. Lu, S. Madden, B. Maffei, G. Mainetti, L. Marchetti, A. M.J. Mortier, H. T. Nguyen, B. O'Halloran, S. J. Oliver, M. J. Page, P. Panuzzo, A. Papageorgiou, C. P. Pearson, I. Pérez-Fournon, M. Pohlen, J. I. Rawlings, D. Rigopoulou, D. Rizzo, I. G. Roseboom, M. Rowan-Robinson, M. Sanchez Portal, B. Schulz, D. Scott, N. Seymour, D. L. Shupe, A. J. Smith, M. Symeonidis, M. Trichas, K. E. Tugwell, M. Vaccari, I. Valtchanov, L. Vigroux, L. Wang, R. Ward, G. Wright, C. K. Xu, and M. Zemcov. HerMES: Far infrared properties of known AGN in the HerMES fields. Astronomy and Astrophysics, 518(2):1, 2010.

T. M. Heckman. An Optical and Radio Survey of the Nuclei of Bright Galaxies. Astronomy & Astrophysics, 87:152, 1980.

Timothy M. Heckman and Philip N. Best. The coevolution of galaxies and supermassive black holes: Insights from surveys of the contemporary universe. Annual Review of Astronomy and Astrophysics, 52:589–660, 2014.

Ryan C. Hickox, Christine Jones, William R. Forman, Stephen S. Murray, Christopher S. Kochanek, Daniel Eisenstein, Buell T. Jannuzi, Arjun Dey, Michael J.I. Brown, Daniel Stern, Peter R. Eisenhardt, Varoujan Gorjian, Mark Brodwin, Ramesh Narayan, Richard J. Cool, Almus Kenter, Nelson Caldwell, and Michael E. Anderson. Host galaxies, clustering, Eddington ratios, and evolution of radio, X-ray, and infrared-selected AGNs. Astrophysical Journal, 696(1):891–919, 2009.

Ryan C. Hickox, James R. Mullaney, David M. Alexander, Chien Ting J. Chen, Francesca M. Civano, Andy D. Goulding, and Kevin N. Hainline. Black hole variability and the star formation-active galactic nucleus connection: Do all star-forming galaxies host an active galactic nucleus? The Astrophysical Journal, 782(1):9–16, 2014.

P Hopkins, L Hernquist, T Cox, and D Kereš. A Cosmological Framework for the Co-Evolution of Quasars, Supermassive Black Holes, and Elliptical Galaxies. I. Galaxy Mergers and Quasar Activity. The Astrophysical Journal Supplement Series, 175:356–389, 2008.

Philip F. Hopkins. Dynamical delays between starburst and AGN activity in galaxy nuclei. Monthly Notices of the Royal Astronomical Society: Letters, 420(1):8–12, 2012.

Philip F. Hopkins and Lars Hernquist. a Characteristic Division Between the Fueling of Quasars and Seyferts: Five Simple Tests. The Astrophysical Journal, 694(1):599–609, 2009.

Philip F. Hopkins and Eliot Quataert. How do massive black holes get their gas? Monthly Notices of the Royal Astronomical Society, 407(3):1529–1564, 2010.

Philip F. Hopkins, Lars Hernquist, Thomas J. Cox, Tiziana Di Matteo, Paul Martini, Brant Robertson, and Volker Springel. Black Holes in Galaxy Mergers: Evolution of Quasars. The Astrophysical Journal, 630(2):705–715, 2005.

Philip F. Hopkins, Thomas J. Cox, Lars Hernquist, Desika Narayanan, Christopher C. Hayward, and Norman Murray. Star formation in galaxy mergers with realistic models of stellar feedback and the interstellar medium. Monthly Notices of the Royal Astronomical Society, 430(3):1901–1927, 2013.

Edwin Hubble. Cepheids in Spiral Nebulae. Popular Astronomy, 33:252, 1925.

Edwin Hubble. A Relation Between Distance and Radial Velocity Among Extra-Galactic Nebulae. Proceedings of the National Academy of Sciences of the United States of America, 15(3):168–173, 1929.

Edwin Hubble and Richard Tolman. Two methods of investigating the nature of the nebular red-shift* edwin hubble and richard c. tolman 1. The Astrophysical Journal, 82:302, 1935.

M. Huertas-Company, R. Gravet, G. Cabrera-Vives, P. G. Pérez-González, J. S. Kartaltepe, G. Barro, M. Bernardi, S. Mei, F. Shankar, P. Dimauro, E. F. Bell, D. Kocevski, D. C. Koo, S. M. Faber, and D. H. McIntosh. A catalog of visual-like morphologies in the 5 candels fields using deep learning. The Astrophysical Journal Supplement Series, 221(1):8, 2015.

Marc Huertas-Company, Vicente Rodriguez-Gomez, Dylan Nelson, Annalisa Pillepich, Connor Bottrell, Mariangela Bernardi, Helena Domínguez-Sánchez, Shy Genel, Ruediger Pakmor, Gregory F. Snyder, and Mark Vogelsberger. The Hubble Sequence at z 0 in the IllustrisTNG simulation with deep learning. Monthly Notices of the Royal Astronomical Society, 489(2):1859–1879, 2019.

Shuowen Jin, Emanuele Daddi, Daizhong Liu, Vernesa Smolcic, Eva Schinnerer, Antonello Calabrò, Qiusheng Gu, Jacinta Delhaize, Ivan Delvecchio, Yu Gao, Mara Salvato, Annagrazia Puglisi, Mark Dickinson, Frank Bertoldi, Mark Sargent, Mladen Novak, Georgios Magdis, Itziar Aretxaga, Grant W. Wilson, and Peter Capak. Super-deblended Dust Emission in Galaxies. II. Far-IR to (Sub) millimeter Photometry and High-redshift Galaxy Candidates in the Full COSMOS Field. The Astrophysical Journal, 864:56, 2018.

R. D. Joseph and G. S. Wright. Recent star formation in interacting galaxies - II. Super startbursts in merging galaxies. Monthly Notices of the Royal Astronomical Society, 214:87, 1985.

Stéphanie Juneau, Mark Dickinson, David M. Alexander, and Samir Salim. A new diagnostic of active galactic nuclei: Revealing highly absorbed systems at redshift >0.3. The Astrophysical Journal, 736(2), 2011.

Jeyhan S. Kartaltepe, Mark Mozena, Dale Kocevski, Daniel H. McIntosh, Jennifer Lotz, Eric F. Bell, Sandy Faber, Harry Ferguson, David Koo, Robert Bassett, Maksym Bernyk, Kirsten Blancato, Frederic Bournaud, Paolo Cassata, Marco Castellano, Edmond Cheung, Christopher J.

Conselice, Darren Croton, Tomas Dahlen, Duilia F. De Mello, Laura Degroot, Jennifer Donley, Javiera Guedes, Norman Grogin, Nimish Hathi, Matt Hilton, Brett Hollon, Anton Koekemoer, Nick Liu, Ray A. Lucas, Marie Martig, Elizabeth McGrath, Conor McPartland, Bahram Mobasher, Alice Morlock, Erin O'Leary, Mike Peth, Janine Pforr, Annalisa Pillepich, David Rosario, Emmaris Soto, Amber Straughn, Olivia Telford, Ben Sunnquist, Jonathan Trump, Benjamin Weiner, and Stijn Wuyts. Candels visual classifications: Scheme, data release, and first results. The Astrophysical Journal Supplement Series, 221(1):1–17, 2015.

Guinevere Kauffmann, Timothy M Heckman, Christy Tremonti, Stéphane Chariot, Simon D M White, Susan E Ridgway, Jon Brinkmann, Masataka Fukugita, Patrick B Hall, Zeljko Ivezic, Gordon T. Richards, and Donald P. Schneider. The host galaxies of active galactic nuclei Guinevere. Monthly Notices of the Royal Astronomical Society, 346:1055, 2003.

Lisa J. Kewley, Brent Groves, Guinevere Kauffmann, and Tim Heckman. The host galaxies and classification of active galactic nuclei. Monthly Notices of the Royal Astronomical Society, 372: 961, 2006.

Johan H. Knapen, Mauricio Cisternas, and Miguel Querejeta. Interacting galaxies in the nearby Universe: Only moderate increase of star formation. Monthly Notices of the Royal Astronomical Society, 454(2):1742, 2015.

Dale D. Kocevski, S. M. Faber, Mark Mozena, Anton M. Koekemoer, Kirpal Nandra, Cyprian Rangel, Elise S. Laird, Marcella Brusa, Stijn Wuyts, Jonathan R. Trump, David C. Koo, Rachel S. Somerville, Eric F. Bell, Jennifer M. Lotz, David M. Alexander, Frederic Bournaud, Christopher J. Conselice, Tomas Dahlen, Avishai Dekel, Jennifer L. Donley, James S. Dunlop, Alexis Finoguenov, Antonis Georgakakis, Mauro Giavalisco, Yicheng Guo, Norman A. Grogin, Nimish P. Hathi, Stéphanie Juneau, Jeyhan S. Kartaltepe, Ray A. Lucas, Elizabeth J. McGrath, Daniel H. McIntosh, Bahram Mobasher, Aday R. Robaina, David Rosario, Amber N. Straughn, Arjen van der Wel, and Carolin Villforth. CANDELS: Constraining the AGN-Merger Connection with Host Morphologies at z 2. The Astrophysical Journal, 744:148, 2012.

Dale D. Kocevski, Murray Brightman, Kirpal Nandra, Anton M. Koekemoer, Mara Salvato, James Aird, Eric F. Bell, Li Ting Hsu, Jeyhan S. Kartaltepe, David C. Koo, Jennifer M. Lotz, Daniel H. McIntosh, Mark Mozena, David Rosario, and Jonathan R. Trump. Are Compton-Thick AGNs the Missing Link Between Mergers and Black Hole Growth? The Astrophysical Journal, 814(2): 104, 2015.

A.M. Koekemoer, H. Aussel, D. Calzetti, P. Capak, M. Giavalisco, J.-P. Kneib, A. Leauthaud, O. Le Fèvre, H.J. Mccracken, R. Massey, B. Mobasher, J. Rhodes, N. Scoville, and P.L. Shopbell. The COSMOS survey: Hubble Space Telescope Advanced Camera for Surveys observations and data processing. The Astrophysical Journal Supplement Series, 172(1):196–202, 2007.

S Komossa, V Burwitz, G Hasinger, P Predehl, J S Kaastra, and Y Ikebe. Discovery of a Binary Active Galactic Nucleus in the Ultraluminous Infrared Galaxy NGC 6240 Using Chandra. The Astrophysical Journal Letters, 582(1):L15–L19, 2003.

John Kormendy and Ralf Bender. A revised parallel-sequence morphological classification of galaxies: Structure and formation of S0 and spheroidal galaxies. Astrophysical Journal, Supplement Series, 198(1), 2012.

John Kormendy and Luis C. Ho. Coevolution (Or Not) of Supermassive Black Holes and Host Galaxies. Annual Review of Astronomy and Astrophysics, 51:511, 2013.

John Kormendy and Douglas Richstone. Inward Bound – The Search for Supermassive Black Holes in Galactic Nuclei. Annual Review of Astronomy and Astrophysics, 33:581, 1995.

Michael Koss, Richard Mushotzky, Ezequiel Treister, Sylvain Veilleux, Ranjan Vasudevan, and Margaret Trippe. Understanding Dual Active Galactic Nucleus Activation in the Nearby Universe. The Astrophysical Journal Letters, 746(2):L22–L28, 2012.

M Lacy, A Sajina, P N Appleton, L Armus, S C Chapman, P I Choi, D Fadda, F Fang, D T Frayer, I Heinrichsen, G Helou, M Im, F R Marleau, F Masci, D L Shupe, B T Soifer, J Surace, H I Teplitz, G Wilson, and L Yan. Obscured and Unobscured Active Galactic Nuclei in the Spitzer Space Telescope First Look Survey. The Astrophysical Journal Supplement Series, 154:166, 2004.

M. Lacy, A. O. Petric, A. Sajina, G. Canalizo, L. J. Storrie-Lombardi, L. Armus, D. Fadda, and F. R. Marleau. Optical Spectroscopy and X-ray Detections of a Sample of Quasars and Active Galactic Nuclei Selected in the Mid-Infrared From Two Spitzer Space Telescope Wide-Area Surveys. The Astronomical Journal, 133:186, 2007.

C. Laigle, H. J. McCracken, O. Ilbert, B. C. Hsieh, I. Davidzon, P. Capak, G. Hasinger, J. D. Silverman, C. Pichon, J. Coupon, H. Aussel, D. Le Borgne, K. Caputi, P. Cassata, Y. Y. Chang, F. Civano, J. Dunlop, J. Fynbo, J. S. Kartaltepe, A. Koekemoer, O. Le Fevre, E. Le Floc'h, A. Leauthaud, S. Lilly, L. Lin, S. Marchesi, B. Milvang-Jensen, M. Salvato, D. B. Sanders, N. Scoville, V. Smolcic, M. Stockmann, Y. Taniguchi, L. Tasca, S. Toft, M. Vaccari, and J. Zabl. The COSMOS2015 Catalog: Exploring the 1<z<6 Universe with half a million galaxies. The Astrophysical Journal Supplement Series, 224(2):24–46, 2016.

G. Lanzuisi, E. Piconcelli, F. Fiore, C. Feruglio, C. Vignali, M. Salvato, and C. Gruppioni. Revealing X-ray obscured quasars in SWIRE sources with extreme mid-IR/optical flux ratios. Astronomy and Astrophysics, 498(1):67–81, 2009.

G Lanzuisi, I Delvecchio, S Berta, M Brusa, A Comastri, R Gilli, C Gruppioni, S Marchesi, M Perna, F Pozzi, M Salvato, M Symeonidis, C Vignali, F Vito, M Volonteri, and G Zamorani. Active galactic nuclei vs. host galaxy properties in the COSMOS field. Astronomy & Astrophysics, 602: A123, 2017.

S. J. Lilly, L. Tresse, F. Hammer, David Crampton, and O. Le Fevre. The Canada-France Redshift Survey. VI. Evolution of the Galaxy Luminosity Function to z˜1. The Astrophysical Journal, 455:108, 1995.

Xin Liu, Jenny E. Greene, Yue Shen, and Michael A. Strauss. Discovery of Four kpc-Scale Binary Active Galactic Nuclei. The Astrophysical Journal Letters, 715(1):L30–L34, 2010.

Xin Liu, Francesca Civano, Yue Shen, Paul Green, Jenny E. Greene, and Michael A. Strauss. Chandra X-ray and Hubble Space Telescope Imaging of Optically Selected Kiloparsec-Scale Binary Activ Galactic Nuclei. I. Nature of the Nuclear Ionizing Sources. The Astrophysical Journal, 762 (2):110–127, 2013.

Jennifer M. Lotz, Joel Primack, and Piero Madau. A New Nonparametric Approach to Galaxy Morphological Classification. The Astronomical Journal, 128(1):163–182, 2004.

Jennifer M. Lotz, Patrik Jonsson, T. J. Cox, and Joel R. Primack. Galaxy merger morphologies and time-scales from simulations of equal-mass gas-rich disc mergers. Monthly Notices of the Royal Astronomical Society, 391(3):1137–1162, 2008.

Jennifer M. Lotz, Patrik Jonsson, T. J. Cox, and Joel R. Primack. The effect of gas fraction on the morphology and time-scales of disc galaxy mergers. Monthly Notices of the Royal Astronomical Society, 404(2):590–603, 2010a.

Jennifer M. Lotz, Patrik Jonsson, T. J. Cox, and Joel R. Primack. The effect of mass ratio on the morphology and time-scales of disc galaxy mergers. Monthly Notices of the Royal Astronomical Society, 404(2):575–589, 2010b.

Jennifer M. Lotz, Patrik Jonsson, T. J. Cox, Darren Croton, Joel R. Primack, Rachel S. Somerville, and Kyle Stewart. The Major and Minor Galaxy Merger Rates at z $<$ 1.5. The Astrophysical Journal, 742(2):103–124, 2011.

D. Lutz, V. Mainieri, D. Rafferty, L. Shao, G. Hasinger, A. Wei, F. Walter, I. Smail, D. M. Alexander, W. N. Brandt, S. Chapman, K. Coppin, N. M. Förster Schreiber, E. Gawiser, R. Genzel, T. R. Greve, R. J. Ivison, A. M. Koekemoer, P. Kurczynski, K. M. Menten, R. Nordon, P. Popesso, E. Schinnerer, J. D. Silverman, J. Wardlow, and Y. Q. Xue. The laboca survey of the extended chandra deep field south: Two modes of star formation in active galactic nucleus hosts? The Astrophysical Journal, 712(2):1287–1301, 2010.

D. Lynden-Bell. Galactic nuclei as collapsed old quasars. Nature, 223:690, 1969.

Witold Maciejewski. Nuclear spirals in galaxies: Gas response to an asymmetric potential - II. Hydrodynamical models. Monthly Notices of the Royal Astronomical Society, 354(3):892–904, 2004.

Piero Madau and Mark Dickinson. Cosmic Star-Formation History. Annual Review of Astronomy and Astrophysics, 52:415, 2014.

Piero Madau, Lucia Pozzetti, and Mark Dickinson. The Star Formation History of Field Galaxies. The Astrophysical Journal, 498:106–116, 1998.

John Magorrian, Scott Tremaine, Douglas Richstone, Ralf Bender, Gary Bower, Alan Dressler, S. M. Faber, Richard Green, Carl Grillmair, John Kormendy, and Tod Lauer. The Demography of Massive Dark Objects in Galaxy Centers. The Astronomical Journal, 115(1):2285–2305, 1998.

R. Maiolino, A. Marconi, M. Salvati, G. Risaliti, P. Severgnini, E. Oliva, F. La Franca, and L. Vanzi. Dust in active nuclei: I. Evidence for anomalous properties. Astronomy and Astrophysics, 365: 28, 2001.

Allison W. S. Man, Andrew W. Zirm, and Sune Toft. Resolving the Discrepency of Galaxy Merger Fraction Measurements at z 03. The Astrophysical Journal, 830(2):89, 2016.

S. Marchesi, F. Civano, M. Elvis, M. Salvato, M. Brusa, A. Comastri, R. Gilli, G. Hasinger, G. Lanzuisi, T. Miyaji, E. Treister, C. M. Urry, C. Vignali, G. Zamorani, V. Allevato, N. Cappelluti, C. Cardamone, A. Finoguenov, R. E. Griffiths, A. Karim, C. Laigle, S. M. LaMassa, K. Jahnke, P. Ranalli, K. Schawinski, E. Schinnerer, J. D. Silverman, V. Smolcic, H. Suh, and B. Trakhtenbrot. The Chandra Cosmos Legacy Survey: Optical/Ir Identifications. The Astrophysical Journal, 817(1):34, 2016.

A. Marconi, G. Risaliti, R. Gilli, L. K. Hunt, R. Maiolino, and M. Salvati. Local supermassive black holes, relics of active galactic nuclei and the X-ray background. Monthly Notices of the Royal Astronomical Society, 351(1):169–185, 2004.

Alessandro Marconi and Leslie K Hunt. The Relation Between Black Hole Mass, Bulge Mass, and Near-Infrared Luminosity. The Astrophysical Journal Letters, 589:21, 2003.

S. Mateos, A. Alonso-Herrero, F. J. Carrera, A. Blain, M. G. Watson, X. Barcons, V. Braito, P. Severgnini, J. L. Donley, and D. Stern. Using the Bright Ultrahard XMM-Newton survey to define an IR selection of luminous AGN based on WISE colours. Monthly Notices of the Royal Astronomical Society, 426(4):3271–3281, 2012.

R. C. McGurk, C. E. Max, A. M. Medling, G. A. Shields, and J. M. Comerford. Spatially Resolved Imaging and Spectroscopy of Candidate Dual Active Galactic Nuclei. The Astrophysical Journal, 811(1):14, 2015.

Alexander J. Mendez, Alison L. Coil, James Aird, Aleksandar M. Diamond-Stanic, John Moustakas, Michael R. Blanton, Richard J. Cool, Daniel J. Eisenstein, Kenneth C. Wong, and Guangtun Zhu. PRIMUS: Infrared and X-ray AGN Selection Techniques at $0.2 < z < 1.2$. The Astrophysical Journal, 770(1):40–64, 2013.

M. Milosavljevic and D. Merritt. Formation of galactic nuclei. The Astrophysical Journal, 563(1): 34–62, 2001.

Ivelina G. Momcheva, Gabriel B. Brammer, Pieter G. van Dokkum, Rosalind E. Skelton, Katherine E. Whitaker, Erica J. Nelson, Mattia Fumagalli, Michael V. Maseda, Joel Leja, Marijn Franx, Hans-Walter Rix, Rachel Bezanson, Elisabete Da Cunha, Claire Dickey, Natascha M. Förster Schreiber, Garth Illingworth, Mariska Kriek, Ivo Labbé, Johannes Ulf Lange, Britt F. Lundgren, Daniel Magee, Danilo Marchesini, Pascal Oesch, Camilla Pacifici, Shannon G. Patel, Sedona Price, Tomer Tal, David A. Wake, Arjen van der Wel, and Stijn Wuyts. the 3D-Hst Survey: Hubble Space Telescope Wfc3/G141 Grism Spectra, Redshifts, and Emission Line Measurements for 100,000 Galaxies . The Astrophysical Journal Supplement Series, 225(2):27, 2016.

Jorge Moreno, Paul Torrey, Sara L. Ellison, David R. Patton, Asa F.L. Bluck, Gunjan Bansal, and Lars Hernquist. Mapping galaxy encounters in numerical simulations: The spatial extent of induced star formation. Monthly Notices of the Royal Astronomical Society, 448(2):1107–1117, 2015.

Jorge Moreno, Paul Torrey, Sara L. Ellison, David R. Patton, Philip F. Hopkins, Michael Bueno, Christopher C. Hayward, Desika Narayanan, Dušan Kereš, Asa F.L. Bluck, and Lars Hernquist. Interacting galaxies on FIRE-2: The connection between enhanced star formation and interstellar gas content. Monthly Notices of the Royal Astronomical Society, 485(1):1320, 2019.

J. R. Mullaney, E. Daddi, M. Béthermin, D. Elbaz, S. Juneau, M. Pannella, M. T. Sargent, D. M. Alexander, and R. C. Hickox. The hidden "agn main sequence": Evidence for a universal black hole accretion to star formation rate ratio since z 2 producing an M BH-M* relation. The Astrophysical Journal Letters, 753:L30, 2012.

J. R. Mullaney, D. M. Alexander, J. Aird, E. Bernhard, E. Daddi, A. Del Moro, M. Dickinson, D. Elbaz, C. M. Harrison, S. Juneau, D. Liu, M. Pannella, D. Rosario, P. Santini, M. Sargent,

C. Schreiber, J. Simpson, and F. Stanley. ALMA and Herschel reveal that X-ray-selected AGN and main-sequence galaxies have different star formation rate distributions. Monthly Notices of the Royal Astronomical Society: Letters, 453:L83, 2015.

F. Müller-Sánchez, R. I. Davies, R. Genzel, L. J. Tacconi, F. Eisenhauer, E. K.S. Hicks, S. Friedrich, and A. Sternberg. Molecular gas streamers feeding and obscuring the active nucleus of NGC 1068. The Astrophysical Journal, 691(1):749–759, 2009.

F. Müller-Sánchez, Julia M. Comerford, Rebecca Nevin, R. Scott Barrows, Michael C. Cooper, and Jenny E. Greene. The Origin of Double-Peaked Narrow Lines in Active Galactic Nuclei. I. Very Large Array Detections of Dual AGNs and AGN Outflows. The Astrophysical Journal, 813(2): 103, 2015.

Ramesh Narayan and Insu Yi. Advection-Dominated Accretion: A Self-Similar Solution. The Astrophysical Journal Letters, 428:L13, 1994.

Dylan Nelson, Annalisa Pillepich, Volker Springel, Rainer Weinberger, Lars Hernquist, Rüdiger Pakmor, Shy Genel, Paul Torrey, Mark Vogelsberger, Guinevere Kauffmann, Federico Marinacci, and Jill Naiman. First results from the IllustrisTNG simulations: The galaxy colour bimodality. Monthly Notices of the Royal Astronomical Society, 475(1):624–647, 2018.

Dylan Nelson, Volker Springel, Annalisa Pillepich, Vicente Rodriguez-Gomez, Paul Torrey, Shy Genel, Mark Vogelsberger, Ruediger Pakmor, Federico Marinacci, Rainer Weinberger, Luke Kelley, Mark Lovell, Benedikt Diemer, and Lars Hernquist. The IllustrisTNG simulations: public data release. Computational Astrophysics and Cosmology, 6(1):1–30, 2019.

Hagai Netzer. Accretion and star formation rates in low-redshift type II active galactic nuclei. Monthly Notices of the Royal Astronomical Society, 399:1907, 2009.

R. Nevin, L. Blecha, J. Comerford, and J. Greene. Accurate Identification of Galaxy Mergers with Imaging. The Astrophysical Journal, 872(1):76, 2019.

Rebecca Nevin, Julia Comerford, Francisco Müller-Sánchez, R. Barrows, and Michael Cooper. The Origins of Double-Peaked Narrow Lines in Active Galactic Nuclei. II. Kinematic Classifications for the Population at z $<$ 0.1. The Astrophysical Journal, 832(1):67–88, 2016.

K. G. Noeske, B. J. Weiner, S. M. Faber, C. Papovich, D. C. Koo, R. S. Somerville, K. Bundy, C. J. Conselice, J. A. Newman, D. Schiminovich, E. Le Floc'h, A. L. Coil, G. H. Rieke, J. M. Lotz, J. R. Primack, P. Barmby, M. C. Cooper, M. Davis, R. S. Ellis, G. G. Fazio, P. Guhathakurta, J. Huang, S. A. Kassin, D. C. Martin, A. C. Phillips, R. M. Rich, T. A. Small, C. N. A. Willmer, and G. Wilson. Star Formation in AEGIS Field Galaxies since z=1.1 : The Dominance of Gradually Declining Star Formation, and the Main Sequence of Star-Forming Galaxies. The Astrophysical Journal Letters, 660:L43, 2007.

P. Padovani, D. M. Alexander, R. J. Assef, B. De Marco, P. Giommi, R. C. Hickox, G. T. Richards, V. Smolčić, E. Hatziminaoglou, V. Mainieri, and M. Salvato. Active galactic nuclei: what's in a name? Astronomy and Astrophysics Review, 25(1), 2017.

David R. Patton, Paul Torrey, Sara L. Ellison, J. Trevor Mendel, and Jillian M. Scudder. Galaxy pairs in the sloan digital sky survey - 6. The orbital extent of enhanced star formation in interacting galaxies. Monthly Notices of the Royal Astronomical Society: Letters, 433(1):59–63, 2013.

M. M. Pawlik, V. Wild, C. J. Walcher, P. H. Johansson, C. Villforth, K. Rowlands, J. Mendez-Abreu, and T. Hewlett. Shape asymmetry: A morphological indicator for automatic detection of galaxies in the post-coalescence merger stages. Monthly Notices of the Royal Astronomical Society, 456(3):3032–3052, 2016.

Chien Y. Peng, Luis C. Ho, Chris D. Impey, and Hans-Walter Rix. Detailed Structural Decomposition of Galaxy Images. The Astronomical Journal, 124:266–293, 2002.

Chien Y. Peng, Luis C. Ho, Chris D. Impey, and Hans-Walter Rix. Detailed Decomposition of Galaxy Images. II. Beyond Axisymmetric Models. The Astronomical Journal, 139(6):2097–2129, 2010.

Ying Jie Peng, Simon J. Lilly, Alvio Renzini, and Marcella Carollo. Mass and environment as drivers of galaxy evolution. II. the quenching of satellite galaxies as the origin of environmental effects. The Astrophysical Journal, 757(1), 2012.

Ryan W. Pfeifle, Shobita Satyapal, Nathan J. Secrest, Mario Gliozzi, Claudio Ricci, Sara L. Ellison, Barry Rothberg, Jenna Cann, Laura Blecha, James K. Williams, and Anca Constantin. Buried Black Hole Growth in IR-selected Mergers: New Results from Chandra . The Astrophysical Journal, 875(2):117, 2019.

Annalisa Pillepich, Dylan Nelson, Lars Hernquist, Volker Springe, Rüdiger Pakmor, Paul Torrey, Rainer Weinberger, Shy Gene, Jill P. Naiman, Federico Marinacci, and Mark Vogelsberger. First results from the illustristng simulations: The stellar mass content of groups and clusters of galaxies. Monthly Notices of the Royal Astronomical Society, 475(1):648–675, 2018.

Planck Collaboration, P. Ade, N. Aghanim, M. Arnaud, and M. Ashdown. Planck 2015 Results XIII. Cosmological Parameters. Astronomy and Astrophysics, 594:A13, 2016.

Chris Power, Sergei Nayakshin, and Andrew King. The accretion disc particle method for simulations of black hole feeding and feedback. Monthly Notices of the Royal Astronomical Society, 412(1):269–276, 2011.

P. Ranalli, A. Comastri, and G. Setti. The 210 keV luminosity as a Star Formation Rate indicator. Astronomy and Astrophysics, 399(1):39–50, 2003.

M.J. Rees. Black Hole Models for Active Galactic Nuclei. Annual Review of Astronomy and Astrophysics, 22:471, 1984.

Angelo Ricarte, Michael Tremmel, Priyamvada Natarajan, and Thomas Quinn. Tracing black hole and galaxy co-evolution in the ROMULUS simulations. Monthly Notices of the Royal Astronomical Society, 489(1):802–819, 2019.

C. Ricci, F. E. Bauer, E. Treister, K. Schawinski, G. C. Privon, L. Blecha, P. Arevalo, L. Armus, F. Harrison, L. C. Ho, K. Iwasawa, D. B. Sanders, and D. Stern. Growing supermassive black holes in the late stages of galaxy mergers are heavily obscured. Monthly Notices of the Royal Astronomical Society, 468(2):1273–1299, 2017.

Vicente Rodriguez-Gomez, Shy Genel, Mark Vogelsberger, Debora Sijacki, Annalisa Pillepich, Laura V. Sales, Paul Torrey, Greg Snyder, Dylan Nelson, Volker Springel, Chung Pei Ma, and

Lars Hernquist. The merger rate of galaxies in the Illustris simulation: A comparison with observations and semi-empirical models. Monthly Notices of the Royal Astronomical Society, 449 (1):49–64, 2015.

Vicente Rodriguez-Gomez, Gregory F. Snyder, Jennifer M. Lotz, Dylan Nelson, Annalisa Pillepich, Volker Springel, Shy Genel, Rainer Weinberger, Sandro Tacchella, Rudiger Pakmor, Paul Torrey, Federico Marinacci, Mark Vogelsberger, Lars Hernquist, and David A. Thilker. The optical morphologies of galaxies in the IllustrisTNG simulation: A comparison to Pan-STARRS observations. Monthly Notices of the Royal Astronomical Society, 483(3):4140–4159, 2019.

D. J. Rosario, G. A. Shields, G. B. Taylor, S. Salviander, and K. L. Smith. The jet-driven outflow in the radio galaxy SDSS J1517+3353: Implications for double-peaked narrow-line active galactic nucleus. The Astrophysical Journal, 716(1):131–143, 2010.

D. J. Rosario, R. C. McGurk, C. E. Max, G. A. Shields, K. L. Smith, and S. M. Ammons. Adaptive Optics Imaging of Quasi-Stellar Objects With Double-Peaked Narrow Lines: Are They Dual Active Galactic Nuclei? The Astrophysical Journal, 739(1):44–51, 2011.

D. J. Rosario, B. Trakhtenbrot, D. Lutz, H. Netzer, J. R. Trump, J. D. Silverman, M. Schramm, E. Lusso, S. Berta, A. Bongiorno, M. Brusa, N. M. Förster-Schreiber, R. Genzel, S. Lilly, B. Magnelli, V. Mainieri, R. Maiolino, A. Merloni, M. Mignoli, R. Nordon, P. Popesso, M. Salvato, P. Santini, L. J. Tacconi, and G. Zamorani. The mean star-forming properties of QSO host galaxies. Astronomy and Astrophysics, 560:A72, 2013.

D.J. Rosario, P. Santini, D. Lutz, L. Shao, R. Maiolino, D.M. Alexander, B. Altieri, P. Andreani, H. Aussel, F.E. Bauer, S. Berta, A. Bongiovanni, W.N. Brandt, M. Brusa, J. Cepa, A. Cimatti, T.J. Cox, E. Daddi, D. Elbaz, A. Fontana, N.M. Förster Schreiber, R. Genzel, A. Grazian, E. Le Floch, B. Magnelli, V. Mainieri, H. Netzer, R. Nordon, I. Pérez Garcia, A. Poglitsch, P. Popesso, F. Pozzi, L. Riguccini, G. Rodighiero, M. Salvato, M. Sanchez-Portal, E. Sturm, L.J. Tacconi, I. Valtchanov, and S. Wuyts. The mean star formation rate of X-ray selected active galaxies and its evolution from z ˜ 2.5: results from PEP- Herschel. Astronomy and Astrophysics, 545:A45, 2012.

Yetli M. Rosas-Guevara, Richard G. Bower, Stuart McAlpine, Silvia Bonoli, and Patricia B. Tissera. The abundances and properties of Dual AGN and their host galaxies in the EAGLE simulations. Monthly Notices of the Royal Astronomical Society, 483(2):2712–2720, 2019.

K. Rubinur, M. Das, and P. Kharb. Searching for dual active galactic nuclei. Journal of Astrophysics and Astronomy, 39(1):1–8, 2018.

R. E. Ryan, S. H. Cohen, R. A. Windhorst, and J. Silk. Galaxy Mergers at z 1 in the HUDF: Evidence for a Peak in the Major Merger Rate of Massive Galaxies1. The Astrophysical Journal, 678(2):751–757, 2008.

Allan Sandage. The Ability of the 200-Inch Telescope to Discriminate Between Selected World Models. The Astrophysical Journal, 133(2):355, 1961.

D. B. Sanders, B.T. Soifer, J.H. Elias, B.F. Madore, K. Matthew, G. Neugebauer, and N.Z. Scoville. Ultraluminous Infrared Galaxies and the Origin of Quasars. The Astrophysical Journal, 325:74, 1988.

Marc Sarzi, Joseph C. Shields, Kevin Schawinski, Hyunjin Jeong, Kristen Shapiro, Roland Bacon, Martin Bureau, Michele Cappellari, Roger L. Davies, P. Tim de Zeeuw, Eric Emsellem, Jesús Falcón-Barroso, Davor Krajnović, Harald Kuntschner, Richard M. McDermid, Reynier F. Peletier, Remco C.E. van den Bosch, Glen van de Ven, and Sukyoung K. Yi. The SAURON project - XVI. On the sources of ionization for the gas in elliptical and lenticular galaxies. Monthly Notices of the Royal Astronomical Society, 402(4):2187, 2010.

Shobita Satyapal, Sara L Ellison, William McAlpine, Ryan C Hickox, David R Patton, and J. Trevor Mendel. Galaxy pairs in the Sloan Digital Sky Survey - IX. Merger-induced AGN activity as traced by the Wide-field Infrared Survey Explorer. Monthly Notices of the Royal Astronomical Society, 441(2):1297–1304, 2014.

Shobita Satyapal, Nathan J. Secrest, Claudio Ricci, Sara L. Ellison, Barry Rothberg, Laura Blecha, Anca Constantin, Mario Gliozzi, Paul McNulty, and Jason Ferguson. Buried AGNs in Advanced Mergers: Mid-infrared Color Selection as a Dual AGN Candidate Finder. The Astrophysical Journal, 848(2):126, 2017.

Kevin Schawinski, Shanil Virani, Brooke Simmons, C. Megan Urry, Ezequiel Treister, Sugata Kaviraj, and Bronika Kushkuley. Do moderate-luminosity active galactic nuclei suppress star formation? Astrophysical Journal, 692(1):19–23, 2009.

Kevin Schawinski, C. Megan Urry, Brooke D. Simmons, Lucy Fortson, Sugata Kaviraj, William C. Keel, Chris J. Lintott, Karen L. Masters, Robert C. Nichol, Marc Sarzi, Ramin Skibba, Ezequiel Treister, Kyle W. Willett, O. Ivy Wong, and Sukyoung K. Yi. The green valley is a red herring: Galaxy Zoo reveals two evolutionary pathways towards quenching of star formation in early-and late-type galaxies. Monthly Notices of the Royal Astronomical Society, 440(1):889–907, 2014.

M. Schmidt. 3C 273: A star-like object with large red-shift, 1963.

Corentin Schreiber, Maurilio Pannella, David Elbaz, Matthieu Béthermin, Hanae Inami, Mark E. Dickinson, Benjamin Magnelli, Tao Wang, Hervé Aussel, Emanuele Daddi, Stéphanie Juneau, Xinwen Shu, Mark T. Sargent, Véronique Buat, Sandra M. Faber, Henry C. Ferguson, Mauro Giavalisco, Anton M. Koekemoer, Georgios Magdis, Glenn E. Morrison, Casey Papovich, Paola Santini, and Douglas Scott. The Herschel view of the dominant mode of galaxy growth from z=4 to the present day. Astronomy and Astrophysics, 575:A74, 2015.

N. Scoville, R. G. Abraham, H. Aussel, J. E. Barnes, A. Benson, A. W. Blain, D. Calzetti, A. Comastri, P. Capak, C. Carilli, J. E. Carlstrom, C. M. Carollo, J. Colbert, E. Daddi, R. S. Ellis, M. Elvis, S. P. Ewald, M. Fall, A. Franceschini, M. Giavalisco, W. Green, R. E. Griffiths, L. Guzzo, G. Hasinger, C. Impey, J.P. Kneib, J. Koda, A. Koekemoer, O. Lefevre, S. Lilly, C. T. Liu, H. J. McCracken, R. Massey, Y. Mellier, S. Miyazaki, B. Mobasher, J. Mould, C. Norman, A. Refregier, A. Renzini, J. Rhodes, M. Rich, D. B. Sanders, D. Schiminovich, E. Schinnerer, M. Scodeggio, K. Sheth, P. L. Shopbell, Y. Taniguchi, N. D. Tyson, C. M. Urry, L. Van Waerbeke, P. Vettolani, S. D. M. White, and L. Yan. COSMOS: Hubble Space Telescope Observations. The Astrophysical Journal Supplement Series, 172(1):38–45, 2007.

J. L. Sérsic. Influence of the atmospheric and instrumental dispersion on the brightness distribution in a galaxy. Boletin de la Asociacion Argentina de Astronomia La Plata Argentina, 6:41, 1963.

Carl K Seyfert. Nuclear Emission in Spiral Nebulae. The Astrophysical Journal, 97:285, 1943.

N. I. Shakura and R. A. Sunyaev. Black Holes in Binary Systems. Observational Appearance. Astronomy & Astrophysics, 24:337, 1973.

Francesco Shankar, David H. Weinberg, and Jordi Miralda-Escudé. Self-consistent models of the AGN and black hole populations: Duty cycles, accretion rates, and the mean radiative efficiency. The Astrophysical Journal, 690:20, 2009.

L. Shao, D. Lutz, R. Nordon, R. Maiolino, D. M. Alexander, B. Altieri, P. Andreani, H. Aussel, F. E. Bauer, S. Berta, A. Bongiovanni, W. N. Brandt, M. Brusa, A. Cava, J. Cepa, A. Cimatti, E. Daddi, H. Dominguez-Sanchez, D. Elbaz, N. M. Förster Schreiber, N. Geis, R. Genzel, A. Grazian, C. Gruppioni, G. Magdis, B. Magnelli, V. Mainieri, A. M. Pérez García, A. Poglitsch, P. Popesso, F. Pozzi, L. Riguccini, G. Rodighiero, E. Rovilos, A. Saintonge, M. Salvato, M. Sanchez Portal, P. Santini, E. Sturm, L. J. Tacconi, I. Valtchanov, M. Wetzstein, and E. Wieprecht. Star formation in AGN hosts in GOODS-N. Astronomy and Astrophysics, 518: L26, 2010.

Yue Shen, Xin Liu, Jenny E. Greene, and Michael A. Strauss. Type 2 active galactic nuclei with double-peaked [O III] lines. II. single agns with complex narrow-line region kinematics are more common than binary AGNs. The Astrophysical Journal, 735(1), 2011.

Ravi K. Sheth and Rien Van De Weygaert. A hierarchy of voids: Much ado about nothing. Monthly Notices of the Royal Astronomical Society, 350(2):517–538, 2004.

T. T. Shimizu, Richard F. Mushotzky, Marcio Meléndez, Michael Koss, and David J. Rosario. Decreased specific star formation rates in AGN host galaxies. Monthly Notices of the Royal Astronomical Society, 452(2):1841–1860, 2015.

T. Taro Shimizu, Richard F. Mushotzky, Marcio Meléndez, Michael J. Koss, Amy J. Barger, and Lennox L. Cowie. Herschel far-infrared photometry of the Swift Burst Alert Telescope active galactic nuclei sample of the local universe - III. Global star-forming properties and the lack of a connection to nuclear activity. Monthly Notices of the Royal Astronomical Society, 466(3): 3161–3183, 2017.

Joseph Silk and Martin J. Rees. Quasars and Galaxy Formation. Astronomy & Astrophysics, 331: L1, 1998.

J. D. Silverman, P. J. Green, W. A. Barkhouse, D.W. Kim, M. Kim, B. J. Wilkes, R. A. Cameron, G. Hasinger, B. T. Jannuzi, M. G. Smith, P. S. Smith, and H. Tananbaum. The Luminosity Function of XRayselected Active Galactic Nuclei: Evolution of Supermassive Black Holes at High Redshift. The Astrophysical Journal, 679:118, 2008.

John D. Silverman, Shenli Tang, Khee-Gan Lee, Tilman Hartwig, Andy Goulding, Michael A. Strauss, Malte Schramm, Xuheng Ding, Rogemar A. Riffel, Seiji Fujimoto, Chiaki Hikage, Masatoshi Imanishi, Kazushi Iwasawa, Knud Jahnke, Issha Kayo, Nobunari Kashikawa, Toshihiro Kawaguchi, Kotaro Kohno, Wentao Luo, Yoshiki Matsuoka, Yuichi Matsuda, Tohru Nagao, Masamune Oguri, Yoshiaki Ono, Masafusa Onoue, Masami Ouchi, Kazuhiro Shimasaku, Hyewon Suh, Nao Suzuki, Yoshiaki Taniguchi, Yoshiki Toba, Yoshihiro Ueda, and Naoki Yasuda. Dual Supermassive Black Holes at Close Separation Revealed by the Hyper Suprime-Cam Subaru Strategic Program. The Astrophysical Journal, 899(2):154, 2020.

B. D. Simmons, C. M. Urry, K. Schawinski, C. Cardamone, and E. Glikman. Moderate-luminosity growing black holes from 1.25 < z < 2.7: Varied accretion in disk-dominated hosts. The Astrophysical Journal, 761(1), 2012.

B. D. Simmons, Chris Lintott, Kyle W. Willett, Karen L. Masters, Jeyhan S. Kartaltepe, Boris Häußler, Sugata Kaviraj, Coleman Krawczyk, S. J. Kruk, Daniel H. McIntosh, R. J. Smethurst, Robert C. Nichol, Claudia Scarlata, Kevin Schawinski, Christopher J. Conselice, Omar Almaini, Henry C. Ferguson, Lucy Fortson, William Hartley, Dale Kocevski, Anton M. Koekemoer, Alice Mortlock, Jeffrey A. Newman, Steven P. Bamford, N. A. Grogin, Ray A. Lucas, Nimish P. Hathi, Elizabeth McGrath, Michael Peth, Janine Pforr, Zachary Rizer, Stijn Wuyts, Guillermo Barro, Eric F. Bell, Marco Castellano, Tomas Dahlen, Avishai Dekel, Jamie Ownsworth, Sandra M. Faber, Steven L. Finkelstein, Adriano Fontana, Audrey Galametz, Ruth Grützbauch, David Koo, Jennifer Lotz, Bahram Mobasher, Mark Mozena, Mara Salvato, and Tommy Wiklind. Galaxy Zoo: Quantitative visual morphological classifications for 48 000 galaxies from CANDELS. Monthly Notices of the Royal Astronomical Society, 464(4):4420–4447, 2017.

Gregory F. Snyder, Vicente Rodriguez-Gomez, Jennifer M. Lotz, Paul Torrey, Amanda C.N. Quirk, Lars Hernquist, Mark Vogelsberger, and Peter E. Freeman. Automated distant galaxy merger classifications from Space Telescope images using the Illustris simulation. Monthly Notices of the Royal Astronomical Society, 486(3):3702–3720, 2019.

Rachel S Somerville, Joel R Primack, and S M Faber. The nature of high-redshift galaxies. Monthly Notices of the Royal Astronomical Society, 320:504–528, 2001.

Rachel S. Somerville, Philip F. Hopkins, Thomas J. Cox, Brant E. Robertson, and Lars Hernquist. A semi-analytic model for the co-evolution of galaxies, black holes and active galactic nuclei. Monthly Notices of the Royal Astronomical Society, 391(2):481–506, 2008.

Volker Springel, Tiziana Di Matteo, and Lars Hernquist. Black Holes in Galaxy Mergers: The Formation of Red Elliptical Galaxies. The Astrophysical Journal Letters, 620:L79, 2005.

F. Stanley, C. M. Harrison, D. M. Alexander, A. M. Swinbank, J. A. Aird, A. Del Moro, R. C. Hickox, and J. R. Mullaney. A remarkably flat relationship between the average star formation rate and AGN luminosity for distant X-ray AGN. Monthly Notices of the Royal Astronomical Society, 453(1):591–604, 2015.

F. Stanley, D. M. Alexander, C. M. Harrison, D. J. Rosario, L. Wang, J. A. Aird, N. Bourne, L. Dunne, S. Dye, S. Eales, K. K. Knudsen, M. J. Michałowski, E. Valiante, G. De Zotti, C. Furlanetto, R. Ivison, S. Maddox, and M. W. L. Smith. The mean star formation rates of unobscured QSOs: searching for evidence of suppressed or enhanced star formation. Monthly Notices of the Royal Astronomical Society, 472(2):2221–2240, 2017.

G. Stasińska, N. Vale Asari, R. Cid Fernandes, J. M. Gomes, M. Schlickmann, A. Mateus, W. Schoenell, and L. Sodré. Can retired galaxies mimic active galaxies? Clues from the Sloan Digital Sky Survey. Monthly Notices of the Royal Astronomical Society: Letters, 391(1):29, 2008.

Lisa K. Steinborn, Klaus Dolag, Julia M. Comerford, Michaela Hirschmann, Rhea-Silvia Remus, and Adelheid F. Teklu. Origin and properties of dual and offset AGN in a cosmological simulation at z=2. Monthly Notices of the Royal Astronomical Society, 458:1013, 2016.

Aaron Stemo, Julia M Comerford, R Scott Barrows, Daniel Stern, Roberto J Assef, and Roger L Griffith. A Catalog of AGN Host Galaxies Observed with HST / ACS : Correlations between Star Formation and AGN Activity. The Astrophysical Journal, 888(2):78, 2020.

Aaron Stemo, Julia M. Comerford, R. Scott Barrows, Daniel Stern, Roberto J. Assef, Roger L Griffith, and Aimee Schechter. A Catalog of 204 Offset and Dual AGNs: Increased AGN Activation in Major Mergers and Separations under 4 kpc. The Astrophysical Journal, page Accepted, 2021.

Daniel Stern. The X-ray to Mid-Infrared Relation of AGNs at High Luminosity. The Astrophysical Journal, 807(2):129–134, 2015.

Daniel Stern, Peter Eisenhardt, Varoujan Gorjian, Christopher S Kochanek, Nelson Caldwell, Daniel Eisenstein, Mark Brodwin, Michael J I Brown, Richard Cool, Arjun Dey, Paul Green, Buell T Jannuzi, Stephen S Murray, Michael A Pahre, and S P Willner. Mid-Infrared Selection of Active Galaxies. The Astrophysical Journal, 631(1):163–168, 2005.

Daniel Stern, Roberto J. Assef, Dominic J. Benford, Andrew Blain, Roc Cutri, Arjun Dey, Peter Eisenhardt, Roger L. Griffith, T. H. Jarrett, Sean Lake, Frank Masci, Sara Petty, S. A. Stanford, Chao-Wei Tsai, E. L. Wright, Lin Yan, Fiona Harrison, and Kristin Madsen. Mid-Infrared Selection of Active Galactic Nuclei With the Wide-Field Infrared Survey Explorer. I. Characterizing WISE-Selected Active Galactic Nuclei in COSMOS. The Astrophysical Journal, 753(1):30–47, 2012.

Nathaniel R. Stickley and Gabriela Canalizo. Stellar velocity dispersion in dissipative galaxy mergers with star formation. Astrophysical Journal, 786(1), 2014.

John P. Stott, David Sobral, Ian Smail, Richard Bower, Philip N. Best, and James E. Geach. The merger rates and sizes of galaxies across the peak epoch of star formation from the HiZELS survey. Monthly Notices of the Royal Astronomical Society, 430(2):1158–1170, 2013.

Richard Tolman. On the Estimation of Distances in a Curved Universe With a Non-Static Line Element. Proceedings of the National Academy of Sciences of the United States of America, 16 (7):511–520, 1930.

Paul Torrey, T. J. Cox, Lisa Kewley, and Lars Hernquist. The metallicity evolution of interacting galaxies. Astrophysical Journal, 746(1), 2012.

E. Treister, K. Schawinski, C. M. Urry, and B. D. Simmons. Major Galaxy Mergers Only Trigger the Most Luminous Active Galactic Nuclei. The Astrophysical Journal Letters, 758(2):L39–L43, 2012.

Scott Tremaine, Karl Gebhardt, Ralf Bender, Gary Bower, Alan Dressler, S. M. Faber, Alexei V. Filippenko, Richard Green, Carl Grillmair, Luis C. Ho, John Kormendy, Tod R. Lauer, John Magorrian, Jason Pinkney, and Douglas Richstone. The Slope of the Black Hole Mass versus Velocity Dispersion Correlation. The Astrophysical Journal, 574(2):740, 2002.

M. Tremmel, M. Karcher, F. Governato, M. Volonteri, T. R. Quinn, A. Pontzen, V. Anderson, and J. Bellovary. The ROMULUS cosmological simulations: A physical approach to the formation, dynamics and accretion models of SMBHs. Monthly Notices of the Royal Astronomical Society, 470(1):1121–1139, 2017.

Jonathan R. Trump, Mouyuan Sun, Gregory R. Zeimann, Cuyler Luck, Joanna S. Bridge, Catherine J. Grier, Alex Hagen, Stephanie Juneau, Antonio Montero-Dorta, David J. Rosario, W. Niel Brandt, Robin Ciardullo, and Donald P. Schneider. The Biases of Optical Line-Ratio Selection for Active Galactic Nuclei and the Intrinsic Relationship Between Black Hole Accretion and Galaxy Star Formation. The Astrophysical Journal, 811(1):26, 2015.

Vivian U, Anne M. Medling, Hanae Inami, Lee Armus, Tanio Díaz-Santos, Vassilis Charmandaris, Justin Howell, Sabrina Stierwalt, George C. Privon, Sean T. Linden, David B. Sanders, Claire E. Max, Aaron S. Evans, Loreto Barcos-Muñoz, Charleston W.K. Chiang, Phil Appleton, Gabriela Canalizo, Giovanni Fazio, Kazushi Iwasawa, Kirsten Larson, Joseph Mazzarella, Eric Murphy, Jeffrey Rich, and Jason Surace. Keck OSIRIS AO LIRG Analysis (KOALA): Feedback in the Nuclei of Luminous Infrared Galaxies. The Astrophysical Journal, 871(2):166, 2019.

Sidney van den Bergh. A New Classification System for Galaxies. The Astrophysical Journal, 206: 883, 1976.

Sandor Van Wassenhove, Marta Volonteri, Lucio Mayer, Massimo Dotti, Jillian Bellovary, and Simone Callegari. Observability of Dual Active Galactic Nuclei in Merging Galaxies. The Astrophysical Journal Letters, 748(1):L7–L11, 2012.

S. Veilleux, D. C. Kim, D. S.N. Rupke, C. Y. Peng, L. J. Tacconi, R. Genzel, D. Lutz, E. Sturm, A. Contursi, M. Schweitzer, K. M. Dasyra, L. C. Ho, D. B. Sanders, and A. Burkert. A deep hubble space telescope h-band imaging survey of massive gas-rich mergers. ii. the quest QSOs. The Astrophysical Journal, 701:587, 2009.

M. Villar-Martín, C. Tadhunter, A. Humphrey, R. Fraga Encina, R. González Delgado, M. Pérez Torres, and A. Martínez-Sansigre. Interactions, star formation and extended nebulae in SDSS type 2 quasars at 0.3 z 0.6. Monthly Notices of the Royal Astronomical Society, 416(1):262–278, 2011.

C. Villforth, F. Hamann, D. J. Rosario, P. Santini, E. J. McGrath, A. v. d. Wel, Y. Y. Chang, Y. Guo, T. Dahlen, E. F. Bell, C. J. Conselice, D. Croton, A. Dekel, S. M. Faber, N. Grogin, T. Hamilton, P. F. Hopkins, S. Juneau, J. Kartaltepe, D. Kocevski, A. Koekemoer, D. C. Koo, J. Lotz, D. McIntosh, M. Mozena, R. Somerville, and V. Wild. Morphologies of z 0.7 AGN host galaxies in CANDELS: no trend of merger incidence with AGN luminosity. Monthly Notices of the Royal Astronomical Society, 439(4):3342–3356, 2014.

C. Villforth, T. Hamilton, M. M. Pawlik, T. Hewlett, K. Rowlands, H. Herbst, F. Shankar, A. Fontana, F. Hamann, A. Koekemoer, J. Pforr, J. Trump, and S. Wuyts. Host galaxies of luminous z ˜ 0.6 quasars: Major mergers are not prevalent at the highest AGN luminosities. Monthly Notices of the Royal Astronomical Society, 466(1):812, 2017.

M. Volonteri, P. R. Capelo, H. Netzer, J. Bellovary, M. Dotti, and F. Governato. Black hole accretion versus star formation rate: theory confronts observations. Monthly Notices of the Royal Astronomical Society: Letters, 452:L6, 2015a.

Marta Volonteri, Francesco Haardt, and Piero Madau. The Assembly and Merging History of Supermassive Black Holes in Hierarchical Models of Galaxy Formation. The Astrophysical Journal, 582(2):559–573, 2003.

Marta Volonteri, Pedro R. Capelo, Hagai Netzer, Jillian Bellovary, Massimo Dotti, and Fabio Governato. Growing black holes and galaxies: Black hole accretion versus star formation rate. Monthly Notices of the Royal Astronomical Society, 449:1470, 2015b.

Katherine E. Whitaker, Pieter G. Van Dokkum, Gabriel Brammer, and Marijn Franx. The star formation mass sequence out to z = 2.5. The Astrophysical Journal Letters, 754:L29, 2012.

Simon D. M. White and Carlos S Frenk. Galaxy Formation through Hierarchical Clustering. The Astrophysical Journal, 379:52–79, 1991.

Simon D. M. White and M.J. Rees. Core Condensation in Heavy Halos: a Two-Stage Theory for Galaxy Formation and Clustering. Monthly Notices of the Royal Astronomical Society, 183:341, 1978.

Vivienne Wild, Timothy Heckman, and Stephane Charlot. Timing the starburst-AGN connection. Monthly Notices of the Royal Astronomical Society, 405(2):933–947, 2010.

Edward L. Wright, Peter R. M. Eisenhardt, Amy K. Mainzer, Michael E. Ressler, Roc M. Cutri, Thomas Jarrett, J. Davy Kirkpatrick, Deborah Padgett, Robert S. McMillan, Michael Skrutskie, S. A. Stanford, Martin Cohen, Russell G. Walker, John C. Mather, David Leisawitz, Thomas N. Gautier, Ian McLean, Dominic Benford, Carol J. Lonsdale, Andrew Blain, Bryan Mendez, William R. Irace, Valerie Duval, Fengchuan Liu, Don Royer, Ingolf Heinrichsen, Joan Howard, Mark Shannon, Martha Kendall, Amy L. Walsh, Mark Larsen, Joel G. Cardon, Scott Schick, Mark Schwalm, Mohamed Abid, Beth Fabinsky, Larry Naes, and Chao-Wei Tsai. the Wide-Field Infrared Survey Explorer (Wise): Mission Description and Initial on-Orbit Performance. The Astronomical Journal, 140(6):1868–1881, 2010.

H.K.C. Yee. A Faint-Galaxy Photometry and Image-Analysis System. Publications of the Astronomical Society of the Pacific, 103(April):396–411, 1991.

Qingjuan Yu, Youjun Lu, Roya Mohayaee, and Jacques Colin. The low frequency of dual active galactic nuclei versus the high merger rate of galaxies: A phenomenological model. The Astrophysical Journal, 738(1):92, 2011.